UNIVERSITÉ DE STRASBOURG

THÈSE présentée par :

Marianna MARINONI

soutenue le : **3 mai 2018**

pour obtenir le grade de : **Docteur de l'université de Strasbourg**

Discipline/ Spécialité : Hydrologie

Implémentation des isotopes dans un modèle hydrogéochimique couplé

Implementation of isotopes into coupled hydrogeochemical modeling

THÈSE dirigée par :
  Philippe ACKERER   Directeur de Recherche, CNRS, Université de Strasbourg

RAPPORTEURS :
  Olivier BILDSTEIN   Directeur de Recherche, CEA, Cadarache
  Yves GODDÉRIS   Directeur de Recherche, CNRS, GET OMP, Toulouse

AUTRES MEMBRES DU JURY :
  Jesús CARRERA   Directeur de Recherche, CSIC, UPC, Barcelone
  Monica RIVA   Professeur, DICA, Politecnico di Milano, Milan

Summary

List of figures

XIII

XVII

List of tables

List of recurrent symbols

Flow and Transport

Symbol	Description	Unit
h	Hydraulic head	[L]
q	Flow rate	[L/T]
K	Conductivity tensor	[L/T]
ρ	density	[M^3/L^3]
ϕ	porosity	
ϕ_e	Effective porosity	
$L(-)$	Transport operator	
$S(-)$	Source term	
α_L	Longitudinal dispersivity	[L]
α_T	Transverse dispersivity	[L]
D	Dispersion tensor	[L^2/T]
D_m	Pore water diffusion coefficient	[L^2/T]

Reaction

Symbol	Description	Unit
[-]	Concentration	[mol/L^3]
{-}	Activity	
α	Isotopic fractionation factor	
A_s	Reactive surface area	[L^2-min/M$_{H2O}$] or [L^2-min/L$^3_{H2O}$]
$a_{i,j}$	Entry of the Stoichiometric matrix for mass action law	
$b_{i,j}$	Entry of the Stoichiometric matrix for mass conservation	

$bcp_{i,j}$	Entry of the Stoichiometric matrix for mass conservation (for solid phase)	
$Beq_{i,j}$	Entry of matrix linking kinetic reactions and primary species	
C_i [1]	Generic species (primary or secondary) at thermodynamic equilibrium	
X_j	Generic primary species at thermodynamic equilibrium	
ξ	$= \ln\{X\}$ unknown of the thermodynamic problem	
Cc_i [1]	Generic kinetic species	
Cp	Generic solid phase at thermodynamic equilibrium	
δ	Isotopic delta	
ε	fractionation	
γ	Activity coefficient	
λ	Activity coefficient for solid solutions	
G	DASPK residuals	
I	Ionic strength	
IC	Isotope concentration	
$\boldsymbol{J}$	Jacobian matrix	
$J_{i,j}$	Entry of the Jacobian matrix	
k	Kinetic constant	[mol/T/L-min^2]
K_i	Equilibrium constant	
K_{EM}	Solubility product of an end member	
K_{pi}	$1/K_S$	
K_S	Solubility product	
K_{SS}	Equilibrium constant for the whole solid solution	
m,n	Exponents in TST reaction rate	
$\boldsymbol{\nu}, \boldsymbol{\nu^*}$	Matrix linking reactions and generic species	
Nc	Number of species	
NCc	Number of kinetic species	

Ncp	Number of equilibrium precipitates	
N_{EM}	Number of end members in a single solid solution	
Nr	Number of reactions	
Nrc	Number of kinetic reactions	
Nss	Number of solid solutions	
Nt	Number of species ($Nc + NCc$)	
Nx	Number of primary species	
N_{Xss}	Number of end members in a solid solution	
Q	Ionic product	
Q_{SS}	Ionic product of the solid solutions	
$R\#$	Reaction number #	
${}^{i}r_{\#}$	Reaction rate of reaction number #	[mol/T/ M_{H2O}] or [mol/T/ L^3_{H2O}]
${}^{i}R(\text{-})$	Isotope Ratio	
SI, Ω	Saturation Index	
t	time	
T^d	Dissolved total for speciation	[mol/L^3]
T^f	Fixed total for speciation	[mol/L^3]
T_j	Total for speciation	[mol/L^3]
x	Mole fraction	
Xss	Number of moles of an end member	[mol]
Xss_{TOT}	Total number of moles of the solid solutions	[mol]
Y	Residual function	[mol/L^3]
z	charge	

[1] Please note that sometimes this symbol is also used to identify concentration of species C_i. This is done to speed up notation when there is no risk of confusing concentrations and activities and it is always declared in the text.

Acknowledgments

This work is the result of the time and the efforts provided by many valuable people. Philippe Ackerer, my advisor, encouraged me from day one: without his positive guidance none of these three hundred and something pages would have existed. I also want to thank my other, non-official advisors: Jérôme Carrayrou, who spent an insane amount of time staring at the screen by my side, always with enthusiasm, and Alain Clément who never denied patient, meticulous advice.

Thank you also to Marwan Fahs, whose contributions on numerical methods have been more than precious, and Fred Delay, whose words of encouragement always came at the right time. A huge thank you is also due to Arnaud Bouissonnié and Damien Daval, who provided experimental results that made an important part of this work possible.

To all these wonderful people: you are not only full of knowledge, you are also full of kindness.

Introduction générale en Français

In order to respect the respect the constraints imposed by the University of Strasbourg, around 10 % of the manuscript must be written in French language. For this reason, an introduction, conclusions and perspective are also presented in French. Besides these initial and final sections, the whole manuscript is in English.

La modélisation hydrogéochimique repose sur un ensemble de formulations mathématiques et de techniques numériques utilisées pour simuler l'évolution spatio-temporelle de certaines espèces chimiques qui peuvent être présentes dans le sol et déplacées par un flux d'eau. Les espèces chimiques ne sont pas inertes au cours de leur déplacement mais interagissent entre elles et avec le sol, modifiant potentiellement ses propriétés physiques. La modélisation hydrogéochimique est couramment connue sous le nom de *transport réactif,* mais il s'agit d'un raccourci qui n'est pas forcément légitime.

Le transport réactif est en réalité un terme générique regroupant des phénomènes qui sont bien plus nombreux et complexes que la modélisation hydrogéochimique seule : par exemple, le transport réactif peut englober des phénomènes mécaniques et thermiques et peut également traiter des fluides autres que l'eau.

Les premiers travaux sur le transport réactif datent d'une trentaine d'années (1990's) et ont été depuis appliqués à de nombreux domaines : en complément à la recherche fondamentale pour aider à la compréhension des mécanismes naturels, pour suivre l'évolution des polluants dans les sols, pour améliorer les connaissances des différents paramètres à prendre en compte dans la gestion durable et le stockage de déchets radioactifs ou encore pour étudier les effets de l'injection de dioxyde de carbone (CO_2) dans les sols. Une vision globale sur le transport réactif, allant de son histoire, jusqu'à son potentiel et ses limites, a déjà été présentée par Steefel et al., (2005).

L'une des caractéristiques qui fait du transport réactif un sujet compliqué est la très forte variabilité de l'échelle spatio-temporelle des phénomènes impliqués. La très forte variabilité, à l'échelle spatio-temporelle, des phénomènes impliqués, rend la compréhension du transport réactif complexe. En effet, l'échelle spatiale peut varier du pore (nanométrique jusqu'à décimétrique) jusqu'à l'aquifère (métrique à kilométrique) tandis que l'échelle temporelle peut s'étendre de la durée d'une expérience en laboratoire jusqu'à des processus naturels durant plusieurs millions d'années. Selon l'échelle spatiale étudiée, différents modèles peuvent être utilisés : *single continuum* (un unique milieu poreux), *pore scale* (valide uniquement à l'échelle du pore) et des modèles de type *multiple continua* (qui prennent en considération une certaine hétérogénéité du milieu poreux).

Même si de nombreuses études ont été effectuées sur la modélisation à l'échelle du pore (modèle 'pore scale'; Yoon et al., 2015 et références associées) et sur les modèles du type *multiple continua* (Pruess and Narasimhan, 1982; MacQuarrie and Mayer, 2005), les modèles 'single continuum' restent les plus utilisés pour décrire le transport et les réactions chimiques; la description mathématique de ces modèles est assurée par des équations aux dérivées partielles (EDP) qui seront présentées au cours de ce manuscrit.

Dans ce travail, seul un modèle du type *single continuum* est présenté, non pas parce que cette méthode est considérée comme étant la meilleure mais parce qu'il s'agit d'une méthode légitime et largement appliquée. En appliquant un modèle single continuum, les propriétés du sol sont moyennées sur un volume de contrôle, qui possède les caractéristiques suivantes :

1) les phases solide, liquide et gaz coexistent dans un point de l'espace ;

2) les réactions hétérogènes sont traitées comme homogènes et l'interface est considérée comme une caractéristique moyenne du volume de contrôle ;

3) le flux d'eau dans le volume de contrôle est décrit par la loi de Darcy et il est donc proportionnel à la charge hydraulique ;

4) les gradients de concentration sont considérés nuls dans le volume de contrôle.

Si les hypothèses ci-dessus ne constituent pas une simplification excessive, alors un modèle de type single continuum peut être appliqué. Les équations utilisées pour décrire ce modèle ainsi que les méthodes et algorithmes utilisés pour les résoudre seront présentés dans cette introduction et détaillés au cours de ce travail.

Les principaux modèles mathématiques

Le bilan de masse du fluide (l'eau) est effectué à l'échelle d'un volume de contrôle et les flux sont exprimés suivant la loi de Darcy :

$$\begin{cases} \nabla \cdot \left(\rho \mathbf{q} \right) + \dfrac{\partial(\rho\phi)}{\partial t} = 0 \\ \mathbf{q} = -\nabla \cdot \mathbf{K} \nabla h \end{cases}$$

où $\mathbf{q}$ [L/T] représente le flux de Darcy, ρ [M$_3$/L$_3$] la densité du fluide, ϕ [-] la porosité (le rapport entre le volume des pores et le volume du milieu poreux), $\mathbf{K}$ la matrice de conductivité hydraulique [L/T] et h, la charge hydraulique [L]. La porosité et la conductivité hydraulique sont deux des propriétés qui sont considérées comme constantes à l'échelle du volume de contrôle. Il est à noter qu'à l'échelle du pore la loi de Darcy n'est plus applicable et doit être remplacé par la loi de Navier-Stokes.

En résolvant le système précédent, une distribution spatiale de la charge hydraulique h et du flux $\mathbf{q}$ est disponible et peut être utilisée pour résoudre l'équation décrivant le transport de solutés. La solution du système est normalement obtenue par voie numérique, soit par différences finies soit par éléments finis (Istok, 1989).

Le transport d'une espèce chimique est décrit par une équation différentielle aux dérivées partielles qui décrit les changements de concentration dans l'espace et le temps. Quand le transport n'est pas conservatif mais réactif, alors un terme source apparait dans l'équation aux dérivées partielles et fournit un lien entre le transport et les réactions :

$$\begin{cases} \dfrac{\partial(\phi_e C_i)}{\partial t} + \nabla.(\mathbf{q}C_i - \mathbf{D}.\nabla C_i) = -\left(\sum_{j=1}^{Nr} v_{ij}S_j + \sum_{m=1}^{Nm} v_{im}S_m \right) \\ \mathbf{D} = D_m \mathbf{I} + (\alpha_L - \alpha_T)\dfrac{\mathbf{qq}}{|\mathbf{q}|} + \alpha_T |\mathbf{q}| \mathbf{I} \end{cases}$$

où ϕ_e [-] représente la porosité efficace, C_i [mol/L$_3$] la concentration d'une espèce primaire i, $\mathbf{D}$ la matrice de dispersion [L$_2$/T], α_L, α_T les dispersivités longitudinale et transversale [L], D_m le coefficient de diffusion dans le milieu poreux [L$_2$/T], $\mathbf{I}$ la matrice unité; S_j [mol/L$_3$/T] et S_m [mol/L$_3$/T] sont les vitesses des réactions homogènes (dans la phase aqueuse) et hétérogènes (avec une phase solide); v représente le coefficient stœchiométrique [-], Nr le nombre de réactions et $\mathbf{q}$ [L/T] le flux de Darcy connu grâce à la résolution du problème d'écoulement.

Une solution analytique pour un problème de transport conservatif n'existe qu'en conditions très simplifiées (milieu homogène, vitesse uniforme, …), et l'on doit recourir aux méthodes numériques comme les différences finies ou les éléments finis (Steefel and MacQuarrie, 1996) pour résoudre cette équation.

Les phénomènes chimiques sont très variés (spéciation, précipitation, adsorption…) et ils sont décrits soit par des modèles à l'équilibre thermodynamique, soit par des modèles cinétiques. Leurs influences sur un problème de transport réactif sont assurées par un terme puits/source dans les équations du transport. Plusieurs espèces présentes simultanément peuvent interagir. Les interactions sont représentées par le premier terme source avec les coefficient v_{ij}.

Les réactions chimiques, qu'il s'agisse d'un modèle à l'équilibre thermodynamique ou d'un modèle cinétique, et le système du transport peuvent être résolus en un seul système d'équations (approche globale) ou séparément (approche séquentielle). Les deux approches sont présentées dans les paragraphes suivants et détaillées dans le chapitre 6.

Les techniques de couplage: séparation d'opérateur et approche globale

En l'absence de modification de densité et de viscosité, les équations décrivant l'écoulement et le transport peuvent être résolues séparément. Ce n'est pas le cas pour le transport réactif où les processus chimiques et de transport interagissent. La stratégie retenue pour décrire ce couplage est essentielle dans la modélisation du transport réactif. D'une part, il est possible de substituer les équations décrivant la chimie dans le système du transport et résoudre un système d'équations non linéaires avec de très nombreuses inconnues,. Dans ce cas, on parle de méthode globale. D'autre part, il est possible de résoudre le transport et la chimie d'une façon séquentielle (et éventuellement itérative). Dans ce cas, on parle de séparation d'opérateur. Une présentation très pédagogique des deux techniques a été réalisée par Steefel and MacQuarrie (1996).

L'approche globale est sans doute plus difficile à mettre en place mais permet d'éviter les erreurs de couplage ; même si la capacité de calcul devient de plus en plus importante, la solution des systèmes globaux pour des problèmes en trois dimensions peut encore générer des temps de calcul critiques. Au contraire, même si la séparation d'opérateur génère une erreur de couplage, elle est beaucoup plus adaptable et permet le couplage de différentes méthodes spécifiques pour la solution du transport et de la chimie.

Même si les deux approches numériques sont allées jusqu'à créer des écoles de pensée, la supériorité d'une approche sur l'autre n'a pas encore été prouvée et elle reste sans doute très dépendante du problème étudié (Fahs et al., 2008).

Le fait d'adopter une approche de séparation d'opérateur ouvre d'autres problématiques spécifiques à l'opérateur de chimie et notamment dans le cas d'une modélisation de l'équilibre thermodynamique. En effet, deux voies sont possibles : la minimisation de l'énergie de Gibbs d'un côté et l'écriture des lois d'action de masse de l'autre. Comme pour le débat sur l'approche globale/séparation d'opérateur, chacune des méthodes présente des avantages et des inconvénients, très souvent liés au problème étudié. Néanmoins, la plupart des codes destinés à la simulation des réactions biogéochimiques utilisent une approche basée sur les lois d'action de masse.

Un univers de codes pour la simulation du transport réactif

Un état de l'art détaillé des codes de transport réactif peut être retrouvé dans le travail de Steefel et al. (2015) ; il s'agit d'une comparaison des caractéristiques numériques et des capacités de douze codes de transport réactif parmi les plus connus : PHREEQC, HP1, PHT3D, OpenGeoSys, HYTEC, ORCHESTRA, TOUGHREACT, eSTOMP, HYDRO-GEOCHEM, CrunchFlow, MIN3P, PFLOTRAN.

Certains de ces codes sont des évolutions de code biogéochimique, comme par exemple PHREEQC, d'autres sont des plateformes très avancées sur le couplage de logiciels pour la simulation de processus chimiques et physiques les plus variés (OpenGeoSys).

Ces codes ne sont qu'une fraction de tous ceux disponibles pour la résolution d'équation de transport réactif et des modules de chimie. De nombreux autres codes sont mis à disposition d'un utilisateur intéressé, parmi lesquels : CHEPROO (Bea et al., 2009), CORE2D (Samper et al., 2009), GEM-Selektor (Kulik et al., 2012), GEOCHEM-EZ (Shaff et al., 2010), GWB Geochemist's WorkBench (Bethke, 2008), RETRASO (Saaltink et al., 2004), WITCH (Goddéris et al., 2006).

En ce qui concerne la simulation de l'écoulement, dix des douze codes analysés par Steefel et al. (2015) sont capables de simuler des problèmes 3D, neuf intègrent l'équation de Richards pour l'écoulement dans un milieu non saturé, huit peuvent travailler à densité variable et six en régime non-isotherme.

Concernant le transport, l'observation la plus marquante est que seulement un code sur douze utilise une matrice de dispersion complète. TOUGHREACT travaille sans dispersion et les dix autres codes utilisent un tenseur diagonal. Neuf codes sur douze peuvent travailler dans le contexte *multiple continua*.

D'un point de vue géochimique, les modèles de Debye-Hükel et de Davies pour le calcul d'activité, les variations de température, la complexation de surface, l'échange ionique, les échanges entre une phase aqueuse et gazeuse, la précipitation cinétique des minéraux et les cinétiques de Monod pour la croissance bactérienne sont considérés comme la base dans tous les codes. Le modèle d'activité de Pitzer et la nucléation minérale, qui sont implémentés dans, respectivement, quatre et six codes sont moins couramment considérés. Neuf codes ont été déclarés capables de traiter les solutions solides.

L'implémentation des isotopes est très récente par rapport aux premières versions des codes de calcul (Wanner and Sonnenthal, 2013; Druhan et al., 2013) et est sans doute motivée par la disponibilité croissante de données isotopiques. Sept codes peuvent traiter le fractionnement isotopique à l'équilibre thermodynamique et huit le fractionnement isotopique cinétique.

D'un point de vue numérique, il n'y a que trois codes parmi les douze analysés dans l'étude de Steefel et al. (2015) qui travaillent avec une approche globale (MIN3P, CrunchFlow, PFLOTRAN), et deux parmi eux (CrunchFlow, PFLOTRAN) permettent également de travailler en séparation d'opérateur.

Finalement, en ce qui concerne le calcul parallèle (la possibilité de distribuer les calculs sur plusieurs processeurs), seul la moitié des codes exploitaient cette technique informatique en 2015.

1.5 Les modèles numériques au LHyGeS

Le patrimoine de modèles numériques au Laboratoire d'Hydrologie et de Géochimie de Strasbourg (LHyGeS) est bien documenté. Plusieurs codes ont été développés au cours des dernières décennies pour la simulation de la réactivité minérale (KINDIS (Madé et al., 1994)), pour la réactivité minérale

couplée avec le transport 1D (KIRMAT, (Gérard et al., 1998)), pour les réactions géochimiques plus générales (SPECY, (Carrayrou et al., 2002)), pour le transport conservatif (TRACES) et de nombreux autres codes pour des problèmes d'hydrologie plus spécifiques (Pan et al. 2015; Weill et al. 2017, Jeannot et al. 2018).

Néanmoins, l'évolution des modèles géochimiques, des méthodes numériques et des techniques informatiques est constante et la mise à jour des codes est nécessaire pour assurer leur survie.

Même si KINDIS est un outil très puissant, et qui t a été appliqué à des très nombreux cas réels, il a deux limitations principales : il n'est pas bien adapté au couplage avec un code de transport multidimensionnel et il a été spécifiquement construit pour la réactivité minérale. SPECY, à l'opposé, a été conçu depuis le début comme un outil avec de nombreuses possibilités d'application et pour être couplé avec des codes de transport. Malgré son potentiel, SPECY n'a été exploité que partiellement pour la simulation de problèmes géochimiques, et est considéré plutôt comme un laboratoire pour expériences numériques.

Bien que TRACES ait été initialement conçu comme un outil pour la simulation du transport réactif, les réaction chimiques prises en compte sont très limitées. La méthode numérique des éléments finis mixtes et discontinus utilisée pour résoudre l'équation décrivant le transport est une des plus performantes et le code a été utilisé surtout pour la simulation du transport conservatif.

Le but de cette thèse est donc de développer un outil pour la simulation des réactions biogéochimiques qui regroupe toutes les capacités des modèles existants en y ajoutant certaines fonctionnalités, comme par exemple le traitement des isotopes dans un environnement numérique moderne. L'outil est conçu comme un module qui doit être adaptable pour être couplé avec d'autres codes, initialement avec TRACES, pour produire un outil fiable pour la simulation du transport réactif.

Compte tenu des codes existants, il est nécessaire de se poser la question de l'utilité d'un autre code pour la simulation du transport réactif. Il faut donc souligner que le but de ce travail n'est pas de cloner un des codes existant ais de créer une alternative qui soit, le plus possible, contrôlable, adaptable, fiable et efficace.

Par ailleurs, Carrayrou et al. (2010) ont montré à l'aide des benchmarks MoMaS que des codes différents peuvent produire des résultats différents, mettant en évidence la nécessité d'avoir plusieurs possibilités de comparaison. Il faut aussi se rappeler que, même si la plupart des codes sont disponibles pour un public scientifique, très peu des codes source sont accessibles. De plus, même si les manuels d'utilisation de ces codes sont de très haute qualité, la compréhension et l'usage correct des dits codes ne sont pas triviaux. De ce fait, les scientifiques souhaitant utiliser de tels codes pour leurs études expérimentales où théoriques rencontrent de nombreuses difficultés d'utilisation après avoir téléchargé un code de transport réactif. En conclusion, l'outil développé dans ce travail est pensé pour contribuer à l'activité expérimentale et comme une base solide pour des futurs développements numériques ; ce manuscrit, est principalement adressé à ceux qui vont potentiellement continuer ce

travail, en fournissant une description détaillée de la modélisation du transport réactif au LHyGeS, de son potentiel et de ses limites.

1.6 Structure du manuscrit

L'implémentation des isotopes dans un code pour la simulation du transport réactif est présentée au cours du chapitre 2. Une étude bibliographique exhaustive a été menée sur le sujet, et a permis de conclure que les isotopes peuvent être introduits dans un code de transport réactif sous la forme d'espèces indépendantes. Le deuxième chapitre s'attache également à l'intérêt croissant porté aux fractionnements isotopiques, qui sont très souvent utilisés comme traceurs de processus et de mécanismes dans de nombreux domaines scientifiques. Traiter les isotopes comme des espèces indépendantes implique d'une part que, pour traiter les isotopes, il ne faut quasiment aucune modification des algorithmes déjà utilisés pour traiter les espèces classiques, et, d'autre part, que cette façon de travailler met en avant la nécessité d'avoir des codes numériquement toujours plus fiables et efficaces.

Les chapitres entre 3 et 5 sont dédiés à la construction de l'opérateur de chimie. Les chapitre 3 est dédié à l'équilibre thermodynamique : l'approche des espèces et des composantes (espèces secondaires et primaires, respectivement) pour une formulation du type loi d'action de masse est introduite avec les méthodes de solution des systèmes non-linéaires qui décrivent le problème. Au cours de ce chapitre, les inconvénients de la méthode de Newton Raphson pour résoudre des systèmes non-linéaires sont mis en évidence et certaines améliorations sont proposées.

Plus précisément, dans le contexte de séparation d'opérateur adopté dans ce travail, le calcul de l'équilibre thermodynamique est un point crucial pour la résolution des problèmes de géochimie. En effet, pour les très grandes échelles temporelles, l'hypothèse d'équilibre peut être justifiée. De plus, dans le contexte d'un mélange de réactions cinétiques et à l'équilibre thermodynamique, l'intégration des équations différentielles commence toujours par une solution à l'équilibre. Des algorithmes adaptés au calcul du mélange équilibre/cinétique peuvent également nécessiter le calcul de l'équilibre thermodynamique (c'est le cas pour le modèle QSSA). Il est donc très rare de résoudre un problème de géochimie en négligeant l'équilibre thermodynamique.

Dans un contexte de phénomènes transitoires, le problème du temps de calcul devient important. Un gain d'efficacité dans une seule opération peut se traduire en une réduction important des temps de calcul globaux. De plus, quand une opération ne converge pas, la simulation de transport réactif peut être compromise dans son entièreté. Les problèmes de robustesse et d'efficacité des méthodes numériques ne sont donc pas secondaires et une importante quantité de travail a été dédiée au développement de techniques numériques pour l'amélioration de la méthode de Newton Raphson, une des techniques les plus utilisées pour la solution de l'équilibre thermodynamique.

Le problème principal de cette méthode est lié à la résolution d'un système linéaire par itération, ce qui peut rapidement devenir compliqué si le système est mal conditionné (ce qui arrive quand la matrice des dérivées du système non-linéaire, ou matrice Jacobienne, est mal conditionnée).

Les techniques qui ont été testées pour augmenter la vitesse et le taux de convergence de la méthode de Newton Raphson sont (i) le scaling de la matrice Jacobienne, (ii) le couplage d'une méthode d'ordre zéro qui évite le calcul de la matrice Jacobienne.

La formulation du système non-linéaire, le fonctionnement de la méthode de Newton Raphson et ses problématiques, le concept de conditionnement et les solutions proposées sont présentées sous forme d'un article publié dans *American Journal of Chemical Engineering* (AiChE Journal) en 2016.

Le chapitre 3 se termine avec une courte section dédiée aux modèles implémentés qui travaillent à l'équilibre thermodynamique.

Le chapitre 4 contient une étude sur la formulation des problèmes lors d'un mélange de réactions à l'équilibre thermodynamique et cinétiques. Dans un contexte où l'on applique les lois d'action de masse, un système d'équations différentielles et algébriques est construit. Dans ce chapitre, il est expliqué comment parvenir à ce système en partant de considérations mathématiques ou à travers une schématisation intuitive des processus.

Sur la base de la littérature consultée, le système a été écrit sous trois formes pour deux cas test et résolu avec le *solver* DASPK (qui adopte une méthode de solution implicite). Une comparaison avec la méthode explicite QSSA implémentée dans SPECY (Carrayrou et al., 2002) est également mise en place. Un des cas test est difficile à résoudre d'un point de vue numérique et l'autre pose des problématiques de formulation du système, en permettant d'identifier les faiblesses de chaque formulation. Pour chaque formulation, le solver DASPK a été testé dans son mode de fonctionnement automatique (la matrice Jacobienne est calculée numériquement) et avec une solution analytique de la matrice Jacobienne.

Le chapitre 5 est dédié aux solutions solides, qui sont des mélanges (non uniquement mécaniques) de plusieurs minéraux. Bien que le concept de solution solide ait déjà été introduit dans le chapitre 2 en connexion avec les isotopes, certaines limites conceptuelles sont discutées. Si la thermodynamique des solutions solides est bien connue, et que ses fondations théoriques sont consolidées, la même chose n'est pas vraie pour leur comportement cinétique.

Deux applications des solutions solides sont présentées : une simulation en système de batch et la simulation d'un précipité composé de fer et chrome lors d'une expérience de transport réactif. La première application permet de vérifier l'algorithme et la cohérence des résultats avec celle d'un autre code (PHREEQC) et la deuxième démontre le potentiel du code développé dans ce travail.

Le couplage entre le module du transport et de chimie et l'implémentation des isotopes sont analysés dans le chapitre 6. Le code pour la simulation du transport réactif qui résulte de ce couplage sera baptisé SpeCTr (Spéciation, Cinétique, Transport). Le chapitre contient aussi une analyse plus détaillée des différentes techniques de couplage (approche globale, séparation d'opérateur) et des

algorithmes qui lient le module du transport et de chimie ainsi que des considérations sur le choix du pas te temps de transport.

Le cas test utilisé pour la vérification du code est un benchmark sur le fractionnement du chrome (proposé par Wanner et al., 2015) et les résultats obtenus avec SpeCTr correspondent à ceux qui avaient été obtenus avec, par exemple, MIN3P et CrunchFlow.

Le septième et dernier chapitre montre le potentiel de SpeCTr à travers son application à un cas de dissolution et précipitation de calcite. Plusieurs modèles de dissolution ont été testés pour la modélisation de résultats expérimentaux obtenus pendant l'étude de dissolution de cristaux de calcite.

Pour ce cas d'étude, des simulations en 1D, 2D et 3D sont proposées afin de montrer l'influence de l'écoulement sur les vitesses de réaction et essayer de réduire la différence entre les taux de réaction mesurés en laboratoire et celles ayant lieu à l'échelle macroscopique.

Le but de cette modélisation n'est pas de calibrer des paramètres pour trouver une correspondance avec les résultats expérimentaux mais, au contraire, de trouver d'autres moyens pour rapprocher les résultats de laboratoire et ceux qui sont mesurés à grand échelle.

Encore, la précipitation du carbonate de Calcium est présentée dans ce chapitre en comparaison avec des résultats publiés par Katz et al. (2009) ; ces simulations ramènent l'attention sur les modèles de changement de porosité et sur leurs implications numériques.

Chapter 1 - General introduction

1.1 Reactive transport

If one were asked to explain what *hydrogeochemical modeling* is to a ten-year-old, a solution would be to say that it is the ensemble of techniques capable to simulate the evolution in space and time of some chemicals that may be moving through the ground transported by water. Chemicals do not remain passive throughout the journey but interact with each other and with the ground, potentially changing its properties. Hence the more familiar term under which hydrogeochemical modeling is known: *reactive transport*.

As usually happens, the truth is far more complicated. Reactive transport modeling is indeed much more than the fore-mentioned process; it is an umbrella covering theoretical, mathematical and numerical tools able to describe the complex patterns of phenomena that take place in the Earth. In fact, *hydrogeochemical modeling* can be intended as a subsection of the wider network of reactive transport, which may include other phenomena such as mechanical or thermal effects, and might deal with fluids other than water.

First reactive transport related studies date back to the eighties of the previous century. Reactive transport has since been applied for various purposes: as a complement to fundamental research in the understanding of natural phenomena, as a monitoring tool of pollutant migration, as a predictive tool to assess the suitability of nuclear waste repository sites or feasibility of carbon dioxide sequestration. An extensive overview of reactive transport modeling, its history, capabilities, and limitations can be found in (Steefel et al. 2005).

One of the characteristics that make reactive transport modeling challenging is the variability of space scales (from pore to aquifer scale) and time scales (from the duration of an experiment to some million years). According to the scale at which the problem is intended to be studied, different models are available: single continuum, pore scale, and multiple continua models. Although pore scale (Yoon et al. 2015 and references therein) and multiple continua models (Pruess and Narasimhan 1982; MacQuarrie and Mayer 2005) are the subjects of multiple studies, single continuum models are, for the moment, those conventionally applied to describe flow, transport and chemical reactions; they are mathematically described by Partial Differential Equations (PDEs) which will be introduced in the next pages.

This work is entirely based on a single continuum approach, not because this method is somehow considered *better* than others but because it is one of the legitimate, widely applied approaches. According to single continuum model, soil properties are averaged over a representative elementary volume (REV) within which the following assumptions are valid:

1) Solid, liquid and gaseous phases all coexist at a single point in space;

2) Heterogeneous reactions are treated as homogeneous and the interface surface is treated as an averaged property;

3) Flow within the porous medium is described through Darcy's law i.e. is proportional to the hydraulic head gradient;

4) No gradients of concentration exist within the elementary volume.

If assumptions 1 to 4 do not represent an excessive simplification of the reality that is intended to be modeled, then the application of single a continuum model is legitimate. Governing equations, their solution strategies and the algorithms employed are introduced in the following paragraphs of the Introduction and will be described throughout the whole manuscript, constituting the very core of this work.

1.2 Governing equations

As anticipated in one of the assumptions, single continuum model description of flux involves both mass balance equation and Darcy's Law (which ceases to be valid at the pore scale, where Navier-Stokes equations take over):

$$\begin{cases} \nabla \cdot \left(\rho \mathbf{q} \right) + \dfrac{\partial(\rho\phi)}{\partial t} = 0 \\ \mathbf{q} = -\nabla \cdot \mathbf{K}\nabla h \end{cases} \tag{1.1}$$

where $\mathbf{q}$ [L/T] is the Darcy flux, ρ [M^3/L^3] is the fluid density, ϕ [-] is the porosity, defined as the ratio between the volume of the voids and the volume of the porous medium, $\mathbf{K}$ is the hydraulic conductivity [L/T] tensor and h is the hydraulic head [L]. Porosity and hydraulic conductivity are an example of the fore-mentioned properties that are considered constants within the elementary volume. Substituting the second equation into the first in system (1.1) provides a differential equation function of h to be integrated together with required Neuman or Dirichlet boundary conditions and initial conditions. The solution of system (1.1), provides a spatial distribution of h and $\mathbf{q}$ which is useful for the solution of transport equations. The solution of system (1.1) may be obtained analytically (for very simple configurations) or through numerical methods such as finite differences of finite elements (Istok 1989).

Transport of a single species in a single continuum model is described by a diffusion/dispersion type partial differential equation (PDE) that determines the variations of concentration in space and time. When transport is not conservative, but *reactive*, a source term appears in the PDE, providing a link between transport and reactions:

$$\begin{cases} \dfrac{\partial(\phi_e C_i)}{\partial t} + \nabla.(\mathbf{q}C_i - \mathbf{D}.\nabla C_i) = -\left(\sum_{j=1}^{Nr} v_{ij}S_j + \sum_{m=1}^{Nm} v_{im}S_m \right) \\ \mathbf{D} = D_m\mathbf{I} + (\alpha_L - \alpha_T)\dfrac{\mathbf{qq}}{|\mathbf{q}|} + \alpha_T|\mathbf{q}|\mathbf{I} \end{cases}$$

(1.2)

where ϕ_e [-] is the effective porosity, C_i [mol/L^3] is the concentration of the ith (primary) species, $\mathbf{D}$ is the dispersion tensor [L^2/T], α_L, α_T are the longitudinal and transverse dispersivity [L], D_m is the pore water diffusion coefficient [L^2/T], $\mathbf{I}$ the unit tensor; S_j [mol/L^3/T] and S_m [mol/L^3/T] are the homogeneous (aqueous phase) and heterogeneous (mineral) source terms (reaction rates), respectively; v stands for the stoichiometric reaction coefficients [-], Nr is the number of reactions and $\mathbf{q}$ [L/T] is the Darcy flux known from the solution of system (1.1).

Analytical solutions for conservative transport exist only for extremely simple, homogeneous regular domains. More likely, system (1.2) is solved through numerical methods such as finite differences or finite elements (Steefel and MacQuarrie 1996).

Chemical phenomena are various (speciation, precipitation, absorption to cite only a few) and described by a number of models (thermodynamic equilibrium, kinetic reactions). Their influence over a reactive transport problem is accounted for through the source terms in the right-hand side of equation (2). If multiple chemical species Ci are present, and a certain number (*Nr*) of chemical reactions take place, coefficient v_{ij} chooses whether or not reaction *j* has an impact on species C_i.

Chemical reactions are described by a number of different models, i.e. algebraic and differential equations that can be solved simultaneously with system (1.2) or separately. The two different approaches are introduced in the following paragraph and detailed in a dedicated Chapter.

1.3 Coupling techniques: operator splitting and global approach

Systems (1.1) and (1.2) are decoupled, therefore they can be solved subsequently. On the contrary, transport and reaction equations are coupled. The approach chosen to solve these two groups of equations represents another watershed in reactive transport modeling. On one hand, it is possible to substitute reaction equations in system (1.2) and to solve a wide, heavy system of differential equations through for example Newton Raphson Method (global approach); on the other hand, it's possible to choose to sequentially (and sometimes iteratively) solve transport and reaction equations (operator splitting approach). A comprehensible introduction to both techniques can be found in (Steefel and MacQuarrie 1996).

Global implicit approach (GA) results harder to implement into a code but avoids coupling errors; although the power computing has grown significantly, the solution of the global system of differential equations may be heavy to solve for complex 3D problems. On the other hand, operator splitting (OS)

approach engenders some coupling errors, but results more *flexible* and allows the coupling of different simulation tools (i.e. one code for the transport and another for the chemical reactions) chosen according to their respective strengths.

The differences between the two approaches and the different coupling techniques (SNIA, SIA, Strang...) for the OS approach will be detailed in Chapter 6, but it is important to understand that almost philosophical differences exist between the two approaches. During a reactive transport modeling workshop it occurred to me to hear the sentence « operator splitting is dead » and although people with such strong opinions exist, the superiority of one method with respect to the other is still to be proven and is strictly problem dependent (Fahs et al. 2008) and references therein.

OS approach opens to other debates that are specific to bio-geochemical solvers, especially related to the technique applied for modeling thermodynamic equilibrium. Two are the possible approaches: minimization of Gibbs Energy or Mass Action Law. The two approaches present strengths and liabilities, which are often linked to the phenomenon that is intended to be simulated; nevertheless, models and codes for biogeochemical reactions based on Mass Action Law constitute the majority.

1.4 A universe of reactive transport codes

A detailed study of the state of the art of reactive transport codes can be found in (Steefel et al. 2015), where twelve world-known codes are compared according to their capabilities and numerical methods. The review produced by Steefel and co-authors provides an overview on PHREEQC, HP1, PHT3D, OpenGeoSys, HYTEC, ORCHESTRA, TOUGHREACT, eSTOMP, HYDRO-GEOCHEM, CrunchFlow, MIN3P, PFLOTRAN. Some of the codes analyzed in the review started as mere tools for reaction simulations that were extended to one-dimensional transport (PHREEQC), others are ambitious platforms engineered to connect software for different chemical-physical phenomena (OpenGeoSys). These codes represent a percentage of all the reactive transport codes and reaction modules that are available to an interested user. Other examples are: CHEPROO (Bea et al. 2009), CORE2D (Samper et al. 2009), GEM-Selektor (Kulik et al. 2012), GEOCHEM-EZ (Shaff et al. 2010), GWB Geochemist's WorkBench (Bethke 2008), RETRASO (Saaltink et al. 2004), WITCH (Goddéris et al. 2006).

Regarding flow, ten over twelve codes revised in Steefel et al. (2015) are capable of tri-dimensional simulations, nine embed Richards equation for unsaturated flow, eight are able to deal with variable density flow and six with non-isothermal flow. Regarding transport, the most remarkable characteristic is that only one code over twelve has a full dispersion tensor, while of the eleven remaining ten have a simple diagonal tensor while TOUGHREACT doesn't use one. Nine codes are declared able to treat transport in multiple continua. From a geochemical point of view, extended Debye-Hükel and Davies activity models, non-isothermal geochemistry, surface complexation, ion exchange, aqueous gas exchange, kinetic mineral precipitation, Monod kinetics are considered the basics and implemented in

nearly every code. Less common are Pitzer activity model and mineral nucleation, which are respectively embedded into four and six codes. Nine codes are declared to be able to treat mineral solid solutions.

Some extra-attention is due to the implementation of isotopes. Equilibrium and kinetic isotope fractionation are implemented in seven and eight codes, and theses implementations are somehow recent with respect to first versions of the codes (Wanner and Sonnenthal 2013; Druhan et al. 2013); one of the reasons for the growing interest in isotopes is the recent improvement of analytic techniques that allow the detection of isotope fractionation.

From a numerical point of view, only three codes analyzed in Steefel et al. (2015) apply a global approach (MIN3P, CrunchFlow, PFLOTRAN) and two of them (CrunchFlow, PFLOTRAN) allow to choose between global approach and operator splitting. Although code parallelization is becoming more and more frequent, allowing sensible reductions of the computational time, only the half of the codes exploited parallelization at the time of the publication of the review.

1.5 LHyGeS numerical models: a garden worth gardening

The patrimony of numerical models and codes at the Laboratory of Hydrology and Geochemistry at the University of Strasbourg is well documented. Codes have been developed for the simulation of mineral reactivity (KINDIS (Madé et al. 1994)), mineral reactivity and 1D transport (KIRMAT, (Gérard et al. 1998)), geochemical reactions (SPECY, (Carrayrou et al. 2002)), conservative transport (TRACES) and a number of other codes for more specific hydrological problems (Pan et al. 2015; Weill et al. 2017, Jeannot et al. 2018). Nevertheless, the evolution of geochemical models, numerical methods, and computing techniques is continuous and a constant update of these models is mandatory to ensure their survival.

Despite being a very powerful instrument, with numerous practical applications that continue at present time, KINDIS has two substantial limitations: it is not well suited for coupling with a multidimensional transport code and it is has been specifically designed for mineral reactivity. SPECY, on the other hand, has been conceived from the beginning as a tool with broader fields of application and to be coupled with transport codes. Nevertheless, it has never been exploited to its full potential, being used more as a laboratory for numerical tests than for the systematic simulation of actual geochemical problems.

In TRACES, who embeds the powerful numerical scheme of mixed and discontinuous finite elements, and who is very efficient for simulations of conservative transport, only very basic reactions were taken into account at the moment of its development.

The aim of this thesis is to develop a tool for the simulation of bio-geochemical reactions gathering all the capabilities of the existing models (and adding some, in particular, the treatment of isotopes) in a modern numerical environment. The tool is conceived as a flexible module to be coupled with other

codes, primarily for the simulation of transport (TRACES) to produce a reliable and up to date tool for the simulation of reactive transport.

With paragraph 1.4 well in mind, one might question the usefulness of another reactive transport code. It is important to highlight that the point is creating neither *clone* nor a *competitor* of the already existing, mainstream reactive transport codes, which would be a quite ambitious goal, but to create an *alternative* which is transparent, controllable, adaptable, reliable and efficient to the maximum extent. Carrayrou et al. (2010), with the application of the MoMaS benchmarks, showed that different codes may still provide different results, thus underlying the necessity of plurality and intercomparisons. It is also useful to remind that although many of the codes mentioned before are available to the scientific public, only a few of them are Open source. Moreover, as clear as their user-guides can be, the comprehension and usage of these tools is not immediate (courses to learn how to model with some mainstream codes are often put in place); this implies that scientist performing experimental or fundamental studies are far from "just downloading" powerful software and running a simulation.

In conclusion, the tool is intended to serve as a complement to experimental activity and a solid basis for further numerical improvements; this manuscript is mainly directed to those potentially continuing the work, to provide an honest picture of reactive transport modeling at LHyGeS, its potential and limitations.

1.6 Structure of the work

The work is ideally organized into three main sections. The first section is focused on the reaction solver and begins with a preliminary study on the implementation of isotopes in reactive transport models (Chapter 2). An extensive bibliographic study was conducted on the topic, concluding that isotopes are implemented as autonomous species in all models taken into consideration. Chapter 2 also gives an overview of the growing interest in isotopes and explains their role (mainly as tracers) in reactive transport studies. Following conclusions of Chapter 2, no substantial modifications of the algorithm are required to implement isotopes in the model; on the other hand, the increase in the number of species and the potentially extremely low concentrations treated stress once more the importance of reliability and efficiency of computations.

Chapters 3 and 4 explore challenges in the solution of systems of equations arising from mathematical formulations of geochemical problems. Chapter 3 is dedicated to Thermodynamic equilibrium formulation. The method of primary and secondary species for Mass Action Law formulation is introduced as well as solution techniques of resulting algebraic non-linear systems. Liabilities of Newton Raphson method for the solution of non-linear systems are examined and solutions are proposed. In Chapter 3 are also listed and briefly explained the capabilities of the code at thermodynamic equilibrium.

Chapter 4 is dedicated to the problem of mixed kinetic and equilibrium reactions. In the context of Mass Action Law formulation, this configuration results in a system of differential and algebraic equations (DAEs). On the basis of the available literature, different mathematical formulations of the system were studied, implemented and tested in the solver DASPK and compared to the explicit solution method present in SPECY (Carrayrou et al. 2002).

Chapter 5 is entirely dedicated to solid solutions, which are basically mixtures (not only mechanical) of a number of minerals. The concept of solid solutions has been exploited in connection with isotopes in Chapter 2, but some clarifications are due. The chapter contains an extensive bibliography on the thermodynamics of solid solutions while kinetic models for solid solutions are only introduced since their theoretical foundations are limited. Two applications of the algorithm are proposed, one in batch and an anticipation of a reactive transport problem involving Iron and Chrome precipitation.

The second section of the work, constituted by Chapter 6, is dedicated to the coupling between the reaction and transport modules, the validation of the resulting reactive transport (called SpeCTr, *Speciation Cinétique Transport* in French) and, at the same time, of the implementation of isotopes.

A thorough analysis of coupling techniques (Global Approach and Operator Splitting) is proposed and the mechanism of coupling adopted is detailed. Both the coupling of the reaction-transport modules and the implementation of isotopes are validated through the solution of a Benchmark involving Chrome fractionation. SpeCTr provides the same results as world know codes such as MIN3P and CrunchFlow.

The last ideal section is constituted by Chapter 7, where a series of applications of SpeCTr are proposed. The problems involve Calcite dissolution and precipitation analyzed through 2D and 3D simulations. Different models for Calcite dissolution were tested to model experimental results obtained by studying the dissolution of Calcite crystals. Precipitation was tested instead in comparison with experimental and numerical results and published by Katz et al (2009).

Chapter 2 – Implementing isotopes

2.1 Theoretical background

2.1.1 What is an isotope?

Chemical properties of molecules depend in the large majority on the atomic structure of the elements they are composed of. Atoms are constituted by a nucleus of *protons* (positively charged) and *neutrons* (not charged), and by a cloud of *electrons* (negatively charged) around the nucleus. If the number of protons and the number of electrons is equal we say that the atom is neutral. If an atom suffers an excess of electrons it becomes a *negative ion*, if it suffers a deficit of electrons it becomes a *positive ion*.

Chemical properties of an element are primarily defined by the number of electrons in its atoms. So, what are neutrons there for? Neutrons have no electrical charge and their presence is required to stabilize the nucleus full of protons, all positives, which experience repulsive Coulomb forces. Usually, in light elements such as Helium, Carbon and Oxygen, the number of neutrons equals the number of protons: Helium (He) has 4 *nucleons*, 2 protons and 2 neutrons; Carbon (C) has 12 nucleons, 6 protons and 6 neutrons; Oxygen (O) has 16 nucleons, 8 protons and 8 neutrons. In heavy elements, however, the number of neutrons is often way higher than the number of protons: for instance, in an atom of Uranium (U) there are 238 nucleons, but only 92 of them are protons.

A relatively important excess of neutrons makes the atom unstable, which is the case for a Carbon atom with 6 protons and 8 neutrons. However, a slight excess of neutrons may result in an atom that is still stable: Carbon atoms with 7 neutrons (1 neutron in excess) or Oxygen atoms with 9 or 10 neutrons (1 and 2 neutrons in excess) are stable. Versions of the same element that differ in their number of neutrons are called *isotopes* of that element, the word coming from the ancient Greek ισο τοποσ that means *at the same place* (in the periodic table). The more stable is a nucleus, the higher the probability of its natural occurrence. On the other hand, unstable isotopes tend to disintegrate over time producing alpha or beta particles and sometimes gamma rays in the process and are also referred to as *radioactive*.

2.1.2 Notation

The number of protons, or the *atomic number*, is usually represented with letter Z. The number of neutrons is often represented with letter N. The number of nucleons (protons and neutrons) is called *mass number* and is usually represented with letter A:

$$A = Z + N \tag{2.1}$$

The usual notation for a nucleus of an element X is:

$$^{A}_{Z}X_{N} \tag{2.2}$$

This notation allows us to easily distinguish between different isotopes of the same element, for example an atom of Carbon in its most common configuration (6 protons, 6 neutrons) is represented as $^{12}_{6}C_{6}$ while one of its less abundant isotopes as $^{13}_{6}C_{7}$.
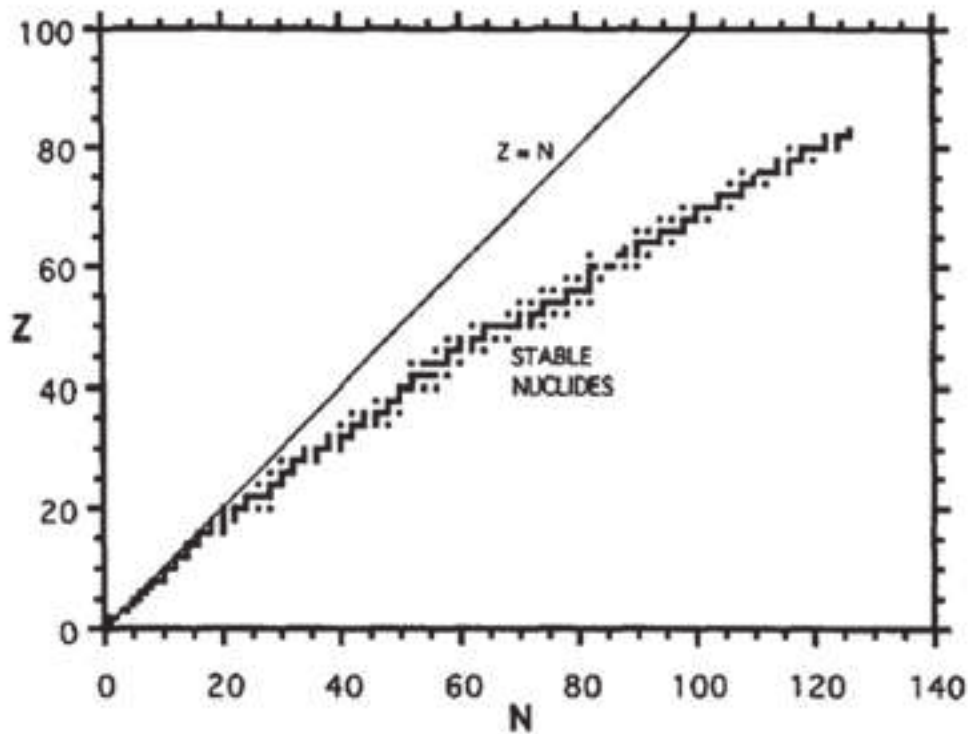
Figure 2.1 – Atomic numbers vs. Number of neutrons in the nuclei of stable isotopes. From *Principle of stable isotopes distribution* (Criss 1999)

2.1.3 Isotopic abundance and its variations

While treating isotopes, the concentration of an element or chemical species containing an isotope is usually referred to as *abundance*. The *isotope (abundance) ratio* is the ratio between the abundance of the *rare isotope* over the abundance of the *abundant*, for example the isotope ratio of ^{13}C (which is less abundant of ^{12}C) is defined as:

$$^{13}R(C) = \frac{\left[^{13}C\right]}{\left[^{12}C\right]} \tag{2.3}$$

Isotope abundance is usually reported through δ formulation, which is the deviation of the isotope ratio from a standard value (Craig 1957):

$$\delta = \frac{^{13}R(C)}{^{13}R(C)_{ST}} - 1 \tag{2.4}$$

Since δ is a very small number, it is often multiplied by 10^3 and expressed in ‰. Another quantity that can be extracted is *isotope concentration*, the ratio between the abundance of the rare isotope and the concentration of the element of interest. For ^{13}C the isotope concentration takes the following form:

$$IC = \frac{\left[^{13}C\right]}{\left[^{12}C +^{13}C\right]} = \frac{^{13}R}{1+^{13}R} \tag{2.5}$$

The isotope ratio of a compound, expressed in equation (2.3), is not a constant. This is true not only if one of the involved isotopes is radioactive (therefore undergoing a decay process), but it may happen during the transition of a compound from one state to another, or between two compounds at chemical equilibrium. This variation in the isotopic composition is called *isotope fractionation* and implies that the chemical properties of isotopes of the same element are very close, but not identical.

Differences in chemical and physical behaviors stem (most of the time) from mass differences in atomic nuclei. Lower molecular weights result in higher mobility, therefore in higher diffusion velocities and higher collision frequencies. At the same time, heavier molecules have higher binding energies that make them less prone to separate from other molecules. These characteristics imply that,

12

in most cases, lighter isotopes react faster or are more prone to react (even though the opposite effect is possible and has been named *inverse kinetic isotope effect*). As anticipated, two are the possible types of stable isotope fractionation: *equilibrium fractionation* and *kinetic fractionation*. Equilibrium fractionation sees isotopic exchanges between species that are at thermodynamic equilibrium. If we think about an equilibrium reaction where the asterisk represents the presence of the rare isotope, like in equation (2.6), the equilibrium constant equals the fractionation factor (equation (2.7)).

$$*C_1 + C_2 \Leftrightarrow C_1 + *C_2 \tag{2.6}$$

$$K = \frac{[*C_1][C_2]}{[C_1][*C_2]} = \frac{[C_2]/[*C_2]}{[C_1]/[*C_1]} = \frac{R_2}{R_1} = \alpha_{2/1} \tag{2.7}$$

Purely kinetic fractionation results from strictly irreversible reactions, such as water evaporation with subsequent withdrawal of vapor, biotic precipitation of carbonates or bacterial decay and is primarily caused by lower binding energies of lighter molecules Purely kinetic fractionation is very hard to monitor, since most of natural processes are not purely kinetic and even in laboratory experiments this condition is tough to guarantee or quantify. For these reasons, natural processes are identified as *non-equilibrium-fractionation*. Isotope fractionation between two chemical species at thermodynamic equilibrium ($C_1 \Leftrightarrow C_2$), or after a chemical or physical transformation ($C_1 \Rightarrow C_2$) is measured through the *isotope fractionation factor*:

$$\alpha_{C_1}(C_2) = \frac{R(C_2)}{R(C_1)} \tag{2.8}$$

Since the variations are very small, the fractionation factor is very close to one and it is easier to represent these variations as its deviation from 1, which is called *fractionation*:

$$\varepsilon_{C_2/C_1} = \alpha_{C_1}(C_2) - 1 = \frac{R(C_2)}{R(C_1)} - 1 \tag{2.9}$$

Since *fractionation* ε is a small number, it is often multiplied by 10^3 and expressed in ‰. If $\varepsilon > 0$ the isotope ratio has increased (with respect to another species, phase or time) and we talk about *enrichment*; vice-versa, if $\varepsilon < 0$ we talk about *depletion*.

Under the assumption of first order, homogeneous fractionation (Criss 1999), an equation tracking the evolution of isotopic ratio can be established. Indicating with N the number of abundant isotopes and

N' the number of the rare isotopes, the evolution of isotopic ratio takes the form of the well-known Rayleigh equation:

$$\frac{N'}{N} = \left(\frac{N'}{N}\right)_0 f^{(\alpha_K - 1)}$$

(2.10)

where $(N/N)_0$ is the initial isotopic ratio, f is the fraction of remaining reactant, and α_K the kinetic fractionation factor.

2.1.5 Why do we care about isotopes?

The increasing interest in isotopes fractionation is due to the insights that this phenomenon can provide insights on a variety of biogeochemical processes. In fact, isotopes are powerful tracers that allow detecting and following processes which are transparent to changes in concentrations of major elements. Studies of isotope fractionation have been applied to different scenarios ranging from *in situ* bioremediation to the understanding of natural cycles. Examples include: Sulfur fractionation proved crucial in detecting subsurface processes during *in situ* bioremediation of a uranium and vanadium ore processing facility (Druhan et al. 2008; Druhan 2012) and Calcium fractionation was used as a tracker in an otherwise blind process in the same site (Druhan et al. 2013; Druhan et al. 2014). Carbon fractionation proved as well to be an indicator of biochemical processes during *in situ* bioremediation from organic contaminants in wetlands (Imfeld et al. 2008; Imfeld et al. 2009; Imfeld et al. 2010; Alvarez-Zaldívar et al. 2016). Isotopes of Lithium and Boron, Magnesium and Calcium gained importance as tracers of natural processes such as clay mineral formation in soils, plant-mineral interactions, and recycling by vegetation (Schmitt et al. 2012). Uranium nuclides have been studied to investigate weathering processes (Chabaux et al. 2011; Maher et al. 2006). Cr fractionation has been proved an indicator of reduction of Cr(VI), a carcinogenic contaminant, to Cr(III), which is less toxic (Wanner et al. 2015 and references therein).

2.2 Modeling isotopes

The increasing attention paid to isotope fractionation resulted in a natural demand of models capable of reproducing experimental data. Analytical models have been proposed to describe water-rock interaction (Richter and DePaolo 1987; DePaolo and Getty 1996; Johnson and DePaolo 1997), sediment transport rates (DePaolo et al. 2006), groundwater residence time (Johnson and DePaolo 1996), vadose zone recharge (Maher et al. 2003; DePaolo et al. 2004; Singleton et al. 2006), flow paths (Johnson and DePaolo 1994; DePaolo et al. 2006) but their applicability is often subordinated to simplifying assumptions. Moreover, the abundance of experimental data itself puts in evidence that well-established models such as Rayleigh equations are not always applicable to experimental data (Breukelen and Prommer 2008; Druhan et al. 2013). Throughout the last ten years, models started being developed to include isotopes in the complex network of reactive transport. To increase the understanding of isotopes fractionation in a mechanistic way, isotopes started being implemented in reactive transport models (and therefore codes) as independent chemical species (Singleton et al. 2004; Maher et al. 2006; Rolle et al. 2010). Some may argue that increasing the number of independent species would increase the computational burden, but two things should be kept in mind: i) when studying isotopes fractionation, scientists are interested in differencing the behavior of some isotopes of a single element, not every possible isotopic combination in the reaction network; ii) computational efficiency has increased to the point that adding some species to the reaction network is largely sustainable.

The implication of such an approach is that, from a numerical point of view, there is no actual difference between two atoms of different elements and between two isotopes of the same element. Moreover, in a variety of occasions, behaviors of different isotopes are described through laws that vary slightly (Singleton et al. 2004; Druhan 2012; Wanner et al. 2015), which is coherent with the fact that differences in the mass do not imply stoichiometric differences. Although isotopes of different elements are all treated as different species, this is the only characteristic that they share. According to reactions present in the network, some models will be more suitable than others, exactly as it happens for major elements: they might precipitate through a standard Transition State Theory (Eyring, 1935; Lasaga, 1995) model or be part of some ion-exchange; therefore there is no universal receipt for *implementing isotopes*.

2.2.1 Modeling stable isotopes equilibrium fractionation

Isotope exchange between species or phases at thermodynamic equilibrium is modeled through adapted equilibrium constants. For example, equilibrium constants for Hydrogen and Oxygen isotope

fractionation during water evaporation in unsatured zones (Singleton et al. 2004) were obtained through temperature-dependent fractionation coefficients (Horita and Wesolowski 1994).

2.2.2 Modeling stable isotopes kinetic fractionation

Kinetic stable isotope fractionation has been modeled in recent years through the adaptation of classic reaction rates. For kinetic reactions that do not imply precipitation (i.e. a certain saturation to be reached), the reaction rate of the abundant isotope corresponds to the rate of the major element, the rate of the rare isotope is an adaptation to some extent of the classic law (Van Breukelen et al. 2005; Druhan et al. 2008; Wanner et al. 2015; Van Breukelen et al. 2017). Whenever precipitation or dissolution is involved, modeling mineral involving rare isotopes as independent is not possible. The most suitable way for treating this kind of processes is exploiting the concept of *solid solutions* (DePaolo 2011; Druhan et al. 2013; Wanner and Sonnenthal 2013). Minerals corresponding to different isotopes are conceived as end-members of a solid solution; a specific reaction rate $^i r$ [mol/T/ M_{H2O}] (or [mol/T/ L^3_{H2O}], depending on the formulation) for each end-member is written in the form:

$$^i r = {}^i k \; A_S \; {}^i x \left(\frac{Q_i}{{}^i K_S \, {}^i x} - 1 \right)^n \tag{2.11}$$

where $^i k$ is the kinetic constant of the element [mol/T/L-min^2], A_s is the reactive surface [L^2-min/M$_{H2O}$] (or [L^2-min/L$^3_{H2O}$], depending on the formulation), $^i x$ is the mole fraction of the isotope i (that may be in the bulk solid or removed from the solid and corresponds to equation (2.5)) [-], Q_i is the ion activity product of the end-member [-], $^i K_S$ is the solubility product, n is the order of the rate. Following this approach, the rates and activities of the end-members/isotopes sum up to the rate of the whole element and a possible equilibrium fractionation is taken into account with suitable modifications of solubility product $^i K_s$ (Druhan et al. 2013). Although this model is very powerful, care should be taken when associating it with solid solutions. In fact, while thermodynamics of solid solutions have a strong theoretical basis, their kinetics is not well established (the problems is addressed in more detail in Chapter 5).

Other versions of equation (2.11) for the formulation of reaction rates of end-members are possible, such as in models TOUGHREACT and FLOTRAN (Wanner et al. 2015):

$$^i r = A_S \left[{}^i k \left(\frac{Q_i}{{}^i K_S} - 1 \right)^n + {}^i k \left({}^i x - 1 \right) \right] \tag{2.12}$$

16

When implementing kinetic stable fractionation in MIN3P (Jamieson-Hanes et al. 2012), solid solutions are not explicitly mentioned. Each isotope precipitates/dissolve according to its own reaction rate:

$$^i r = \,^i k \; A_S \left(\frac{Q}{K_S} - 1 \right)^n \tag{2.13}$$

where the only difference between end-members is the kinetic coefficient $^i k$ (which is not a constant anymore); $^i k$ is obtained through equation (2.14) for the abundant isotope and through equation (2.15) for the rare isotope:

$$^i k = \frac{k}{1 + \,^i R} \tag{2.14}$$

$$^i k = \frac{k \,^i R}{1 + \,^i R} \tag{2.15}$$

where $^i R$ is the isotopic ratio as defined in equation (2.3) i.e. the ratio between the rare and the abundant isotope. It is worth reminding that models in equations (2.11) to (2.15) were developed starting from the exigency of reproducing experimental results showing fractionation (mostly of Chromium and Calcium) and that they are not derived from a detailed knowledge of mechanisms governing fractionation. All the studies used kinetic fractionation as a tracer for other processes and were not focused on the mechanism of fractionation itself.

Although this approach proved successful in modeling Calcium fractionation (Druhan et al. 2013) and Cr fractionation (Wanner et al. 2015), there are also examples of integrations of analytical models in numerical codes to treat very peculiar conditions (Druhan et al. 2013).

2.2.3 Conclusions about modeling isotopes

Stable isotopes fractionation has gained attention as a powerful complementary tool to understand physical and geochemical processes and to track the evolution of environmental engineering actions. Isotopes of chemical elements are introduced in reactive transport codes as independent species with their own constants and responding to their own reaction rates (linked only by mass conservation).

It is true that the presence of different isotopes of the same element in a mineral is well described by a solid solution (it is indeed the closest approximation of an ideal solid solution). Nevertheless, care should be taken not to infer that all solid solutions could be treated kinetically as in equations (2.11) to (2.15), which are specific to isotopes.

Although the formulation of widely applicable models such as transition state theory (TST) adapted according to solid solutions' concepts work in a variety of contexts, ad-hoc models are still being developed to treat peculiar problems. For instance, for Chlorine and Hydrogen fractionation during microbial sequential reduction dechlorination (SRD) have been recently developed (Van Breukelen et al. 2017) proving that, although isotopes are treated as different species and kinetic isotope fractionation is obtained to the application of different reaction rates, the formulation of these reaction rates can vary substantially according to the examined phenomena and to its the degree of knowledge.

Chapter 3 – Thermodynamic equilibrium

In the context of Operator Splitting approach adopted in this work, computation of thermodynamic equilibrium is a fundamental step toward the solution of geochemical problems. This is true because i) within extremely large time-scales, equilibrium assumption may be justified for all reactions ii) whenever a mix of kinetic and equilibrium reactions take place, integration in time of differential equations through a solver must start from an equilibrated solution iii) ad-hoc algorithms for the computation of mixed kinetic and equilibrium reactions may require computation of thermodynamic equilibrium throughout their functioning. It is though very rare solving a geochemical problem leaving out the computation of thermodynamic equilibrium.

Whenever the interest is not just finding the combination of concentrations that satisfies thermodynamic equilibrium for a reaction network, but a succession of these solutions in space and time, the issue of computational time becomes important. A small gain in the efficiency of a single operation implies a consistent gain of the global computational cost. Moreover, whenever a single operation does not converge to the solution in a reactive transport simulation, it compromises the whole system and the simulation fails.

Hence, the issues of robustness and efficiency in solving thermodynamic equilibrium are not secondary. For this reason, a consistent amount of work has been dedicated to developing some numerical techniques to make Newton Raphson method, one of the (if not *the*) most used algorithm to solve the non-linear system of equations arising from chemical equilibrium, safer and faster. The principal liability of Newton Raphson method is the iterative solution of a linear system, which is potentially challenging if the system is ill-conditioned. The linear system is ill-conditioned whenever the Jacobian matrix (i.e. the matrix of derivatives of the non-linear system) is ill-conditioned. The techniques that were tested to improve the convergence rate of Newton Raphson method are i) scaling of the Jacobian matrix and ii) coupling Newton Raphson algorithm with a zero-order method that avoids the computation of the Jacobian matrix when this is ill-conditioned, by-passing the problem. The formulation of the non-linear system arising from equations, the functioning of Newton Raphson algorithm and its liabilities, the concept of ill-conditioning and the proposed numerical solutions is illustrated in the following pages through an article published on the American Journal of Chemical Engineering (AiChE Journal) in 2016.

3.1 Thermodynamic equilibrium solutions through a modified Newton Raphson method

Marianna Marinoni, Jérôme Carrayrou, Yann Lucas, Philippe Ackerer
Laboratoire d'Hydrologie et de Géochimie de Strasbourg, Université de Strasbourg /EOST-CNRS
UMR 7517, 1 Rue Blessig, 67084 Strasbourg, France

3.1.1 Abstract

In numerical codes for reactive transport modeling, systems of nonlinear chemical equations are often solved through the Newton Raphson method (NR). NR is an iterative procedure that results in a sequential solution of linear systems. The algorithm is known for its effectiveness in the vicinity of the solution but also for its lack of robustness otherwise. Therefore, inaccurate initial conditions can lead to non-convergence or excessive numbers of iterations, which significantly increase the computational cost. In this work, we show that inaccurate initial conditions can lead to very ill-conditioned system matrices, which makes NR inefficient. This efficiency is improved by preconditioning techniques and/or by coupling the NR method with a zero-order method called the Positive Continuous Fraction (PCF) method. Numerical experiments that are based on 7 different test cases show that the ill-conditioned linear systems within NR represent a problem and that coupling NR with a method that bypasses the computation of the Jacobian matrix significantly improves the robustness and efficiency of the algorithm.

3.1.2 Introduction

Reactive transport modeling is applied in different fields of science and engineering, including combustion, catalysis, atmospheric chemistry, water chemistry, and geochemistry. Reactive transport modeling copes with the solution of transport equations that are coupled with biogeochemical reactions. In this context, two approaches exist: a *global implicit* (or *one step*) approach, and a *sequential iterative* or *sequential non-iterative* approach (the so-called operator splitting approach) (Saaltink et al. 2000; Saaltink et al. 2001; Steefel et al. 2015). The global implicit approach consists of introducing reaction equations into transport equations and solving the resultant system, while the operator splitting approach consists of sequentially solving transport equations and biogeochemical reactions.

Although the numerical results that are provided in this paper can be widely applied to all reactive transport simulations, we use reactive transport in soils and groundwater resources for illustration in this study. Several numerical codes are available to simulate reactive transport in this type of porous material (Steefel et al. 2015). Some of these codes adopt the global implicit approach, such as PFLOTRAN (Lichtner et al. 2015) or MIN3P (Mayer et al. 2002; Henderson et al. 2009); others adopt the operator splitting approach, such as HPx (Jacques and Šimůnek 2005; Šimůnek et al. 2012; Simunek et al. 2013), PHT3D (Prommer and Post 2010), HYTEC (van der Lee et al. 2003), TOUGHREACT (Xu and Pruess 2001; Xu et al. 2006, 2011; Tianfu Xu et al. 2014) or eSTOMP (White and McGrail 2005; White and Oostrom 2006); and others allow the user to choose between the two (e.g., Crunchflow (Steefel 2009), HYDROGEOCHEM (Yeh and Tsai 2013; Tsai et al. 2013)). Each methodology has its own advantages and disadvantages, as determined by research that has been conducted on these methods (M. W. Saaltink, Carrera, and Ayora 2000; Maarten W. Saaltink, Carrera, and Ayora 2001). The operator-splitting approach is often performed by coupling modules that solve transport equations with modules that are designed to solve biogeochemical equations. For instance, HPx and PHT3D rely on the geochemical code PHREEQC (Parkhurst et al. 1999; Steefel et al. 2015) to solve for the chemistry, while the geochemical portion of HYTEC (van der Lee et al. 2003) is solved by the code CHESS (van der Lee and Windt 2002; Steefel et al. 2015). The platform OpenGeoSys (Kolditz et al. 2012) has been specifically developed to facilitate interactions between modules that deal with problems from different fields. Examples of geochemical modules that are designed to be coupled with transport codes include CHEPROO (Bea et al. 2009) and MINTEQA2 (Allison et al. 1991). In the context of the operator splitting approach, the chemical equations must be solved potentially several thousands of times per time step, once for each cell/node (Van der Lee 1998) of the mesh that is designed to solve the transport equation (typically, several tens of thousands of cells/nodes for 2D problems and several hundreds of thousands for 3D). Moreover, the entire transport computation must be repeated with a smaller time step when the chemical system cannot be resolved. Thus, efficient (i.e., robust and fast) solution techniques are mandatory. In the majority of

geochemical codes, a nonlinear system of equations is solved through Newton Raphson-based algorithms. The Newton Raphson method is an iterative procedure that provides a solution of nonlinear systems of chemical equations through the repeated resolution of linear systems. As with all iterative procedures, Newton Raphson requires a set of initial guesses to begin its path to the solution. This method is appreciated for its quadratic rate of convergence when favorable initial guesses are picked; on the other hand, an unlucky combination of initial guesses will likely prevent the algorithm from converging (Van der Lee 1998). For this reason, the Newton Raphson method is often implemented alongside techniques that utilize a preliminary selection of initial solutions (Parkhurst et al. 1999). Depending on the problem, the coefficients that appear in a system of equations can be very different, potentially causing the solutions of linear systems to be ill-conditioned (Buzzi-Ferraris and Manenti 2014). The accuracy of the numerical solution of an ill-conditioned system can be very poor and may provide results that are very different from the exact solution, i.e., the wrong descent direction of an iterative procedure. Techniques such as *line search* (Press et al. 1997) (or *one dimensional search* (Buzzi-Ferraris and Manenti 2014)) or similar methods (Van der Lee 1998) that deal with the amplitude of the step but leave the direction unchanged are exposed to the same risk. The motivation of this paper is to explore the effects of ill-conditioned linear systems from NR on the outcome of the algorithm and to compare different solutions to improve its efficiency. Several techniques exist to ameliorate the condition of a linear system (Chen 2005), which vary widely in their computational demand. In the context of reactive transport, computations are likely to be called thousands of times, so we studied the impact of the simplest preconditioning technique, which is known as *scaling* (Golub and Van Loan 1996), on the evaluation of thermodynamic equilibrium for a selection of numerically challenging problems. A declination of scaling techniques is proposed and their consequences on the robustness of the Newton Raphson method are presented. In practice, the Newton Raphson method is often coupled with other algorithms, so we compared the effects of scaling techniques with the effects of coupling the Newton Raphson algorithm with the Positive Continuous Fraction method (Carrayrou et al. 2002), an effective zero-order technique that was initially proposed to treat linear concentrations. Here, we adapt this method to work with concentrations on a logarithmic scale. Other approaches have been adopted in order to overcome the liabilities of Newton Raphson Method: other zero order methods, like simplex method (Wood 1993) were applied to equilibrium problems; QR factorization method (Hoffmann 2010) has been used solve linear system; Newton-Krylov methods were also applied (Kern and Amir 2007). Those proposed in this paper are certainly not the only solutions; they merely represent a widely used alternative among others.

3.1.3 Thermodynamic equilibrium: governing equations

Modeling chemical reactions at equilibrium is a basic feature in many reactive transport codes and is the principal objective of other computational modules. Although not a unique alternative (Kulik et al.

2012), thermodynamic equilibrium is often described through a combination of mass conservation and mass action laws that are written in terms of *species* and *components* (Saaltink et al. 2001). The formulation of species and components has been adopted by many modelers (Reed (1982), Westall et al. (1976), Cedeberg et al. (1985), Yeh and Tripathi (1991), Steefel and Lasaga (1994), Parkhurst and Appelo (1999)) and is currently implemented in codes such as CHESS (van der Lee and Windt 2002), CHEPROO (Bea et al. 2009), TOUGHREACT (Xu et al. 2014), Crunchflow (Steefel 2009), PHREEQC (Parkhurst et al.1999) among others.

One can individuate a subset of *components* within all *chemical species* in a chemical system at thermodynamic equilibrium to entirely describe the system. Components (often addressed as primary species) are linearly independent, and their combinations recreate all chemical species (secondary species). The relationship between components and other chemical species is mathematically expressed as follows:

$$\sum_{j=1}^{Nx} b_{i,j} X_j \Leftrightarrow C_i \quad i = 1,...,N_C , \tag{3.1}$$

Where X_j represents a generic component; C_i is a generic chemical species; $b_{i,j}$ is a generic stoichiometric coefficient; and N_x and N_c are the number of components and dissolved chemical species, respectively. Equation (3.1) describes a qualitative relationship between components and other chemical species and does not provide quantitative information regarding the concentrations or activities of different elements. Quantitative relationships are provided by the conservation law (3.2) and mass action law (3.3):

$$\left[T_j \right] = Total(X_j) = \sum_{i=1}^{Nc} b_{i,j} \left[C_i \right] \quad j = 1,\ldots,N_X \tag{3.2}$$

$$\left\{ C_i \right\} = K_i \prod_{j=1}^{Nx} \left\{ X_j \right\}^{b_{i,j}} \quad i = 1,...,N_C \tag{3.3}$$

where [-] defines a concentration, {-} defines an activity, $[T_j]$ is the total concentration of component X_j that is conserved in the system through chemical reactions (expressed in moles per unit volume), K_j is the thermodynamic equilibrium constant, and $b_{i,j}$ is a generic stoichiometric coefficient that is related to the formation of chemical species C_i based on the components X_j. If present, precipitates that constitute the solid phase are identified with the symbol Cp_l, with $l=1,...,N_{Cp}$, where N_{Cp} is the total number of precipitates. Thus, equation (3.2) undergoes a modification:

$$[T_j] = Total(X_j) = \sum_{i=1}^{Nc} b_{i,j}[C_i] + \sum_{l=1}^{Ncp} bp_{l,j}[Cp_l] \quad j=1,...,N_X , \qquad (3.4)$$

Where $[Cp_l]$ is the concentration of precipitate l. Cp_l and $bp_{i,j}$ is the related stoichiometric coefficient. The concentrations of precipitates must be computed within the chemical equilibrium solution, but their activity $\{Cp_l\}$ remains constant and equal to one because the quantity of precipitates is no longer available for reactions. Thus, whenever precipitation occurs, $[Cp_l]$ cannot be deduced through the mass action law and must be treated as an additional unknown(Carrayrou, Mosé, and Behra 2002). Equation (3.5) is included in the system to balance this supplementary unknown. Precipitation occurs only when condition (3.6) is satisfied.

$$K_S^l = \prod_j \{X_j\}^{bp_{l,j}} \qquad (3.5)$$

$$K_S^l > \prod_j \{X_j\}^{bp_{l,j}} \qquad (3.6)$$

The relationship between the concentration and activity of a generic species C_i is expressed through equation (3.7), where the activity coefficient γ_i is computed based on the ionic force.

$$\{C_i\} = \gamma_i [C_i] \qquad (3.7)$$

Substituting the mass action law (3.3) into mass conservation (3.2) while considering the relationship between the concentrations and activities (3.7) provides a set of N_x equations, where the total conserved concentration can be computed as a sole function of the concentration of components $[X_j]$ and precipitated species $[Cp_l]$:

$$[T_j] = \sum_{i=1}^{Nc} \frac{b_{i,j}}{\gamma_i} K_i \prod_{k=1}^{Nx} (\gamma_k [X_k])^{b_{i,k}} + \sum_{l=1}^{Ncp} bp_{l,j}[Cp_l] \quad j=1,...,N_x . \qquad (3.8)$$

In the previous equations, the stoichiometric coefficients $b_{i,j}$ and $bp_{i,j}$ and the thermodynamic equilibrium constant K_i are known. Activity coefficients γ can be expressed as functions of species' concentrations and therefore of components' concentrations $[X_j]$. As already stated, equation (3.8) represents mass conservation, this meaning that even if a given component X_j is involved in different species with different proportions and those proportions may vary, its total concentration $[T_j]$ (in a closed system) does not change. The total concentration of a component X_j, $[T_j]$, can be measured or

deduced from system characteristics and become a known quantity. We will refer to these data with the symbol $[\tilde{T}_j]$ in order to differentiate them from their mathematical/conceptual definition $[T_j]$. To exploit this information, equation (3.8) may be rewritten in the following form:

$$Y_j = \left[\tilde{T}_j \right] - \left[T_j \right] = \left[\tilde{T}_j \right] - \sum_{i=1}^{Nc} \frac{b_{i,j}}{\gamma_i} K_i \prod_{k=1}^{Nx} \left(\gamma_k \left[X_k \right] \right)^{b_{i,k}} - \sum_{l=1}^{Ncp} bp_{l,j} \left[Cp_l \right] \quad j = 1, \dots, N_x.$$

(3.9)

Equation (3.9) describes a nonlinear system of N_x equations with $N_t = N_x + N_{Cp}$ unknowns. Supplementary equations are then introduced to equilibrate the system based on equation (3.5):

$$Y_{N_X + l} = 1 - \prod_j \frac{\left(\gamma_j \left[X_j \right] \right)^{bp_{l,j}}}{K_S^l} \quad l = 1, \dots, N_{Cp}.$$

(3.10)

To simplify the notation, the N_t unknowns are grouped into a vector $\mathbf{X}$, and the nonlinear system at thermodynamic equilibrium can be rewritten as follows:

$$\mathbf{Y}(\mathbf{X}) = 0.$$

(3.11)

3.1.4 Newton Raphson algorithm

One of the most applied algorithms for solving nonlinear systems such as (3.11) is the Newton Raphson method (Van der Lee 1998). The Newton Raphson method is iterative and implies the repetition of a given procedure until the solution is reached, i.e., until a given stopping or convergence criterion is satisfied. At each iteration n, the algorithm converges to the solution by updating the unknowns:

$$\mathbf{X}_{n+1} = \mathbf{X}_n + \mathbf{\Delta X}_n.$$

(3.12)

The increment $\mathbf{\Delta X}_n$ is computed through the solution of a linear system (3.13):

$$\mathbf{J}_n \mathbf{\Delta X}_n = \mathbf{-Y}_n,$$

(3.13)

where $\mathbf{J}_n$ is the Jacobian matrix of the system (3.11) and $\mathbf{Y}_n$ is the vector of residuals, both of which are computed with the values $\mathbf{X}_n$. The solution of the linear system (3.13) is usually performed with a dedicated solver. Amongst the numerous solvers that are available to accomplish this task, we choose LU decomposition (Van der Lee 1998) with quadruple precision. Quadruple precision reduces the effects of round-off errors and has been shown as the most robust and efficient solver of numerical experiments, as described in Machat and Carrayrou (2016).

The Jacobian matrix $\mathbf{J}$ is an $N_t \times N_t$ matrix that contains the derivatives of each row of the nonlinear system with respect to each unknown. These derivatives are computed analytically and take the following forms:

$$J^n_{j,k}\Big|_{\substack{j=1,N_X \\ k=1,N_X}} = \sum_{i=1}^{Nc} b_{i,j} \cdot b_{i,k} \frac{[C_i]^n}{[X_k]^n}, \tag{3.14}$$

$$J^n_{j,k}\Big|_{\substack{j=N_X,N_t \\ k=N_X,N_t}} = b_{i,j}. \tag{3.15}$$

Because Newton Raphson is an iterative procedure, the algorithm is initialized with a set of initial guesses for the unknowns (concentrations of components). The Newton Raphson algorithm is known to be very effective when the initial guesses are picked in the vicinity of the solution but can likely fail to converge if the initial guesses are far from the solution in the unknowns' space (Buzzi-Ferraris and Manenti 2014). Thus, the Newton Raphson method is often coupled with other techniques to estimate these initial guesses (Parkhurst et al. 1999).

3.1.5 Condition of the linear system

The reliability of the solution of the linear system (3.13) is measured through the evaluation of the condition number of the Jacobian matrix $\mathbf{J}$ (Kiusalaas 2005) . The lower the condition number, the more likely the numerical solution of the linear system is to coincide with the exact solution. According to Golub and van Loan (1996), if $\mathbf{\Delta X}_n$ is the solution that is computed by Gaussian elimination and $\mathbf{\Delta X}_{Exact}$ is the exact solution, one can link the relative error with the condition number of $\mathbf{J}$, $\kappa(\mathbf{J})$, and the relative error in the computation of $\mathbf{J}$, $\varepsilon(\mathbf{J})$:

$$\frac{\|\mathbf{\Delta X}_n - \mathbf{\Delta X}_{Exact}\|}{\|\mathbf{\Delta X}_{Exact}\|} \le \kappa(\mathbf{J})\varepsilon(\mathbf{J}) \tag{3.16}$$

If we assume that the relative error in the computation of J is on the order of the round-off error, 10^{-d}, and that condition number is approximately 10^q, the solution of the system from a direct solver (i.e.,

LU decomposition) will have at least *d-q* correct decimal digits. For double-precision real numbers, *d* is equal to 16, which means that the solution might have no significant digits for κ(**J**)>10^{16}. In our context, the analytical solution of system (3.13) coincides with a step towards the solution. Thus, a bad solution of the linear system may result in a poor choice of the direction in our path to thermodynamic equilibrium and, therefore, significantly increase the number of iterations that are required to reach convergence.

The techniques that are used to evaluate the condition number are diverse. In its general definition, this number corresponds to the product between the norm of a given matrix and the norm of its inverse (3.17), no matter which norm is chosen (Chapra and Canale 2015). In the presence of symmetric and nonsingular matrices (Chen 2005), the condition number may also be computed as the ratio between the highest and lowest modules of the eigenvalues λ of the matrix (3.18). In this particular case, the condition number obtained through equation (3.18) corresponds to the one computed through (3.17) choosing norm 2 as norm of the Jacobian matrix and its inverse.

$$\kappa\left(\mathbf{J}\right) = \left\|\mathbf{J}\right\|\left\|\mathbf{J}^{-1}\right\|, \tag{3.17}$$

$$\kappa\left(\mathbf{J}\right) = \frac{\left|\lambda_{max}\right|}{\left|\lambda_{min}\right|} = \left\|\mathbf{J}\right\|_2 \left\|\mathbf{J}^{-1}\right\|_2. \tag{3.18}$$

A possible choice for the norm in equation (3.17) is the norm 1, $\left\|\mathbf{J}\right\|_1$ (the maximum absolute column sum), or the infinity norm $\left\|\mathbf{J}\right\|_\infty$ (the maximum absolute row sum):

$$\begin{cases} \left\|\mathbf{J}\right\|_1 = \max_j\left(\sum_i\left|J_{i,j}\right|\right) \\ \left\|\mathbf{J}\right\|_\infty = \max_i\left(\sum_j\left|J_{i,j}\right|\right) \end{cases}. \tag{3.19}$$

The evaluation of the condition number is subordinated to the inversion of the matrix in one case or to the evaluation of the eigenvalues in the other. Therefore, the standard algorithms for the computation of the condition number encounter difficulties in the presence of very ill-conditioned matrices.

The condition number of a given linear system can be modified in different ways. For instance, one can simply multiply its rows or columns by constant values, producing a potentially infinite series of condition numbers. Thus, Buzzi-Ferraris (2011) defined *system conditioning* as a particular condition number of a system in what this author called its standard form. This standard form is obtained by dividing each row of the system by its infinity norm, which is computed along the right-hand side of

the system and by dividing each column by its infinity norm (Buzzi-Ferraris 2011). This approach is useful because it provides a univocal index to compare results while searching for different and more effective formulations of the problem instead of attempting to ameliorate the condition of a given problem. In this context, searching for a different formulation of the problem means looking for another set of basic components to describe the chemical system. Nevertheless, this approach will not be studied here.

3.1.6 Working on a logarithmic base

A solution that allows some numerical facilities is a change in the variables from equation (3.9). Instead of working with the general unknown concentration $[X_j]$, one should work with the logarithmic transformation of the corresponding *activity*:

$$\xi_j = \ln\left(\{X_j\}\right). \tag{3.20}$$

The consequences of this transformation on the system are limited. Equation (3.3) becomes equation (3.21), while equations (3.9) and (3.10) take the form of equations (3.22) and (3.23):

$$\{C_i\} = \exp\left(\ln(K_i) + \sum_{j}^{N_X} b_{i,j}\xi_j\right), \tag{3.21}$$

$$Y_j = \left[\tilde{T}_j\right] - \sum_{i=1}^{Nc} \frac{b_{i,j}}{\gamma_i} \exp\left(\ln\left(K_i\right) + \sum_{k}^{N_X} b_{i,j}\xi_k\right) + \sum_{l=1}^{Ncp} bp_{l,j}\left[Cp_l\right] = 0 \quad j = 1,...,N_x, \tag{3.22}$$

$$\ln K_S^l = \sum_{j}^{Nx} bp_{l,j}\xi_j \quad l = 1,...,N_{Cp}. \tag{3.23}$$

This transformation has the advantage of ensuring the symmetry of the Jacobian matrix and improving its conditioning. This transformation has already been used and implemented, for example, in EQ3/6 (Wolery and Jarek 2003). The Jacobian matrix entries become as follows (see Annex I):

$$J_{j,k}^n\Big|_{\substack{j=1,N_X \\ k=1,N_X}} = \sum_{i=1}^{Nc} b_{i,j} \cdot b_{i,k} \left[C_i\right]^n, \tag{3.24}$$

$$J_{j,k}^n\Big|_{\substack{j=N_X,N_t \\ k=N_X,N_t}} = bp_{i,j} \quad J_{j,k}^n\Big|_{\substack{j=k \\ j,k\in(N_X+N_{Cp})}} = 0. \tag{3.25}$$

In fact, the concentration of the component j that was present in equation (3.14) disappears from the denominator in equation (3.24), reducing the possibility of fluctuations over an order of magnitude. Equation (3.24) could be rewritten in its matrix form (3.26). This notation for the upper left block highlights the influence of the range of concentrations on the condition number.

$$\mathbf{J} = \mathbf{B}^T diag(\mathbf{C})\mathbf{B} \tag{3.26}$$

3.1.7 Preconditioning

Techniques and procedures that are used to reduce the condition number of a given system fall under the definition of *preconditioning*. An accurate summary of these techniques is available in the literature (Chen 2005). Some preconditioning techniques, such as preconditioning through an approximate inverse, require consistent computational effort. If the required computational time for preconditioning is significantly higher than some Newton Raphson iterations, the algorithm will not reduce the computer time that is required to reach the solution. Therefore, we focus our work on methods that improve matrix conditioning without significant computational costs. Those techniques are known as *scaling* (Golub and Van Loan 1996; Chen 2005). Scaling is a procedure that is operated by multiplying one or more rows and/or columns of the linear system by a constant. The only limitation is that multiplying all the lines by the same constant would produce no effects. The idea behind scaling is to solve system (3.27) instead of the regular linear system that is solved in the standard Newton Raphson algorithm:

$$\mathbf{D}_1^{-1}\mathbf{J}_n\mathbf{D}_2^{-1}\Delta\hat{\mathbf{X}}_n = -\mathbf{D}_1^{-1}\mathbf{Y}_n , \tag{3.27}$$

where $\mathbf{D}_1$ and $\mathbf{D}_2$ are diagonal matrices and $\Delta\hat{\mathbf{X}}_n = \mathbf{D}_2\Delta\mathbf{X}_n$ is a linear combination of the increments. The previous system is analytically equivalent to (3.13) but hopefully better conditioned. The entries of $\mathbf{D}_1$ and $\mathbf{D}_2$ may be chosen with respect to the diagonal values of the original matrix $\mathbf{J}$ (Marquardt 1963) or according to a given norm of lines and/or columns (Knight et al. 2014). Setting $\mathbf{D}_1 = \mathbf{I}$ corresponds to performing scaling only over columns, while setting $\mathbf{D}_2 = \mathbf{I}$ corresponds to performing scaling only over rows. A further step beyond scaling is matrix *equilibration* (Bradley 2010; Knight et al. 2014), which sets the norms of rows and columns of a given matrix to a fixed value and repeats a certain scaling procedure until the norms meet the requirements. However, Golub and Van Loan (1996) warned that reactions to scaling are strongly problem dependent and that its implementation is by no means a guarantee of success in the computation of increments.

3.1.8 Scaling procedures in this work

In our work, we tested five different combinations of $\mathbf{D_1}$ and $\mathbf{D_2}$ or, more precisely, four different combinations of $\mathbf{D_1}$ and $\mathbf{D_2}$ and one procedure for matrix equilibration. We tested both scaling techniques that involve rows and columns and techniques that modify only rows. Simple row-scaling of the Jacobian matrix and its right-hand term is obtained by imposing $\mathbf{D_2} = \mathbf{I}$ and choosing different values of the constants of $\mathbf{D_1}$.

RI – Row Identity scaling. If each row in the Jacobian matrix is defined as a vector $\mathbf{a}_i$ and each element of its diagonal is $J_{i,i}$, one possible choices of the entries of the diagonal matrix is:

$$D_{1i,i} = \left\| \mathbf{a}_i \right\|_{\infty},\qquad (3.28)$$

where the infinity norm is $\left\| \mathbf{a}_i \right\|_{\infty} = \max \left| \mathbf{a}_i \right|$. We refer to scaling through $\mathbf{D_2} = \mathbf{I}$ and the elements of $\mathbf{D_1}$, as in equation (3.28), with the name Row Identity (RI) scaling.

DI – Diagonal Identity scaling. While matrix $\mathbf{D_2} = \mathbf{I}$, the elements of $\mathbf{D_1}$ are picked as in equation (3.29):

$$D_{1i,i} = J_{i,i},\qquad (3.29)$$

sDsD – Square Diagonal scaling. Two methods of performing scaling that affect both rows and columns were also tested. The first method was already proposed by Marquardt (Marquardt 1963) and is also known by the name *Jacobi preconditioning* (Golub and Ortega 1993) . Matrices $\mathbf{D_1}$ and $\mathbf{D_2}$ become:

$$\begin{aligned} D_{1,i} &= \sqrt{J_{i,i}} \\ D_{2,i} &= \sqrt{J_{i,i}} \end{aligned}.\qquad (3.30)$$

Equation (3.30) is valid for $i = 1, ..., Nx$ because the diagonal entries of the matrix become zero (Annex I) in the presence of precipitates. We refer to this scaling technique with the expression Square Diagonal scaling (sDsD).

RC – Row and Column scaling. The second procedure that acts on both rows and columns (Row and Column scaling – RC) performs only one iteration of a matrix equilibration technique that was proposed by Knight et al. (2014). After defining $\mathbf{c}_i$ column-vectors of the matrix $\mathbf{J}$, these authors proposed to choose entries of $\mathbf{D_1}$ and $\mathbf{D_2}$ as in equation (3.31):

$$D_{1,i} = \sqrt{\|\mathbf{a}_i\|_\infty}$$
$$D_{2,i} = \sqrt{\|\mathbf{c}_i\|_\infty} \, , \tag{3.31}$$

where $\|\mathbf{a}_i\|_\infty = \max|\mathbf{a}_i|$. If the original matrix was symmetric, then $\mathbf{a}_i = \mathbf{c}_i$, which ensures the symmetry of the scaled matrix.

MEq – Matrix Equilibration. This preconditioning technique consists of repeating RC scaling (equation (3.31)) until each row and column of the Jacobian matrix has an infinity norm equal to one. Some remarks on the choice of the preconditioners $\mathbf{D_1}$ and $\mathbf{D_2}$ are necessary. One can also choose $\mathbf{D_1} = \mathbf{I}$, i.e., scaling only the columns of the Jacobian matrix. In this case, the right-hand side of the linear system would have been left untouched. We avoid this possibility because the accuracy of the system's solution also depends on the right-hand side. On the other hand, scaling only the rows of the system prevents us from re-scaling computed increments, which makes Row Identity (RI) scaling and Diagonal Identity (DI) scaling the easiest alternatives. Additionally, the scaling of each line or column is not necessary (Delay et al. 2007). However, "automatizing" the choice of constant values in some fashion is necessary in the context of an iterative procedure where the solution of the linear system occurs repeatedly. Row Column scaling (RC) is interesting because it can maintain the symmetry of the matrix and reduce gaps on the scale of orders of magnitude between columns, not only between rows, while the effectiveness of matrix equilibration (MEq) has already been proven through the methodology that was proposed by Knight (Ruiz and Uçar 2011).

3.1.9 Positive continuous fraction method

The positive continuous fraction method was presented by Carrayrou (Carrayrou et al. 2002) as a development of the continuous fraction method, a zero-order method whose variant has been implemented in PHREEQC (Parkhurst et al. 1999). According to the positive continuous fraction method, an approximation of equilibrium can be obtained for a given dissolved component X_j through the iteration of the following equation:

$$\left[X_j\right]^{n+1} = \theta_j^n \left[X_j\right]^n \left(\frac{sum_j^{prod,n}}{sum_j^{react,n}}\right)^{1/a_{i0,j}} + \left(1 - \theta_j^n\right)\left[X_j\right]^n , \tag{3.32}$$

where *reactive sum* and *product sum* are defined in (3.33) and (3.35) and in (3.34) and (3.36), respectively; θ_j is a weighting factor; and $a_{i0,j}$ is the smallest value of strictly positive stoichiometric coefficients that are linked to the component X_j. The definitions of *reactive sum* and *product sum* vary

according to the sign of the total conserved concentration $\left[\tilde{T}_j\right]$ (negative total concentrations may arise with ion exchange, while null totals occur in the presence of H^+).

If $\left[\tilde{T}_j\right] \geq 0$:

$$sum_j^{reac} = \sum_{a_{i,j}>0} a_{i,j}\left[C_i\right], \tag{3.33}$$

$$sum_j^{prod} = \left[\tilde{T}_j\right] - \sum_{a_{i,j}<0} a_{i,j}\left[C_i\right]. \tag{3.34}$$

If $\left[\tilde{T}_j\right] < 0$:

$$sum_j^{reac} = \left\|\left[\tilde{T}_j\right]\right\| + \sum_{a_{i,j}>0} a_{i,j}\left[C_i\right], \tag{3.35}$$

$$sum_j^{prod} = -\sum_{a_{i,j}<0} a_{i,j}\left[C_i\right]. \tag{3.36}$$

The positive continuous fraction method is an empirical method. Once the equilibrium solution is found, the reactive sum equals the product sum. This method is another formulation for the conservation equation (3.2). Thanks to the repartition between the reactive materials and products, one can check if the component concentration value $[X_j^n]$ is too high (*product sum* greater than *reactive sum*) or too low (*reactive sum* lower than *product sum*). The component concentrations should then be updated according to formula (3.37), which increases or decreases the component concentration depending on the respective values of the reactive and product sums:

$$\left[X_j\right]^{n+1} = \left[X_j\right]^n \left(\frac{sum_j^{prod,n}}{sum_j^{react,n}}\right)^{1/a_{i0,j}}. \tag{3.37}$$

Nevertheless, formula (3.37) does not consider simultaneous changes in all the components' concentrations. A weight factor θ_j is introduced into equation (3.32) to avoid unfavorable oscillations. In this work, we exploit the same approach and structure by simply turning equation (3.32) into the following:

$$\xi_j^{n+1} = \left(1-\theta_j^n\right)\xi_j^n + \frac{\theta_j^n}{a_{i0,j}}\left(\ln(sum_j^{prod,n}) - \ln(sum_j^{reac,n})\right). \tag{3.38}$$

Then, we define the weight factor θ_j as follows:

$$if\left(sum_j^{reac} > sum_j^{prod}\right)then \quad \theta_j^n = \alpha - \frac{sum_j^{prod}}{sum_j^{reac}}\cdot\beta$$

$$if\left(sum_j^{prod} > sum_j^{reac}\right)then \quad \theta_j^n = \alpha - \frac{sum_j^{reac}}{sum_j^{prod}}\cdot\beta$$
(3.39)

where α and β are constants that control the amplitude of the step towards the solution. The step should be allowed to be large at the beginning (when sum_j^{reac} and sum_j^{prod} are different) but should be limited near the solution (when the two quantities are similar) In this work, these constants are set at $\alpha = 0.1$ and $\beta = 0.08$. The weighting factor is updated only if $\theta_j^n > \theta_j^{n-1}$.

3.1.10 Numerical experiments

A first simplified numerical example is proposed in order to highlight the effects of matrix conditioning and round-off errors on chemical equilibria solutions. The simplified chemical system is composed of three species and two components and is detailed in Table 3.1. The system is solved by the Newton Raphson method (NR), NR with Row-Column scaling (NR-RC), the positive continuous fraction (PCF) method, and PCF coupled with NR. For the initial conditions that are defined in Table 3.1, the associated matrix for the NR method has a condition number of $1.4 \ 10^3$ and the scaled matrix (NR-RC) has a condition number of $9.3 \ 10^2$. These condition numbers are defined in equation (17) by using the infinity norm. As shown by equation (16), the accuracy of the solution depends on the condition number and the round-off errors. Figure 3.1 shows the effects of the round-off errors on the path from the initial guesses to the solution of the above system.

	ξ_1	ξ_2	K
ξ_1	1	0	1.0
ξ_2	1	1	1.0
$\xi_1\xi_2$	-1	3	2000.0
T	1.0	1.0	
ξ Initial	6.0	3.0	

Table 3.1 - Stoichiometric coefficients, thermodynamic constant (K), totals of the components ξ_1 and ξ_2 (T), and logarithm of the initial activity (ξ Initial).
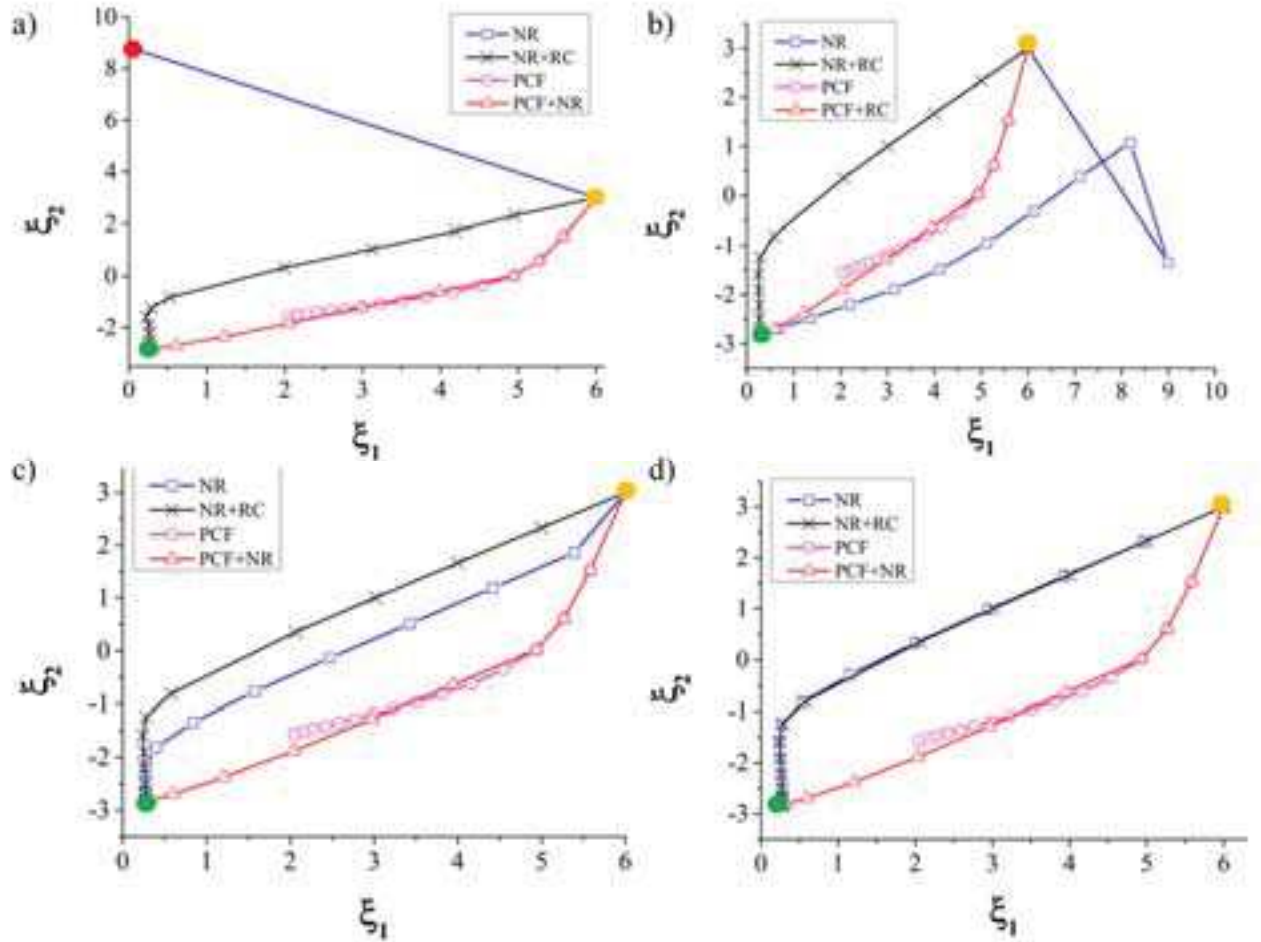
Figure 3.1 - Effect of the round-off error 10^{-d} on the iterative solution. The picture shows the path throughout the solution of four variants of the same simplified problem. Figures (a), (b), (c) and (d) show the results for different values of d, the exponent of the round-off error (d=3, 4, 5 and 6 for, respectively). Since the problem has only two unknowns (components ξ_1 and ξ_2) the path from the common initial guesses (ξ_1 =6.0 and ξ_2 =3.0) to the solution (ξ_1 =0.3 and ξ_2 = -2.9) is easily represented on a 2D graph. Within a single variant of the problem, different paths occur with different algorithms. When round-off error is higher (a) the implementation of scaling makes the difference between reaching the solution or not.

This example shows that the NR method is sensitive to the computational accuracy. In the worst case, the method does not converge (Figure 3.1a) or converges after some amount of iterations, even if the system is not accurately solved during the first iterations (Figure 3.1b and c). Once an acceptable accuracy is defined, NR and NR+RC lead to very similar solutions (Figure 3.1d). NR+RC is much less sensitive to the accuracy because the matrix is better conditioned, even if the contrast in the condition numbers is not very high for this example. The path to the solution does not change for the studied round-off errors. PCF is a first-order method that does not require a system to be solved. The method is provided here to illustrate its advantages and drawbacks; specifically, the method is robust far from the solution but inefficient in the neighborhood of the solution (the computation is stopped after 15

iterations for this example). Finally, the association of PCF and NR provides an interesting alternative. The algorithm starts with a prescribed number of PCFs (3 in this example) and switches to NR to reach the solution. This association is not sensitive to the round-off errors in this example. Finally, NR may reach the solution in fewer iterations than NR+RC even if the system matrix is not solved properly (Figure 3.1c). The wrong direction of descent for the first iteration is more efficient than the correct one. This process may occur a very few times and is not reliable.

Real or realistic experiments involve a larger number of species and components than those involved in the previous experiment. A visual representation is therefore impossible, but the issues remain the same as before. The efficiencies of the different algorithms on more complex experiments are studied with 7 test cases of increasing complexity. Each test case is solved through the technique clarified in the previous sections: the concentrations of all the chemical species C_i in the system are computed based on a set of fixed components X_j, assuming their total amount $\left[\tilde{T}_j\right]$ in the system is known. The majority of the test cases are available in the literature and considered to be numerically challenging in reason of large range of stoichiometric coefficients and equilibrium constants . The number of species and components for each test case are summarized in Table 3.2.

	Dissolved species	Adsorbed species	Precipitates	Components	$\log_{10}K_{min}$-$\log_{10}K_{max}$
Gallic Acid	17	-	-	3	-39.56 - -4.15
MoMaS Easy	9	3	-	5	-12 – 35
Pyrite	40	-	-	4	-520.6 – 19.17
Pyrite M	40	-	3	4	-520.6 – 19.17
Fe Cr	40	-	-	7	-83.17 – 80.9
Fe Cr Min	40	-	3	7	-83.17 – 80.9
MoMaS Hard	12	3	2	6	-12 – 35

Table 3.2 - Summary of the test cases for thermodynamic equilibrium study.

The first and simplest test case is Gallic Acid, a system proposed by Brassard and Bodurtha (2000) as an example of the onset of problems in numerical methods. The system was originally studied in relation to Al(III) speciation in natural waters (Öhman 1983). This first test case is characterized by the presence of 17 chemical species that can be described through the combination 3 components. Since no solid phase is taken into consideration here, the Jacobian matrix has size 3x3, the smallest of the whole set of test cases. Also the range of variation of equilibrium constants is the smallest of those examined. Increasing complexity is found in MoMaS Easy test case, a synthetic benchmark designed to evaluate the performances of computational codes and published in a special issue of

Computational Geosciences (Carrayrou et al. 2009). This test case is characterized by the presence of only 12 species and the number of base components required to describe the system is 5 (2 more than those needed for Gallic acid). At the same time the interval of variation of equilibrium constants is higher (47 against 35 orders of magnitude) than in the previous case. Complexity increases significantly approaching Pyrite[31] test cases. This example describes the environment for the potential precipitation of Pyrite (FeS_2). In a first variant of the test case precipitation of a solid phase is denied and the system is composed of 40 dissolved species described through 4 components. The number of components is limited but the differences between equilibrium constants are huge: the lowest is -520 and the highest 19. A second variant of the test case, Pyrite Mineral, is examined. This example is a copy of the previous enriched with the test for the formation of 3 minerals ($Fe, FeSO4, FeS_2$). The size of the Jacobian matrix becomes 7x7. Continuing in the presentation of test cases, it becomes harder to precisely assess the order of complexity. MoMaS Hard test case comes from the same set of synthetic examples of MoMaS Easy (Carrayrou et al. 2009). It's characterized by the presence of 12 chemical species and described through 6 components. Two minerals are tested for precipitation, making the Jacobian matrix 8x8 while the range of equilibrium constants remains the same of MoMaS Easy. Two test cases involving iron and chrome are also studied. Fe Cr test case is the simplest and describes a chemical system of 40 species and 7 components with no test for precipitates. In this case the number of components is higher than in the Pyrite test cases but the range of variation of equilibrium constants is considerably smaller. Fe Cr Min is a variant of the previous case in which 3 minerals are tested for precipitation, making the Jacobian matrix size 10x10. The whole sets of equilibrium constants and a complete description of the chemical species and components are presented in Annex II.

Because the motivation of this work is to evaluate the behavior of the Newton Raphson method and associated algorithms, we only compute the first solution of the chemical system, i.e., if precipitation occurs and no precipitation was assumed, the computation is not repeated. Therefore, we also assumed that the activity coefficients were constant and equal to one. Because the efficiency of the Newton Raphson method is very sensitive to the initial guesses, we searched the solutions of chemical equilibria for 30000 initial component concentrations X_j, except for Gallic Acid (10000), which appeared to be the easiest test case. We assumed that 30000 (10000 for Gallic Acid) simulations would adequately represent the behaviors of the convergence rates for each example because the percentage of failure (actually the mean number of iterations that is required to converge) remains unchanged after 25000 runs at most.

Usually, initial guesses for the Newton Raphson method are chosen with great care (i.e., from the concentrations at the previous time step in transient computations). However, initial guesses are not always known, especially for the first time step or for sharp fronts, where the concentrations show abrupt changes from cell to cell in the reactive transport code. Because the aim of this work is to test

the robustness of the method no matter the initial conditions, these conditions are chosen randomly in a reasonable interval, as described and explained in Annex III. The robustness of the procedure is also enhanced by prescribing boundaries to the NR increments (Annex III).

We remark that the 30000 solutions are intended for a coupling test case/method of resolution. This means that each test case has been solved 30000 times with each method of resolution. To sum up, different resolutions methods are: regular Newton Raphson method, Newton Raphson method implemented with the four scaling techniques and with the matrix equilibration procedure, regular Newton Raphson coupled with Positive Continuous fractions (implemented at different degrees of ill-conditioning).

The convergence criterion is written based on the residual $Y_j = \left[\tilde{T}_j \right] - \left[T_j \right]$ and the quantity $W_j = \left[\tilde{T}_j \right] + \sum_i \left| a_{i,j} \left[C_i \right] \right|$. The totals that appear in the previous equations were defined in equation (3.9). In the presence of precipitates, W_j is not computed and the value of the convergence criterion corresponds to the residual:

$$
\begin{aligned}
err_j &= \frac{Y_j}{W_j} \quad j = 1, ..., N_X \\
err_j &= Y_j \quad j = N_X + 1, ..., Nx + Ncp
\end{aligned}
$$
(3.40)

The Newton Raphson iterations end when the convergence criterion is satisfied, i.e., when the highest residual is lower than a given threshold ($tol = 10^{-12}$). The Newton iterations are also stopped when the maximum number of iterations exceeds 2000. When possible (with symmetric matrices), the evaluation of the condition number is performed with two approaches: (i) the absolute value of the ratio between the highest and lowest eigenvalues of the Jacobian matrix (3.18) and (ii) the product of the norm one of matrix $\mathbf{J}$ and its inverse $\mathbf{J}^{-1}$ (3.17). The subroutine DE3LRG in the IMSL library is used to evaluate the eigenvalues. The linear systems (3.13) and/or (3.27) within the Newton Raphson procedure are solved through LU factorization with quadruple precision. The matrix equilibration algorithm performs scaling on the Jacobian matrix until the infinity norm of each row and column equals one. We set a maximum number of iterations $n_{max}^R = 5$ to avoid excessive slowdowns in the computation. The algorithm starts with positive continuous fractions when implemented and depending on the condition number, i.e., the algorithm is activated if the condition number is higher than a fixed threshold. Only ten iterations of this method are performed because the aim is to use the algorithm as a type of preconditioner and not to reach the solution (also in light of the results in Figure 3.1).

3.1.11 Numerical simulations: discussion

The purpose of scaling is to reduce the condition number of a linear system. We evaluated the condition number of the Jacobian matrix of the nonlinear system before and after scaling. We presented the results for problems with condition numbers at different orders of magnitude and for a round-off error of 10^{-32}.

When the condition number was on the order of 10^{60} or lower (as in Figure 2a), both methods of computing the condition number (as the product of the norm one of the Jacobian matrix and its inverse (equation (3.17)) and as the ratio of the eigenvalues (equation (3.18))) were effective and provided the same results.
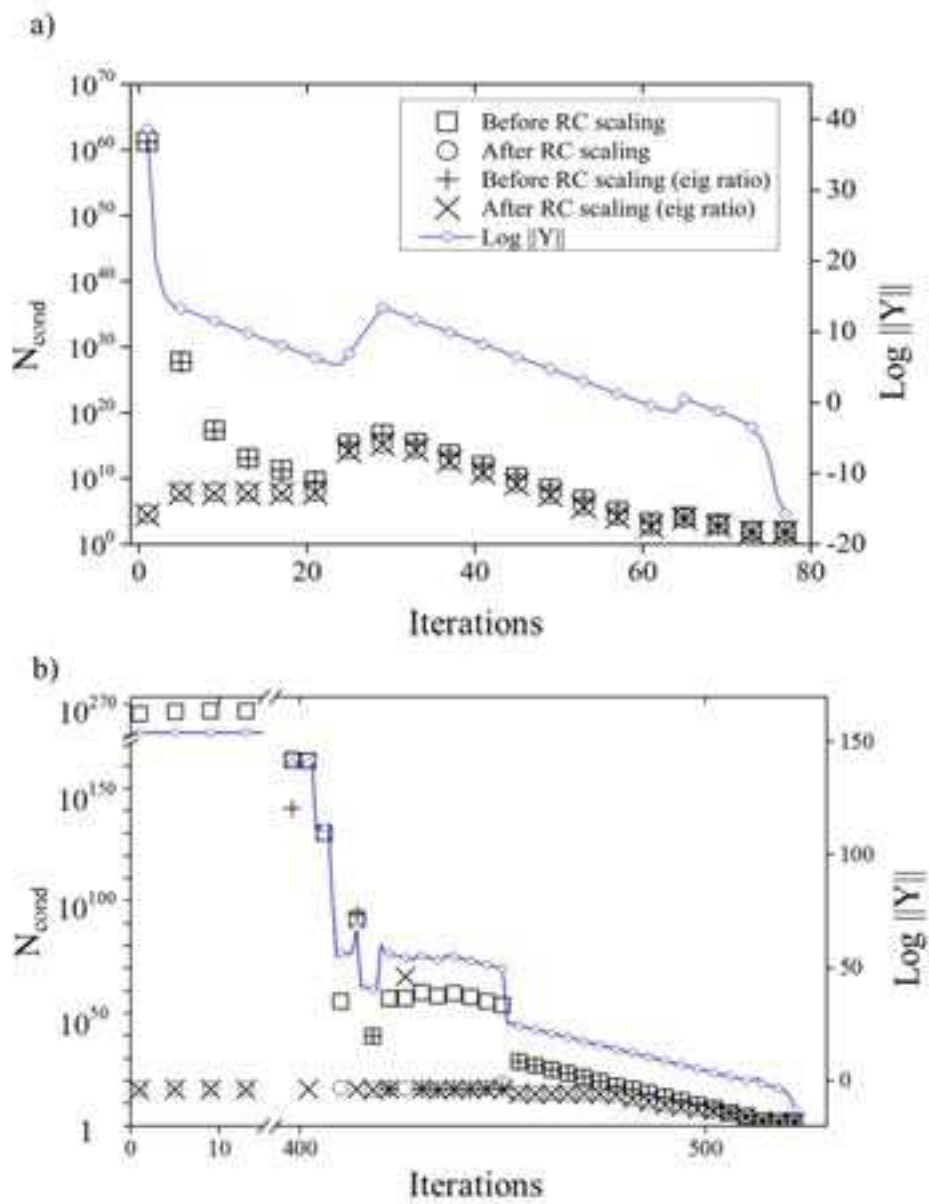
Figure 3.2 - Variation in condition numbers throughout the minimization for the Pyrite test case with favorable initial guesses (a) and poor initial guesses (b) of the component concentrations.

Under this circumstance, the condition number was generally reduced by RC scaling, even if the amplitude of this reduction varied widely. When the Jacobian matrix had a condition number on the order of 10^{200} or more (Figure 3.2b), the estimation of the condition number was no longer reliable: the inversion of the Jacobian matrix was heavily imprecise, and the DE3LRG subroutine from IMSL failed to estimate the eigenvalues for condition numbers that were greater than 10^{50}. RC scaling was effective except for condition numbers that were approximately 10^{120}-10^{150}, which shows that scaling may be useful but not universally so. Figure 3.2 shows that the condition number decreased with the distance from the solution. When a large number of iterations were required to converge, the initial values of the condition number were extreme. When a modest number of iterations were necessary to reach the solution, the condition number had smaller values and showed more regular behavior (Machat and Carrayrou 2016).

		No scaling	RC scaling	RI scaling	MEq	PCF def
Gallic Acid	50%	20	20	20	20	<20
	70%	40	40	40	40	<20
	90%	120	120	120	120	<20
MoMaS E.	50%	50	50	50	50	75
	70%	80	80	80	80	<80
	90%	340	240	220	140	<80
Pyrite	50%	90	90	90	90	<40
	70%	680	300	340	320	40
	90%	>2000	>2000	>2000	1800	<50
Fe Cr	50%	120	120	120	120	50
	70%	180	180	180	180	60
	90%	260	260	260	260	80
Pyrite M.	50%	45	50	50	50	40
	70%	60	60	60	65	45
	90%	90	90	90	95	50
MoMaS H.	50%	45	45	45	560	35
	70%	85	70	80	860	40
	90%	>2000	>2000	>2000	1330	45
Fe Cr Min	10%	35	35	35	40	35
	30%	75	55	90	55	45
	50%	>2000	>2000	>2000	>2000	75

Table 3.3 - Number of iterations that are required to solve 50, 70 and 90% of the studied problems for each test case (10, 30 and 50% for Fe Cr Min).

The results are presented through the relative number of obtained solutions as a function of the number of iterations for each test case (Figures 3.3 to 3.9). When the solution is obtained for all the initial conditions (N_{tot}=30000 for all test cases except Gallic Acid), the relative number equals 1. The distributions of the initial condition numbers are also provided in Figures 3.3 to 3.9. Table 3.3

provides the number of iterations that are required to solve 50%, 70% and 90% of the problems for each test case and each algorithm. The number of failures (solution not reached after 2000 iterations) is listed in Table 3.4. The results vary widely between test cases, particularly for the implementation of scaling techniques.

	MoMaS E	Pyrite	Pyrite M	MoMaS H	Fe Cr Min
No Scaling	4.1	13.8	3.3	16.8	54.2
RC	2.1	12.3	2.2	13.1	51.5
RI	4.4	17.9	2.0	15.1	58.3
sDsD	5.0	22.1	3.8	13.3	50.3
DI	10.0	18.8	3.2	15.4	62.8
MEq	1.9	7.5	4.2	5.2	52.0
PCF cond >10^{40}	1.7	0.0	1.4	0.7	45.1
PCF cond >10^{10}	0.1	0.0	1.4	0.0	43.0
PCF def	0.0	0.0	1.0	0.0	43.0

Table 3.4 - Failure % of the different algorithms for each test case (NB: no failure for Gallic Acid and FeCr test cases).

In the case of **Gallic Acid** speciation (Figure 3.3), no differences existed among the curves that represented the standard Newton Raphson method, Newton Raphson with scaling techniques or PCF, which were activated when the condition number was greater than 10^{20}, because most of the condition numbers were below 10^{20} (Figure 3.3a). Because the condition numbers were smaller than the threshold (10^{32}) that complicates the computation of reliable digits in terms of the round-off error (10^{-32}), the system was solved accurately with or without scaling. When PCFs were performed by default, the number of iterations that were required to solve 100% of the problems dropped from 250 to approximately 30. The results that correspond to the activation of PCFs when the condition number was greater than 10^{10} provide an intermediate result because some computations were run without PCFs (condition number less than 10^{10}).

The distribution of the initial condition numbers reached 10^{90} for the **MoMaS Easy** test case (Figure 4a). Newton Raphson when implemented with scaling performed better than standard Newton Raphson except for DI (Figure 3.4b). 90% of the problems were solved within 140 iterations with the matrix equilibrium technique where other scaling techniques required more than 200 (Table 3.3). The solution of NR coupled with PCFs constantly outperformed the integration of scaling (Tables 3.3 and 3.4). This test case also demonstrated the main shortcoming of the PCF method: as shown in Figure 3.4, PCFs can slow down the solution process in the neighborhood of the solution. When PCFs were applied by default (i.e., regardless if they were needed), almost no solutions were obtained within 20 iterations and only a few within 40. This result confirms that the NR method needs no strengthening when the initial conditions are favorable.
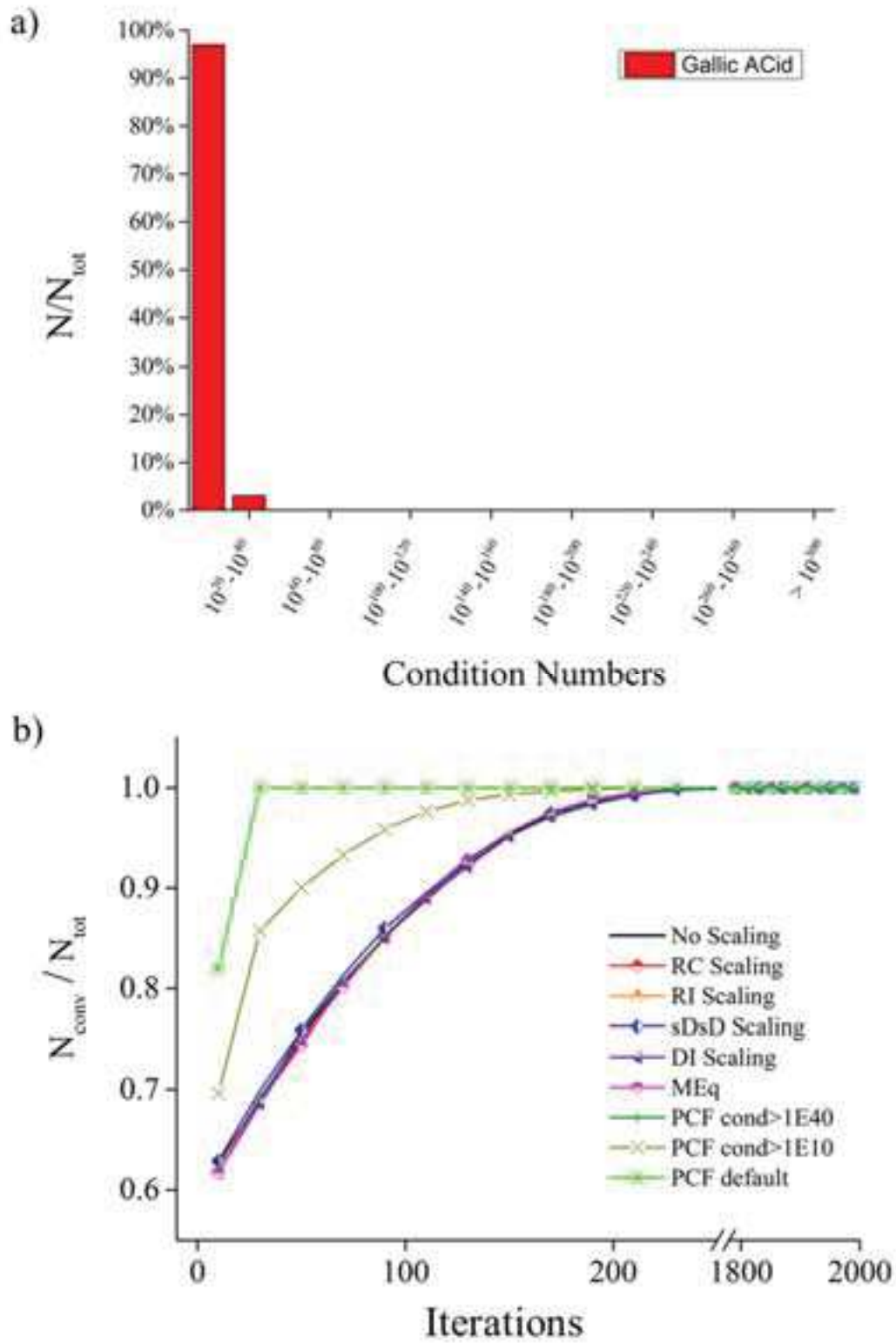
Figure 3.3 - Initial condition number and relative number of solutions for the Gallic Acid test case.
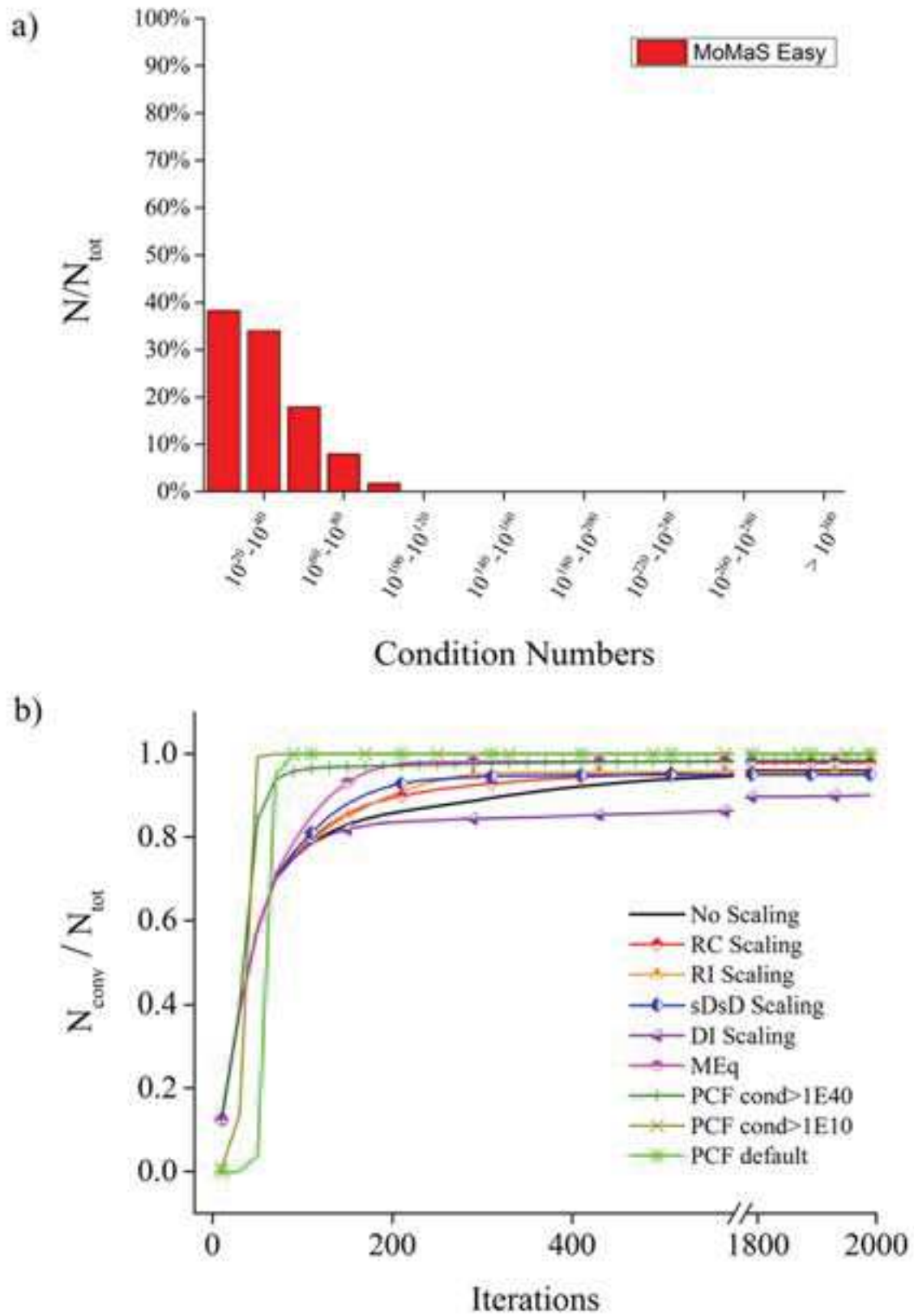
Figure 3.4 - Initial condition number and relative number of solutions for the MoMaS Easy test case.

The difficulty in finding a solution increased for the **Pyrite** test case, which exhibited numerous condition numbers that were greater than 10^{200} (Figure 3.5a). Approximately 85% of the problems were solved by NR or NR with scaling with the same efficiency, except the matrix equilibration technique which was able to solve 90% of the problems in about 1800 iterations (Table 3.3) and solved 95% of the problems (Table 3.4). The increase in the number of iterations (from approximately 200 to 600) did not change the probability of success in solving the problem. This probability slightly increased after 1000 iterations, but none of the NR methods could solve all the problems. Scaling by MEq was the most efficient scaling technique for this example. The PCFs appeared to be very efficient, solving all the problems with about 50 iterations.

Most of the condition numbers of the standard NR ranged from 10^{40} to 10^{160} for the **Fe Cr** test case (Figure 3.6a). Scaling did not improve the convergence probability (Figure 3.6b and Table 3.3) for that range of condition numbers. The scaling techniques improved the system's matrix properties but not enough to compute an accurate solution of the system. Therefore, scaling was inefficient in this case. Moreover, no significant differences existed in the activation of PCFs after different thresholds of condition numbers, which means that the large majority of the problems had a condition number that was greater than 10^{40}. **Pyrite Mineral**, exhibited high contrasts in the condition numbers, with 1/3 of the system matrices having a condition number that was greater than 10^{300} (Figure 3.7a). At this level of complexity, scaling techniques were not efficient enough to reduce the high condition numbers. Condition numbers that were greater than 10^{300} were indeed reduced but still remained enormous (10^{260}-10^{280}) (Figure 3.7a). Therefore, NR with scaling was as efficient as NR without scaling at solving this system of equations (Figure 3.7b). Again, the PCFs appeared to be very efficient, and 90% of the problems were solved in fewer than 50 iterations (Table 3.3). The **MoMaS Hard** test case contemplated the presence of precipitates, and its condition numbers ranged from 10^{10} to 10^{200} (Figure 8a). Therefore, some problems were solved with a small number of iterations (less than 50 for more than 50% of the initial conditions – Table 3.3), except for the MEq. For more difficult problems, the implementation of scaling techniques (except MEq) improved the situation slightly. MEq reduced the condition numbers significantly (Figure 3.8a) and the number of failures more than other scaling techniques but made the process of convergence slower (Figure 3.8b). The implementation of PCFs coupled with the standard Newton Raphson method improved in a more noticeable way both the robustness and speed of the convergence. Again, the standard PCFs required more iterations than the adapted PCFs to solve the easiest problems.
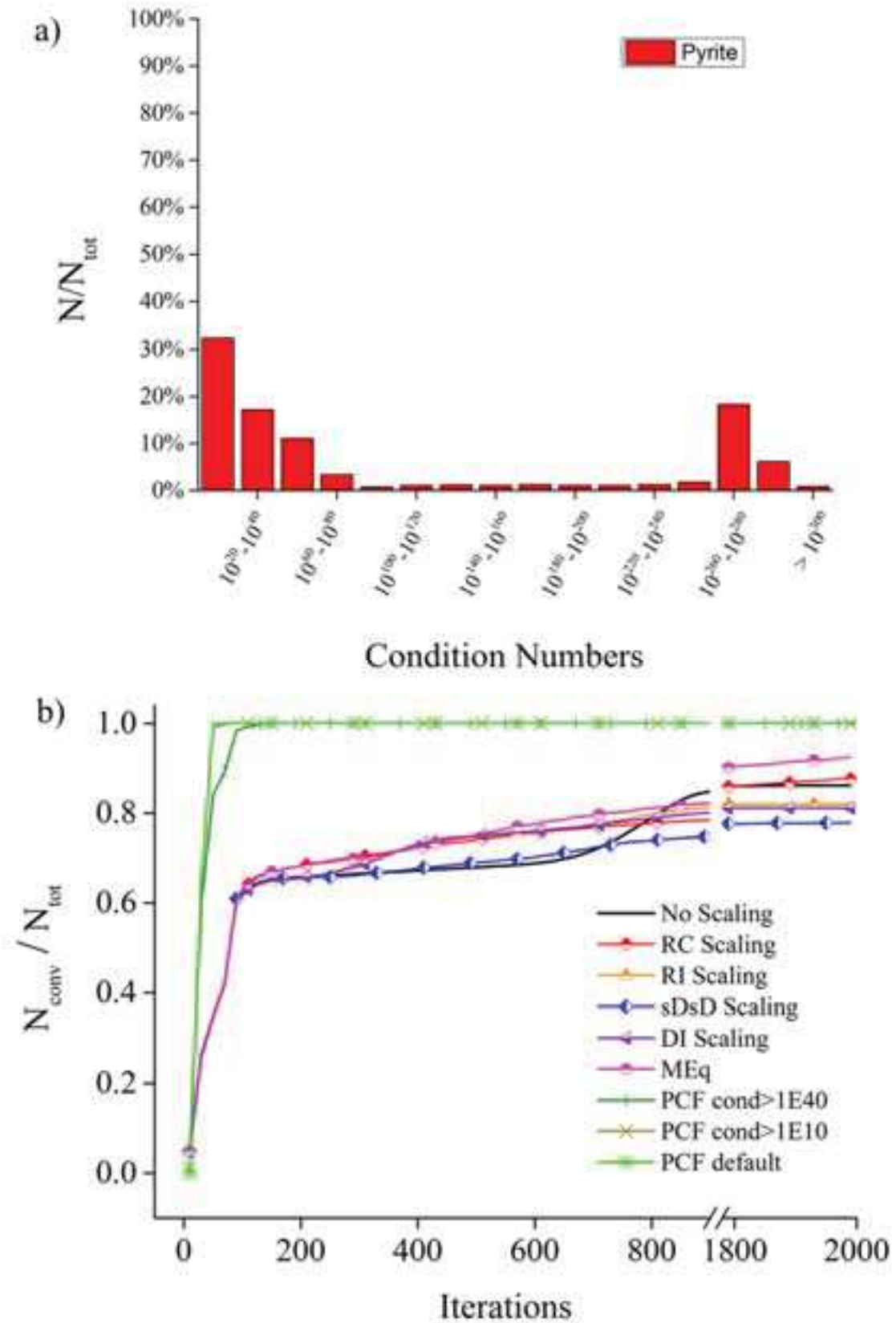
Figure 3.5 - Initial condition number and relative number of solutions for the Pyrite test case.
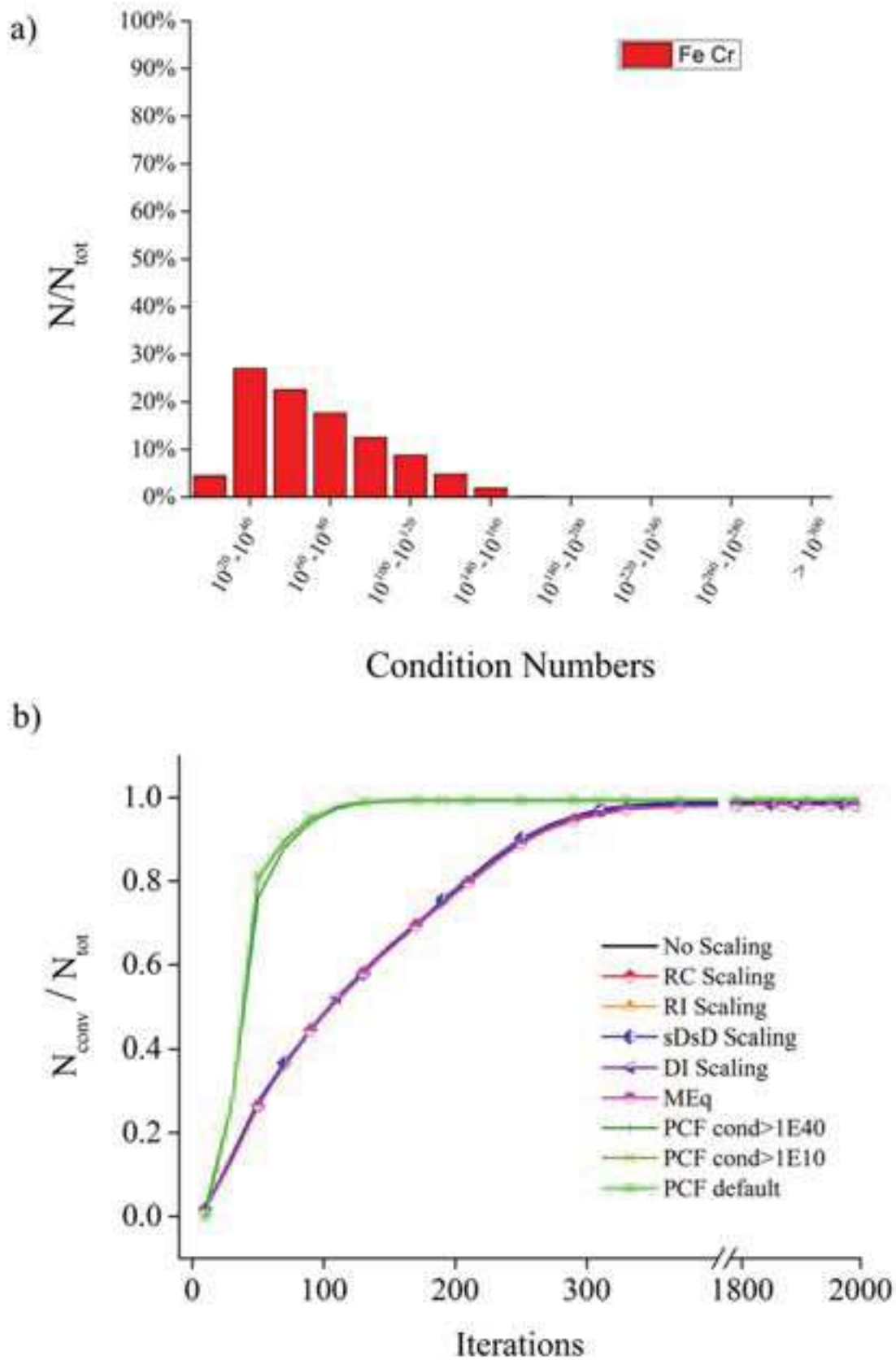
Figure 3.6 - Initial condition number and relative number of solutions for the Fe Cr test case.
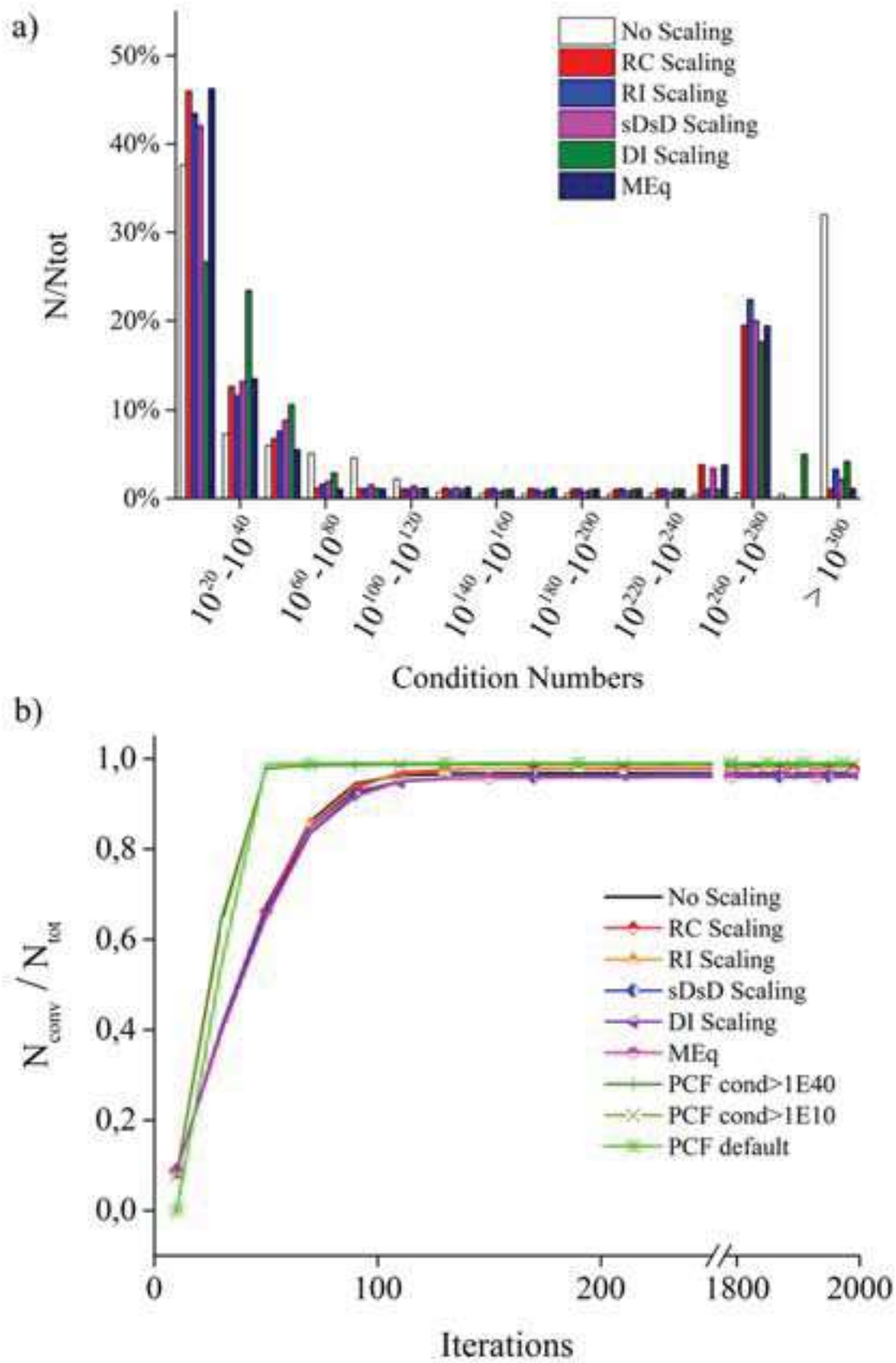
Figure 3.7 - Initial condition number and relative number of solutions for the Pyrite Mineral test case.
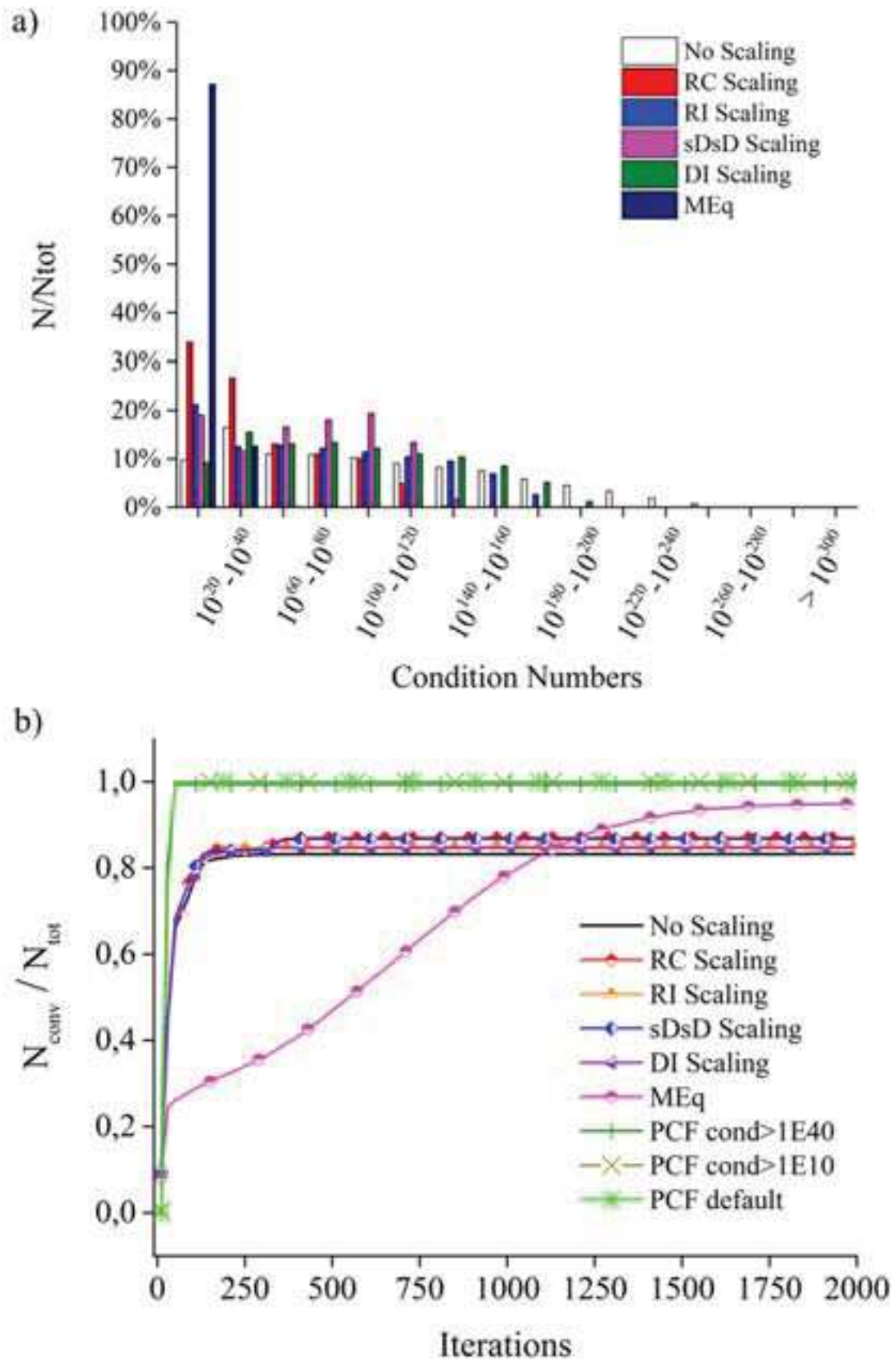
Figure 3.8 - Initial condition number and relative number of solutions for the MoMaS Hard test case.
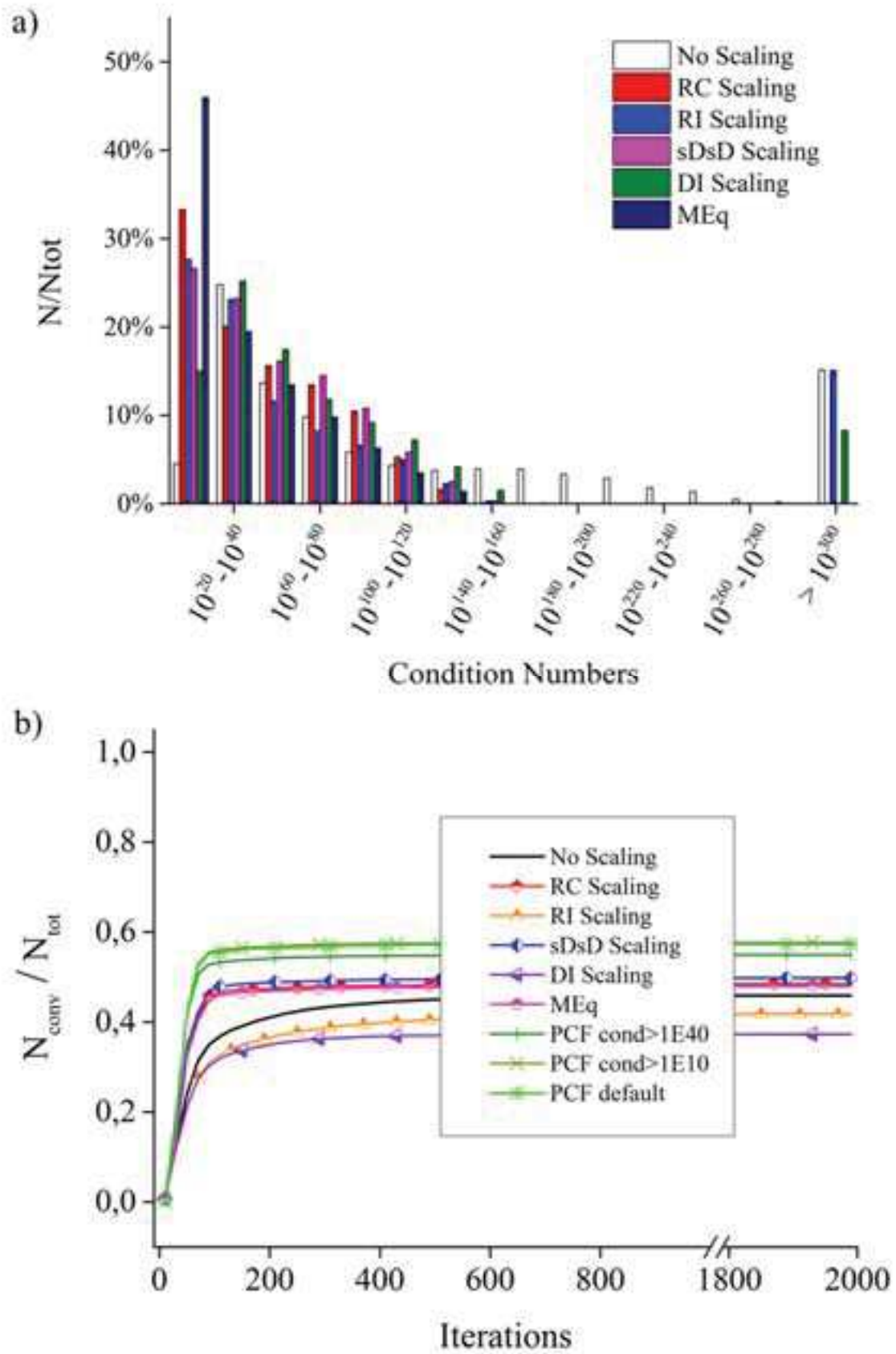
Figure 3.9 - Initial condition number and relative number of solutions for the Fe Cr Mineral test case.

For the **Fe Cr Min** test case, the addition of precipitates considerably changed the matrix properties compared to **Fe Cr** (Figure 3.9a). All scaling techniques dealing with both rows and columns reduced the number of failures and improved the robustness of the algorithm (Figure 3.9b). For this example, the sDsD scaling method was the most appropriate. At this level of complexity, some scaling techniques (RI and DI scaling) were inefficient and, in particular, less efficient than NR without scaling at solving this system of equations. Even if the PCFs provided a further improvement in terms of speed and robustness, nearly the half of problems remained unsolved (Table 3.4).

The effects on CPU time were negligible for all the scaling procedures with the exception of matrix equilibration (MEq), which increased the duration of a single iteration by approximately 20%. However, this significant increase in the CPU time for one iteration is compensated by the total number of iterations that are required to solve a given percentage of the problems (Table 3.3). Solving 70% of the problems for the Pyrite test case with the standard Newton Raphson method required approximately 700 iterations. On the other hand, only 350 iterations were necessary for the Newton Raphson method with matrix equilibration to solve the same percentage of problems. This same situation occurred for the MoMaS Easy test case, where solving 90% of the problems with standard Newton Raphson required approximately double the iterations of Newton Raphson with matrix equilibration. The computational effort for PCFs for one iteration was significantly smaller than that for any NR method because this method did not require the computation of the Jacobian matrix and its solution. The effects of coupling the NR method with scaling techniques or positive continuous fractions on the robustness were evaluated by counting the number of failures (i.e., non-convergence events within 2000 Newton Raphson iterations) while searching for the solution.

The percentages of failures (computed with respect to 30000 attempts for the test cases) are reported in Table 3.4. While positive continuous fractions improved the robustness of the code without exception, the outcomes of implementing scaling techniques strongly depended on the test case. The MoMaS Easy test reduced the number of failures when RC scaling and matrix equilibration were applied, while other techniques were counterproductive in terms of robustness (if the limit of the Newton Raphson number of iterations was set to 2000). In the Pyrite test case, RC scaling and matrix equilibration increased the robustness of the method, while other scaling procedures induced the opposite effect. For the MoMaS Hard test case, very small increments of robustness were registered for RI scaling, matrix equilibration and DI scaling. All the preconditioners (but DI scaling) for the Fe Cr Min test case seemed to significantly reduce the number of failures. A global look at the bottom half of Table 4 suggests that PCFs drastically outperformed scaling techniques in terms of reducing the number of failures after 2000 NR iterations. Among the scaling techniques, matrix equilibration and RC scaling worked the best, significantly reducing the number of non-convergences in some cases.

3.1.12 Conclusions about the strategies to improve Newton Raphson method

The results of scaling strongly depended on the test case. In problems such as the Pyrite, MoMaS Easy or MoMaS Hard test cases, scaling techniques (especially Row-Column scaling and matrix equilibration) generally exerted a positive impact. Meanwhile, the utility of scaling was questionable for other problems, such as the Fe Cr Min and Pyrite Mineral test cases. These results suggest three possible classifications:

- − 'Easy' problems, such as the Gallic Acid test case, which are insensitive to scaling because NR without scaling is efficient. The reduction in the condition numbers by scaling does not improve the efficiency of NR because the initial condition numbers are already small enough (i.e., smaller than the round-off error);

- − Problems where scaling reduces the condition numbers to values on the order of magnitude of the round-off error;

- − Problems that are very difficult to solve and where scaling does not reduce the condition numbers sufficiently, providing unpredictable reactions to scaling. This was the case when precipitation were included (3 last test cases).

Among the scaling techniques, matrix equilibration and RC appeared to be globally useful in terms of increasing the robustness of the algorithm and sometimes reducing the number of iterations that were required to reach the solution. However, the drawback of this scaling method was the additional computational costs.

The coupling of NR with positive continuous fractions produced results that were quite similar for every test case. This coupling drastically reduced the number of failures, the number of iterations that were required to reach convergence, and their variability (the cumulated frequency curves are nearly vertical). However, PCFs alone should be avoided because they are very slow when they approach the solution. The previous results seem to indicate that the ill-conditioned linear systems that arise in Newton Raphson iterations are only an obstacle to fast convergence for problems that are not too easy or tough. When the condition numbers are too high, they are no longer the cause of an eventual failure and become a symptom of the Newton Raphson method's inadequacy. PCFs bring the values of the unknowns close to the solution, where the Newton Raphson algorithm is known to be extremely efficient. This coupling seems to bypass the problem of ill-conditioned linear systems, transforming tough problems into more easy problems and avoiding the intermediate zone. This behavior enforces the idea that the condition numbers of the Jacobian matrix decrease while approaching the solution.

At this stage of our work, we strongly recommend coupling PCFs with NR. PCFs should only be activated when needed, i.e., when the condition number of the Jacobian matrix is greater than a given threshold. Because the computation of the condition number might require some computational costs, this process can be replaced by the norm of the residuals and a corresponding user's defined threshold.

Moreover, the Jacobian matrix can be scaled by the RC method, which is the first iteration of the MEq scaling technique, to improve the robustness of NR without increasing the CPU time.

3.2 Thermodynamic capabilities of the code

Numerical experiments described in the paper were conducted on aqueous speciation, surface adsorption independent of electrostatic potential and equilibrium precipitation based on the computation of a saturation index. Nevertheless, the code is equipped with functions to model other equilibrium phenomena such as *surface complexation* and *ion exchange*. In order to implement these models, the residual functions Y_j and consequently some entries of the Jacobian matrix has to be slightly modified, but the solution of the non-linear system is still carried out with Newton Raphson method in its modified version.

3.2.1 Modeling surface complexation

Surface complexation is a mechanistic way of describing adsorption (Sigg et al. 2000; Goldberg et al. 2007), a phenomenon taking place at the interface between liquid and solid phase, when ions in the solution occupy some specific sites of the solid surface (Dzombak and Morel 1990). Adsorption may be modeled through empiric models (such as Langmuir and Freundlich isotherms) but these laws fail to provide a connection between the phenomenon and thermodynamic conditions. Surface complexation is a way of describing adsorption through mass action laws that allows taking into account charge effects on the surface. An example of surface complexation reaction may be:

$$\equiv S - OH + M^{2+} \Longleftrightarrow \equiv S - OM^+ + H^+ \tag{3.41}$$
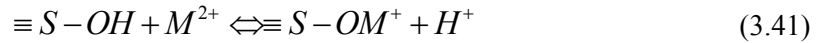
where $\equiv$*S-OH* is the surface site that may release an atom H^+ in order to receive a generic ion M (with a possible different charge). The surface may then be charged under the constraint that electroneutrality with the solution is respected in its vicinity. The mass action law corresponding to previous reaction would be:

$$K(z,\psi) = \frac{\{S - OM^+\}\{H^+\}}{\{S - OH\}\{M^{2+}\}} \tag{3.42}$$

Previous equation is different from a classical mass action law in the fact that constant K may be function of the electric charge z and the potential Ψ of the surface $\equiv$*S-*. If the surface is charged, the same but opposite charge is going to appear in the solution in the vicinity of the surface. Several models may be adopted to describe the phenomena in the proximity of the surface: Constant Capacity Model (Stumm et al. 1980) and Diffuse Layer Model (Dzombak and Morel 1990), Basic Stern and Triple Layer Model (See Figure 10).
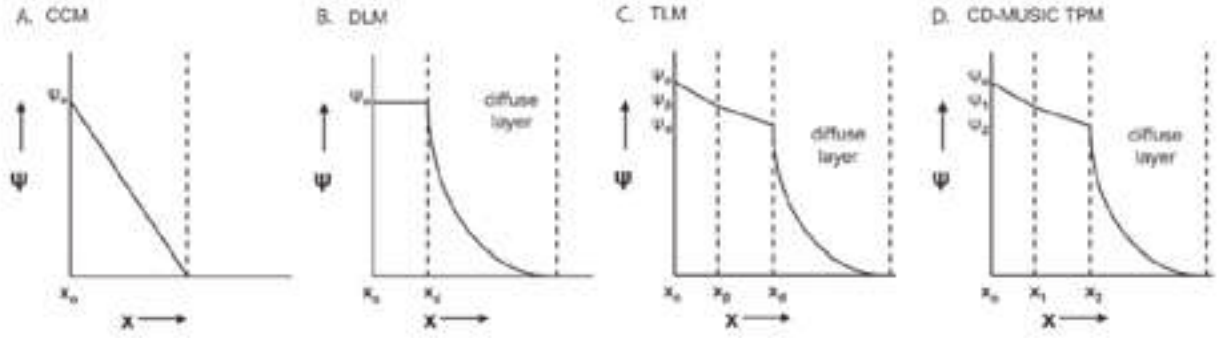
Figure 3.10 – Different surface complexation models: a) constant capacity model b) Double layer model c) Triple layer model d) CD-MUSIC triple layer model (not treated here) (Figure from (Goldberg et al. 2007)).

According to the model adopted, and therefore to the number of different potentials Ψ used in the model, supplementary components are added to the reaction network (one component for each potential); this is done in order to take into account the dependence of the equilibrium constant K from the charge and the potential (Carrayrou 2001). The theoretical form of the new component is:

$$X_\Psi = \exp\left(-\frac{F}{RT}\Psi\right) \tag{3.43}$$

For each additional component, a residual function is added to the system:

$$Y_\Psi = -T_\Psi^{EL} + T_\Psi^{CdM} \tag{3.44}$$

where T_Ψ is the total concentration of charges fixed on the surface; T_Ψ^{EL} computed through electric consideration and T_Ψ^{CdM} through mass balance equations must coincide. T_Ψ^{CdM} is computed through:

$$T_\Psi^{CdM} = \sum_{i=1}^{Nc} z_i \left[C_i\right] \tag{3.45}$$

where z_i is the charge of the adsorbed species and C_i their concentration. For each model, one or more different formulations of T^{EL} are available. Equations written as functions of $\xi_\Psi = log(X_\Psi)$ take the following form:

i)   for Constant Capacity Model:

$$T_\Psi^{EL} = -RT \frac{Cap S_j M_j}{F^2} \xi_\Psi \qquad (3.46)$$

ii)   for Diffuse Layer Model:

$$T_\Psi^{EL} = \frac{S_j M_j}{2F} \sqrt{8RT\varepsilon\varepsilon_0 I} \left(\exp^{-\frac{Z_{el}}{2}\xi_\Psi} - \exp^{\frac{Z_{el}}{2}\xi_\Psi} \right) \qquad (3.47)$$

iii)   for Basic Stern Model:

$$T_{\Psi0}^{EL} = -RT \frac{Cap S_j M_j}{F^2} \left(\xi_{\Psi0} - \xi_{\Psi1} \right)$$

$$T_{\Psi1}^{EL} = T_{\Psi0}^{EL} + \frac{S_j M_j}{2F} \sqrt{8RT\varepsilon\varepsilon_0 I} \left(\exp^{-\frac{Z_{el}}{2}\xi_\Psi} - \exp^{\frac{Z_{el}}{2}\xi_\Psi} \right) \qquad (3.48)$$

iv)   for Triple Layer Model:

$$T_{\Psi0}^{EL} = -RT \frac{Cap_0 S_j M_j}{F^2} \left(\xi_{\Psi0} - \xi_{\Psi1} \right)$$

$$T_{\Psi1}^{EL} = -RT \frac{Cap_0 S_j M_j}{F^2} \left(\xi_{\Psi1} - \xi_{\Psi2} \right)$$

$$T_{\Psi2}^{EL} = -RT \frac{Cap_1 S_j M_j}{F^2} \left(\xi_{\Psi2} - \xi_{\Psi1} \right) + \frac{S_j M_j}{2F} \sqrt{8RT\varepsilon\varepsilon_0 I} \left(\exp^{-\frac{Z_{el}}{2}\xi_{\Psi2}} - \exp^{\frac{Z_{el}}{2}\xi_{\Psi2}} \right)$$

$$(3.49)$$

where S_j is the solid specific surface, M_j the concentration of the solid, F is the Faraday constant ($F = 96487$ C/mol) , R is the ideal gas constant, T is the temperature, Cap is the capacitance, ε is the dielectric constant of water, ε_0 is the vacuum permittivity, I is the ionic strength, Z_{el} is he charge of the surface and $\xi_{\psi p}$ are additional components $X_{\psi p}$ ($p=1 \dots N_\Psi$) in their logarithmic form.

3.2.2 Modeling ion exchange

Ion exchange takes place whenever an ion is released into the solution and another ion, that was solute, takes its place. Ion exchange may be *homovalent* (when the number of ions fixed is the same of the number of ion released) or *heterovalent* (when a different number of ions is fixed and released). Examples of homovalent and heterovalent ion exchange reactions are:

$$Mg^{2+} + \equiv SCa \leftrightarrow Ca^{2+} + \equiv SMg$$
$$2Na^+ + \equiv S_2Ca \leftrightarrow Ca^{2+} + 2 \equiv SNa$$

$$(3.50)$$
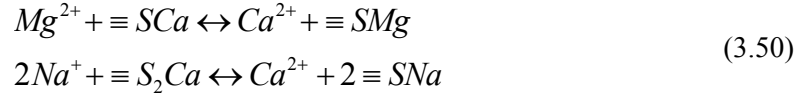
For both previous cases it is possible to write mass action laws:

$$K = \frac{\{Ca^{2+}\}\{\equiv SMg\}}{\{Mg^{2+}\}\{\equiv SCa\}} \quad K = \frac{\{Ca^{2+}\}\{\equiv SNa\}^2}{\{Na^+\}^2\{\equiv SCa\}}$$

$$(3.51)$$

It would be possible to pick three of the species as components and treat the fourth as a secondary species, but another strategy is to pick as components the two ions and a fictive component called surface $\equiv S$, treating the two remaining surface terms as secondary species. The two morel tables would become:

	Ca^{2+}	Mg^{2+}	$\equiv S$	K
Ca^{2+}	1	0	0	1
Mg^{2+}	0	1	0	1
$\equiv SCa$	1	0	1	K_{Ca}
$\equiv SMg$	0	1	1	K_{Mg}
	$[T_{Ca}]$	$[T_{Mg}]$	$[CEC]$	

Table 3.5 – Morel table for a simple example of homovalent ionic exchange.

	Ca^{2+}	Na^+	$\equiv S$	K
Ca^{2+}	1	0	0	1
Na^+	0	1	0	1
$\equiv S_2Ca$	1	0	2	K_{Ca}
$\equiv SNa$	0	1	1	K_{Na}
	$[T_{Ca}]$	$[T_{Mg}]$	$[CEC]$	

Table 6 - Morel table for a simple example of heterovalen ionic exchange.

where $K_{Ca}/K_{Mg} = K$ and $K_{Ca}/K_{Na} = K$. Total concentrations are computed as usual and [CEC] is the Cation Exchange Capacity (a given value), therefore there are no explicit modifications to make to the residual functions and to the Jacobian matrix and Newton Raphson method is carried out as usual.

Chapter 4 – Mixed equilibrium and kinetics

4.1 Theoretical background and generic formulation

4.1.1 Generic formulation I

Whenever time is a variable of interest in a chemical reaction, thermodynamic equilibrium becomes an inadequate simplification. All phenomena happen during a certain amount of time, this amount being potentially very small (reactions with a fast rate) or very big (reactions with a slow rate). According to this general approach, in a generic chemical system where *Nr* reactions take place, the variations of concentration [-] of a generic species C_i can be written as follows (Chilakapati 1995; Fang et al.2003):

$$\frac{d[C_i]}{dt} = r_i\big|_{Nr} \quad i = 1, N_t \tag{4.1}$$

where $r_i\big|_{Nr}$ is the production/consumption rate of species C_i due to all *Nr* reactions and *Nt* is the total number of species that take part in the system. Previous equation can be also written in its matrix form (Chilakapati et al. 1998; Steefel and MacQuarrie 1996):

$$\mathbf{I}\frac{d\mathbf{C}}{dt} = \mathbf{vr} \tag{4.2}$$

where **I** is the identity matrix of dimension *Nt x Nt*, **C** is the vector containing all *Nt* concentrations of chemical species, **v** is a *Nt x Nr* matrix defining which reactions intervene in the variation of a species *i* and **r** is the vector containing the rates of all *Nr* reactions. Equations (4.1) and (4.2) describe a system of Ordinary Differential Equations (ODEs). The previous system could be solved through a variety of ODE solvers but the solution in this form arises several numerical difficulties (Fang et al. 2003): throughout years of research on reactive transport modeling, authors (Chilakapati 1995; Steefel and MacQuarrie 1996; Fang et al. 2003; Molins et al. 2004) came up with suitable modifications. A synthetic but effective explanation of how the system of ODEs arises and can be rewritten is provided by Steefel and MacQuarrie (1996); the authors illustrate through an example the procedure adopted to identify *components* and *secondary species*. They provide the following chemical system:

$$
\begin{aligned}
CaCO_3 &\Leftrightarrow Ca^{2+} + CO_3^{-2} \quad R1 \quad (r_1) \\
HCO_3^- &\Leftrightarrow CO_3^{-2} + H^+ \quad R2 \quad (r_2) \\
H_2CO_3 &\Leftrightarrow CO_3^{-2} + 2H^+ \quad R3 \quad (r_3) \\
H^+ + OH^- &\Leftrightarrow H_2O \quad R4 \quad (r_4)
\end{aligned}
\tag{4.3}
$$
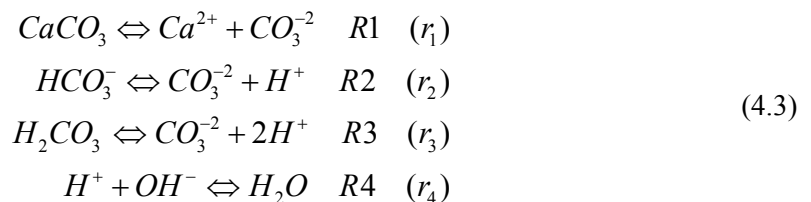
To this point, no assumption is made upon the nature of the *Nr=4* reactions (they may be reversible or irreversible) that connect the *Nt=7* species in reaction network (4.3). The concentration of each species is supposed to vary according to the rates (r_j) of the reactions it is involved in. For instance, moles of H^+ are produced when reactions R2 and R3 take place while they are consumed with reaction R4. This straightforward observation brings us to a system in the form of equation (4.1):

$$\frac{d\left[H_2CO_3\right]}{dt} = -r_3$$

$$\frac{d\left[HCO_3^-\right]}{dt} = -r_2$$

$$\frac{d\left[CaCO_3\right]}{dt} = -r_1$$

$$\frac{d\left[OH^-\right]}{dt} = -r_4 \tag{4.4}$$

$$\frac{d\left[H^+\right]}{dt} = r_2 + 2r_3 - r_4$$

$$\frac{d\left[Ca^{2+}\right]}{dt} = r_1$$

$$\frac{d\left[CO_3^{2-}\right]}{dt} = -r_1$$

System (4.4) can be rewritten in its matrix form. Diagonal identity matrix (**I** in equation (4.2)) and vector d**C**/dt appear in the left-hand side; matrix **v** and vector **r** of equation (4.2) appear in the right-hand side:

$$
\begin{bmatrix}
1 & 0 & 0 & 0 & 0 & 0 & 0 \\
0 & 1 & 0 & 0 & 0 & 0 & 0 \\
0 & 0 & 1 & 0 & 0 & 0 & 0 \\
0 & 0 & 0 & 1 & 0 & 0 & 0 \\
0 & 0 & 0 & 0 & 1 & 0 & 0 \\
0 & 0 & 0 & 0 & 0 & 1 & 0 \\
0 & 0 & 0 & 0 & 0 & 0 & 1
\end{bmatrix}
\begin{bmatrix}
\dfrac{d\left[H_2CO_3\right]}{dt} \\[2mm]
\dfrac{d\left[HCO_3^-\right]}{dt} \\[2mm]
\dfrac{d\left[CaCO_3\right]}{dt} \\[2mm]
\dfrac{d\left[OH^-\right]}{dt} \\[2mm]
\dfrac{d\left[H^+\right]}{dt} \\[2mm]
\dfrac{d\left[Ca^{2+}\right]}{dt} \\[2mm]
\dfrac{d\left[CO_3^{2-}\right]}{dt}
\end{bmatrix}
=
\begin{bmatrix}
0 & 0 & -1 & 0 \\
0 & -1 & 0 & 0 \\
-1 & 0 & 0 & 0 \\
0 & 0 & 0 & -1 \\
0 & 1 & 2 & -1 \\
1 & 0 & 0 & 0 \\
1 & 1 & 1 & 0
\end{bmatrix}
\begin{bmatrix}
r_1 \\
r_2 \\
r_3 \\
r_4
\end{bmatrix}
\tag{4.5}
$$

First four species are all associated to four different reactions, while the last three species are involved in several. The last three species are then well suited to be the *primary species*, or *components*, while the remaining will be considered, at a first attempt, as *secondary species*. The matrix form is also well suited for working on the transformation of the system. Through Gauss-Jordan elimination on matrix **v**, the system can be rewritten through new matrixes:

$$\mathbf{M}\frac{d\mathbf{C}}{dt} = \mathbf{v} * \mathbf{r} \tag{4.6}$$

$$
\begin{bmatrix}
1 & 0 & 0 & 0 & 0 & 0 & 0 \\
0 & 1 & 0 & 0 & 0 & 0 & 0 \\
0 & 0 & 1 & 0 & 0 & 0 & 0 \\
0 & 0 & 0 & 1 & 0 & 0 & 0 \\
2 & 1 & 0 & -1 & 1 & 0 & 0 \\
0 & 0 & 1 & 0 & 0 & 1 & 0 \\
1 & 1 & 1 & 0 & 0 & 0 & 1
\end{bmatrix}
\begin{bmatrix}
\dfrac{d[H_2CO_3]}{dt} \\[2mm]
\dfrac{d[HCO_3^-]}{dt} \\[2mm]
\dfrac{d[CaCO_3]}{dt} \\[2mm]
\dfrac{d[OH^-]}{dt} \\[2mm]
\dfrac{d[H^+]}{dt} \\[2mm]
\dfrac{d[Ca^{2+}]}{dt} \\[2mm]
\dfrac{d[CO_3^{2-}]}{dt}
\end{bmatrix}
=
\begin{bmatrix}
0 & 0 & -1 & 0 \\
0 & -1 & 0 & 0 \\
-1 & 0 & 0 & 0 \\
0 & 0 & 0 & -1 \\
0 & 0 & 0 & 0 \\
0 & 0 & 0 & 0 \\
0 & 0 & 0 & 0
\end{bmatrix}
\begin{bmatrix}
r_1 \\
r_2 \\
r_3 \\
r_4
\end{bmatrix}
\tag{4.7}
$$

Re-writing explicitly the system object of Gauss Jordan, it becomes clear that such system is a juxtaposition of two groups of ODEs.

$$\frac{d[H_2CO_3]}{dt} = -r_3$$

$$\frac{d[HCO_3^-]}{dt} = -r_2$$

$$\frac{d[CaCO_3]}{dt} = -r_1$$

$$\frac{d[OH^-]}{dt} = -r_4 \tag{4.8}$$

$$\frac{d}{dt}\left([H^+] + 2[H_2CO_3] + [HCO_3^-] - [OH^-]\right) = 0$$

$$\frac{d}{dt}\left([Ca^{2+}] + [CaCO_3]\right) = 0$$

$$\frac{d}{dt}\left([CO_3^{2-}] + [H_2CO_3] + [HCO_3^-] + [CaCO_3]\right) = 0$$

The first four ODEs represent the kinetic evolution of secondary species, while the last three differential equations are conservation equations of what proved to be primary species H^+, Ca^{++} and CO_3^{--}. An inconvenient of ODEs systems is that, whenever significant differences arise among reaction rates, the system becomes *stiff*, a condition that could expose to numerical problems. In fact, in stiff problems, the limitation imposed on the stepsize to obtain stability is stricter than the one imposed by accuracy (Press et al. 1997). Stiff systems of ODEs are cumbersome to solve, at the point that some systems of Differential Algebraic Equations (DAEs), may represent a suitable alternative (Chilakapati et al. 1998). In order to transform the system of ODEs in a system of DAEs, it is sufficient to rely on something that we know well: the thermodynamic equilibrium formulation. The fastest reactions (the question of what makes a reaction fast enough is not trivial but is not be addressed here) are replaced with the corresponding Mass Action Laws (algebraic equations) and the system becomes DAE. In the case of the previous chemical system, reactions R2 and R4 could evolve so fast with respect to other reactions that they could be considered at equilibrium. The differential equation describing their evolution could be substituted by the algebraic equation of mass action law (in **blue** in system (4.9)), where {-} is the symbol of activity:

$$\frac{d\left[H_2CO_3\right]}{dt} = -r_3$$

$$\left\{HCO_3^-\right\} = \frac{\left\{H^+\right\}\left\{CO_3^{2-}\right\}}{K_{HCO_3^-}}$$

$$\frac{d\left[CaCO_3\right]}{dt} = -r_1$$

$$\left\{OH^-\right\} = \frac{1}{\left\{H^+\right\}K_w} \tag{4.9}$$

$$\frac{d}{dt}\left(\left[H^+\right] + 2\left[H_2CO_3\right] + \left[HCO_3^-\right] - \left[OH^-\right]\right) = 0$$

$$\frac{d}{dt}\left(\left[Ca^{2+}\right] + \left[CaCO_3\right]\right) = 0$$

$$\frac{d}{dt}\left(\left[CO_3^{2-}\right] + \left[H_2CO_3\right] + \left[HCO_3^-\right] + \left[CaCO_3\right]\right) = 0$$

Re-ordering equations in system (4.9) with conservation equations at the top, followed by mass action laws and kinetic species evolving according to their kinetic rate and putting it in a more general form provides a system applicable to every problem written through a stoichiometric approach:

$$\begin{cases} \dfrac{dT_{X_j}}{dt} = \displaystyle\sum_{i=1}^{Nc} b_{i,j} \dfrac{d[C_i]}{dt} = \sum_{m=1}^{Nrc} Beq_{j,m} r_m \qquad j = 1, Nx \\[3mm] \{C_i\} = \displaystyle\prod_{j=1}^{Nx} \dfrac{\{X_j\}^{a_{i,j}}}{K_i} \qquad i = Nc - Nx, Nc \\[3mm] \dfrac{d[Cc_l]}{dt} = r_l \qquad l = 1, NCc \end{cases} \qquad (4.10)$$

where T_{Xj} is the total of primary species (components: H^+, Ca^{2+}, CO_3^{2-}) X_j available for speciation, C_i is a generic species (primary or secondary) and b_{ij} is the stoichiometric coefficient (for mass conservation) linking component X_j and species C_i ; r_m is the reaction rate of a generic kinetic reaction m and $Beq_{j,m}$ is the coefficient reflecting the influence of kinetic reaction m on component X_j ; the second line of the system contains classic mass action laws (K_i is the equilibrium constant for the formation of species C_i and $a_{i,j}$ is the stoichiometric coefficient for mass action law); Cc_l is a generic kinetic species and r_l is its evolution rate. Nc is the number of species involved in the equilibrium reaction network, Nx is the number of primary species, Nrc is the number of kinetic reactions and NCc is the number of kinetic species (Nrc and NCc do not necessarily correspond). Considering that the conservation equations imply that the total concentration of primary species H^+, Ca^{2+} and CO_3^{--} is constant throughout the evolution of the (closed) system, the last three equation of system (4.9) could be rewritten as their algebraic equivalent:

$$\frac{d[H_2CO_3]}{dt} = -r_3$$

$$\{HCO_3^-\} = \frac{\{H^+\}\{CO_3^{2-}\}}{K_{HCO_3^-}}$$

$$\frac{d[CaCO_3]}{dt} = -r_1$$

$$\{OH^-\} = \frac{1}{\{H^+\}K_w} \qquad (4.11)$$

$$[H^+] + 2[H_2CO_3] + [HCO_3^-] - [OH^-] = TOTH^+$$

$$[Ca^{2+}] + [CaCO_3] = TOTCa^{2+}$$

$$[CO_3^{2-}] + [H_2CO_3] + [HCO_3^-] + [CaCO_3] = TOTCO_3^{2-}$$

The number of unknowns in the previous system of DAEs can be further reduced exploiting mass action laws and activity coefficients that link concentrations [-] and activities {-} and system (4.11) can be rewritten as in (4.12).

$$\frac{d\left[H_2CO_3\right]}{dt} = -r_3$$

$$\frac{d\left[CaCO_3\right]}{dt} = -r_1$$

$$\left[H^+\right] + 2\left[H_2CO_3\right] + \frac{\{H^+\}\{CO_3^{2-}\}}{\gamma_{HCO_3^-} K_{HCO_3^-}} - \frac{1}{\{H^+\} K_w} = TOTH^+ \qquad (4.12)$$

$$\left[Ca^{2+}\right] + \left[CaCO_3\right] = TOTCa^{2+}$$

$$\left[CO_3^{2-}\right] + \left[H_2CO_3\right] + \frac{\{H^+\}\{CO_3^{2-}\}}{\gamma_{HCO_3^-} K_{HCO_3^-}} + \left[CaCO_3\right] = TOTCO_3^{2-}$$

The system counts now five equations for five unknowns. The impact of this simplification is rather modest here but may be very effective while considering a great number of species at thermodynamic equilibrium. Previous system written in a more general way takes the following form:

$$\begin{cases} T_{X_j} = \sum_{i=1}^{Nc} b_{i,j} \prod_{j=1}^{Nx} \frac{\{X_j\}^{a_{i,j}}}{\gamma_i K_i} = \sum_{m=1}^{Nrc} Beq_{j,m}\left[Cc_m\right] & j = 1, Nx \\ \dfrac{d\left[Cc_l\right]}{dt} = r_l & l = 1, NCc \end{cases} \qquad (4.13)$$

where T_{Xj} is the total of primary species (components: H^+, Ca^{2+}, CO_3^{2-}) X_j available for speciation, $b_{i,j}$ is the stoichiometric coefficient (for mass conservation) linking component X_j and species C_i, which is written as a function of primary species (K_i is the equilibrium constant for the formation of species C_i and $a_{i,j}$ is the stoichiometric coefficient for mass action law, γ_i is the activity coefficient.). Cc_m is a kinetic species and $Beq_{j,m}$ is the coefficient reflecting the influence of kinetic reaction m on component X_j; the second line of the system contains Cc_l a generic kinetic species and r_l is its evolution rate. Nc is the number of species involved in the reaction network, Nx is the number of primary species, Nrc is the number of kinetic reactions and NCc is the number of kinetic species (in this case Nrc and NCc are necessarily equal).

4.1.2 Generic formulation II

Another way of seeing the problem of introducing kinetic equations is the approach adopted by Leal (Leal at al. 2015) and somehow by Carrayrou (2001). It consists in looking at the problem under the assumption of *partial equilibrium* (Helgeson 1968; Helgeson et al. 1969; Helgeson et al. 1970). This means that a certain number of species are at thermodynamic equilibrium while some other species evolve kinetically. The system is then described through what Leal defines *partitioning*: equilibrium species are ideally put in the *equilibrium partition* while kinetic species are placed in the *kinetic partition* (see Figure 4.1). According to the principle of mass conservation, the total amount of moles contained in the system (i.e. the two partitions together) is constant. Nevertheless, mass exchanges between the two partitions are allowed. Time step after time step, mass is taken-from/put-into the equilibrium partition, where a state of equilibrium under new conditions is restored.
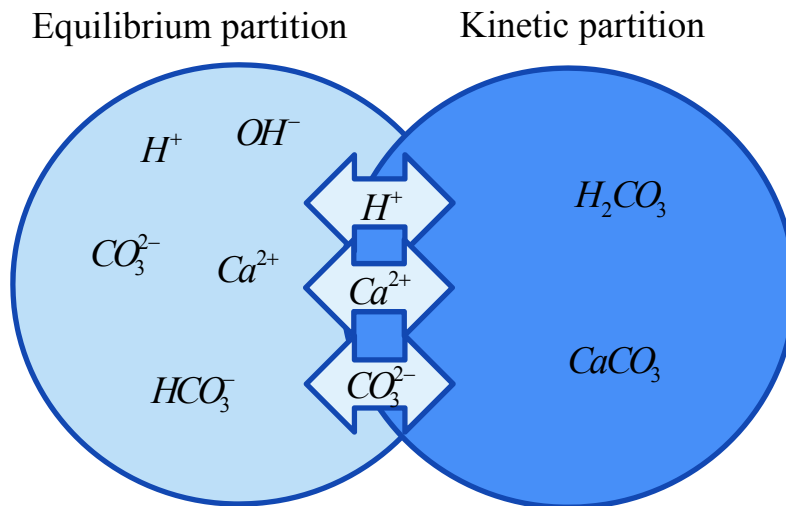
Figure 4.1 - Graphical representation of the concept of *partition* Leal et al. (2015) for the example provided by Steefel and MacQuarrie (1996)

Following this effective conceptualization of the problem, one question remains: how to model the effect of kinetic reactions on equilibrium species? Leal (2015) choses to represent the exchange of mass as an exchange of number of atoms of each element and then to compute equilibrium through the minimization of Gibbs Energy, therefore abandoning the stoichiometric approach (Leal et al. 2014). Exploiting the conceptual model while preserving the stoichiometric approach for the equilibrium speciation means that we have to describe the mass transfer between the two partitions in a way that is compatible with the nonlinear system introduced in the previous chapter:

$$\begin{cases} Y_j = \left[\tilde{T}_j\right] - \sum_{i=1}^{Nc} \frac{b_{i,j}}{\gamma_i} K_i \prod_{k=1}^{Nx} \left(\gamma_k\left[X_k\right]\right)^{b_{i,k}} - \sum_{l=1}^{Ncp} bp_{l,j}\left[Cp_l\right] \quad j=1,...,N_x \\ Y_{N_x+l} = 1 - \prod_j \frac{\left(\gamma_j\left[X_j\right]\right)^{bp_{l,j}}}{K_S^l} \quad l=1,...,N_{Cp} \end{cases}$$

(4.14)

where Y is the residual function, X_j is a generic component, K_i is a generic equilibrium constant for a secondary species I, $b_{i,j}$ is a generic coefficient of the stoichiometric matrix linking secondary species i and primary species j, and $bp_{l,j}$ is a generic stoichiometric coefficient linking a precipitate l to component j, γ are activity coefficients and K_s the solubility product.
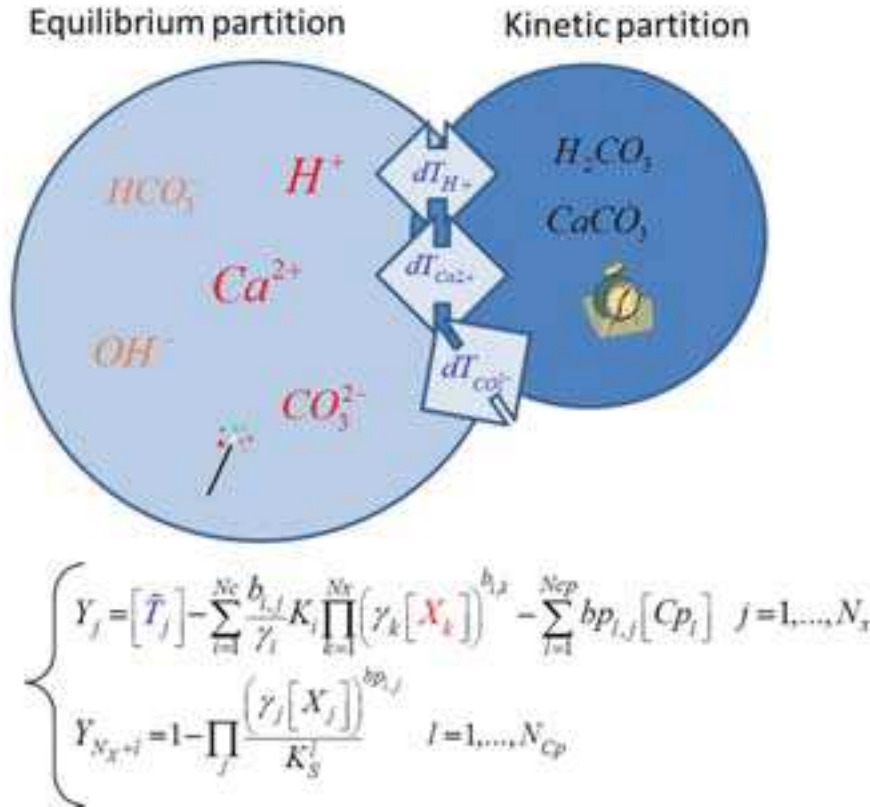
Figure 4.2 – Adaptation of the concept of partitioning to the stoichiometric approach for the example provided by Steefel and MacQuarrie (1996). The equation included in the Figure is a copy of (4.14), with totals available for speciation in blue, primary species in red (as they are represented in the picture. Secondary species are reported in orange in the equilibrium partition.

Considering that the total concentration $[\tilde{T}_j]$ of a generic component X_j is in fact the available mass to be shared between species, an interaction with a kinetic partition would affect this quantity, taking-

from/putting-into the equilibrium partition a certain $\Delta[\tilde{T}_j]$. The continuous interaction between the two *partitions* could be synthetized as follows:

$$\left.\frac{d\tilde{T}_j}{dt}\right|_{Eq} = \left.\frac{d\tilde{T}_j}{dt}\right|_{Kin} \tag{4.15}$$

The total concentration of a primary species *j* available for speciation varies accordingly to changes generated from kinetic chemical reactions, i.e. according to kinetic rates; previous equation becomes:

$$\left.\frac{d\tilde{T}_j}{dt}\right|_{Eq} = \sum_{i=1}^{Nrc} Beq_{j,i} r_i \tag{4.16}$$

where $Beq_{j,i}$ is the entry of the matrix linking *Nrc* kinetic reactions and *Nx* primary species. Looking at the example presented by Steefel and MacQuarrie (1996) in paragraph § 4.1 and at system (4.14), mass conservation for the sole equilibrium partition becomes:

$$T_{H^+} = \left[H^+\right] + \frac{\{H^+\}\{CO_3^{2-}\}}{\gamma_{HCO_3^-} K_{HCO_3^-}} - \frac{1}{\{H^+\} K_w}$$

$$T_{Ca^{2+}} = \left[Ca^{2+}\right] \tag{4.17}$$

$$T_{CO_3^{2-}} = \left[CO_3^{2-}\right] + \frac{\{H^+\}\{CO_3^{2-}\}}{\gamma_{HCO_3^-} K_{HCO_3^-}}$$

At the same time, in the kinetic partition (Figure 4.1), there are two kinetic species evolving according to their reaction rates:

$$\frac{d\left[H_2CO_3\right]}{dt} = -r_3$$

$$\frac{d\left[CaCO_3\right]}{dt} = -r_1 \tag{4.18}$$

The description of how reactions R1 and R3 impact on the equilibrium components H^+, Ca^{++} and CO_3^{--} must follow. Looking at reactions in system (4.3), we can see that the kinetic consumption of species $CaCO_3$ produces components Ca^{++} and CO_3^{--}, while the kinetic consumption of one mole of H_2CO_3 produces one mole of CO_3^- and two moles of H^+; this means that whenever reactions R1 and R3 take place in the sense of their writing, the total available concentration for equilibrium speciation of primary species increases. Therefore, equation (4.16) for primary species becomes:

66

$$\frac{dT_{H^+}}{dt} = \frac{d}{dt}\left(\left[H^+ \right] + \frac{\{H^+\}\{CO_3^{2-}\}}{\gamma_{HCO_3^-} K_{HCO_3^-}} - \frac{1}{\{H^+\} K_w} \right) = 2r_3$$

$$\frac{dT_{Ca^{2+}}}{dt} = \frac{d}{dt}\left[Ca^{2+} \right] = r_1 \qquad (4.19)$$

$$\frac{dT_{CO_3^{2-}}}{dt} = \frac{d}{dt}\left(\left[CO_3^{2-} \right] + \frac{\{H^+\}\{CO_3^{2-}\}}{\gamma_{HCO_3^-} K_{HCO_3^-}} \right) = r_1 + r_3$$

That, rewritten in terms of kinetic species according to equation (4.18), becomes:

$$\frac{d}{dt}\left(\left[H^+ \right] + \left[HCO_3^- \right] - \left[OH^- \right] \right) = -2\frac{d\left[H_2CO_3 \right]}{dt}$$

$$\frac{dT_{Ca^{2+}}}{dt} = \frac{d}{dt}\left[Ca^{2+} \right] = -\frac{d\left[CaCO_3 \right]}{dt} \qquad (4.20)$$

$$\frac{dT_{CO_3^{2-}}}{dt} = \frac{d}{dt}\left(\left[CO_3^{2-} \right] + \left[HCO_3^- \right] \right) = -\frac{d\left[CaCO_3 \right]}{dt} - \frac{d\left[H_2CO_3 \right]}{dt}$$

Or, together with mass action laws and ODEs of kinetic species, the system exactly like (4.9):

$$\frac{d\left[H_2CO_3 \right]}{dt} = -r_3$$

$$\{HCO_3^-\} = \frac{\{H^+\}\{CO_3^{2-}\}}{K_{HCO_3^-}}$$

$$\frac{d\left[CaCO_3 \right]}{dt} = -r_1$$

$$\{OH^-\} = \frac{1}{\{H^+\} K_w} \qquad (4.21)$$

$$\frac{d}{dt}\left(\left[H^+ \right] + 2\left[H_2CO_3 \right] + \left[HCO_3^- \right] - \left[OH^- \right] \right) = 0$$

$$\frac{d}{dt}\left(\left[Ca^{2+} \right] + \left[CaCO_3 \right] \right) = 0$$

$$\frac{d}{dt}\left(\left[CO_3^{2-} \right] + \left[H_2CO_3 \right] + \left[HCO_3^- \right] + \left[CaCO_3 \right] \right) = 0$$

4.1.3 Systems of equations

To summarize, starting from a general formulation of the problem in its matrix form, or starting from a description of the physical process, the resulting system of equations is the same, although it can be written in at least three ways (please, note that from now on square brackets [-] for concentrations will be omitted to speed up the notation, while {-} still defines activities):

I. As a system of DAEs such as systems (4.9) and (4.21), composed of *Nt* equations: *Nx* (primary species) plus *NCc* (kinetic species) ODEs and *Nc-Nx* (*Nc* being the number of equilibrium species) algebraic equations, the mass action laws:

$$
\begin{cases}
\dfrac{dT_{X_j}}{dt} = \displaystyle\sum_{i=1}^{Nc} b_{i,j} \dfrac{dC_i}{dt} = \sum_{m=1}^{Nrc} Beq_{j,m} r_m & j = 1, Nx \\[4mm]
\{C_i\} = \displaystyle\prod_{j=1}^{Nx} \dfrac{\{X_j\}^{a_{i,j}}}{K_i} & i = Nc - Nx, Nc \\[4mm]
\dfrac{dCc_l}{dt} = r_l & l = 1, NCc
\end{cases}
\tag{4.22}
$$

II. As a system of *Nt-(Nc-Nx)* DAEs such as system (10), composed of *Nx* algebraic equations describing mass conservation, and *NCc* ODEs for the evolution of kinetic species:

$$
\begin{cases}
T_{X_j} = \displaystyle\sum_{i=1}^{Nc} b_{i,j} \prod_{j=1}^{Nx} \dfrac{\{X_j\}^{a_{i,j}}}{\gamma_i K_i} = \sum_{m=1}^{Nrc} Beq_{j,m} Cc_m & j = 1, Nx \\[4mm]
\dfrac{dCc_l}{dt} = r_l & l = 1, NCc
\end{cases}
\tag{4.23}
$$

III. As a system of *Nt-(Nc-Nx)* ODEs writing mass action laws into mas conservation equations in system (8)

$$
\begin{cases}
\dfrac{dT_{X_j}}{dt} = \displaystyle\sum_{i=1}^{Nc} b_{i,j} \dfrac{d}{dt} \prod_{j=1}^{Nx} \dfrac{\{X_j\}^{a_{i,j}}}{\gamma_i K_i} = \sum_{m=1}^{Nrc} Beq_{j,m} r_m & j = 1, Nx \\[4mm]
\dfrac{dCc_l}{dt} = r_l & l = 1, NCc
\end{cases}
\tag{4.24}
$$

Which is the most efficient way of writing the system? Authors agree that solutions of systems such as (4.23) and (4.24) should be preferred whenever a large number of equilibrium reactions take place, which is the case of natural problems, and whenever a large number of solutions of the chemical problem are required from spatial discretization, which is the case of reactive transport modeling. Nevertheless, although system (4.22) is indubitably larger than the other two, it contains equations that are less complicated. In fact, system (4.24) requires the derivative of the mass action law with respect to time and consequently the derivative of the activity coefficient, which can be either derived (additional computations) either neglected (inevitable approximations).

On the other hand, system (4.23) may result impractical whenever kinetic reactions between primary species exist, since it requires a kinetic species for every kinetic reaction to account for mass conservation. Moreover, in system (4.23), adding concentrations (that may be very low) to kinetic species, that can be very important (such as minerals constituting a porous medium), may result in loss of accuracy throughout computations.

Computational cost also depends on the solution technique adopted. A bigger system could be solved faster than a small one if the first solution is carried out with a more efficient solver.

Testing all three ways of writing the system will provide a broader understanding of the problem and will be useful to assess to which point the solution technique is important.

4.2 Solving the systems of equations

Once the mathematical description of the problem is defined, and at least three of them were identified, it is necessary to provide a tool for its solution. The presence of differential equations implies the choice of a method of integration in time. Methods of numerical integration of ODEs can be *explicit* or *implicit*, *one-step* or *multistep*, they may have a *constant* or an *adaptive* time step. Explicit methods compute a general state variable $\Phi(t+\Delta t)$ as a function of $\Phi(t)$ only, on the other hand, implicit methods require the solution of a system of equations $G(\Phi(t), \Phi(t+\Delta t)) = 0$. One-step methods compute the solution at the instant $t+\Delta t$ using as the previous solution in time only the one in t while multistep methods compute the solution in $t+\Delta t$ as a function not only of t but also $t - \Delta t^1$, $t - \Delta t^1 - \Delta t^2$, $t - \Delta t^1 - ... - \Delta t^n$. Regarding the *adaptive* or *constant* nature of the time step, in the first case the increment Δt is fixed, in the second case, it varies according to the error accepted on the problem to be solved. It is important to underline that almost every combination of the previous features are allowed: a method can be explicit with an adaptive time step or implicit with a constant time step and so on.

§

The previous version of SPECY (Carrayrou 2001) used an *explicit* method to solve problems that involved both thermodynamic and kinetic reactions, precisely a Richardson extrapolated form of QSSA (Quasi Steady State Approximation (Sandu et al. 1997)) method with *variable time-step* size control. The choice of this method was justified as a compromise between a good performance and a reasonable computational effort. Nevertheless, as Sandu et al. (1997) remind, explicit methods such as extrapolated QSSA are not standard and their implementation requires the development of dedicated subroutines or sections of the code. On the opposite side, there are several ODEs solvers and some DAEs solvers that were developed professionally and applied to more diverse fields of science and engineering and whose reliability has been proven. It is difficult to generalize whether implicit methods are *better* than explicit methods, given the extremely problem dependent nature of the performances. It seemed therefore reasonable to implement, as an alternative to the extrapolated QSSA explicit method, an implicit solver for ODEs/DAEs systems.

4.2.1.1 Implicit and explicit methods

As anticipated, one of the possible ways of gathering numerical methods for integration in time is between explicit and implicit. Consider a variable evolving in time, for example concentration C, between two instants t^n and t^{n+1}; explicit methods allow writing the concentration at time t^{n+1} as a function of the concentration at time t^n:

$$C^{n+1} = f(C^n) \qquad (4.25)$$

The simplest explicit method is the standard (also called *forward*) Euler method which dates back to 1768. It's based on the first order Taylor approximation:

$$C(t^{n+1}) = C(t^n) + hC'(t^n) + \frac{h}{2!}C''(t^n) + ... \qquad (4.26)$$

where h is the time-step between the two subsequent instants t^n and t^{n+1}, $C'(t^n)$ is the first derivative of the concentration with respect to time and computed at instant t^n. To clear and speed up the writing, we define $C(t^n) = C^n$ and $F(t^n, C^n) = C'(t^n)$; equation (4.26) becomes:

$$C^{n+1} = C^n + hF(t^n, C^n) \qquad (4.27)$$

Previous equation can be rearranged in the following form, providing a more intuitive insight on a finite differences explicit method applied to evolving concentrations, where r is again the reaction rate:

$$\frac{C^{n+1} - C^n}{t^{n+1} - t^n} = r(C^n) \qquad (4.28)$$

Another series of explicit methods is the family of Runge Kutta (RK) methods (Press et al. 1997), that computes the solution at t^{n+1} as a weighted average of several approximations over the increment h. According to the number n of approximations taken into the average, the method is called n^{th} *order RK*. Second order RK method is based on a second order Taylor approximation and the solution then becomes:

$$C^{n+1} = C^n + hF\left(t^n + \frac{h}{2}, C^n + \frac{h}{2}F(t^n, C^n)\right) \qquad (4.29)$$

Although Runge Kutta method provides a solution computed on the basis of several values of the variable, they are included between instant t^n and t^{n+1}. As it will be detailed in next paragraphs, to be classified as multistep, RK method should compute the variable at t^{n+1} on the basis of the variable at previous time steps t^{n-1}, t^{n-2}... therefore RK method is not multistep (Press et al. 1997).

Implicit methods are less straightforward since the state variable at the time step t^{n+1} is present both in the left and right hand member. This is the case of the backward Euler method, i.e. the implicit variant of standard Euler method:

$$C^{n+1} = C^n + hF(t^{n+1}, C^{n+1})$$ (4.30)

As for the forward Euler method, previous equations can be rewritten in a more intuitive formulation:

$$\frac{C^{n+1} - C^n}{t^{n+1} - t^n} = r(C^{n+1})$$ (4.31)

A compromise between forward and backward Euler methods is presented in equation (4.32), where ε varies between 0 (forward explicit) and 1 (backward implicit). Whenever $\varepsilon=0.5$ we have *centered-time* or *Crank-Nicolson* temporal weighting.

$$\frac{C^{n+1} - C^n}{t^{n+1} - t^n} = \varepsilon\, r(C^{n+1}) + (1 - \varepsilon)\, r(C^n)$$ (4.32)

Although explicit methods are simpler and implicit methods may require a higher computational effort, explicit methods have some inconvenient. Whenever several kinetic reactions are present, the time-step's amplitude is dictated by the fastest reaction. This happens not only to guarantee accuracy but also because the stability of explicit methods is limited. As anticipated, *stiff* systems of ODEs may require additional limitation of the time-steps to avoid oscillations (Kee et al. 1985; Press et al. 1997).

4.2.1.2 One-step and multi-step methods

Equations (4.25) to (4.32) all describe one-step methods, in the sense that the value of the state variable $C(t^{n+1})$ is computed on the basis of the sole $C(t^n)$. This is true even for equation (4.29), where a sort of intermediate solution is computed *within* the time-step h. In multi-step methods, on the other hand, $C(t^{n+1})$ is computed on the basis of $C(t^n)$ but also of $C(t^{n-1})$, $C(t^{n-2})$, $C(t^{n-3})$, and so on until $C(t^{n+1-k})$. One of the most used multi-step numerical integration methods is the Backward Differentiation Formula, or BDF. BDF is an implicit method (Gear 1971) implemented in several numerical solvers for ODEs (LSODE (Hindmarsh 1983) VODE (Brown et al. 1989)) and DAEs (DASPK (Brenan et al. 1996)). BDF method is theoretically based on the search for a polynomial $q(t)$

interpolating previous computed values of C and whose first derivative in time $q'(t^{n+1})$ is equal to $F(t^{n+1}, C^{n+1})$, the first derivative of $C(t)$.
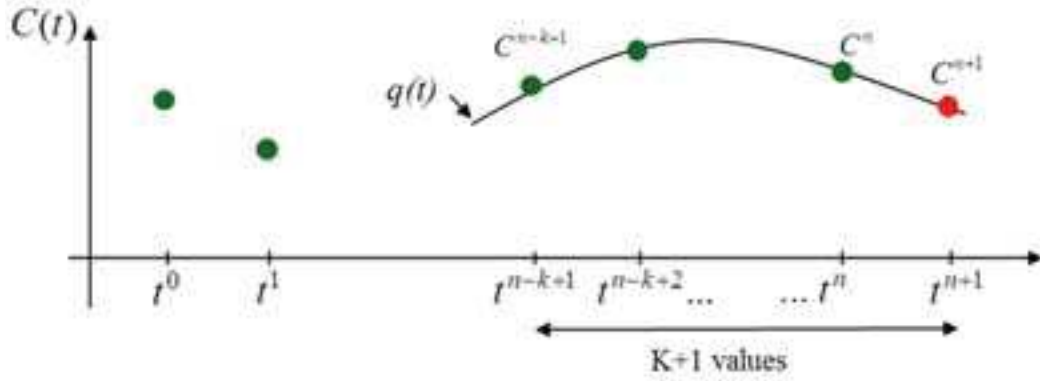
Figure 4.3 – Graphical explanation of Backward Differentiation Formula (BDF) method

Being BDF a multistep method, polynomial $q(t)$ is supposed to interpolate several solutions back in time. For a polynomial of k order, the interpolation will be pushed back in time until instant t^{n+1-k}. Once $q(t)$ and its first derivative $q'(t)$ are written as functions of C and h, if the time-stepping is constant, the following system has to be solved:

$$\sum_{j=1}^{k} \frac{1}{j} \nabla^j C_{n+1} = h F_{n+1} \tag{4.33}$$

For $k=1$ previous equation becomes:

$$C_{n+1} - C_n = h F_{n+1} \tag{4.34}$$

which corresponds to equations (4.30) and (4.31), therefore to backward Euler method. For k ranging from 2 to 6, equation (4.33) becomes instead:

$$k = 2 \quad \frac{3}{2}C_{n+1} - 2C_n + \frac{1}{2}C_{n-1} = hF_{n+1}$$

$$k = 3 \quad \frac{11}{6}C_{n+1} - 3C_n + \frac{3}{2}C_{n-1} - \frac{1}{3}C_{n-2} = hF_{n+1}$$

$$k = 4 \quad \frac{25}{12}C_{n+1} - 4C_n + 3C_{n-1} - \frac{4}{3}C_{n-2} + \frac{1}{4}C_{n-3} = hF_{n+1} \tag{4.35}$$

$$k = 5 \quad \frac{137}{60}C_{n+1} - 5C_n + 5C_{n-1} - \frac{10}{3}C_{n-2} + \frac{5}{4}C_{n-3} - \frac{1}{5}C_{n-4} = hF_{n+1}$$

$$k = 6 \quad \frac{147}{60}C_{n+1} - 6C_n + \frac{15}{2}C_{n-1} - \frac{20}{3}C_{n-2} + \frac{15}{4}C_{n-3} - \frac{6}{5}C_{n-4} + \frac{1}{6}C_{n-5} = hF_{n+1}$$

Previous equations derive from the assumption that the stepsize h is constant. If a variable stepsize is to be preferred, three strategies are possible for BDF: fixed coefficients, variable coefficients and fixed leading coefficients (Jackson and Sacks-Davis 1980). In the case of Fixed Leading Coefficients (FLCBDF) (Jackson and Sacks-Davis 1980), a first *predictor* polynomial of k order, ω_p, is computed as an interpolation of C values between C^n and C^{n-k} and the predicted value of C^{n+1} is computed as:

$$\omega_p(t^{n+1}) = C_p^{n+1} \tag{4.36}$$

A second step of *correction* is performed through the computation of another polynomial of k order, ω_c. It interpolates C^{n+1} and the prediction polynomial ω_p:

$$\omega_c\left(t^{n+1} - ih^{n+1}\right) = \omega_p\left(t^{n+1} - ih^{n+1}\right) \tag{4.37}$$

where $i = 1,...,k$. Considered that ω_p and ω_c are both k order polynomials, they can be written according to the following relation:

$$\omega_c(t) = \omega_p(t) + \alpha(t)\left[\omega_c(t^{n+1}) - \omega_p(t^{n+1})\right] \tag{4.38}$$

The combination of ω_c and ω_p with polynomial $\alpha(t)$ written as a function of different stepsizes allows the computation of C^{n+1} as:

$$C^{n+1} = C_p^{n+1} + h^{n+1}\beta\left(F_{n+1} - C_p'^{n+1}\right) \tag{4.39}$$

where $\beta = 1/(1 + 1/2 + 1/3 + ... + 1/k)$. For k=2, the previous equation takes the following form:

$$C^{n+1} = \left(1 + \frac{\rho^2}{3}\right)C^n - \frac{\rho^2}{3}C^{n-1} + \frac{2}{3}C^{n+1}h^{n+1}F_{n+1} - \left(\frac{\rho-1}{3}\right)h^{n+1}F_n \tag{4.40}$$

where $\rho = h^{n+1}/h^n$.

The multistep method presented here is implicit, but other explicit multistep methods exist, such as Adams method (Press et al. 1997).
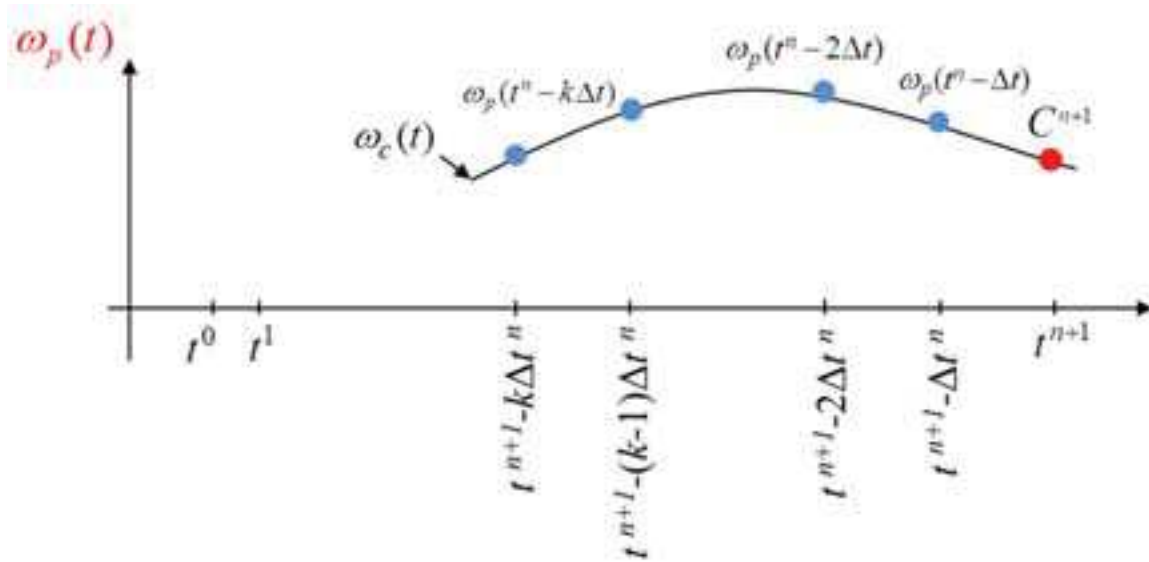
Figure 4.4 – Graphical explanation of Fixed Leading Coefficients Backward Differentiation Formula (FLCBDF), with predictor polynomial ω_p and corrector polynomial ω_c, first step.
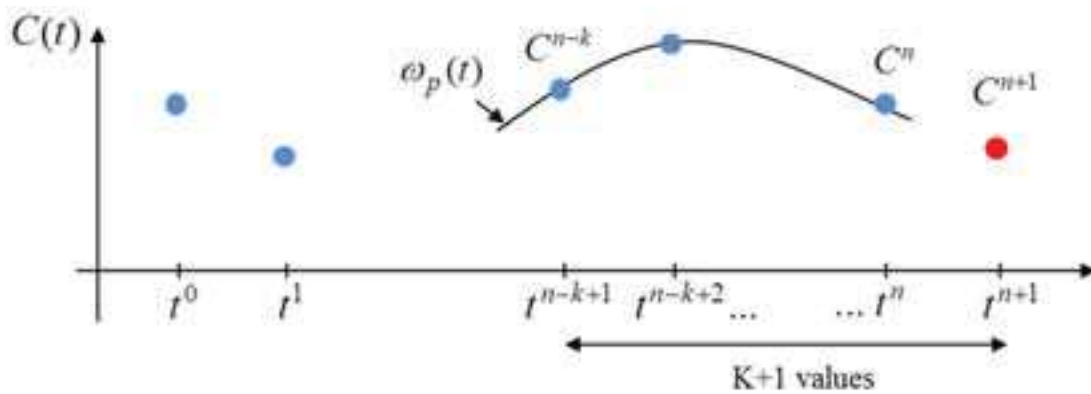
Figure 4.5 – Graphical explanation of Fixed Leading Coefficients Backward Differentiation Formula (FLCBDF), with predictor polynomial ω_p and corrector polynomial ω_c, second step.

4.2.1.3 Variable stepsize

Most of the numerical methods introduced above (with the exception of FLCBDF) use a fixed step size to move forward in the computation of the solution. Press et al. (1997) suggest that whenever heavy calculations have to be performed, an adaptive time step should be employed. Usually, whenever implementing a variable stepsize, together with the computation of the solution requires an evaluation of its accuracy. If the accuracy satisfies imposed criteria, the solution is accepted; otherwise it is computed again with a smaller stepsize.

4.2.2 An implemented explicit method: Richardson extrapolation of QSSA method

QSSA stands for Quasi Steady State Approximation and it is an explicit, one step, first order precision method with variable stepsize for ODEs solutions (Carrayrou 2001; Sandu et al. 1997). Its Richardson extrapolation (Sandu et al. 1997; Press et al. 1997) consists in applying the standard QSSA over three different segments of the time-step h and then computing an average of the three. The standard QSSA provides concentrations at time $t^{n+1} = t+h$:

$$\mathbf{C^{n+1}} = e^{-h\mathbf{L}^n}\mathbf{C^n} + (\mathbf{Id} - e^{-h\mathbf{L}^n})\mathbf{L}^{-1}\mathbf{P}^n \qquad (4.41)$$

where $\mathbf{L}$ and $\mathbf{P}$ are vectors symbolizing loss and production of a given C in a form suitable for atmospheric chemistry (Sandu et al. 1997). Richardson extrapolation computes equation (4.41) between $0 \rightarrow h$, $0 \rightarrow h/2$ and $h/2 \rightarrow h$ and provides an estimation of kinetic species Cc^{n+1} as:

$$Cc(h) = 2Cc(h/2 \rightarrow h) - Cc(0 \rightarrow h) \qquad (4.42)$$

QSSA method was adapted by Carrayrou (Carrayrou 2001) to the problem of mixed kinetic and equilibrium reactions, treating conserved totals of components (primary species) as kinetic species evolving in time. With this method, thermodynamic equilibrium is computed twice at each time step, and computations are carried out with the solver described in previous chapter.

4.2.3 An implemented implicit method: BDF in DASPK

DASPK is a solver for systems of DAEs, differential algebraic equations, that works with an implicit Fixed Leading Coefficients BDF. As explained in previous paragraphs, FLCBDF is based on the combination of a predictor polynomial ω_p and a corrector polynomial ω_c. The combination of the two polynomials provides a nonlinear system to be solved in order to obtain C^{n+1}. A detailed description of the functioning of DASPK and its predecessor DASSL can be found in the reference (Brenan et al. 1996) and we provide a very rough summary only. To speed up notation, we will say that, at each time step, the following nonlinear system must be solved:

$$G(t, C, \alpha C + \beta) = 0 \qquad (4.43)$$

where variables C are computed at t^{n+1}, α changes with the time-steps and order and β remains constant throughout the solution. The nonlinear system is solved through Newton method and the

solution of the linear systems therein may be carried out by a direct solver or by preconditioned Krylov iterative method (Generalized Minimum Residual (GMRES)).

Solving linear system through direct methods requires a Jacobian matrix (or iteration matrix) **J** that can be computed numerically or may be provided by the user:

$$\mathbf{C}_{m+1} = \mathbf{C}_m - c\mathbf{J}^{-1}\mathbf{G}(t, \mathbf{C}_m, \alpha\mathbf{C}_m + \beta) \tag{4.44}$$

$$\mathbf{J} = \alpha\frac{\partial\mathbf{G}}{\partial\mathbf{C}'} + \frac{\partial\mathbf{G}}{\partial\mathbf{C}} \tag{4.45}$$

Iteration matrix **J** should be, in theory, reevaluated at each step. However, changes in the entries may be so small to be considered negligible over several time steps. Since the process of computing **J** may be expensive in terms of computing costs, whenever possible the last computed iteration matrix is used instead. The iteration matrix is computed for the first iteration and used until one of these scenarios occurs: i) the time step changes significantly ii) the order change significantly iii) the solver failed to converge. For the direct solution of the linear system, matrix **J** can be computed *numerically* through perturbations by the solver or *analytically* through a subroutine provided by the user. What is non-optional is the subroutine computing the residuals **G**.

Values for absolute (ATOL) and relative (RTOL) error tolerances are required as input and they define the degree of accuracy of the solution. According to the technical notes of the solver, tolerances are used in a local error test conceptually ensuring that $|err(C_i)| \leq RTOL|C_i| + ATOL$. Actually, previous inequality is not directly applied but implemented in the solver through a root-mean-square norm used to measure the size of error vectors.

Although DASPK was conceived as a DAEs solver (Brenan et al.1996), it is also well suited for solving systems of ODEs. This characteristic makes DASPK the ideal tool to test different configurations of the equations such as equations (4.22) to (4.24).

4.2.4 Solving systems with DASPK

4.2.4.1 Residual computation for DASPK 1

Solver DASPK needs a subroutine to provide the computation of residuals of the DAEs system (4.22). The first Nx residuals refer to the variations in time of the Nx total concentrations available for equilibrium speciation:

$$\frac{dT_{X_j}}{dt} = \sum_{i=1}^{Nc} b_{i,j} \frac{dC_i}{dt} - \sum_{m=1}^{Nrc} Beq_{j,m} r_m = res \qquad j = 1, Nx \qquad (4.46)$$

Then Nc-Nx lines follow: they correspond to the mass action laws and/or solubility products that link primary to secondary species.

$$\{C_i\} - \prod_{j=1}^{Nx} \frac{\{X_j\}^{a_{i,j}}}{K_i} = res \qquad i = Nc - Nx, Nc \qquad (4.47)$$

The last NCc lines correspond to variation in time of the NCc kinetic species:

$$\frac{dCc_l}{dt} - r_l = res \qquad l = 1, NCc \qquad (4.48)$$

Equations (4.46) to (4.48) result in a system of $Nc+NCc$ equations into $Nc+NCc$ unknowns. Even though the system to be solved is bigger than in other configurations of the problem, operations to be solved are easier and fewer approximations are required.

The numerical evaluation of the Jacobian matrix is described in the reference material (Brenan et al. 1996) whereas the analytical computation requires the implementation of a subroutine to provide the so-called iteration matrix, which is the Jacobian matrix:

$$\mathbf{J} \;=\; \frac{\mathbf{dG}}{\mathbf{dC}} + CJ \frac{\mathbf{dG}}{\mathbf{dC'}} \qquad (4.49)$$

where $\mathbf{G}$ is the vector of residuals, $\mathbf{C}$ and $\mathbf{C'}$ are the vectors containing concentrations and their time derivatives, and CJ a coefficient that varies throughout computations. Visually, the Jacobian matrix related to our DAEs problem appears like:

78
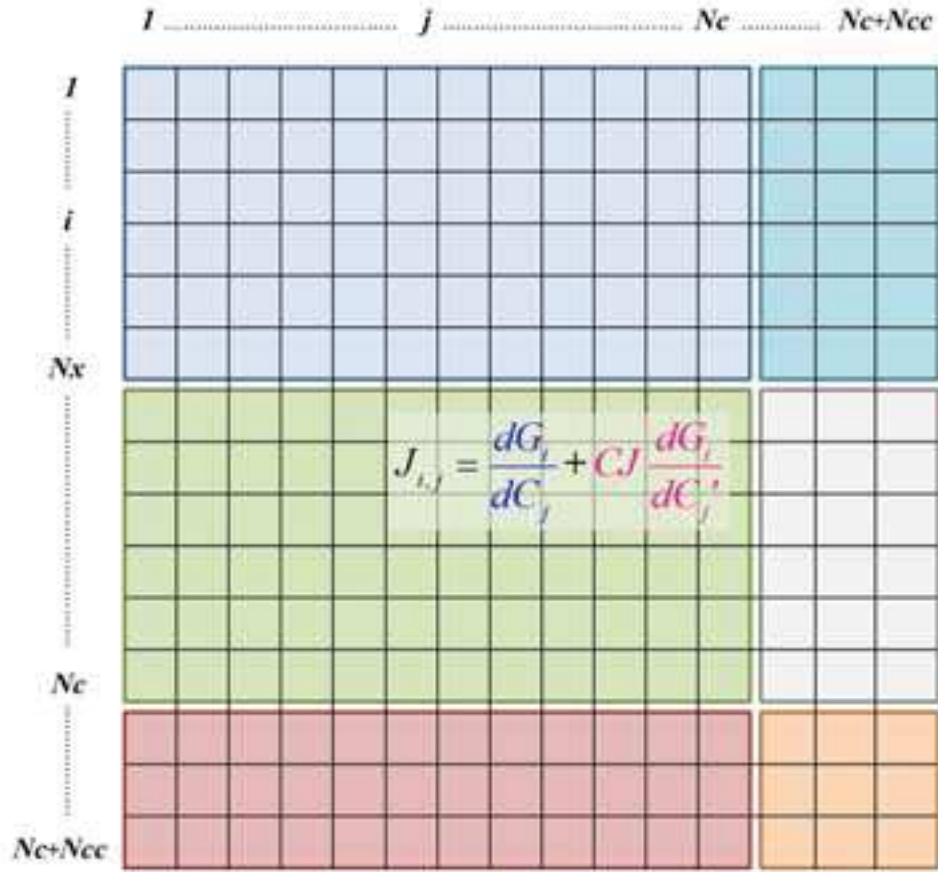
Figure 4.6 – Structure of the iteration (or Jacobian) matrix for DAEs system (4.22) or DASPK 1.

The structure follows that of the residuals vector **G**. The first Nx lines of the Jacobian matrix refer to the variations in time of the Nx total concentrations, followed by $Nc-Nx$ lines corresponding to the mass action laws and/or solubility products and by NCc lines correspond to variation in time of the kinetic species (Figure 4.6). Every generic element of the Jacobian matrix has to be built as a sum of two contributions:

$$J_{ij} = \frac{dG_i}{dC_j} + CJ \frac{dG_i}{dC'_j} \tag{4.50}$$

The structure of the vector of residuals **G** can be exploited to fill the entries of the Jacobian matrix in a smart way, block after block (see Figure 4.7 below). In fact, in our system of DAEs, both terms in equation (4.50) are not always simultaneously needed. Let's concentrate on the second term of the right-hand side of equation (4.50):

$$CJ \frac{dG_i}{dC'_j}$$

79

To have it different from zero, a time derivative of the state variable C'$_j$ has to be present. We know that mass action laws are written under the form of algebraic equations, so they do not involve time derivatives of any kind. Therefore the term is not present in the block going from lines $Nx + 1$ to Nc (BLOCK 2 in Figure 4.7). On the other hand, it is going to be computed in the block of first Nx equations (BLOCK 1 in Figure 4.7) and in the block in the right low corner (BLOCK 3). According to the first Nx residuals in vector **G** (see equation (4.46)) the Jacobian Matrix entries of BLOCK 1 have the following form, where $B_{i,j}$ is the matrix of stoichiometric coefficients:

$$CJ \frac{dG_i}{dC'_j} = CJ * b_{i,j} \qquad (4.51)$$
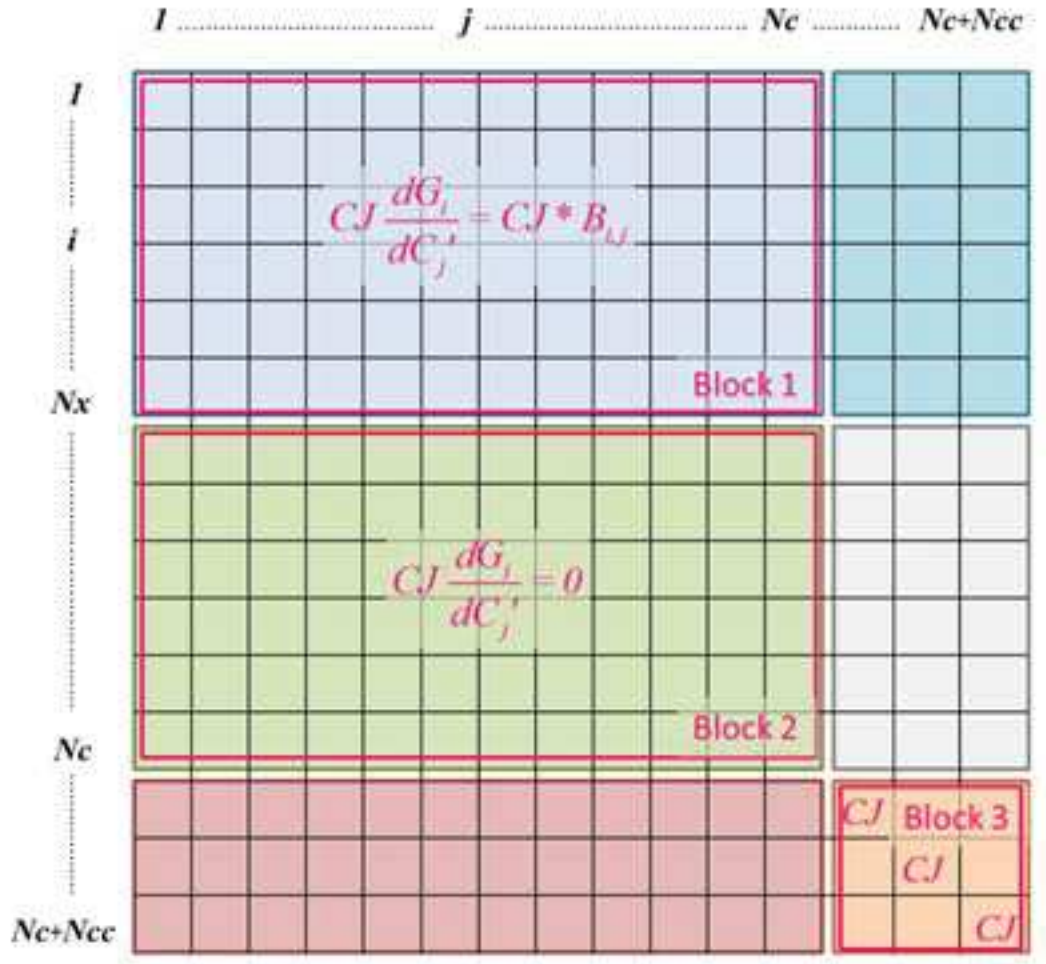
Figure 4.7 – The iteration matrix for DASPK 1 is filled block by block: BLOCK 1 is related to derivatives of mass conservation, BLOCK 2 to mass action lass and BLOCK 3 to kinetic species.

Let's now look at the other term required by DASPK: dG_i/dC_j. It will be computed only in the blocks that account for residuals where concentrations actually appear. Concentrations appear in the reaction rates (BLOCK 1 and BLOCK 6, Figures 4.7 and 4.9) and in mass action laws (BLOCK 2, Figure 4.8). We recall that mass action laws express secondary species as functions of primary species, therefore no interaction between secondary species exists: the *Nc-Nx* rows and columns of BLOCK 2 form a diagonal square matrix. On the contrary, *mass action laws are functions of components* and the entries of the first *Nx* columns (BLOCK 4) are filled with:

$$\frac{dG_i}{dU_j} = K_i \prod_{m=1}^{Nx} \frac{(\gamma_m C_m)^{a_{i,m}}}{C_j} \tag{4.52}$$
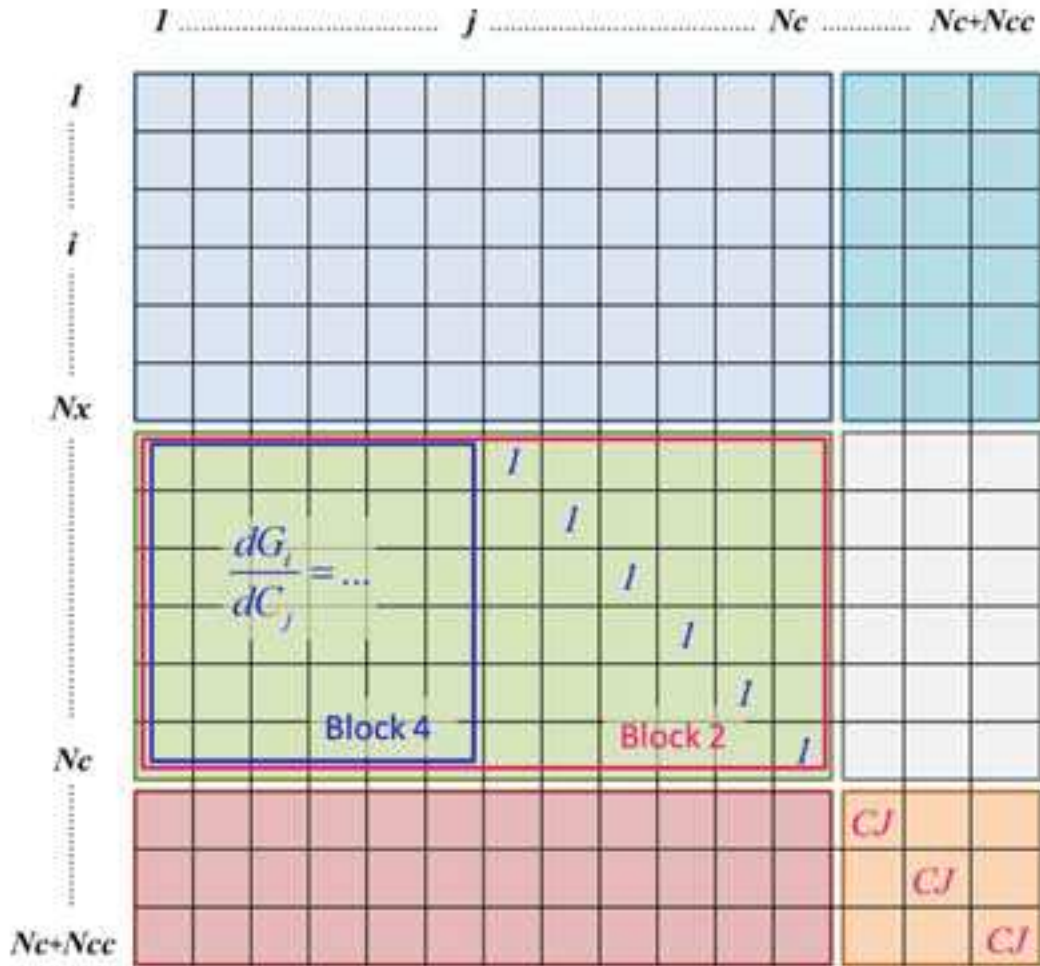
Figure 4.8 – The iteration matrix for DASPK 1 is filled block by block. BLOCK 2 accounts for derivatives of mass action laws, but only BLOCK 4 has to be actually filled.

All the previous modifications to the entries of the Jacobian matrix are independent of the kind of kinetic law governing reactions. On the contrary, all the following modifications are made according to the reaction rates. Different types of kinetic laws are implemented in the code: *standard* kinetic reactions (equation (4.53)), *Monod* reactions (equation (4.55)) and *precipitation dissolution* reactions (equation (4.57)) based on Transition State Theory (Eyring, 1935; Lasaga, 1995). Reaction rates and their derivatives with respect to generic concentrations (activity coefficients are assumed constant within one iteration and not depending on concentrations) are provided below. For s*tandard* kinetic reactions reaction rates are:

$$r_i = r_f^i - r_b^i = k_f^i \prod_{m=1}^{Nc+NCc} (\gamma_m C_m)^{l1_{i,m}} - k_b^i \prod_{m=1}^{Nc+NCc} (\gamma_m C_m)^{l2_{i,m}} \tag{4.53}$$

$$\frac{\partial r_i}{\partial C_j} = \frac{\partial \left(r_f^i - r_b^i \right)}{\partial C_j} = k_f^i \prod_{m=1}^{Nc+NCc} \frac{(\gamma_m C_m)^{l1_{i,m}}}{C_j} - k_b^i \prod_{m=1}^{Nc+NCc} \frac{(\gamma_m C_m)^{l2_{i,m}}}{C_j} \tag{4.54}$$

where **l1** and **l2** are matrixes whose entries are 0 or 1 (built on the basis of *Beq***)** that establish whether a species participates at the kinetic reaction rate. If $l1_{i,m} = 0$ then the chemical species C_m does not appear in the reaction rate r_i. For *Monod* reactions we have:

$$r = \mu_i C_{bio} + \sum_{m=1}^{N} \frac{C_m}{(k_{Mm} + C_m)} \tag{4.55}$$

$$\frac{\partial r_i}{\partial U_{j \neq bio}} = \mu_i C_{bio} r_i \frac{k_{Mj}}{C_j (k_{Mj} + C_j)}$$

$$\frac{\partial r_i}{\partial C_{bio}} = \mu_i \frac{r_i}{C_{bio}} \tag{4.56}$$

Reaction rates coming from *TST* theory for precipitation/dissolution of minerals give instead:

$$r_i = -k\, a \left(1 - \frac{Q_i}{K_S} \right)^n \tag{4.57}$$

$$\frac{\partial r_i}{\partial C_j} = -n\, k\, a \left(1 - \frac{Q_i(\mathbf{C})}{K_S} \right)^{n-1} \frac{Q_i(\mathbf{C})}{K_S C_j}$$

where k is the kinetic constant [mol/T/L-min^2], a groups a series of other constants (i.e. reactive surface A_S [L^2-min/M$_{H2O}$] (or [L^2-min/L$^3_{H2O}$], depending on the formulation)), K_S [-] is the solubility product and $Q_i(\mathbf{C})$ [-] is ion activity product. Please note that a minus appears in equation (4.57) with

respect to previous versions of the TST reaction rate because a positive reaction rate is associated to precipitation. Once the analytical expressions of the derivatives of the kinetic laws are written, what remains to be determined is in which entries they should be added. We remind that reaction rates influence the available totals of primary species and/or may describe the augmentation/reduction of a kinetic species. In no case kinetic rates intervene on mass action laws. The influence over totals concentrations of primary species is accounted for in BLOCK5. Matrix $\mathbf{B_{eq}}$ tells us if a kinetic reaction (and therefore its rate) affects the total concentration of a component. Matrix $\mathbf{B_{cin}}$ tells us if a kinetic reaction (and therefore its rate) affects other kinetic reactions.
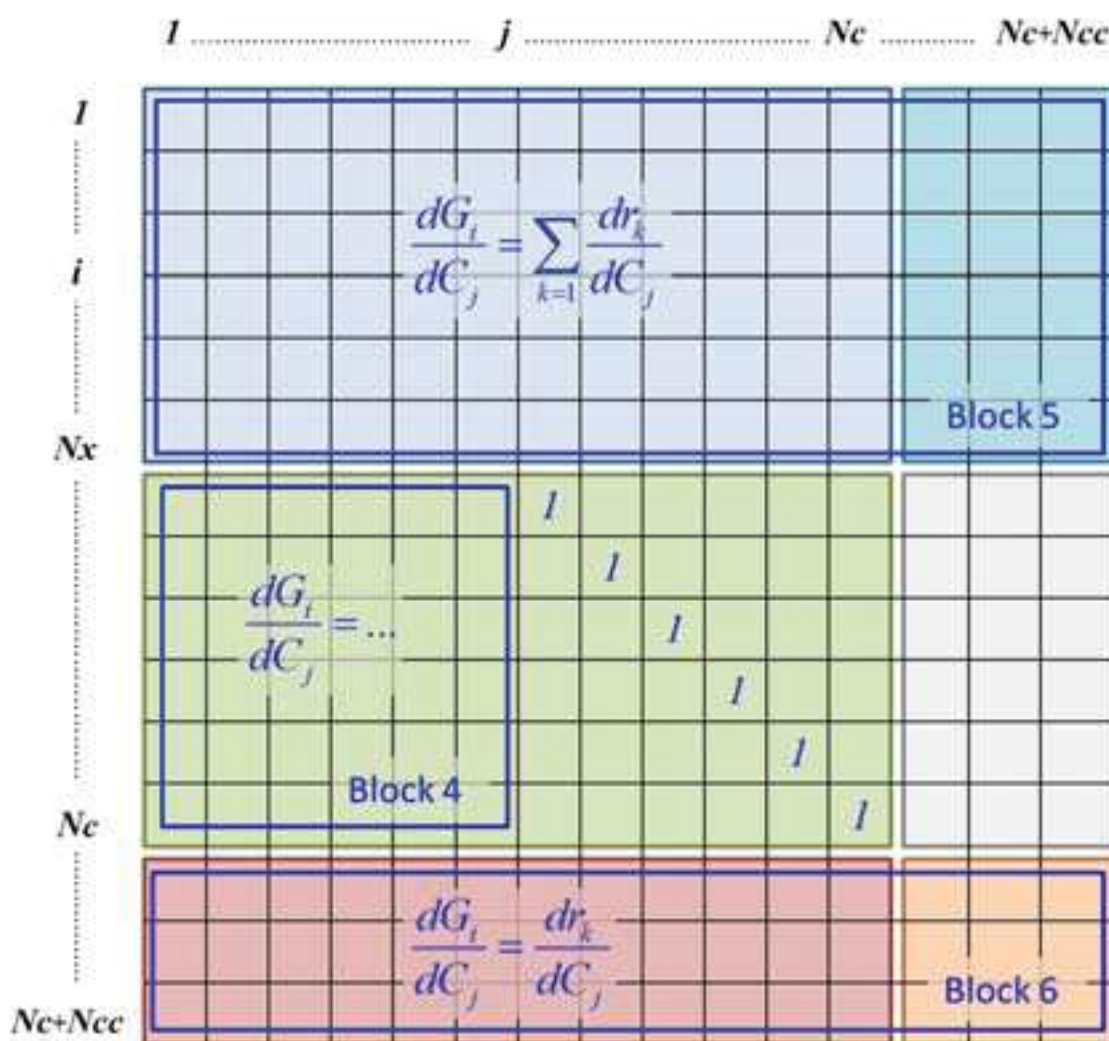
Figure 4.9 - The iteration matrix for DASPK 1 is filled block by block with derivatives of reaction rates in BLOCK 6 and BLOCK 5.

The second version of the DAEs system is made of *Nx* algebraic equations describing mass conservation, and *NCc* ODEs for the evolution of kinetic species. In this configuration the algebraic equations are the conservation equations written with the help of mass action laws. The system becomes:

$$-\tilde{T}_{X_j} + \sum_{i=1}^{Nc} b_{i,j} \prod_{j=1}^{Nx} \frac{\{X_j\}^{a_{i,j}}}{\gamma_i K_i} - \sum_{m=1}^{Nrc} Beq_{j,m} Cc_m = res \qquad j = 1, Nx \qquad (4.58)$$

$$\frac{dCc_l}{dt} - r_l = res \qquad l = 1, NCc \qquad (4.59)$$

It must be pointed out that, while the first *Nx* lines of the previous system were written as a function of kinetic rates R$_i$, now they are written as a function of kinetic species Cc. This is important because it implies that every kinetic reaction must correspond a kinetic species. This will have consequences for some case studies.

The reduced number of equations will result in a Jacobian matrix of reduced size (see Figure XX). The nonlinear solver requires again entries structured as in equation (4.50). It is clear that the second term equation (4.50), which requires the presence of first derivatives to exist, will be present only in the low right corner of the Jacobian matrix. The derivatives of the first *Nx* residuals then become in BLOCK 1 of Figure 10:

$$\frac{dG_i}{dC_j} = \sum_{l=1}^{Nc} b_{l,j} a_{l,j} \prod_{m=1}^{Nx} \frac{(\gamma_m C_m)^{a_{l,m}}}{K_l \gamma_l C_j} \qquad (4.60)$$

And for BLOCK 2:

$$\frac{dG_i}{dC_j} = -Beq_{i,j} \qquad (4.61)$$

The derivatives of the last *NCc* residuals do not change with respect to the previous version, except for the fact that reaction rates have to be written as functions of primary species:

$$\frac{dG_i}{dC_j} = \frac{dr_i}{dC_j} \qquad (4.62)$$
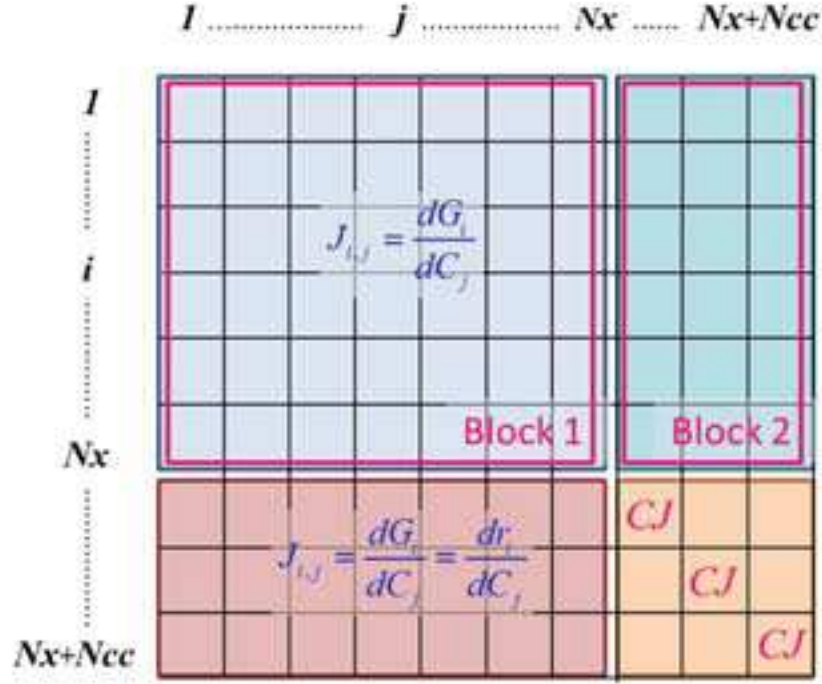
Figure 4.10 - The iteration matrix for DASPK 2 is filled block by block. BLOCK 1 accounts for derivatives of mass conservation equations (algebraic equations) with respect to primary species, BLOCK 2 accounts for the derivatives of mass conservation equations with respect to kinetic species.

4.2.4.3 Residual computation for DASPK 3

A third possible form for our DAEs system consists in degrading it to an ODEs system of *Nx+NCc* equations in *Nx+NCc* unknowns. Writing mass action laws into mass conservation in their differential form, we obtain the following residuals:

$$\sum_{i=1}^{Nc} b_{i,j} \frac{d}{dt}\left(\prod_{j=1}^{Nx} \frac{\{X_j\}^{a_{i,j}}}{\gamma_i K_i} \right) - \sum_{m=1}^{Nrc} Beq_{j,m} r_m = res \qquad j = 1, Nx \qquad (4.63)$$

$$\frac{dCc_l}{dt} - r_l = res \qquad l = 1, NCc \qquad (4.64)$$

The system is smaller but some assumptions upon activity coefficients are required in order to work with reasonable derivatives. To reduce the number of simplifications, the system is written *as a function of the activities* of components and not of their concentration.

In this case like in version II, the reduced number of equations will result in a Jacobian matrix of reduced size. This time the variables U and their first derivatives are U' are simultaneously present in the first *Nx* rows and columns of the Jacobian matrix. According to equation (4.50) a generic entry in BLOCK 1 of Figure 11 takes the following form:

$$J_{ij} = \frac{C_i}{C_j}\left(\tau - \frac{b_{i,j}}{C_j}C'_j + CJ\frac{b_{i,j}}{C_j}\right) \tag{4.65}$$

where $\tau = \sum_{j=1}^{Nx}\frac{a_{i,j}}{C_j}C'_j$. In this formulation of the system, activity coefficients appearing in equation (4.63) are considered constants throughout a single iteration and therefore treated as constants in the Jacobian matrix. They are the only activity coefficients present in the equations since they are written as functions of activities. BLOCK 2 is filled with zeroes since kinetic species do not appear explicitly in conservation equations as before. Last *NCc* rows are filled exactly as in the previous version and the same consideration is true for BLOCK 1 where reaction rates must be taken into account.
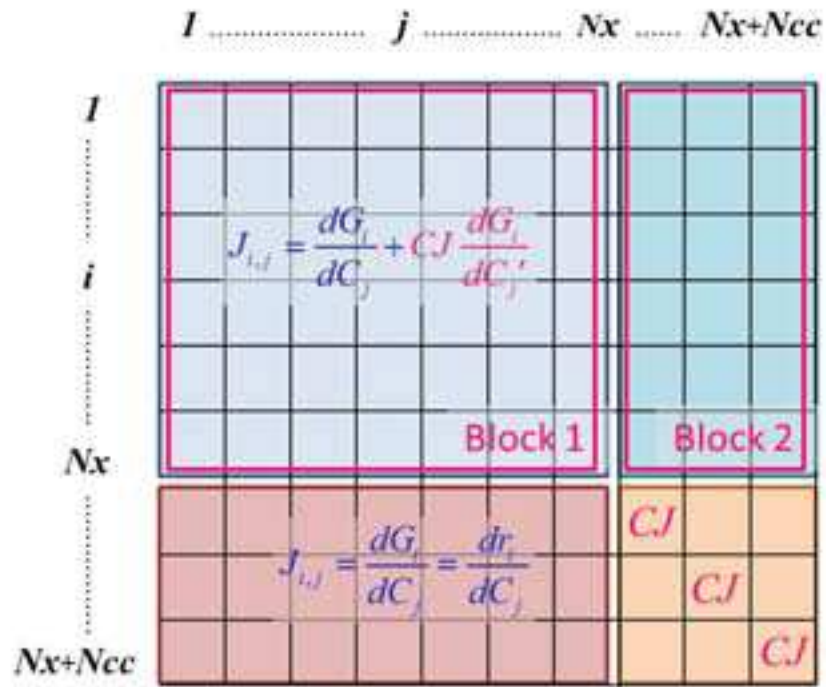
Figure 4.11 - The iteration matrix for DASPK 3 is filled block by block. BLOCK 1 accounts for derivatives of mass conservation equations (differential equations) with respect to primary species, BLOCK 2 accounts for the derivatives of mass conservation equations with respect to kinetic species (entries equal to zero).

4.3 Numerical simulations

4.3.1 TST model, verification of results with PHREEQC and KINDIS

4.3.1.1 Description of the problem

A chemical system H_2O-Halite-Magnesite-Calcite-Dolomite was tested to ensure the correct implementation of linear TST kinetic model together with the computation of activity coefficients and their influence on the computation of the analytical Jacobian. The system is a slight simplification of one proposed in the literature (Leal et al. 2015) to illustrate the concept of partitioning of mixed equilibrium kinetic reactions. Since a published solution wasn't available, a reference solution was computed with software KINDIS (Madé et al.1994) and PHREEQC (Parkhurst et al. 1999). The reaction network is composed of 10 reactions: R1-R7 are modeled at equilibrium (6 involved only dissolved species, 1 involves a solid phase) and R8-R10 are the kinetic dissolutions of minerals:

$$H_2O_{(l)} - H^+ \Leftrightarrow OH^- \qquad\qquad R1$$

$$H_2CO_{3(aq)} \Leftrightarrow HCO_3^- + H^+ \qquad\qquad R2$$

$$CO_3^{-2} + H^+ \Leftrightarrow HCO_3^- \qquad\qquad R3$$

$$CaCO_{3(aq)} + H^+ \Leftrightarrow HCO_3^- + Ca^{2+} \quad R4$$

$$MgCO_{3(aq)} + H^+ \Leftrightarrow HCO_3^- + Mg^{2+} \quad R5$$

$$CaCl_{2(aq)} \Leftrightarrow Ca^{2+} + 2Cl^- \qquad\qquad R6$$

$$NaCl_{(s)} \Leftrightarrow Na^+ + Cl^- \qquad\qquad R7$$

$$CaCO_{3(s)} \Leftrightarrow -H^+ + HCO_3^- + Ca^{2+} \qquad\qquad R8$$

$$MgCO_{3(s)} \Leftrightarrow -H^+ + HCO_3^- + Mg^{2+} \qquad\qquad R9$$

$$(CaMg)(CO_3^-)_{2(s)} \Leftrightarrow -2H^+ + 2HCO_3^- + Mg^{2+} + Ca^{2+} \quad R10$$
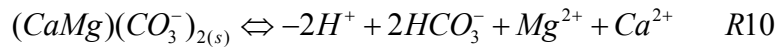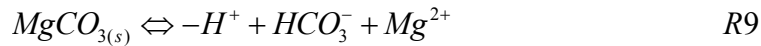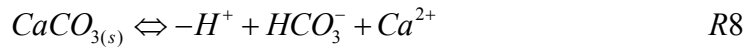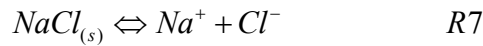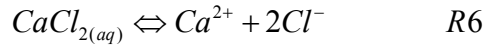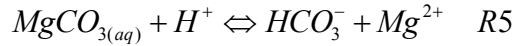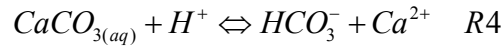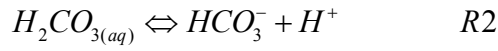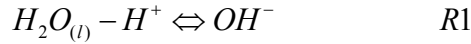
Calcite ($CaCO_{3(s)}$), Magnesite ($MgCO_{3(s)}$), and Dolomite ($(CaMg)(CO_3^-)_{2(s)}$), are supposed to dissolve kinetically (subsequent precipitation is not allowed) according to the classic TST theory (equation (4.57)) that provides the following reaction rate r [mol/T/ M_{H2O}] (or [mol/T/ L^3_{H2O}] according to the formulation):

$$r = -k\, A_S \left(1 - \frac{Q}{K_S}\right)^n$$

where A_S is the reactive surface of the mineral $[L^2\text{-min}/M_{H2O}]$ (or $[L^2\text{-min}/L^3_{H2O}]$ according to the formulation), Q is its ion activity product [-], K_S is the solubility product [-], $n=1$ and k is the kinetic constant $[\text{mol/T/L-min}^2]$ (the temperature of the system is supposed 25 °C, T=298.15 [K]). Equilibrium and kinetic constants are provided in Tables 4.6 and 4.7. Please note that a minus appears in equation (4.57) because a positive reaction rate is associated to precipitation.

	H+	H2O	HCO3-	Ca2+	Mg2+	Cl-	Na+	$Log_{10}K_{eq}$
H+	1	0	0	0	0	0	0	0
H2O	0	1	0	0	0	0	0	0
HCO3-	0	0	1	0	0	0	0	0
Ca2+	0	0	0	1	0	0	0	0
Mg2+	0	0	0	0	1	0	0	0
Cl-	0	0	0	0	0	1	0	0
Na+	0	0	0	0	0	0	1	0
OH-	-1	1	0	0	0	0	0	-14.0
H2CO3(l)	1	0	1	0	0	0	0	6.35
CO3--	-1	0	1	0	0	0	0	-10.33
CaCO3(l)	-1	0	1	1	0	0	0	-7.11
MgCO3(l)	-1	0	1	0	1	0	0	-7.35
CaCl2	0	0	0	1	0	2	0	-0.64
NaCl(s)	0	0	0	0	0	1	1	1.59

Table 4.1 – Morel table for the test case. Equilibrium constants taken from Thermoddem database (http://thermoddem.brgm.fr/)

	$Log_{10}K_S$	A_S	k
$CaCO_{3(s)}$	1.85	0.5	$5.38 \ 10^{-3}$
$MgCO_{3(s)}$	1.41	0.5	$1.95 \ 10^{-3}$
$(CaMg)(CO_3^-)_{2(s)}$	3.53	0.5	$2.40 \ 10^{-6}$

Table 4.2 - Constants for kinetic rates. Constants taken from Palandri (2004).

Activity coefficients γ_i are computed according to Debye-Huckel formulation:

$$\log_{10} \gamma_i = -\frac{A\, z_i\, \sqrt{I}}{1.0 + a_i^0\, B\, \sqrt{I}} + C\, I \qquad (4.66)$$

where I is the ionic strength of the solution, z_i is the charge of the considered ion, a_i^0 is the effective radius of the considered ion and A, B and C are the Debye-Huckel constants (A=0.5114, B=0.3288, C=0.41). We recall that the ionic strength is computed as:

$$I = \sum_{i=1}^{N_C} C_i z_i^2 \qquad (4.67)$$

The test case is well suited for testing the three configurations of the system DASPK 1, DASPK 2 and DASPK 3 since for each kinetic reaction R8 to R10 there is a corresponding kinetic species: $CaCO_{3(s)}$ for R8, $MgCO_{3(s)}$ for R9 and $(CaMg)(CO_3^-)_{2(s)}$ for R10. The number of reactions is reasonable to test a first implementation, but is not trivial from a numerical point of view: because of chosen values of reactive surface area, kinetic reactions are fast and equilibrium reactions span over an interval of twenty orders of magnitude (that makes the test case not as challenging as those presented in Chapter 3 but still not trivial).

4.3.1.2 Numerical simulations: results

Resulting curves obtained with KINDIS and DASPK solver (DASPK 1, numerical Jacobian: curves obtained through the other versions of DASPK were redundant and then omitted) are perfectly superimposed and those obtained with PHREEQC are in very good agreement. Small differences are due to the fact that PHREEQC takes other aqueous species into account and/or to small differences in the computation of activity coefficients. We report here results for the minerals (Calcite, Magnesite, and Dolomite, Figures 4.12, 4.13 and 4.14) and some dissolved species: $CaCO_{3(aq)}$, $MgCO_{3(aq)}$ (Figure 4.15) and H^+ (Figure 4.16). Results show that the implementation of the kinetic law for mineral precipitation and dissolution is correct and that DASPK solver converges in presence of activity coefficients. Plotted curves were obtained with absolute and relative tolerances ATOL = 10^{-12} and RTOL = 10^{-14} (these are the lowest admissible values).
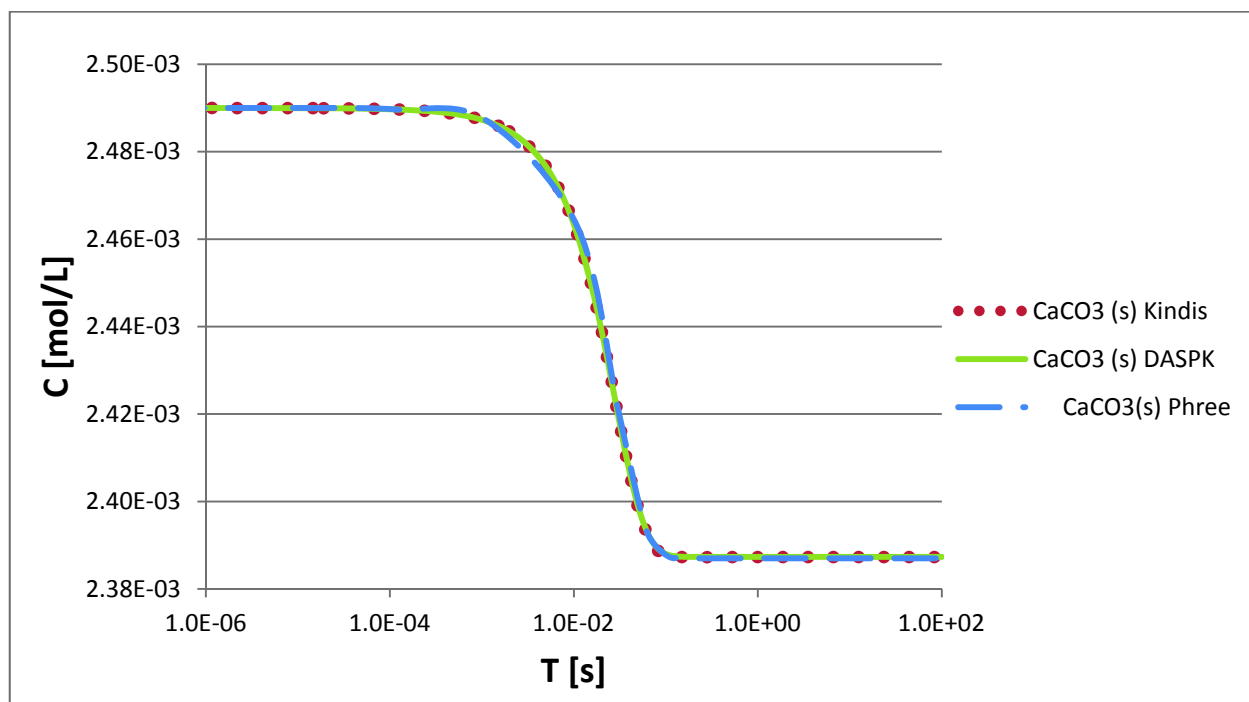
Figure 4.12 – Evolution of Calcite CaCO$_{3(s)}$
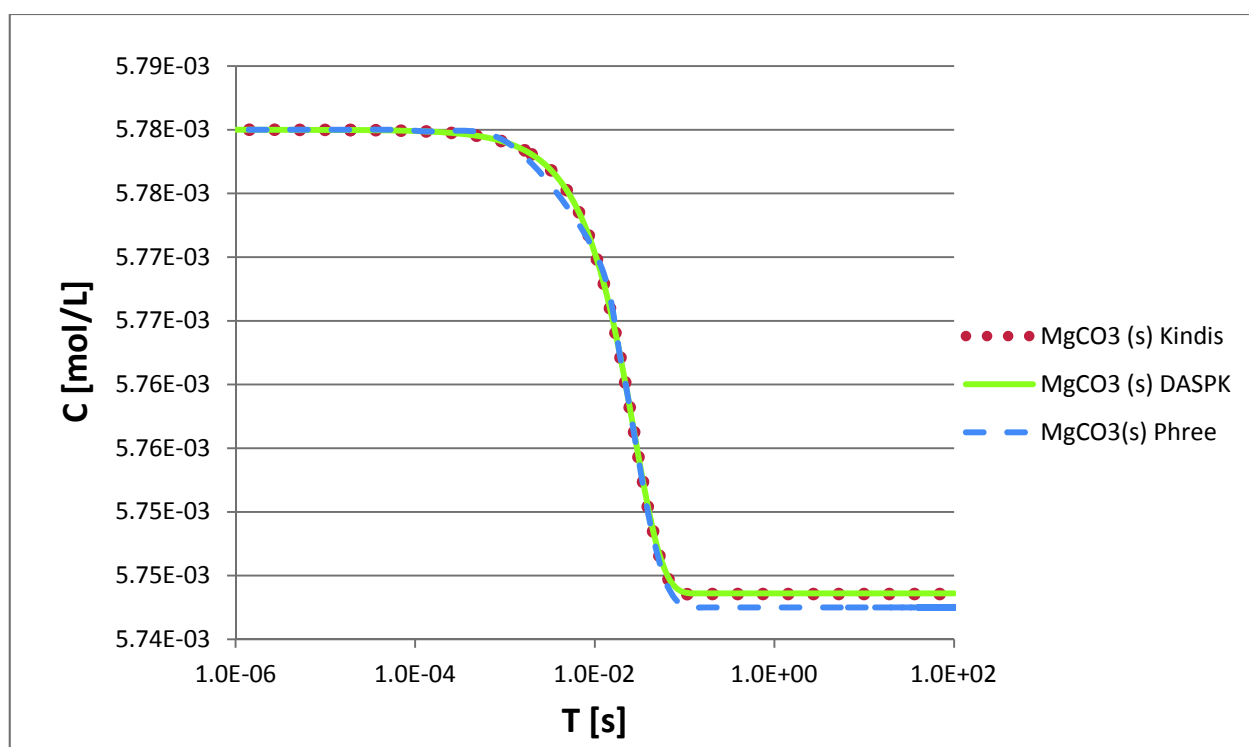
Figure 4.13 – Evolution of Magnesite MgCO$_{3(s)}$
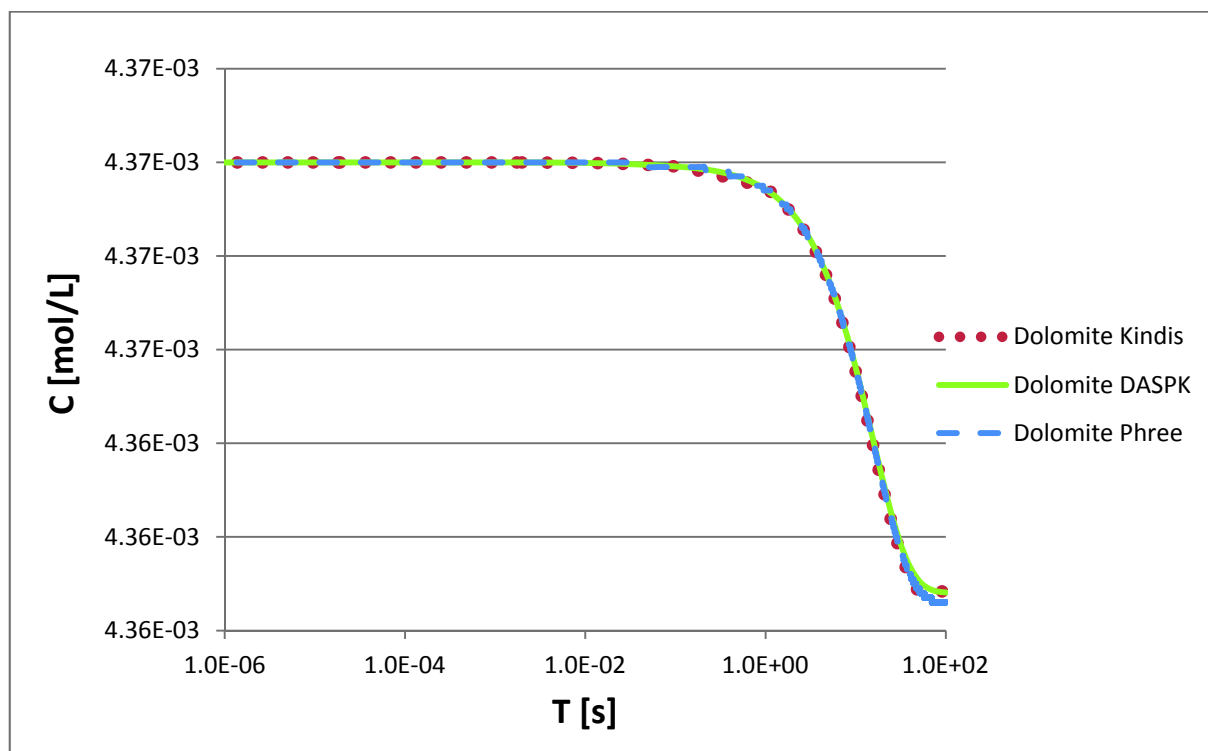
Figure 4.14 – Evolution of Dolomite $(CaMg)(CO_3^-)_{2(s)}$
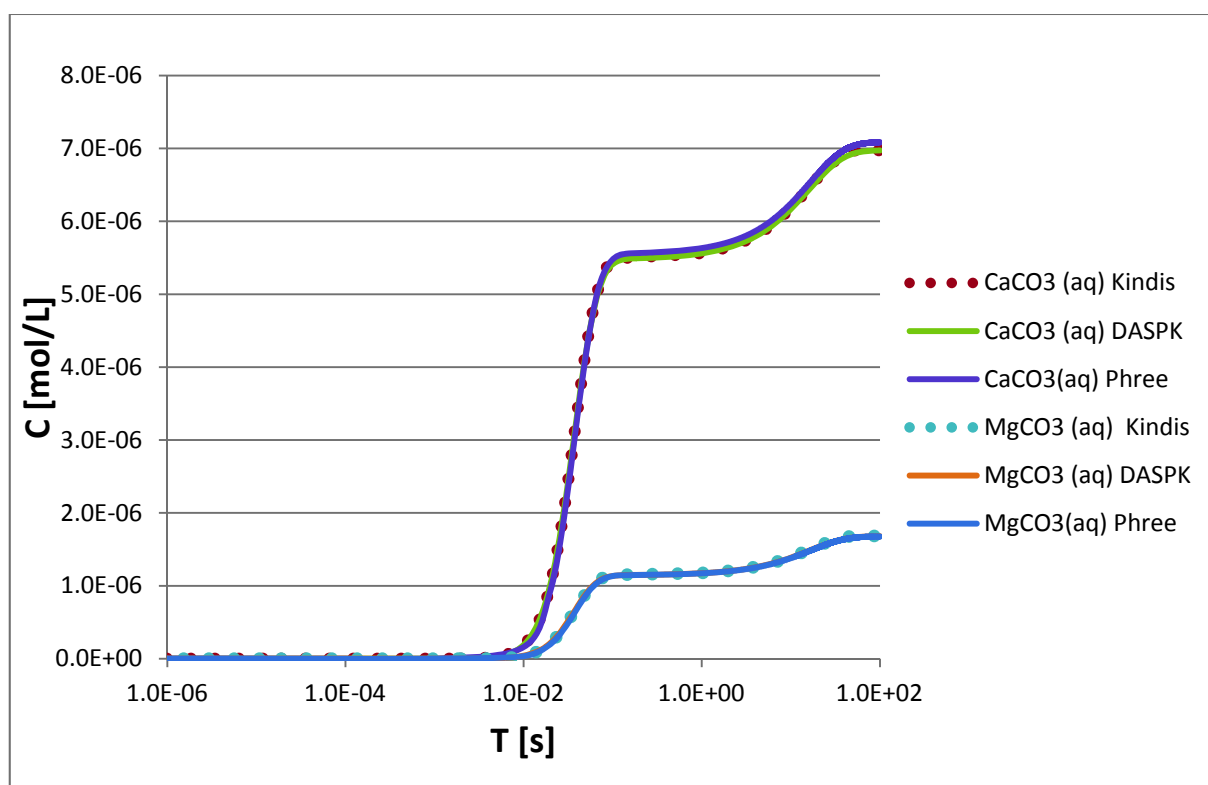
Figure 4.15 – Evolution of dissolved species $CaCO_{3(aq)}$ and $MgCO_{3(aq)}$
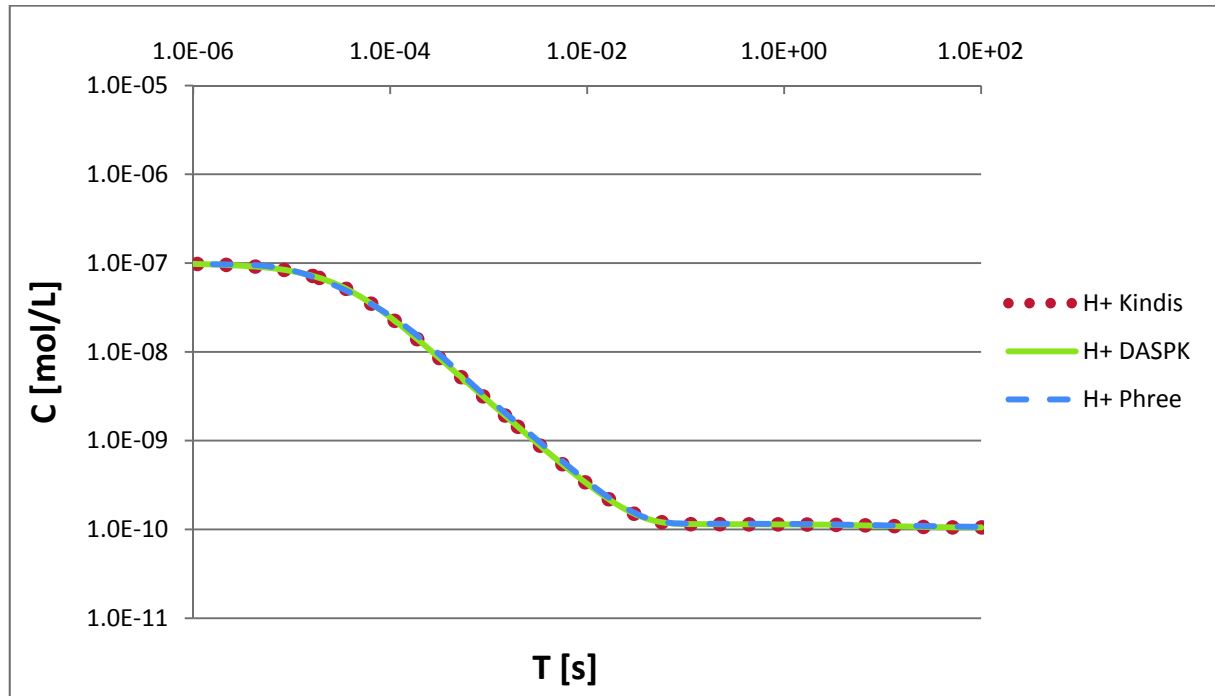
Figure 4.16 – Evolution of dissolved species H^+

Once verified that DASPK provides results comparable with those obtained with well-established codes, it is possible to begin with the analysis of the performances of the different configurations of the system of equations. In the following, an analysis of the number of time steps and the CPU time is proposed. Tests started from values of absolute tolerance (ATOL) of 10^{-12} and relative tolerance (RTOL) of 10^{-14} (these values were used to produce Figures 4.12 to 4.16 and identified as the limit of DASPK solver failing). Then tolerances were increased by one order of magnitude at a time (lowering progressively the quality of the solution).

All tests were performed with a version of the code compiled in Release mode in order to avoid slow computations typical of the execution in Debug mode. CPU time was computed solving 100 times the same problem, monitoring the total time and dividing it by a factor of 100. This average of results was made necessary by the extremely fast convergence of DASPK, which made impossible registering the execution time of a single solution. Results are reported in Table 4.3 for DASPK 1, Table 4.4 for DASPK 2 and 4.5 For DASPK 3; a graphic representation is available in Figure 4.17.

Surprisingly, looking at Figure 4.17a and 4.17b, the global CPU time required to reach convergence was slightly smaller for DASPK 1 (which counts $Nc+Ncc$ unknowns) than for DASPK 2 and 3 (which both count $Nx+Ncc$ unknowns) for both analytical and numerical iteration matrixes. On the other hand, DASPK 2 required systematically more CPU time to converge.

DASPK 1 TOL NUM	TIME STEPS	RES EVAL	NL ITER	CPU
A 10^{-12} R 10^{-14}	387	2496	859	6.40 10^{-3}
A 10^{-11} R 10^{-13}	327	2017	705	5.15 10^{-3}
A 10^{-10} R 10^{-12}	265	1495	507	4.05 10^{-3}
A 10^{-9} R 10^{-11}	-	-	-	-
A 10^{-8} R 10^{-10}	-	-	-	-

DASPK 1 TOL AN	TIME STEPS	RES EVAL	NL ITER	CPU
A 10^{-12} R 10^{-14}	396	878	874	4.68 10^{-3}
A 10^{-11} R 10^{-13}	367	719	716	4.05 10^{-3}
A 10^{-10} R 10^{-12}	307	533	531	3.28 10^{-3}
A 10^{-9} R 10^{-11}	-	-	-	-
A 10^{-8} R 10^{-10}	-	-	-	-

Table 4.3 – Numerical information about the solution of the system Halite-Calcite-Magnesite-Dolomite system with DASPK 1.

DASPK 2 TOL NUM	TIME STEPS	RES EVAL	NL ITER	CPU
A 10^{-12} R 10^{-14}	602	1863	1001	7.38 10^{-2}
A 10^{-11} R 10^{-13}	392	1311	669	5.16 10^{-2}
A 10^{-10} R 10^{-12}	276	1081	499	4.10 10^{-2}
A 10^{-9} R 10^{-11}	197	932	360	3.39 10^{-2}
A 10^{-8} R 10^{-10}	-	-	-	-

DASPK 2 TOL AN	TIME STEPS	RES EVAL	NL ITER	CPU
A 10^{-12} R 10^{-14}	684	1193	1191	6.30 10^{-2}
A 10^{-11} R 10^{-13}	478	778	776	4.34 10^{-2}
A 10^{-10} R 10^{-12}	344	613	611	3.36 10^{-2}
A 10^{-9} R 10^{-11}	229	398	396	2.31 10^{-2}
A 10^{-8} R 10^{-10}	-	-	-	-

Table 4.4 – Numerical information about the solution of the system Halite-Calcite-Magnesite-Dolomite system with DASPK 2.

DASPK 3 TOL NUM	TIME STEPS	RES EVAL	NL ITER	CPU
A 10^{-12} R 10^{-14}	408	1908	797	1.57 10^{-2}
A 10^{-11} R 10^{-13}	362	1490	668	1.28 10^{-2}
A 10^{-10} R 10^{-12}	243	1203	451	1.06 10^{-2}
A 10^{-9} R 10^{-11}	190	1276	334	1.06 10^{-2}
A 10^{-8} R 10^{-10}	-	-	-	-

DASPK 3 TOL AN	TIME STEPS	RES EVAL	NL ITER	CPU
A 10^{-12} R 10^{-14}	495	967	965	1.03 10^{-2}
A 10^{-11} R 10^{-13}	390	674	672	7.64 10^{-3}
A 10^{-10} R 10^{-12}	295	474	472	5.46 10^{-3}
A 10^{-9} R 10^{-11}	204	392	390	4.84 10^{-3}
A 10^{-8} R 10^{-10}	147*	274*	272*	3.90 10^{-3}

Table 4.5 – Numerical information about the solution of the system Halite-Calcite-Magnesite-Dolomite system with DASPK 3 (*the solution is computed but clearly degraded)

Looking at Figure 4.17c and 4.17d, it is clear that although DASPK 2 required more iterations to converge, the sole (slight) number of iterations cannot be at the origin of such a difference in the CPU time demand. The solver was indubitably penalized by the fact that the code had to be compiled with quadruple precision to ensure convergence.

Differences (between Figure 4.17c and 4.17d) in the number of iterations between the analytical and the numerical evaluation of the Jacobian matrix (or Iteration matrix as in the DASPK terminology) may be explained through the approximation of considering activity coefficients constant throughout the single iteration. Anyway, despite the higher number of iterations (especially when using versions DASPK 2 and DASPK 3), the solution obtained with analytical Jacobian matrix globally demanded less CPU time.

The fact that for DASPK 1 the number of iterations between the numerical and analytical Jacobian remained the same, shows that fears expressed in paragraph § 4.13 about the drawbacks of working with more complicated equations were legitimate. On the other hand, from Figure 4.17 is also visible that DASPK 1 failed to converge before the other two when low precision was required.
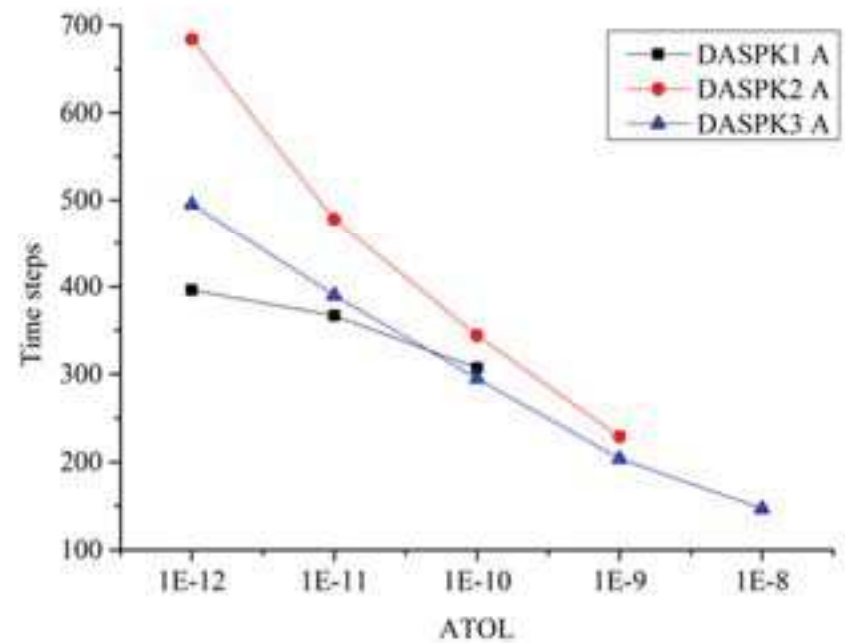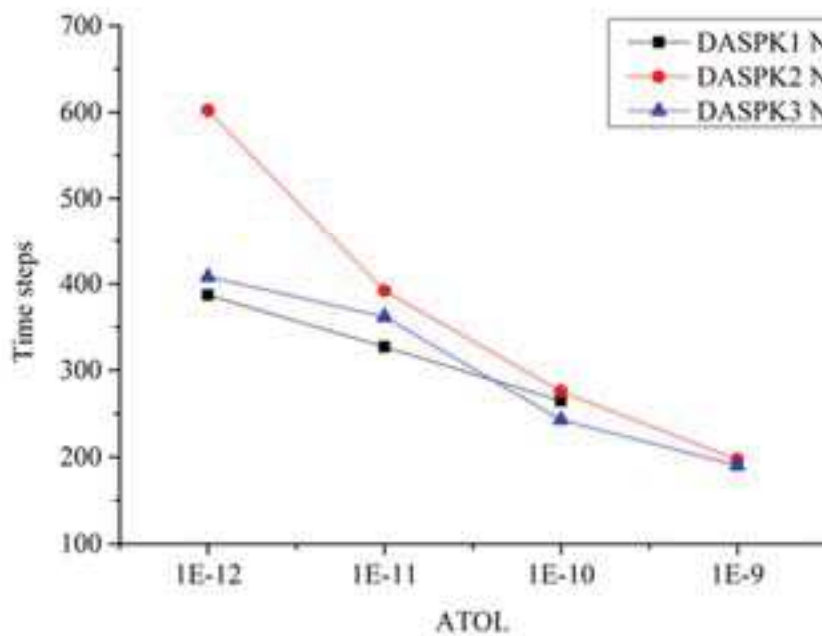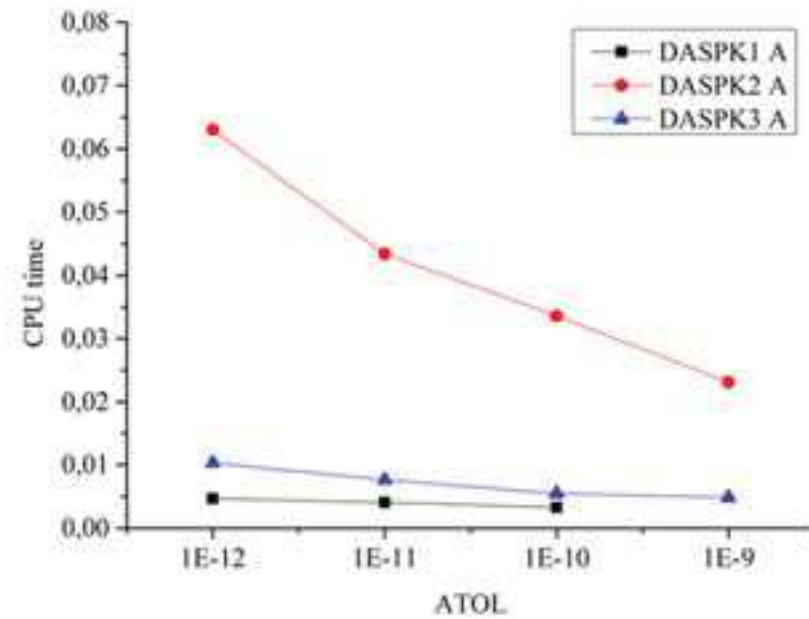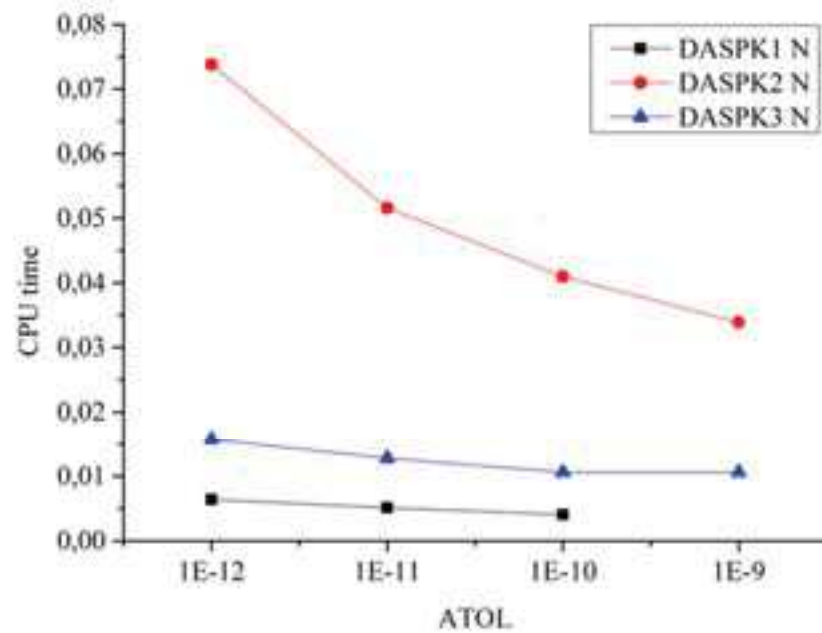
Figure 4.17 – CPU time to convergence for DASPK solver I, II, III with a) numerical Jacobian and b) analytical Jacobian; Number of time steps to reach convergence for DASPK I, II, III with c) numerical Jacobian and d) analytical Jacobian

4.3.2 Chilakapati test case: verification with publication

4.3.2.1 Description of the problem

The second example used to test the performances of the solvers was first published by Chilakapati in 1998 and then used by Fang in 2003 as a benchmark; it is an exhaustive example of combinations of equilibrium and kinetic reactions, involving nonlinear elementary and Monod reactions. The system describes the process of transformation of a metal organic chelate contaminant, Co(II)EDTA, in other complexes. EDTA, or ethylenediaminetetraacetic acid, is a synthetic chelate that is widely present in surface and groundwater and is considered dangerous because it facilitates the mobilization of heavy metals and radionuclides like Co. Co(II)EDTA cannot be degraded by bacteria, but EDTA and Fe(III)EDTA can. In this example, Co(II)EDTA is adsorbed on iron-oxide sediments and subsequently EDTA and Fe(III)EDTA are released in the solution, available for biodegradation. In the process, some of the Co(II)EDTA undergoes oxidation and is transformed in Co(III)EDTA, a stable and weakly reactive complex. The transformation of Co(II)EDTA may be described through 64 reactions but Chilakapati simplified the system describing it through 10 reactions and 15 species reported below. Adsorption/desorption reactions are very fast compared to other processes and therefore are modeled through equilibrium (R1-R5). Dissolution reactions, oxidation and biogeochemical degradation are modeled as kinetics (R6-R10). The two biogeochemical reactions are expressed through Monod reactions law while other kinetic reactions are expressed through nonlinear elementary rates.

$$Co(II)_{(aq)} + S_{neg} \Leftrightarrow S_{neg} - Co \qquad R1$$

$$Co(II)EDTA_{(aq)} + S_{pos} \Leftrightarrow S_{pos} - Co(II)EDTA \qquad R2$$

$$Fe(III)EDTA_{(aq)} + S_{pos} \Leftrightarrow S_{pos} - Fe(III)EDTA \qquad R3$$

$$EDTA_{(aq)} + S_{pos} \Leftrightarrow S_{pos} - EDTA \qquad R4$$

$$Co(III)EDTA_{(aq)} + S_{pos} \Leftrightarrow S_{pos} - Co(III)EDTA \qquad R5$$

$$S_{pos} - Co(II)EDTA \leftrightarrow Co(II)_{(aq)} + S_{pos} - EDTA \qquad R6$$

$$S_{pos} - EDTA \leftrightarrow Fe(III)EDTA_{(aq)} + S_{pos} \qquad R7$$

$$Co(II)EDTA \leftrightarrow Co(III)EDTA \qquad R8$$

$$Fe(III)EDTA_{(aq)} + 6O_2 \rightarrow 3CO_2 + Biom \qquad R9$$

$$EDTA_{(aq)} + 6O_2 \rightarrow 3CO_2 + Biom \qquad R10$$
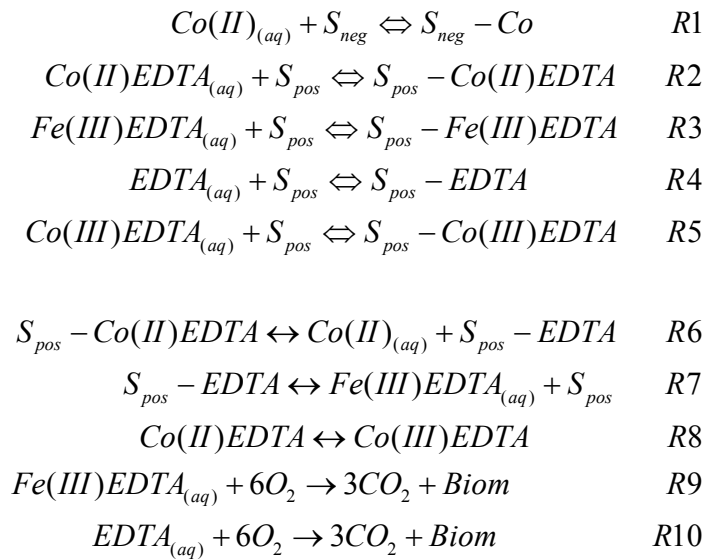
Reaction R1-R5 are adsorption/desorption reactions, R6 and R7 are dissolution reactions, R8 is an oxidation reaction and R9 and R10 describe biodegradation process. Considering only the five equilibrium equations, the chemical species involved in those reactions are 12. This means that *12 - 5 = 7* components have to be chosen among the species to describe the equilibrium partition of the system. We chose as components the following species, colored in the next set of reactions: $Co(II)_{aq}$, S_{neg}, $Co(II)EDTA_{aq}$, S_{pos}, $Fe(III)EDTA_{aq}$, $EDTA_{aq}$, $Co(III)EDTA_{aq}$.

$$
\begin{aligned}
Co(II)_{aq} + S_{neg} &\Leftrightarrow S_{neg} - Co & R1 \\
Co(II)EDTA_{aq} + S_{pos} &\Leftrightarrow S_{pos} - Co(II)EDTA & R2 \\
Fe(III)EDTA_{aq} + S_{pos} &\Leftrightarrow S_{pos} - Fe(III)EDTA & R3 \\
EDTA_{aq} + S_{pos} &\Leftrightarrow S_{pos} - EDTA_{aq} & R4 \\
Co(III)EDTA_{aq} + S_{pos} &\Leftrightarrow S_{pos} - Co(III)EDTA & R5
\end{aligned}
\tag{4.68}
$$
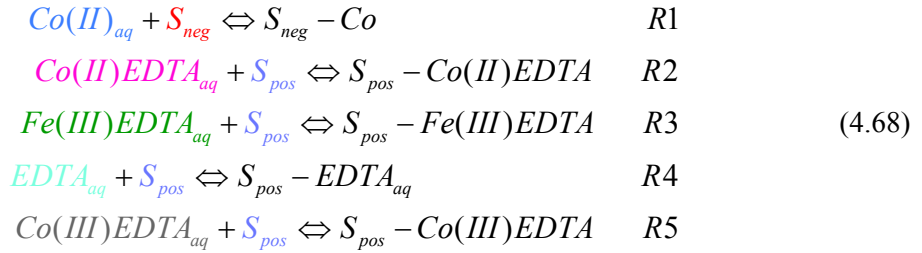
Remaining species, casually all at the right hand side of the reactions are secondary species that can be deduced through mass action law, while mass conservation equations are written for the seven components. Mass action laws are listed in the following system (activity coefficients taken all equal to 1.0):

$$
\begin{cases}
\left[S_{neg} - Co \right] = K_1 \left[S_{neg} \right] \left[Co(II)_{aq} \right] \\
\left[S_{pos} - Co(II)EDTA \right] = K_2 \left[S_{pos} \right] \left[Co(II)EDTA_{aq} \right] \\
\left[S_{pos} - Fe(III)EDTA \right] = K_3 \left[S_{pos} \right] \left[Fe(III)EDTA_{aq} \right] \\
\left[S_{pos} - EDTA \right] = K_4 \left[S_{pos} \right] \left[EDTA_{aq} \right] \\
\left[S_{pos} - Co(III)EDTA \right] = K_5 \left[S_{pos} \right] \left[Co(III)EDTA_{aq} \right]
\end{cases}
\tag{4.69}
$$

where the equilibrium constants (note that they are not in logarithmic form) have the following values: K_1=12, K_2=25, K_3=9, K_4=25, K_5=2.5. Once components are defined and mass action laws are written, it is convenient to represent the problem under the form of a Morel table, such as in Table 1. This formulation helps writing the mass conservation equations, since they can be easily deduced from the column of the Morel table (equation (4.70)).

	$Co(II)_{aq}$	S_{neg}	$Co_{(II)}EDTA_{aq}$	S_{pos}	$Fe_{(III)}EDTA_{aq}$	$EDTA_{aq}$	$Co_{(III)}EDTA_{aq}$	K_s
$Co(II)_{aq}$	1	0	0	0	0	0	0	1
S_{neg}	0	1	0	0	0	0	0	1
$Co_{(II)}EDTA_{aq}$	0	0	1	0	0	0	0	1
S_{pos}	0	0	0	1	0	0	0	1
$Fe_{(III)}EDTA_{aq}$	0	0	0	0	1	0	0	1
$EDTA_{aq}$	0	0	0	0	0	1	0	1
$Co_{(III)}EDTA_{aq}$	0	0	0	0	0	0	1	1
$S_{neg}-Co$	1	1	0	0	0	0	0	12
$S_{pos}-Co_{(II)}EDTA$	0	0	1	1	0	0	0	25
$S_{pos}-Fe_{(III)}EDTA$	0	0	0	1	1	0	0	9
$S_{pos}-EDTA$	0	0	0	1	0	1	0	25
$S_{pos}-Co_{(III)}EDTA$	0	0	0	1	0	0	1	2,5

Table 4.6 – Morel table for the equilibrium partition, stoichiometric matrix B, which is diagonal in the first Nx x Nx block.

$$
\begin{aligned}
T_{Co(II)_{aq}} &= \left[Co_{(II)aq} \right] + \left[S_{neg} - Co \right] \\
T_{S_{neg}} &= \left[S_{neg} \right] + \left[S_{neg} - Co \right] \\
T_{S_{pos}} &= \left[S_{pos} \right] + \left[S_{pos} - Co_{(II)}EDTA \right] + \left[S_{pos} - Fe_{(III)}EDTA \right] + \\
&\quad + \left[S_{pos} - EDTA \right] + \left[S_{pos} - Co_{(III)}EDTA \right] \\
T_{Co(II)EDTA_{aq}} &= \left[Co_{(II)}EDTA_{aq} \right] + \left[S_{pos} - Co_{(II)}EDTA \right] \\
T_{Fe(III)EDTA_{aq}} &= \left[Fe_{(III)}EDTA_{aq} \right] + \left[S_{pos} - Fe_{(III)}EDTA \right] \\
T_{EDTA_{aq}} &= \left[EDTA_{aq} \right] + \left[S_{pos} - EDTA \right] \\
T_{Co(III)EDTA_{aq}} &= \left[Co_{(III)}EDTA_{aq} \right] + \left[S_{pos} - Co_{(III)}EDTA \right]
\end{aligned}
\tag{4.70}
$$

As already discussed in paragraph 4.1, total concentrations T_j constitute the link between the equilibrium partition and the kinetic partition. In order to explicit the link between kinetic reactions and primary species, mass action laws substitute secondary species in in kinetic equations:

$$K_2^e \left[Co(II)EDTA_{aq} \right] \left[S_{pos} \right] \leftrightarrow Co(II)_{(aq)} + K_4^e \left[EDTA_{aq} \right] \left[S_{pos} \right] \qquad R6$$

$$K_4^e \left[EDTA_{aq} \right] \left[S_{pos} \right] \leftrightarrow Fe(III)EDTA_{(aq)} + S_{pos} \qquad R7$$

$$Co(II)EDTA_{aq} \leftrightarrow Co(III)EDTA \qquad R8 \qquad (4.71)$$

$$Fe(III)EDTA_{(aq)} + 6O_2 \rightarrow 3CO_2 + Biom \qquad R9$$

$$EDTA_{(aq)} + 6O_2 \rightarrow 3CO_2 + Biom \qquad R10$$
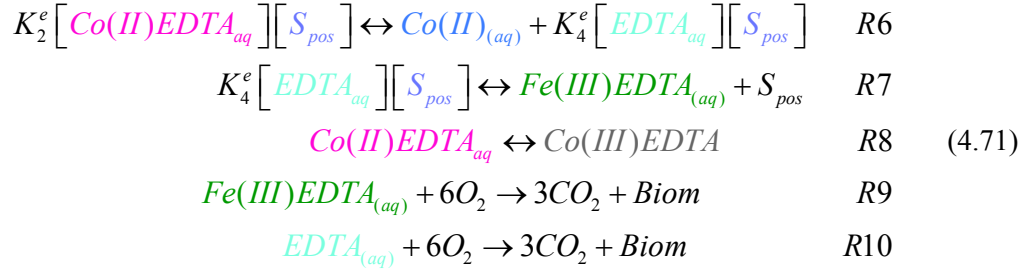
We can therefore write a system in which the influence of each kinetic reaction on the totals is clearly represented:

$$\frac{dT_{Co(II)_{aq}}}{dt} = r_6$$

$$\frac{dT_{S_{neg}}}{dt} = 0$$

$$\frac{dT_{S_{pos}}}{dt} = r_6 - r_6 + r_7 - r_7 = 0$$

$$\frac{dT_{Co(II)EDTA_{aq}}}{dt} = r_6 - r_8 \qquad (4.72)$$

$$\frac{dT_{Fe(III)EDTA_{aq}}}{dt} = r_7 - r_9$$

$$\frac{dT_{EDTA_{aq}}}{dt} = -r_{10} + r_6 - r_7$$

$$\frac{dT_{Co(III)EDTA_{aq}}}{dt} = r_8$$

The only kinetic reaction that could modify the total concentration of Co(II) is R6. Another component in equilibrium speciation is $EDTA_{aq}$. Its total concentration is increased when reaction R6 takes place ($EDTA_{aq}$ is a product in R6) and is at the same time decreased when reactions R7 and R7 take place ($EDTA_{aq}$ is a reactant in R7 and R10). Previous system provides 7 differential equations, 5 more algebraic equations come from equation (4.69). This results in a system of 12 equations and 15 unknowns. 3 more equations have to be provided to track the evolution of kinetic species that do not take part in the equilibrium speciation:

$$\frac{d[Biom]}{dt} = r_9 + r_{10}$$

$$\frac{d[CO_2]}{dt} = 3r_9 + 3r_{10} \qquad (4.73)$$

$$\frac{d[O_2]}{dt} = -6r_9 - 6r_{10}$$

r_6-r_{10} are the reaction rates of kinetic reaction R6-R10: r_6-r_8 are nonlinear elementary production consumption rates while r_9, r_{10} are nonlinear Monod reaction rates. Parameters involved in equations (4.74) are reported in Table 4.2.

$$r_6 = k6a * \left[S_{pos} - Co(II)EDTA \right] - k6b * \left[Co(II)_{aq} \right] * \left[S_{pos} - EDTA \right]$$

$$r_7 = k7a * \left[S_{pos} - EDTA \right] - k7b \left[S_{pos} \right] \left[Fe(III)EDTA_{aq} \right]$$

$$r_8 = k8a \left[Co(II)EDTA \right] - k8b \left[Co(III)EDTA \right]$$

$$r_9 = \frac{\mu_1 \left[Fe(III)EDTA \right] \left[O_2 \right] \left[Biom \right]}{\left(k_{11} + \left[Fe(III)EDTA \right] \right) \left(k_{21} + \left[O_2 \right] \right)}$$

$$r_{10} = \frac{\mu_2 \left[EDTA_{aq} \right] \left[O_2 \right] \left[Biom \right]}{\left(k_{12} + \left[EDTA_{aq} \right] \right) \left(k_{22} + \left[O_2 \right] \right)}$$

(4.74)

Parameter	Value	Unit
$k6f$	1.0	h^{-1}
$k6b$	1.0 10^{-3}	$LmM^{-1}h^{-1}$
$k7f$	2.5	h^{-1}
$k7b$	0.0	$LmM^{-1}h^{-1}$
$k8f$	1.0 10^{-3}	h^{-1}
$k8b$	0.0	h^{-1}
μ_1	2.5 10^{-4}	h^{-1}
k_{11}	1.0 10^{-5}	mML^{-1}
k_{21}	1.0 10^{-5}	mML^{-1}
μ_2	0.025	h^{-1}
k_{12}	1.0 10^{-5}	mML^{-1}
k_{22}	1.0 10^{-5}	mML^{-1}

Table 4.7 – Parameters for standard and Monod kinetic reactions.

Equations (4.72) together with (4.69) and (4.73) describe the system of differential algebraic equations generalized in equation (4.22). As already explained, this is the system with the highest number of unknowns but contains the simplest equations. Writing equations (4.69) into equations (4.72) would provide a system such as (4.24). This second configuration of the system allows the reduction of the number of unknowns from Nc+Ncc to Nx+Ncc and reduces the system to an ODE.

This test case, that is numerically less challenging than the previous (equilibrium constants are of the same order of magnitude, activity coefficients are set equal to 1, reactions are not as fast as in the previous example) presents some characteristics that show how challenging may be writing a system like (4.23), or DASPK 2. In fact, it requires concentrations of kinetic species to be included in mass conservation and not their rate. The test-case was indeed presented by Fang as highly coupled (kinetic reactions occur between primary species) and was used to introduce a more sophisticated system of picking components and kinetic variables (Fang et al. 2003). Moreover, regardless of how complicated is to write the equations, the main drawback of this approach is that, for some problems where the concentrations of kinetic species are very high (i.e. minerals within a porous medium) implying the addition of quantities in the order of 10^1 to quantities of around 10^{-12}. To be able to compute such problems with DASPK it proved necessary compiling the whole software in quadruple precision, which is an unwanted complication due to computer time. For all these inefficiencies, and on the basis of results presented in paragraph 4.3.1.2, this problem was not solved with DASPK 2. In order to test the implicit formulation with respect to the method implemented in SPECY (Carrayrou 2001), the problem was also solved with explicit QSSA.

In the following pages, we provide solutions obtained through QSSA method and through solver DASPK for different arrangements of system of equations (we will refer to them as DASPK 1 for system (4.46)-(4.48), DASPK 3 for system (4.63)-(4.64)) compared with results published by Chilakapati (Figure 4.18).
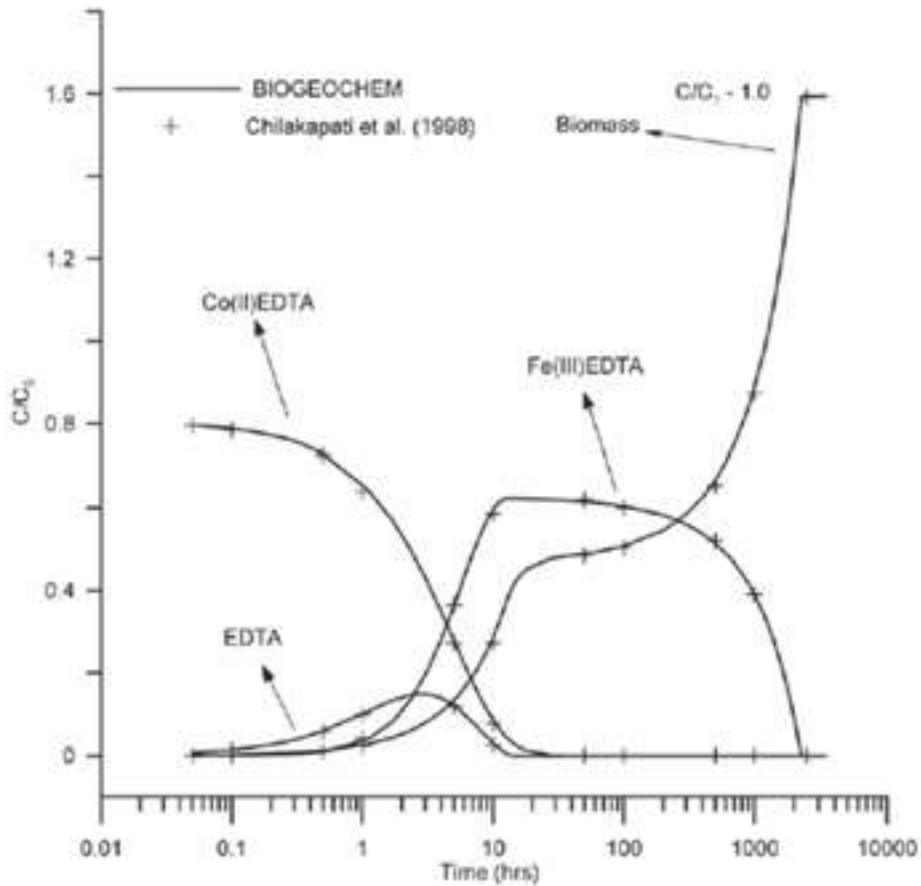
Figure 4.18 –Experimental points and interpolation through software Biogeochem (Fang et al. 2003).

The dynamic of the chemical system is illustrated by Figure 4.18. Co(II)EDTA is transformed in EDTA and Fe(III)EDTA, that are systematically consumed by the Biomass that keeps growing. EDTA is the first species to disappear, followed by Co(II) EDTA and Fe(III)EDTA. When the nutrition for Biomass is not available, growing stops.   Figure 4.19 shows that all methods are able to reproduce correctly the numerical experiment. The formulation solved through DASPK 1 allows tracking secondary species (Figure 4.20) throughout the duration of the experiment whereas they have to be computed a posteriori for DASPK 3.
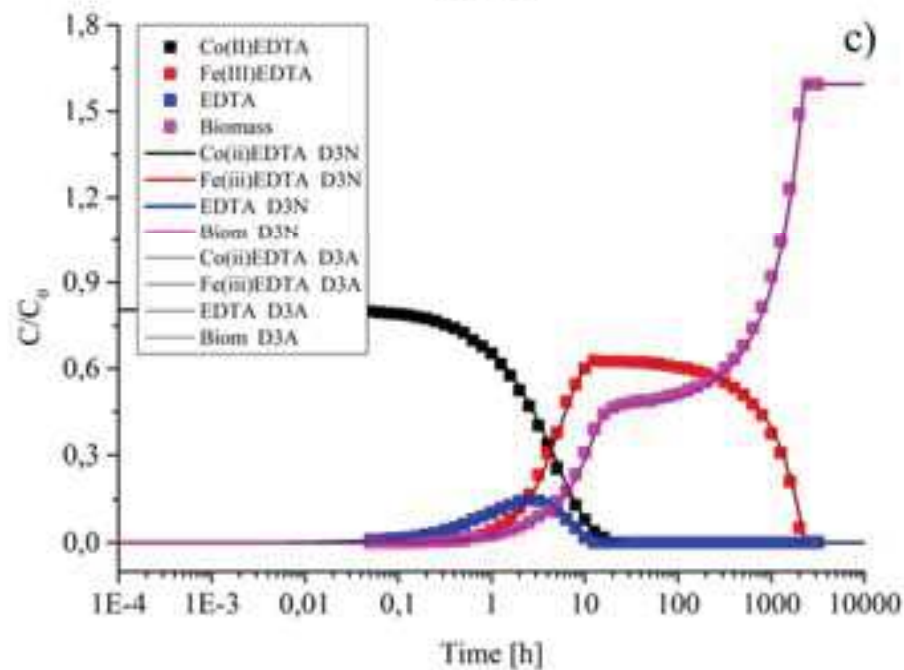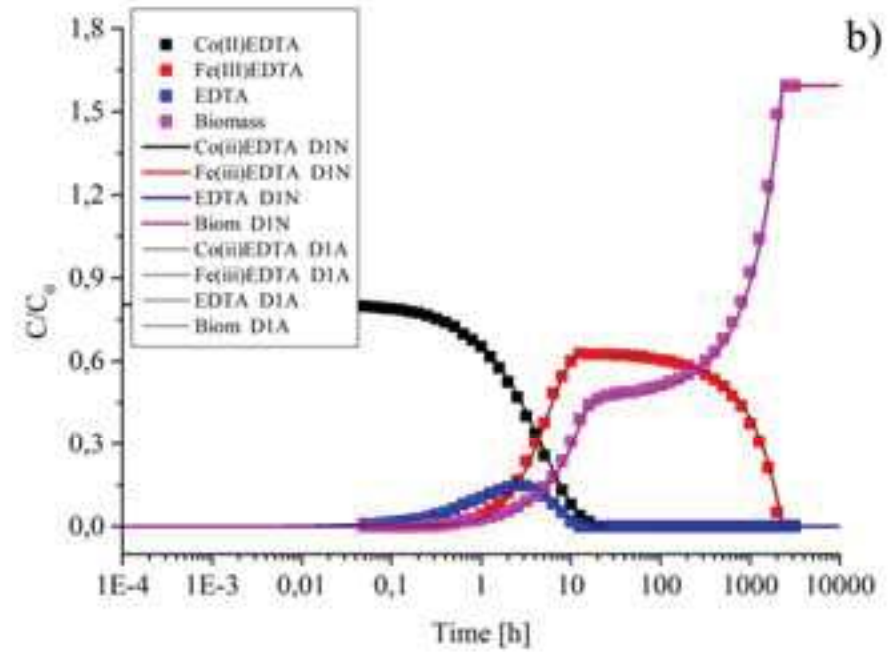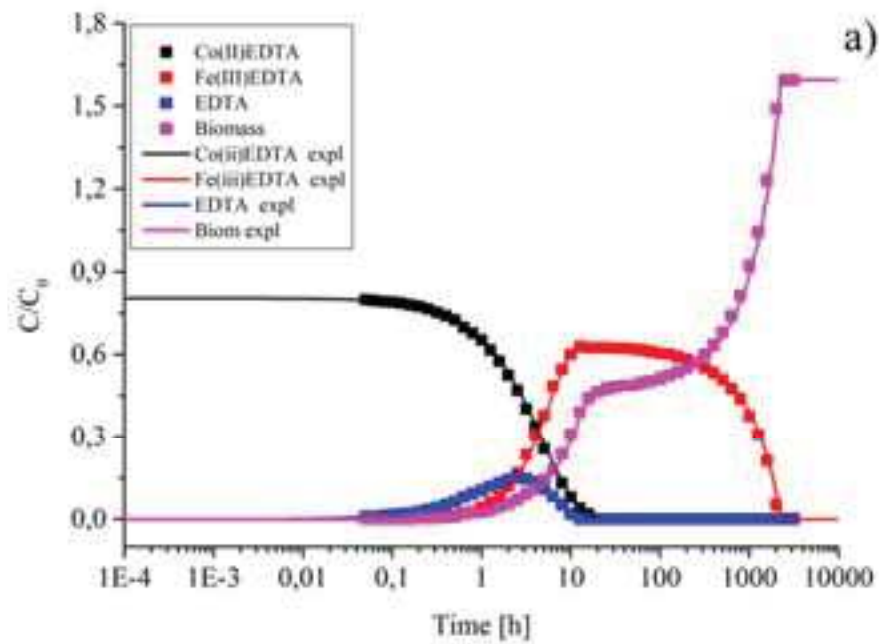
Figure 4.19 – Curves for some of the major elements of the test case obrained with a) explict QSSA, b) implicit DASPK solver with system configuration DASPK 1 (system of DAEs) c) implicit DASPK solver with system configuration DASPK 3 (system of ODEs).
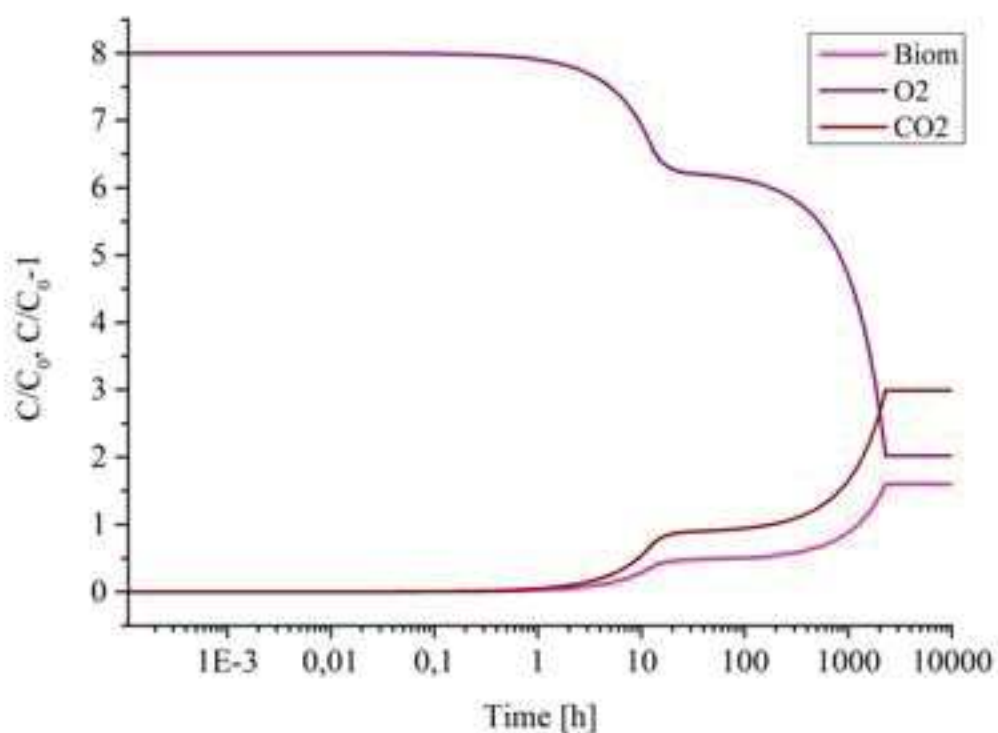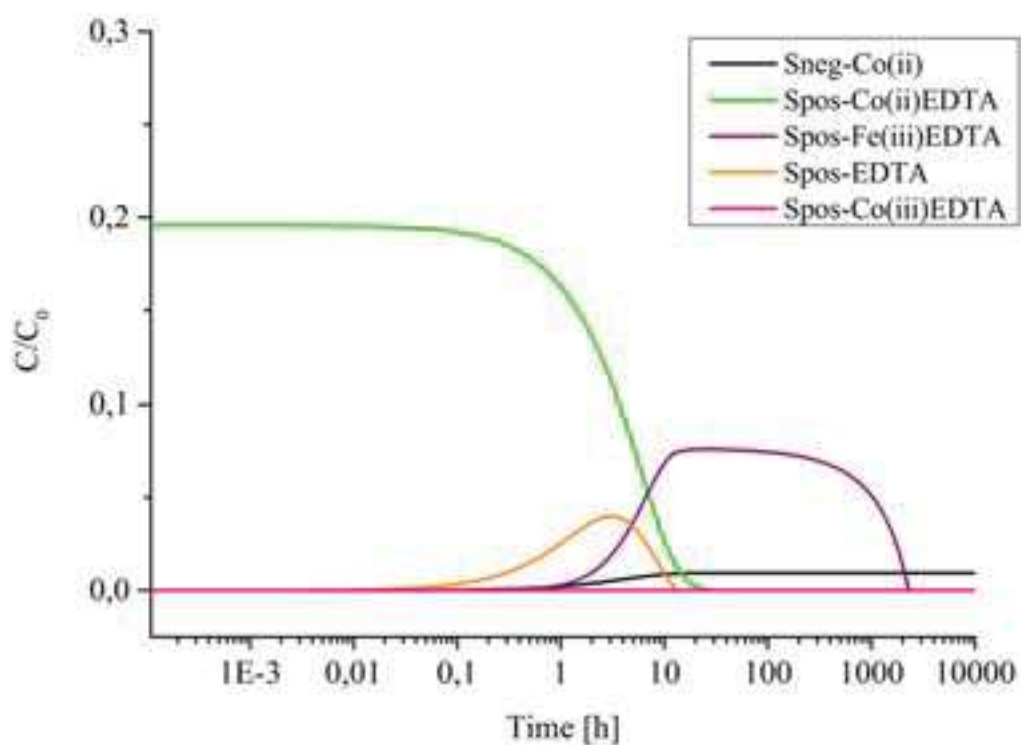
Figure 4.20 – Curves for some of the secondary species obtained with DASPK 1. This formulation of the system allows tracking secondary species, a feature that can be useful while monitoring batch experiments.

As anticipated in paragraph 4.2.1, both explicit and implicit numerical schemes are implemented with an adaptive stepsize. This means that whenever a solution is rejected the stepsize is reduced, and is increased otherwise. What makes a solution accepted or rejected is the meeting of convergence criteria that can be much or less severe. In Figure 4.21, the effect of two different convergence criteria, $ATOL=10^{-6}$ and $ATOL=10^{-12}$ (see paragraph 4.2.3), in the DASPK solver on the amplitude (and therefore the number) of stepsizes.
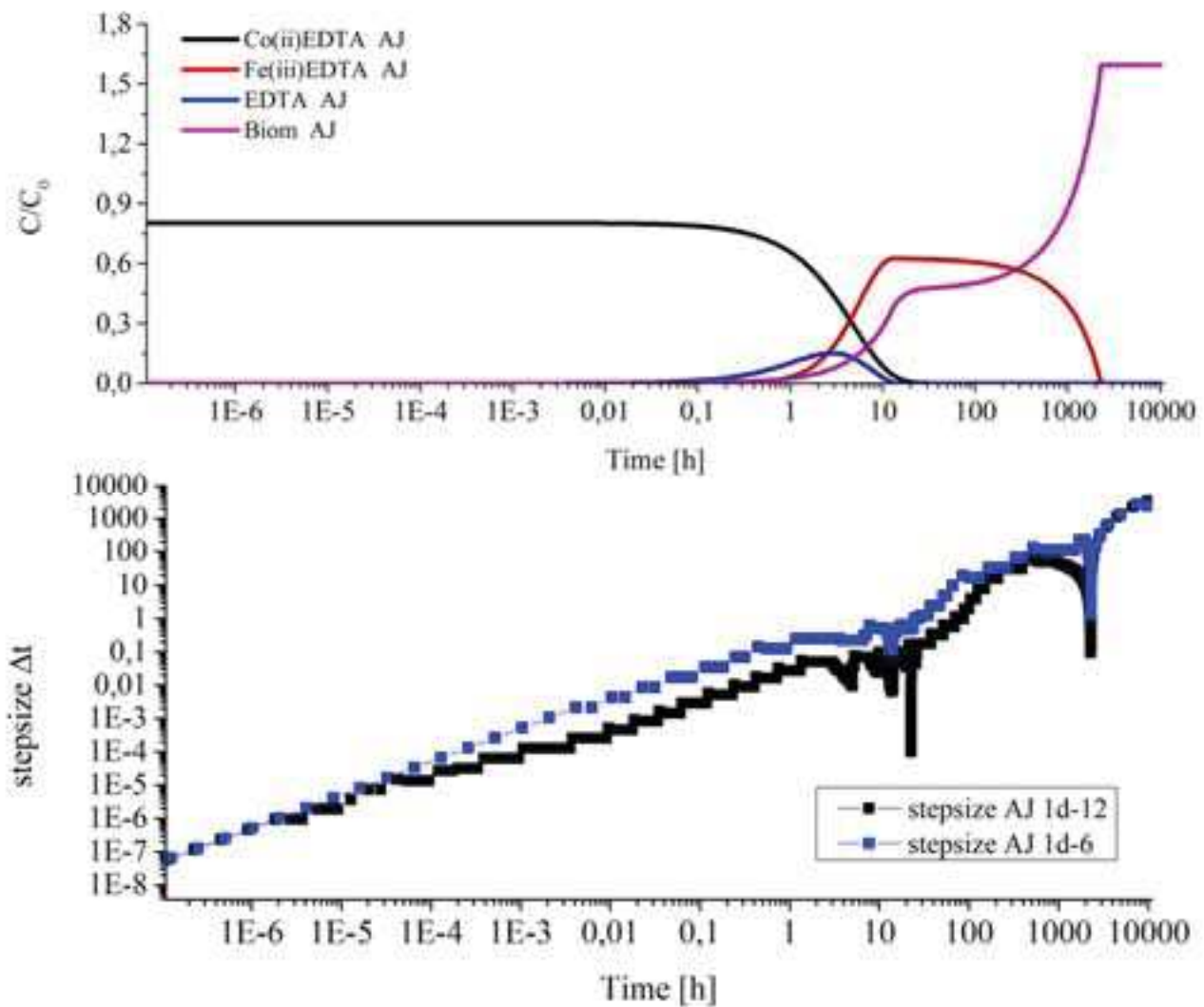
Figure 4.21 – Effect of different convergence criteria on the stepsize amplitude in DASPK1 (Analytical Jacobian) towards the solution of the problem.

With the absolute tolerance of ATOL = 10^{-6} (blue squares) the increase of the stepsize is constant and the stepsize is systematically higher than the one computed to satisfy ATOL = 10^{-12}. When, at around 20 h from the beginning of the experiment, EDTA and CO(II)EDTA are completely consumed (reaction rate R_{10} goes to zero), the time step is reduced to ensure required accuracy. The same happens at around 2000 h when the system runs out of Fe(III)EDTA (reaction rate R_9 goes to zero).

RICHARDSON TOL	TIME STEPS	CPU
10^{-12}	67010000	3602,65
10^{-9}	2110000	107,37
10^{-8}	670000	35,45
10^{-7}	210000	11,59
10^{-6}	60000	4,69
10^{-5}	20000	1,51
10^{-4}	9953	0,702

Table 4.8 – Number of time-steps and CPU time varying with the required tolerances for Richardson extrapolation of QSSA method

DASPK 1 TOL NUM	TIME STEPS	RES EVAL	NL ITER	CPU
A 10^{-12} R 10^{-14}	1427	3871	2202	4.83 10^{-2}
A 10^{-11} R 10^{-13}	1030	2830	1537	3.57 10^{-2}
A 10^{-10} R 10^{-12}	752	2396	1179	2.98 10^{-2}
A 10^{-9} R 10^{-11}	509	2020	833	2.52 10^{-2}
A 10^{-8} R 10^{-10}	336	1690	533	2.07 10^{-2}
A 10^{-7} R 10^{-9}	258	1500	463	1.86 10^{-2}
A 10^{-6} R 10^{-8}	177	1274	327	1.56 10^{-2}

DASPK 1 TOL AN	TIME STEPS	RES EVAL	NL ITER	CPU
A 10^{-12} R 10^{-14}	1418	2217	2213	2.96 10^{-2}
A 10^{-11} R 10^{-13}	1081	1645	1642	2.23 10^{-2}
A 10^{-10} R 10^{-12}	832	1298	1296	1.75 10^{-2}
A 10^{-9} R 10^{-11}	509	836	834	1.15 10^{-2}
A 10^{-8} R 10^{-10}	336	535	533	7.49 10^{-3}
A 10^{-7} R 10^{-9}	258	465	463	6.55 10^{-3}
A 10^{-6} R 10^{-8}	177	329	327	4.84 10^{-3}

Table 4.9 – Number of time-steps, residual evaluations, number of non-linear iterations and CPU time varying with the required tolerances for DASPK1, system of *Nc+Ncc* equations

DASPK 3 TOL NUM	TIME STEPS	RES EVAL	NL ITER	CPU
A 10^{-12} R 10^{-14}	1407	2915	2003	2.87 10^{-2}
A 10^{-11} R 10^{-13}	962	2346	1474	2.32 10^{-2}
A 10^{-10} R 10^{-12}	643	1842	970	1.78 10^{-2}
A 10^{-9} R 10^{-11}	467	1585	743	1.54 10^{-2}
A 10^{-8} R 10^{-10}	331	1427	555	1.39 10^{-2}
A 10^{-7} R 10^{-9}	258	1177	415	1.15 10^{-2}
A 10^{-6} R 10^{-8}	168	1035	293	1.01 10^{-2}

DASPK 3 TOL AN	TIME STEPS	RES EVAL	NL ITER	CPU
A 10^{-12} R 10^{-14}	1353	1928	1926	1.99 10^{-2}
A 10^{-11} R 10^{-13}	961	1470	1468	1.53 10^{-2}
A 10^{-10} R 10^{-12}	642	959	957	9.83 10^{-3}
A 10^{-9} R 10^{-11}	467	741	739	7.80 10^{-3}
A 10^{-8} R 10^{-10}	331	554	552	6.24 10^{-3}
A 10^{-7} R 10^{-9}	258	417	415	4.83 10^{-3}
A 10^{-6} R 10^{-8}	168	295	293	3.59 10^{-3}

Table 4.10 – Number of time-steps, residual evaluations, number of non-linear iterations and CPU time varying with the required tolerances for DASPK3, system of $Nx+Ncc$ equations

As for the previous test case, an analysis of the number of the time steps and of the CPU time of different solvers and different configurations of a given solver varying absolute and relative tolerances is proposed. Again, the analysis started from values of absolute tolerance (ATOL) of 10^{-12} and relative tolerance (RTOL) of 10^{-14}, then tolerances were increased by one order of magnitude at a time.

Also for this test case, all tests were performed with a version of the code compiled in Release mode in order to avoid slow computations typical of the execution in Debug mode and CPU time was computed as a mean value of 100 problems for DASPK. The content of Table 4.8, Table 4.9 and Table 4.10 in graphic form is reported in Figure 4.22. Although convergence criteria in Richardson extrapolation of QSSA method and in DASPK solver work differently and cannot be directly compared, they are studied in their respective reasonable ranges. From Figure 4.22c it is clear that the explicit solver requires a higher number of time-steps to converge with respect to the implicit. One might argue that a higher number of time steps do not necessarily imply higher computational cost, but in Figure 4.22d it is shown that even though an explicit time-step might be faster than an implicit, the global result is that explicit QSSA converges globally slowly. Figure 4.22d also puts in evidence that although the numerical and analytical computations of the Jacobian matrix (for DASPK1) don't affect the number of time steps (Figure 4.22c, which confirms the rightfulness of the analytical Jacobian)
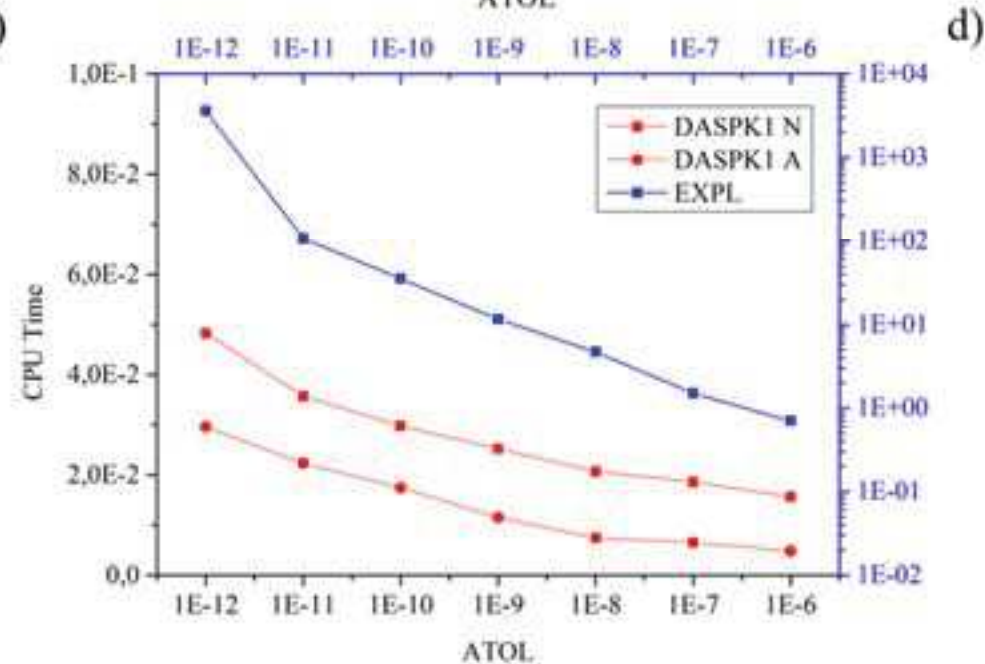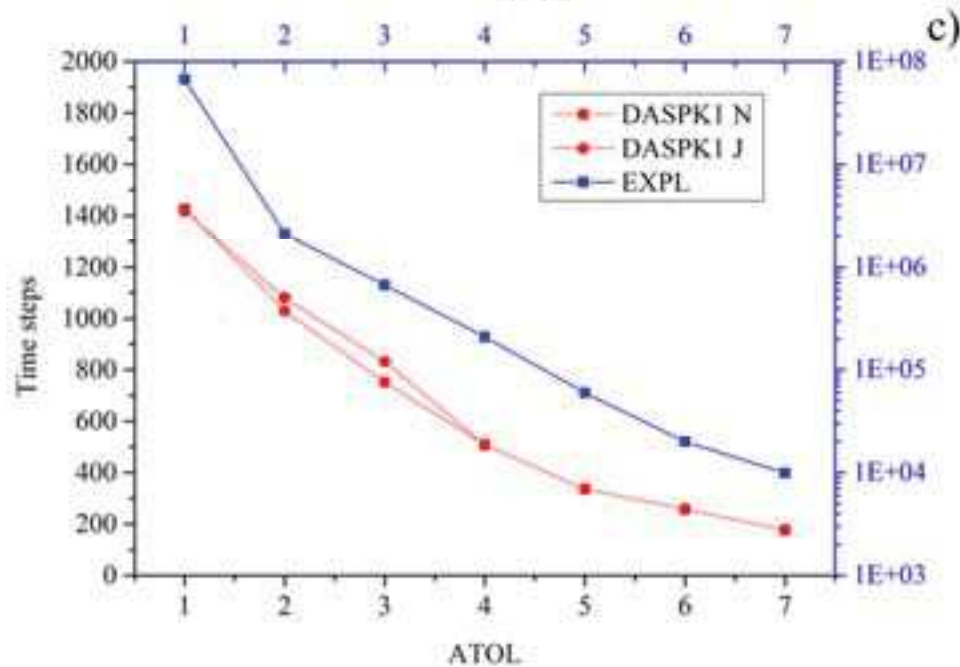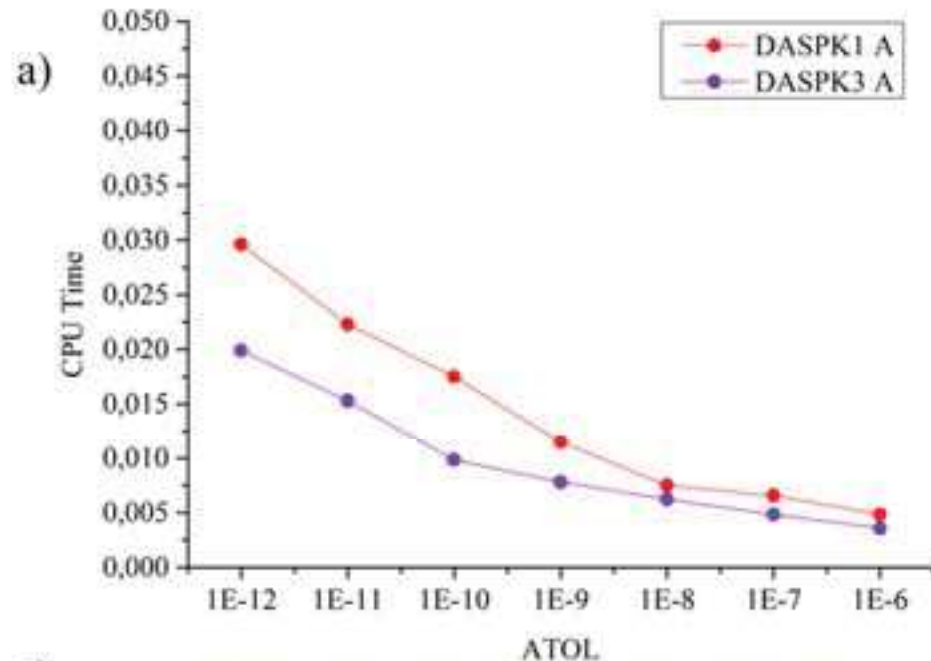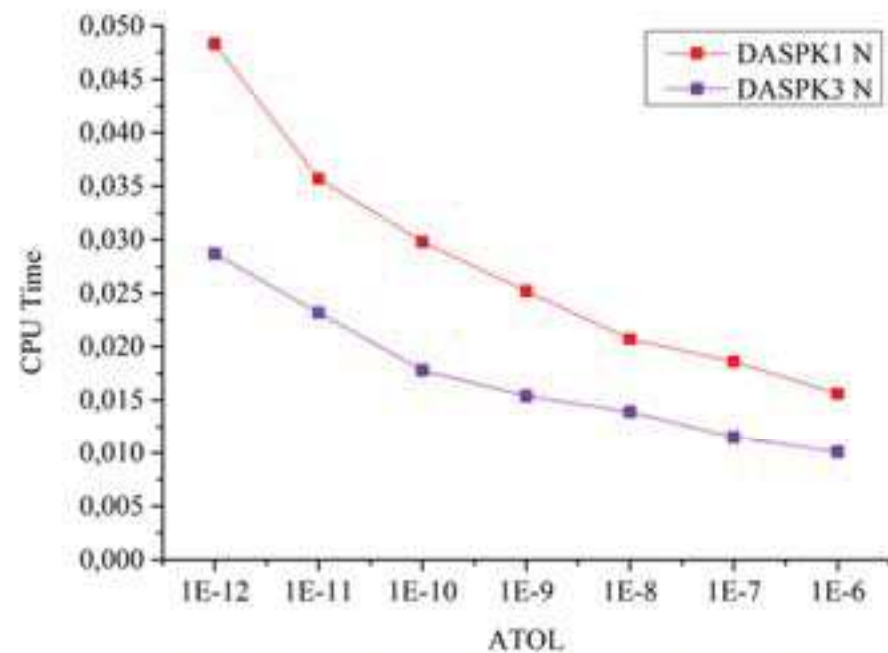
Figure 4.22 – CPU time required to converge for DASPK 1 and DASPK 3 with numerical a) and analytical b) computation of the Jacobian matrix; number of time-steps c) and CPU time d) required to converge for explicit QSSA and implicit BDF in DASPK 1; note different scales.

convergence is faster with the analytical Jacobian. This is certainly due to the number of residual evaluations that is sensibly smaller when computing the Jacobian analytically. Figures 4.22a and 4.22b, on the other hand, show the comparison between the CPU time required to solve the problem with DASPK 1 and DASPK 3 with numerical and analytical Jacobian matrix respectively. In both cases, DASPK 3 solves the problem faster than DASPK 1, especially at higher precisions. The difference between these results and those in 4.3.1 (where DASPK1 computed solutions faster than DASPK 3) is probably due to the absence of activity coefficients in the Chilakapati test case. The absence of activity coefficients avoids problems linked to neglecting them when they are actually there, especially when they should be derived.

4.4 Conclusions about mixed equilibrium and kinetics

In this Chapter the problem of mixed equilibrium and kinetic reactions was approached with two different strategies: one based on mathematical considerations the other on a representation of the processes. Three ways of writing the system were proposed: a system of DAEs where mass action laws are left explicit (the algebraic equations are mass action laws), a system of DAEs where mass action laws are written into conservation equations (the algebraic equations are the conservation equations), and a system of ODEs where mass action laws are included in conservation equations, that are written in their differential form. Left aside more advanced strategies to pick primary and secondary species such as in Fang et al. (2003) and Molins et al. (2004), and the possibility of writing such equations in a logarithmic form, the three systems are the three possible alternatives of resulting of equations.

From the two tests performed (easy enough to allow implementation of DASPK from scratch but not trivial from a numerical and mathematical standpoint), it resulted that the first system of DAEs (referred to as DASPK 1) and the system of ODEs (DASPK 3) are the more efficient. Although DASPK 3 is recommended for the reduction of the size of the system, whenever activity coefficients have to be taken into account, approximations of derivatives of complicated equations may slow down convergence.

Certain conclusions are that regardless the version of DASPK applied, the solver is faster than the previous QSSA explicit. Within each formulation of DASPK, the analytical computation of the Jacobian matrix globally outperformed the numerical computation in all circumstances, even when approximations (i.e. neglecting derivatives of activity coefficients) engendered an increase of the number of iterations.

Chapter 5 – Solid solutions

5.1 Introduction and theoretical background

5.1.1 The interest in solid solutions

Solid solutions are homogeneous crystalline structures in which one or more of the original atoms or molecules are substituted in the structure with compatible alternatives. The conceptual description of a solid solution is not far from that of an aqueous multicomponent solution. A multicomponent solution is, in fact, a mix of various species with a fixed stoichiometry that are present in different concentrations. In solid solutions, the role of chemical species is played by the so-called *end-members*: they have a fixed stoichiometry but may be present in different concentrations and their mix is not merely mechanical (Bruno 2007). An example is the binary solid solution $(Sr,Ca)CO_3$ whose end-members are $CaCO_3$ and $SrCO_3$, coexisting in a mixture that could be noted as $(1-x)$ $CaCO_3 + x SrCO_3$, x being the mole fraction of $SrCO_3$. The mole fraction x may vary between 0 (pure Calcite) and 1 (pure Strontianite), and it is determined by the thermodynamic configuration of the system.

Finding pure minerals in actual natural systems is more the exception than the rule, and modeling through precipitation of pure minerals constitutes a simplification. This simplification may be acceptable in many cases but solid solutions remain an essential tool for the modeling of natural processes. For example, following the dissolution of several pure minerals, the subsequent re-precipitation of a disordered mixture may occur. Moreover, circumstances exist in which solid solutions modeling is the only way to reproduce experimental or field data (Ferry et al. 2005).

Solid solutions also constitute a subject of interest in studies of performance assessment for nuclear repository sites. Radionuclides may, in fact, substitute original atoms in host solid phases such as Calcite or C-S-H systems in Ordinary Portland Cement; again, most of the compounds involved in the fuel cycle are considered as solid solutions. Solid solutions are believed to be a fundamental tool in performance assessment at the point that specific guidelines were written on the issue (Bruno 2007).

Another important advantage of solid solutions is that they have the potential to be exploited for modeling geochemical reactions that include isotopes. In fact, the atom of Sr^{2+} that substitutes the one of Ca^{2+} in the solid solution mentioned above might be as well a nuclide of $^{44}Ca^{2+}$ substituting $^{40}Ca^{2+}$. Moreover, whereas the thermodynamics of the so-called *real* solid solutions is rather complicated and hard to model, substitution of isotopes is the closest approximation to an *ideal* solid solution, which is far easier to treat (Anderson and Crerar 1993). In fact, ideal solid solutions inspired a powerful model for stable isotope kinetic fractionation (Wanner and Sonnenthal 2013; Druhan et al. 2013).

5.1.2 Theoretical background: Thermodynamics of solid solutions

Solid solutions are the result of complex structural interactions at atomic and molecular levels and a thermodynamic formulation must take these complexities into account. Gibbs energy (which is supposed to decrease in case of spontaneous reactions (Anderson and Crerar 1993)) for a solid solution of two end-members with composition $Ax,B(1-x),C$ (see equation (5.1)) is equal to the sum of Gibbs energy of the end-members taken separately plus terms due to their mixing (equation (5.2)).

$$xAC + (1-x)BC \Rightarrow A(x)B(1-x)C \tag{5.1}$$
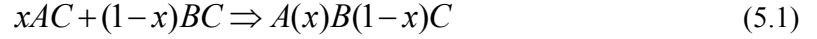
$$\Delta G(SS,T) = xG^0(AC,T) + (1-x)G^0(BC,T) + \Delta G(mix) - RT(x\ln(x) + (1-x)\ln(1-x)) \tag{5.2}$$

where x and $(1-x)$ [-] are the molar fractions of species A and B, G^0 [J/mol] is the Gibbs energy of the pure end-members, $\Delta G(mix)$ [J/mol] is the excess of energy of mixing, R [J/K/mol] is the gas constant and T [K] is the temperature. The first two terms of the right-hand side describe a merely mechanical mixing and the last term is the ideal entropy of mixing. The mixing term $\Delta G(mix)$ may be written as a function of the excess enthalpy ΔH and entropy ΔS of mixing:

$$\Delta G(mix) = \Delta H(mix) - T\Delta S(mix) \tag{5.3}$$

The excess of entropy, which is the deviation from the ideal entropy of mixing appearing in equation (5.2), may be neglected under the assumption of configurational entropy and perfect randomness (Noguera et al. 2016). According to the structural configuration of the solid solution (if, for example, the substituted and substituting atoms are nearly alike) variations in volume may be neglected and the enthalpy of mixing can be also considered zero. If this is the case, the solid solution is defined *ideal*, otherwise, the solid solution is *real* and ΔH(mix) can be written as a function of Guggenheim expansions (Glynn 1990). Details of how ideal (and real) solid solutions are described through activities and mole fractions can be found, for example, in Anderson and Crerar (1993).

Ideality has an impact on the computation of the *activities* of the end-members. In fact, whereas the activity of a pure mineral is considered equal to 1, this is not the case for end-members in solid solutions; for ideal solid solutions, activities of the end-members are equal to their molar fractions:

$$a_{EM} = x_{EM} \tag{5.4}$$

while for real solid solutions an activity coefficient λ_{EM} is needed and could be written for example, as a function of the Guggenheim expansions mentioned before:

$$a_{EM} = \lambda_{EM} x_{EM} \qquad (5.5)$$

A comprehensive analysis of solid solution thermodynamics is beyond the scope of this work; interested readers should refer to the available, extensive literature (Lippman 1977; Thorstenson and Plummer 1977; Tardy and Fritz 1981; Lippman 1980; Plummer and Busenberg 1987; Glynn 1990; Glynn and Reardon 1990; Glynn 1991; Glynn et al. 1992; Königsberger and Gamsjäger 1990; Königsberger and Gamsjäger 1992; Anderson and Crerar 1993; Glynn 2000; Gamsjäger et al. 2000; Bruno 2007).

5.1.3 Modeling solid solutions and their interaction with the aqueous phase

Standard forward chemical modeling may be carried out through two different approaches: Gibbs free energy minimization (e.g. Kulik et al. 2012 and Leal et al. 2014) or mass action law models (e.g. Parkhurst et al. 1999 and Steefel 2009). According to Bruno (2007) modeling solid solutions interaction with aqueous phase through Gibbs energy minimization should be preferred since this approach is considered more rigorous and theoretically based. Always according to (Bruno 2007), the implementation of solid solutions (at equilibrium) into mass action law codes is considered cumbersome and empiric at the point that the Geochemists Workbench GWB (Bethke 2008) amongst others recommend to avoid it.

On the other hand, other world-known mass action law based codes such as PHREEQC (Parkhurst et al. 1999) are able to treat ideal and real binary solid solutions. In a local (but not less effective) context, numerical models KINDIS (Madé et al. 1994) and KIRMAT (Gérard et al. 1998) treat complex mineral precipitation at equilibrium with ideal and real binary solid solutions.

Attempts to take into account kinetic processes in solid solution formation also exist: an extension of numerical model KINDIS (Nourtier-Mazauric et al. 2005) has been performed and (Lichtner and Carey 2006) proposed a discretization of the solid solution considering only a finite number of compositions (a grid over the composition space). A step further in the understanding solid solution nucleation is the module implemented in the code NANOKIN (Noguera et al. 2010), which started treating only ideal binary solid solutions; an extension to real binary solid solutions (Noguera et al. 2016) has been studied but still not implemented in the code.

As mentioned in the introduction, the concept of solid solutions has also inspired a powerful tool for modeling kinetic stable isotope fractionation; the model has been implemented in world-known codes for reactive transport modeling such as CRUNCHFLOW, TOUGHREACT, FLOTRAN and MIN3P

(Wanner et al. 2015). Although the approach is considered as effective for the simulation of stable kinetic isotope fractionation, it shouldn't be mistakenly considered as a theoretically-based way to treat solid solutions kinetically to a more general extent.

5.1.3.1 Equilibrium models for solid solutions

Considered that the code object of this work has been built on a mass action law approach, implementing solid solutions with a Gibbs energy minimization is not an option. Solid solutions at thermodynamic equilibrium were implemented following the example of codes KINDIS and PHREEQC. Although the algorithms are implemented slightly differently in PHREEQC and KINDIS, equation (5.6) has to be respected in both models. For each end-member, the following mass action law is verified at thermodynamic equilibrium (P. D. Glynn 1990):

$$K_{EM} = \frac{Q_{EM}}{a_{EM}} = \frac{Q_{EM}}{\lambda_{EM} x_{EM}} = \frac{Q_{EM}}{\lambda_{EM} \dfrac{Xss_{EM}}{Xss_{TOT}}} \quad EM = 1,...,N_{EM} \tag{5.6}$$

where Q_{EM} is the ion activity product of the species involved in the precipitation of the mineral/end-member EM, K_{EM} is the solubility product for the mineral/end-member in its pure phase, λ_{EM} is the activity coefficient of the end-member and Xss_{TOT} is the total amount of solid solution ([mol]). As mentioned in the previous paragraph, when solid solutions are treated as ideal, λ_{EM} is set to 1.0. If the solid solution is considered non-ideal, the parameter might be computed according to models (for example derived from Guggenheim expansion series (Glynn 1990; Glynn and Reardon 1990)). Equation (5.6) is true for each end-member EM of the N_{EM} end-members that participate in the solid solution.

At this point, it is worth mentioning that thermodynamic equilibrium as in equation (5.6) is not the only thermodynamic state of interest in studying the interaction between an aqueous and a solid solution. Thorstenson and Plummer (1977) suggested that under the hypothesis of i) a short equilibration period ii) a high ratio solid/liquid phase iii) low temperature and iv) consequent absence of recrystallization or precipitation, the dissolution of a solid solution could be treated as the dissolution of a pure phase, naming this approximation *stoichiometric saturation*. Equation (5.7) describes stoichiometric saturation for the binary solid solution $(Sr,Ca)CO_3$ introduced before, where x is the mole fraction of Sr^{2+}, Q_{ss} the ionic product in the solution and K_{ss} is the equilibrium constant for the solid solution:

$$K_{ss} = \frac{\left\{Sr^{2+}\right\}^{x}\left\{Ca^{2+}\right\}^{1-x}\left\{CO_3^{2-}\right\}}{1} = Q_{ss} \tag{5.7}$$

Another thermodynamic state of interest is the so-called *primary saturation*. It occurs when a solid solution dissolves and the aqueous solid solution is at thermodynamic equilibrium with another (secondary) solid solution. Glynn and Reardon (1990) focus on the distinction between actual thermodynamic equilibrium, primary saturation and stoichiometric saturation; however, these last two models are not treated in this work.

Going back to actual thermodynamic equilibrium, directly from equation (5.6), for an ideal solid solution at thermodynamic equilibrium, we have:

$$\sum_{EM=1}^{N_{EM}} x_p = \sum_{EM=1}^{N_{EM}} \frac{Q_{EM}}{K_{EM}} = \sum_{EM=1}^{N_{EM}} SI_{EM} = 1.0 \qquad (5.8)$$

where SI_{EM} is the solubility index of end-member EM and x_{EM} its mole fraction. Equations (5.6) and (5.8) define the condition of solid solutions at equilibrium; how can they be exploited in an algorithm to determine aqueous concentrations and mole fractions in the solid phase? Starting from the assumption that, given an aqueous solution, the solid solution is not present, equilibrium is computed once and a test is performed afterward. Equation (5.8) works as a criterion of existence of the solid solution whenever:

$$\sum_{EM=1}^{N_{EM}} \frac{Q_{EM}}{K_{EM}} \geq 1.0 \qquad (5.9)$$

If equation (5.9) is satisfied, the assumption of non-existence is wrong and a solid solution exists. Otherwise, the assumption is correct and no solid solution is formed. It's interesting to stress how the criterion accounting for the existence/non-existence of the solid solution is based on the combination of solubility indexes of all involved minerals and that there is no threshold to be satisfied on the amount of a single mineral/end-member. In fact, at thermodynamic equilibrium, none of the end-members is supersaturated (P. D. Glynn 1990). This characteristic could be exploited while treating isotopes, which are present in traces and would never be supersaturated if treated as a single mineral. Whenever the solid solution exists, a series of new unknowns Xss_{EM} (with $p=1, N_{EM}$) for each involved solid solution has to be computed. The actual number of unknowns is:

$$N_{Xss} = \sum_{i=1}^{Nss} N_{EM\_i} \qquad (5.10)$$

where Nss is the number of existing solid solutions and N_{EM_i} is the number of end members of solid solution i. Consequently, N_{Xss} equations have to join the nonlinear system **Y=0** presented in Chapter 3.

116

From now on, we will consider the interaction of the aqueous solution with only one solid solution, therefore $Nss=1$ and N_{EM} additional unknowns Xss_{EM}. For each end-member, an equation similar to equation (5.6) is added to the system. In order to simplify the computational burden and be coherent with the logarithmic formulation of Chapter 3, equation (5.6) is implemented in the following logarithmic form:

$$Y_{EM} = \ln\left(\frac{Q_{EM}}{K_{EM}}\right) - \ln\left(\lambda_{EM}\frac{Xss_{EM}}{Xss_{TOT}}\right) = 0 \quad EM = 1,...,N_{EM} \tag{5.11}$$

Where Y_{EM} is the residual function associated to end member EM, $Xss_{TOT} = \sum_{EM=1}^{N_{EM}} Xss_{EM}$ is the number of moles in the solid solution (and all other symbols are defined above). The nonlinear system takes the following dimensions: ($N_X + N_{Cp} + N_{Xss}$) equations for ($N_X + N_{Cp} + N_{Xss}$) unknowns. Although equation (5.11) is the only extension in the size of the system and the number of equations is now equal to the number of unknowns, further modifications to the system **Y=0** are required. In fact, each unknown Xss_{EM} accounts for some mass that must be included in mass conservation equations. The mass conservation equation for a generic primary species becomes:

$$Y_j = \left[\tilde{T}_j\right] - \sum_{i=1}^{Nc}\frac{b_{i,j}}{\gamma_i}\exp\left(\ln(K_i) + \sum_{k}^{N_X}b_{i,j}\xi_k\right) - \sum_{l=1}^{Ncp}bp_{l,j}\left[Cp_l\right] - \sum_{EM=1}^{Nss}\sum_{EM=1}^{N_{EM}}bss_{EM,j}Xss_{EM} = 0 \quad j = 1,...,N_x$$
$$\text{(5.12)}$$

Given that the nonlinear system is going to be solved through Newton Raphson method, and that this method implies the computation of the Jacobian matrix, modifications of the size and content of the system imply modifications of the Jacobian matrix. Considered that the size of the matrix corresponds to the number of unknowns, an increase in the number of unknowns results in an increase of the size of the matrix, which now becomes ($N_X + N_{Cp} + N_{Xss}$) rows for ($N_X + N_{Cp} + N_{Xss}$) columns. New rows and columns of the Jacobian matrix have to be filled. In the first N_X rows, mass conservation equations such as equation (5.12) must be derived with respect to new unknowns Xss_{EM}:

$$\frac{\partial Y_j}{\partial Xss_{EM}} = bss_{j,EM} \tag{5.13}$$

At the same time, new residual functions such as equation (5.11) must be derived with respect to old ($\xi_j = ln(\{X_j\})$ where $\{X_j\}$ is the activity of jth primary species) and new (Xss_{EM}) unknowns:

$$\frac{\partial Y_{Xss_{EM}}}{\partial \xi_j} = bss_{j,EM}$$

$$\left.\frac{\partial Y_{Xss_{EM}}}{\partial Xss_i}\right|_{i \neq EM} = \frac{1}{Xss_{TOT}}$$

$$\left.\frac{\partial Y_{Xss_{EM}}}{\partial Xss_i}\right|_{i = EM} = \frac{1}{Xss_{TOT}} - \frac{1}{Xss_{EM}}$$

(5.14)

To conclude this section, it must be mentioned that a number of solid solutions may coexist, while an end-member cannot coexist with a pure mineral of the same stoichiometric composition (because of equation (5.8), the end-member will precipitate systematically before the pure phase reaches saturation).

5.1.3.2 Kinetic models for solid solutions

Whereas solid solutions at different equilibrium stages have been studied in details, kinetic models for solid solutions are a more recent topic of interest. A number of experimental works have provided information about solid solution nucleation and growth (Prieto et al. 1997; Sánchez-Pastor et al. 2006) but the development of kinetic models is still ongoing. For instance, in the guidelines for nuclear waste repositories performance assessment (Bruno 2007), only a small paragraph is dedicated to a possible kinetic approach to solid solutions.

In both the works of Nourtier-Mazauric (2005) and Lichtner and Carey (2006), transition state theory (TST) for precipitation/dissolution rates is introduced and applied to solid solutions, although always with a fixed composition. In Nourtier-Mazauric (2005), a unique reaction rate is established for the solid solution and in Lichtner and Carey (2006), a solid solution of variable composition is substituted with a grid of solid solutions of fixed composition treated as pure minerals.

5.1.3.3 Exploiting solid solutions concept for stable kinetic isotope fractionation

The expression "solid solutions" related to stable kinetic isotope fractionation first appears in Druhan (2012), Druhan et al. (2013) and Wanner and Sonnenthal (2013). Models in these works are strongly inspired by the work of DePaolo (2011), who, nevertheless, never talks about "solid solutions".

Druhan (2013) starts from the classical transition state theory (TST) for Calcite precipitation (see equation (5.15), where r_f and r_b are the forward and backward rates, k_f and k_b are forward and

backward kinetic constants, a_i is the activity of the chemical species, r_{net} is the global rate of the reaction, $K_s = k_b / k_f$ is the solubility product). While the activity coefficient of a mineral pure phase is usually considered equal to *1.0*, this is not the case for solid solution treat (Anderson and Crerar 1993). For *ideal* solid solutions (simplification that is justified in that different nuclides are the closest approximation to an ideal solid solution) equation (5.4) is valid and the solid activities may be substituted with the mole fractions in the solid.

$$
\begin{aligned}
r_f &= k_f \left\{ Ca^{2+} \right\} \left\{ CO_3^{2-} \right\} \\
r_b &= k_b \left\{ CaCO_3 \right\} \\
r_{net} = r_f - r_b &= k_b \left\{ CaCO_3 \right\} \left(\frac{\left\{ Ca^{2+} \right\} \left\{ CO_3^{2-} \right\}}{K_S \left\{ CaCO_3 \right\}} - 1 \right)
\end{aligned}
\tag{5.15}
$$

Therefore, two equations may be rewritten for the two Calcium isotopes $^{40}Ca^{2+}$ and $^{44}Ca^{2+}$, which are then considered as two end members of a solid solution, each one with its own kinetic constant:

$$
\begin{aligned}
{}^{40}r_{net} &= {}^{40}k \, {}^{40}x \left(\frac{\left\{ {}^{40}Ca^{2+} \right\} \left\{ CO_3^{2-} \right\}}{K_S \, {}^{40}x} - 1 \right) \\
{}^{44}r_{net} &= {}^{44}k \, {}^{44}x \left(\frac{\left\{ {}^{44}Ca^{2+} \right\} \left\{ CO_3^{2-} \right\}}{K_S \, {}^{44}x} - 1 \right)
\end{aligned}
\tag{5.16}
$$

According to the situation, different models for the molar fraction x can be adopted. Equations (5.16) (also presented in their second-order variant) proved extremely efficient in describing Calcium fractionation when implemented in code CrunchFlow.

A slightly different implementation of the same concept (i.e. assimilating the different minerals containing different isotopes to end-members of a solid solution) was performed in the same year (Wanner and Sonnenthal 2013) in the numerical model TOUGHREACT (Xu et al. 2011) to reproduce Chrome fractionation.

Chrome fractionation was used before to prove the effectiveness of another model implemented in MIN3P (Jamieson-Hanes et al. 2012); although "solid solutions" are never mentioned in the work, the model is similar to those of Druhan et al. (2013) and Wanner and Sonnenthal (2013). In fact, MIN3P considers precipitation of the two different isotopes as the precipitation of the same mineral with two different rates:

$$^{40}r_{net} = {}^{40}k \left(\frac{\{Ca^{2+}\}\{CO_3^{2-}\}}{K_S} - 1 \right)$$

$$^{44}r_{net} = {}^{44}k \left(\frac{\{Ca^{2+}\}\{CO_3^{2-}\}}{K_S} - 1 \right)$$

(5.17)

The difference between the two reaction rates is ensured by two different kinetic coefficients (that are not constant, but functions of the isotopic ratio):

$$^{40}k = \frac{k_{Bulk}}{1 + R({}^{44}Ca / {}^{40}Ca)}$$

$$^{44}k = \frac{k_{Bulk} R({}^{44}Ca / {}^{40}Ca)}{1 + R({}^{44}Ca / {}^{40}Ca)}$$

(5.18)

where k_{Bulk} is the kinetic constant for $CaCO_3$ and R is the isotopic ratio. While establishing a benchmark through codes CrunchFlow, TOUGHREACT, FLOTRAN, and MIN3P (Wanner et al. 2015) write that all codes embed kinetic solutions to treat precipitation of different isotopes.

5.2 Numerical simulations of solid solutions

5.2.1 Modeling solid solutions at thermodynamic equilibrium

5.2.1.1 Verification with PHREEQC

A partial verification of the correct implementation of the algorithm treating thermodynamic equilibrium between an aqueous and a solid solution was performed following the evolution of an Aragonite Strontianite $((Sr,Ca)CO_3)$ ideal solid solution with both SpeCTr (the reactive transport code resulting from the reaction module developed through Chapter 3,4,5 and a transport module detailed in Chapter 6) and PHREEQC. The case study simulates the evolution of an ideal solid solution constituted of two end-members: Aragonite (which has the same stoichiometry of Calcite, $CaCO_3$, but a different molecular structure) and Strontianite $(SrCO_3)$. The setup of the numerical experiment is the following: an aqueous solution with only Calcium and Carbon gradually receives $SrCO_3$ contributions and $CaCO_3$ becomes the end-member of the forming solid solution. Input quantities for SpeCTr and PHREEQC are reported in Table 5.1 (input files are built differently) while equilibrium constants are provided in Table 5.2.

	SpeCTr			PHREEQC	
T_{Ca}	$3.932 \ 10^{-3}$	mol/Kg$_{H2O}$	T_{Ca}	$3.932 \ 10^{-3}$	mol/Kg$_{H2O}$
T_{H2O}	55.5	mol/Kg$_{H2O}$	T_C	$7.864 \ 10^{-3}$	mol/Kg$_{H2O}$
T_{CO3}	$7.864 \ 10^{-3}$	mol/Kg$_{H2O}$	pH	7.0	
T_{H+}	$7.864 \ 10^{-3}$	mol/Kg$_{H2O}$			
T_{Sr2+}	10^{-5}	mol/Kg$_{H2O}$			

Table 5.1 – Total aqueous concentrations for batch solid solution experiment.

Equilibrium constants	
$Log_{10}K_{CaCO3}$	-8.336
$Log_{10}K_{SrCO3}$	-9.271

Table 5.2 – Equilibrium constants for solid solution end-members Aragonite $(CaCO_3)$ and Strontianite $(SrCO_3)$.

$SrCO_3$ is gradually added to the system, starting from a negligible concentration and arriving to 1.0 mol/Kg$_{H2O}$. In the code SPECY, contributions of $SrCO_3$ (actually, contributions of total concentrations

of components, T_{Sr2+} and T_{CO32-}) are added through *titration* module over 100 steps on a logarithmic scale ranging from a negligible value to 1 mol/Kg_{H2O}. In PHREEQC, on the other hand (the code does not allow to add on a logarithmic scale), $SrCO_3$ was administrated at irregular intervals (from 0 to 0.005 mol/Kg_{H2O} in 500 steps, then from 0.005 to 0.1 mol/Kg_{H2O} in 20 steps and then from 0.1 to 1 mol/Kg_{H2O} in 20 steps); the input file of PHREEQC is available in Annex IV.

Figure 5.1 shows the results provided by PHREEQC and SpeCTr, especially the evolution of the composition of the solid solution throughout the simulation: continuous black (Aragonite) and red (Strontianite) lines represent solutions obtained with SpeCTr, black and red squares represent results obtained with PHREEQC.
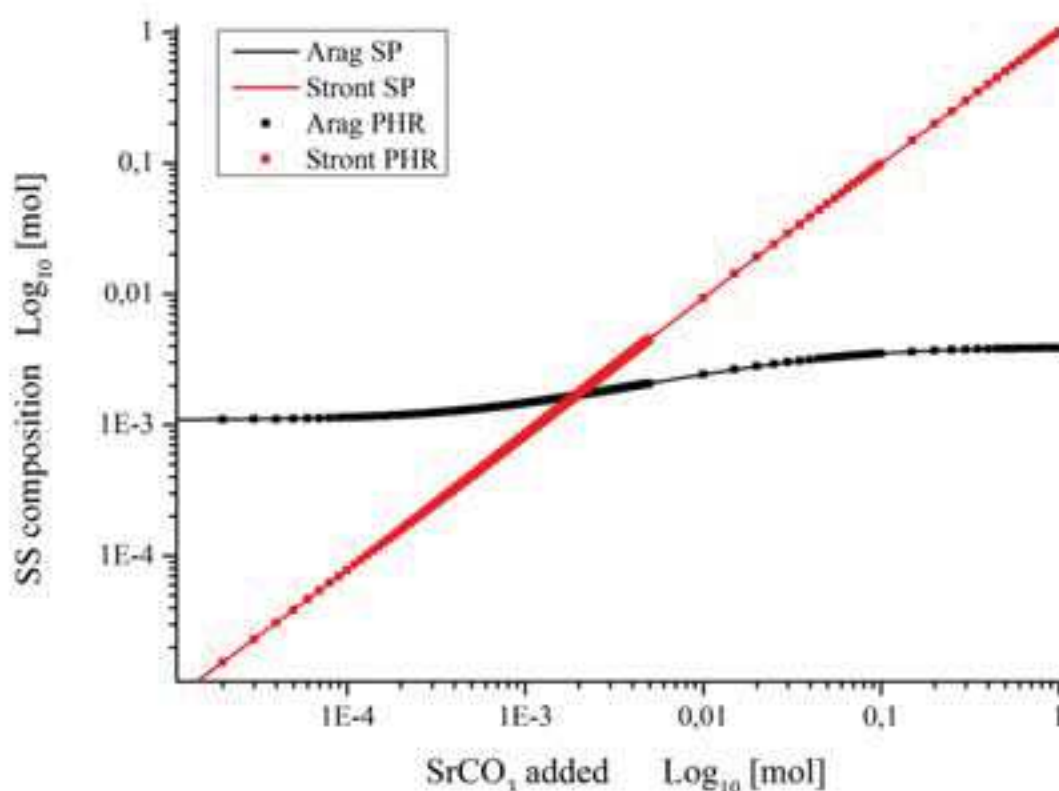
Figure 5.1– Graphic representation of the evolution of the number of moles of Aragonite ($CaCO_3$) and Strontianite ($SrCO_3$) end-members vs. the number of moles of $SrCO_3$ added in the system; results are obtained with both SpeCTr (continuous lines) and PHREEQC (squares).

This example shows that the algorithm introduced in paragraph § 5.1.3 was successfully implemented in the code (major mistakes in the implementation would prevent the solution to converge). Limitation to ideal solid solutions could be easily removed re-introducing λ_p activity coefficients in equation (5.6) for real (binary) solid solutions. The code is now equipped to potentially treat dissolution and precipitations of multiple solid solutions with multiple poles at thermodynamic equilibrium; these features could be exploited for both classic and isotopic chemistry.

122

5.2.1.2 Fe-Cr redox reaction, a reactive transport example

The following reactive transport example involves precipitation of a Fe-Cr solid solution. It is presented in order to provide another application of the algorithm described in paragraph § 5.1.3.1, in conditions that are numerically different from the $(Sr,Ca)CO_3$ solid solution in batch reactor. The aim is purely to show that the algorithm converged and that provided solutions compatible with experimental results; the choice of parameters used in the model is beyond the scope of this chapter.

The problem involves Fe-Cr redox reaction with consequent precipitation of a solid phase, modeled as a solid solution at thermodynamic equilibrium. Results were obtained and presented by Dr. Jérôme Carrayrou at *MAMERN VII–2017 International Conference on Approximation Methods and Numerical Modeling in Environment and Natural Resources*.
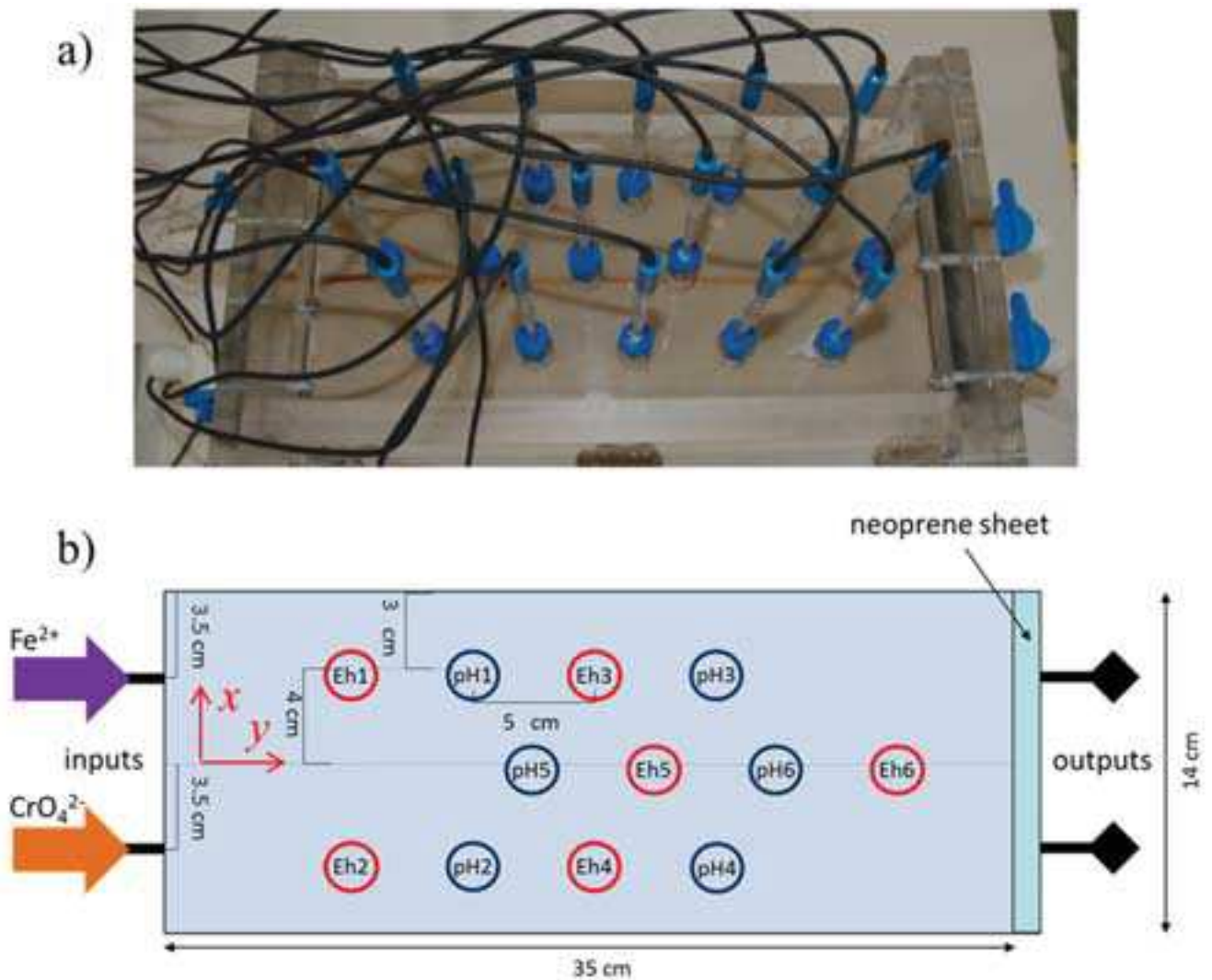
Figure 5.2 – Photo a) and schema b) of the experimental setup of the Fe-Cr redox reaction.

The simulation reproduced a laboratory scale experiment in which two solutions are injected into a porous medium (ϕ_0=0.35, porosity is considered variable) through separate tubes at the inlet: a Cr(VI) solution (3.0 10^{-3} mol/L) is injected in the $x < 0$ part of the domain, while in the $x > 0$ part is injected a Fe(II) solution (9.0 10^{-3} mol/L); precipitation occurs at the interface, generating a solid phase composed at around 75% of Fe and 25 % of Cr. Figure 5.2 shows the experimental setup and the locations of pH and Eh in situ measurements (pH1-pH6, electric potential, Eh1-Eh6) during the experiment (980 min).

Parameter	Value	Unit
Porosity ϕ	0.35	[-]
Conductivity	10^{-3}	[cm/min]
V_x	0.5	[cm/min])
α_L	0.1	[cm]
α_T	0.05	[cm]
D	10^{-4}	[cm^2/min]

Table 5.3 – Main flow and transport parameters used in the Fe-Cr solid solution simulation.

For the numerical simulations, the domain has been discretized with two different meshes, one of square cells of 5mm side and the other of 1 mm side. From a chemical point of view, the experiment is modeled through 44 chemical species represented by 9 primary species; the minerals are allowed to precipitate are FeOOH and CrOOH. The two minerals were modeled as end-members of a binary solid solution, principle reactions are resumed in the Morel table (Table 5.4).

	H+	e-	Fe++	CrO4--	K+	SO4--	H$_2$CO$_3$	Cl-	SiO$_{2(aq)}$	K$_{EQ}$
H+	1	0	0	0	0	0	0	0	0	1.0
Fe++	0	0	1	0	0	0	0	0	0	1.0
CrO4--	0	0	0	1	0	0	0	0	0	1.0
K+	0	0	0	0	1	0	0	0	0	1.0
SO4--	0	0	0	0	0	1	0	0	0	1.0
HCO3-	-1	0	0	0	0	0	1	0	0	1.0
Cl-	0	0	0	0	0	0	0	1	0	1.0
OH-	-1	0	0	0	0	0	0	0	0	1.0 10^{-14}
O2	-4	-4	0	0	0	0	0	0	0	1.48 10^{-85}
H2	2	2	0	0	0	0	0	0	0	1.0
H2O2	-2	-2	0	0	0	0	0	0	0	1.0 10^{-59}

Species										Constant
H2CO3	0	0	0	0	0	0	1	0	0	1.0
CO3--	-2	0	0	0	0	0	1	0	0	$2.51\ 10^{-17}$
HSO4-	1	0	0	0	0	1	0	0	0	$9.44\ 10$
H2SO4	2	0	0	0	0	1	0	0	0	$9.53\ 10^{-2}$
SiO2(aq)	0	0	0	0	0	0	0	0	1	1.0
FeOH+	-1	0	1	0	0	0	0	0	0	$4.84\ 10^{-10}$
FeOOH-	-3	0	1	0	0	0	0	0	0	$6.2\ 10^{-30}$
Fe(OH)2	-2	0	1	0	0	0	0	0	0	$2.51\ 10^{-22}$
FeHCO3+	-1	0	1	0	0	0	1	0	0	$1.26\ 10^{-5}$
Fe(CO3)2--	-4	0	1	0	0	0	2	0	0	$1.12\ 10^{-26}$
Fe(OH)CO3-	-3	0	1	0	0	0	1	0	0	$1.86\ 10^{-23}$
FeSO4	0	0	1	0	0	1	0	0	0	$1.58\ 10^{2}$
FeCl+	0	0	1	0	0	0	0	1	0	$6.84\ 10^{-1}$
FeCl2(aq)	0	0	1	0	0	0	0	0	0	$6.59\ 10^{-9}$
FeO(aq)	-2	0	1	0	0	0	0	0	0	$3.87\ 10^{-21}$
Fe+++	0	-1	1	0	0	0	0	0	0	$8.55\ 10^{-14}$
FeOH++	-1	-1	1	0	0	0	0	0	0	$5.33\ 10^{-16}$
Fe(OH)2+	-2	-1	1	0	0	0	0	0	0	$6.50\ 10^{-21}$
FeSO4+	0	-1	1	0	0	1	0	0	0	$7.06\ 10^{-12}$
FeOOH(aq)	-3	-1	1	0	0	0	0	0	0	$8.15\ 10^{-26}$
FeO+	-2	-1	1	0	0	0	0	0	0	$1.91\ 10^{-19}$
FeO2-	-4	-1	1	0	0	0	0	0	0	$2.06\ 10^{-35}$
FeCl++	0	-1	1	0	0	0	0	1	0	$2.55\ 10^{-12}$
Cr++	8	4	0	1	0	0	0	0	0	$1.23\ 10^{68}$
Cr+++	8	3	0	1	0	0	0	0	0	$9.55\ 10^{74}$
CrOH++	7	3	0	1	0	0	0	0	0	$1.48\ 10^{71}$
Cr(OH)2+	6	3	0	1	0	0	0	0	0	$8.92\ 10^{64}$
Cr(OH)4-	4	3	0	1	0	0	0	0	0	$3.16\ 10^{47}$
HCrO4-	1	0	0	1	0	0	0	0	0	$3.16\ 10^{6}$
KCrO4-	0	0	0	1	1	0	0	0	0	3.72
HSiO3-	-1	0	0	0	0	0	0	0	1	$1.46\ 10^{-10}$
Fe(s)	0	2	1	0	0	0	0	0	0	$2.43\ 10^{-17}$
SiO2(s)	0	0	0	0	0	0	0	0	1	$5.65\ 10^{3}$
FeOOH(s)	-3	-1	1	0	0	0	0	0	0	$*1.37\ 10^{18}$
CrOOH(s)	5	3	0	1	0	0	0	0	0	$*1.27\ 10^{-69}$

Table 5.4 - Reduced Morel Table for the problem Fe-Cr redox reaction (*Equilibrium constants were calibrated on the basis of experimental results)

The spatial distribution of the solid phase at the end of the simulation is reported in Figure 5.4 for the two meshes. It is evident from Figures 5.4a (coarse mesh) and 5.4b (fine mesh) that the mesh size has an impact on results; in both Figures 5.4a and 5.4b, the plume of precipitate appears more concentrated in the first half of the domain, a behavior that is consistent with the experimental plume in Figure 5.2a. The plume is wider in Figure 5.4a than in 5.4b, being this last more consistent with experimental results. With both meshes, some precipitation occurs at the outlet placed in the Fe^{2+} section. With the coarse mesh, the precipitate at the outlet remains isolated, while with the finer mesh it is linked to the main plume. Although the bifurcation of the plume that is visible in Figure 5.4b does not correspond to the experimental reality, the simulation properly reproduces the deviation of the plume towards the outlet, which is clearly visible in photos taken of the experiment (Figure 5.5a).

The fine mesh also better captions the asymmetric nature of the precipitation, which is evident in Figure 5.3a, a picture of the bottom of the transparent flow cell taken at the end of the experiment. Figures 5.3b and 5.3c compare the numerical simulation at the same location. The asymmetric precipitation is also visible in Figure 5.5b, where the solid phase on the right (Cr) side is less diffused than the one on the left (Fe) side of the flow cell.
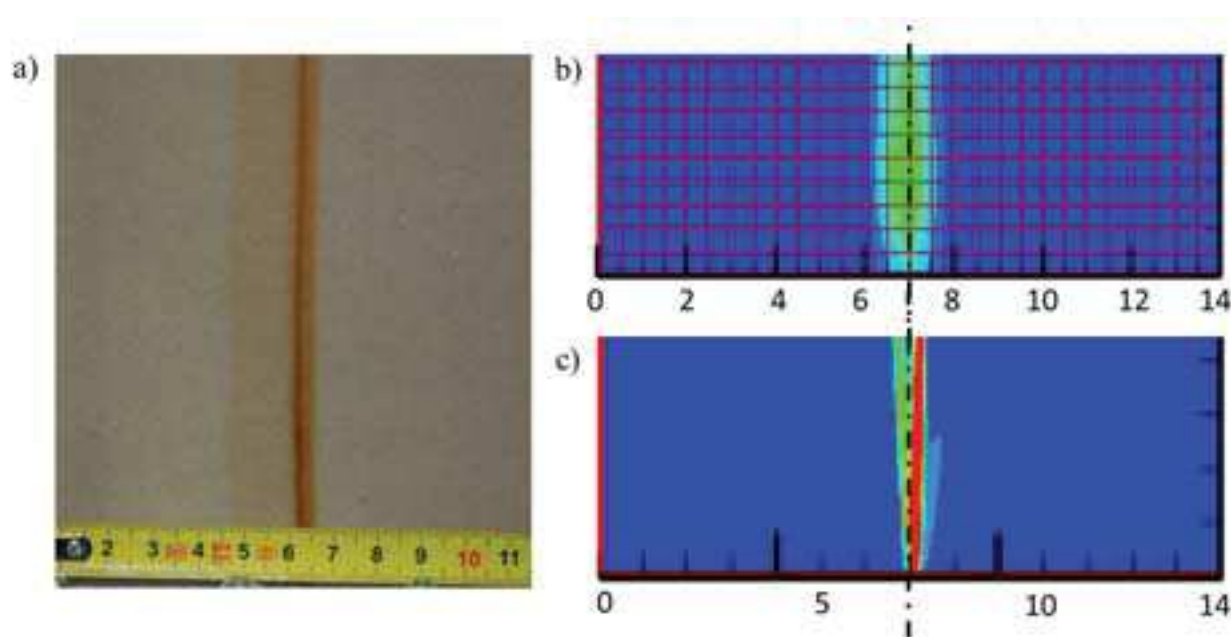
Figure 5.3 – In the first 4.5 cm of the domain, the 5mm mesh (b) misses the asymmetric precipitation detected in the experiment (a) whereas the 1mm is able to properly reproduce this behavior.

Comparisons between the measured data and the simulated curves are provided in Figure 5.6 for pH and in Figure 5.7 for the electric potential Eh. Experimental data are reported with continuous lines while simulated curves with dashed lines. While experimental and simulated curves at the different observation points are in quite good agreement for the pH, and the mesh only slightly modifies results, the electric potential shows a more troubled behavior. Although Figures 5.7a shows more oscillations

126

with respect to Figure 5.7b on curves Eh2, Eh4 and Eh1, Eh3, the curves obtained with the coarse mesh seem to be in better agreement with experimental results (particularly Eh5 and Eh6, which should reach an asymptote at 0.7 V and they instead grow until 0.8 V for the coarse mesh and 0.9 for the finer mesh). Reasons of some of the discrepancies between simulated and measured values are indubitably numerical, for example in the case of oscillations of Eh1 and Eh3 or Eh2 and Eh4 values (the extension of the oscillations is reduced with the mesh size). Additional tests should be performed on the transport time-stepping since other test-cases in this work showed dependence from the stepsize.
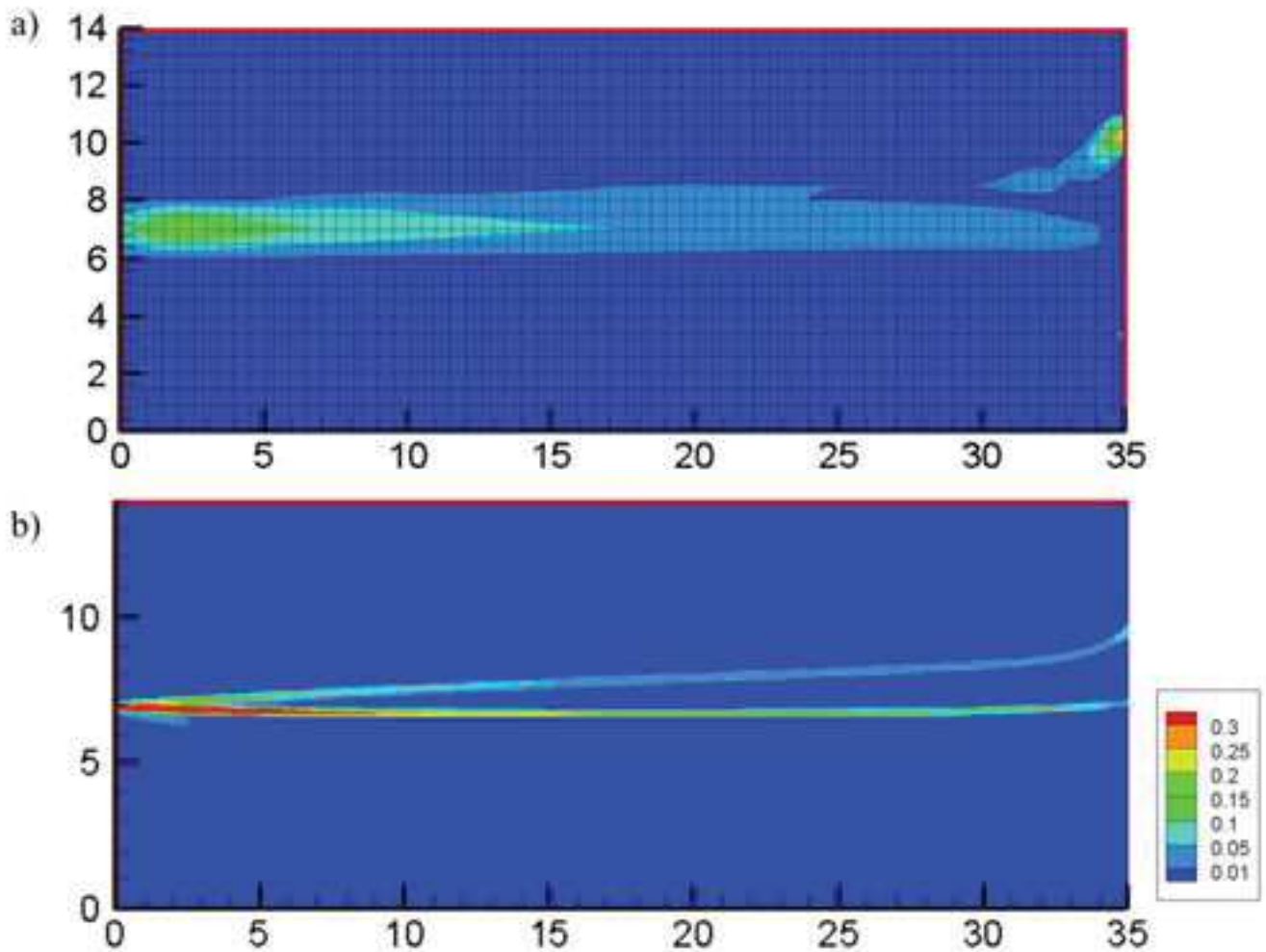
Figure 5.4 – Graphic representation of the solid phase over the domain at the end of the simulation with the 5 mm mesh a), and with the 1 mm mesh b).

Other mismatches may instead be due to retarded response of the probes, which indeed show unstable behavior between 50 and 150 min after the beginning of the simulation. Concerning the values of the asymptotes, it is also possible that probes measure a certain volume of water collected from a zone

corresponding to more than one element of the mesh, creating artificial manipulations of concentrations.
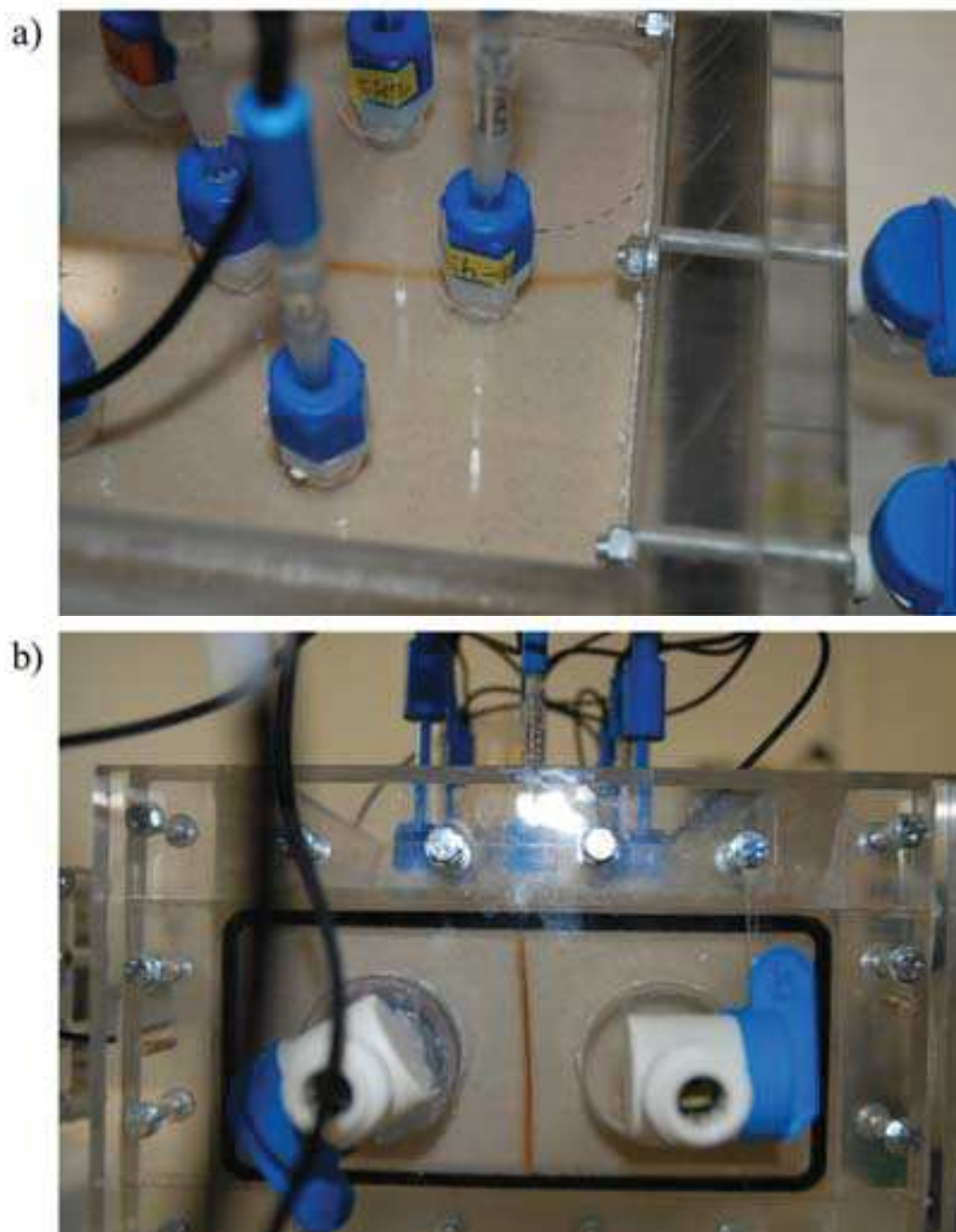
Figure 5.5 – a) the deviation of the plume in the direction of the outlet and b) the vertical section at the inlet showing some asymmetric precipitation of the solid solution
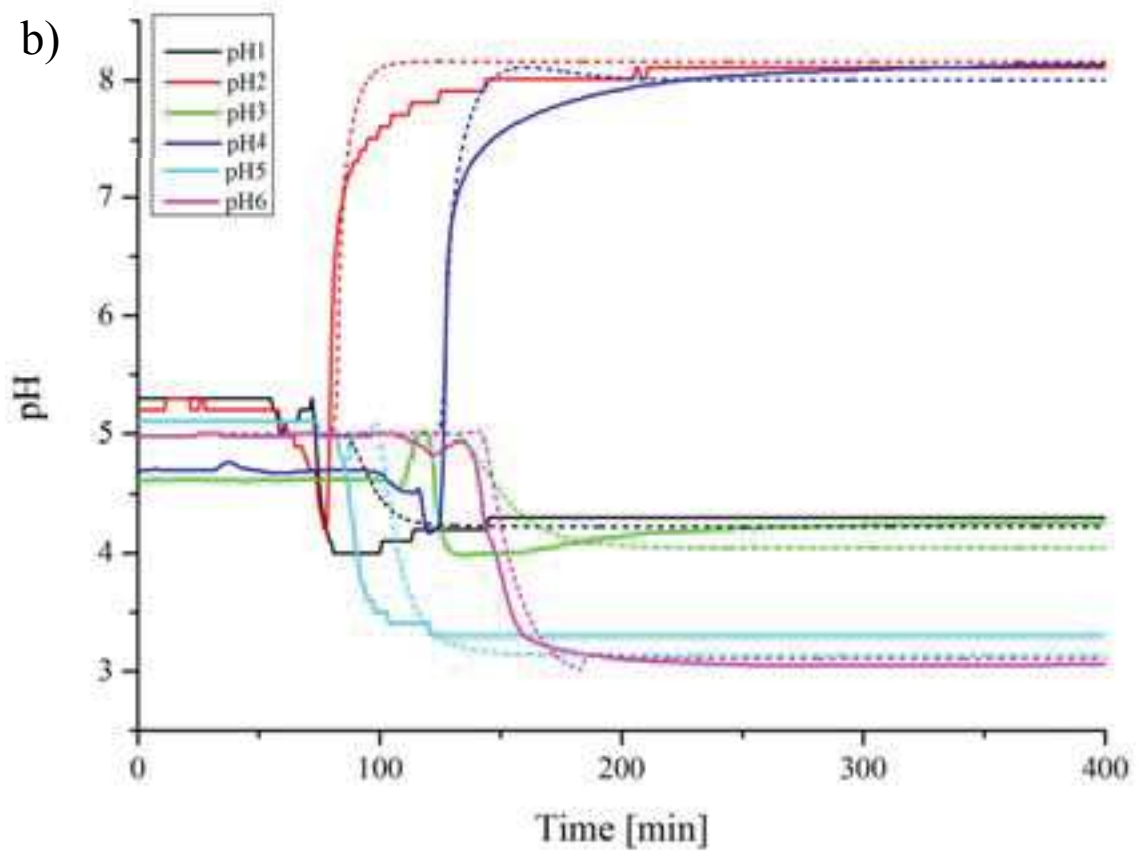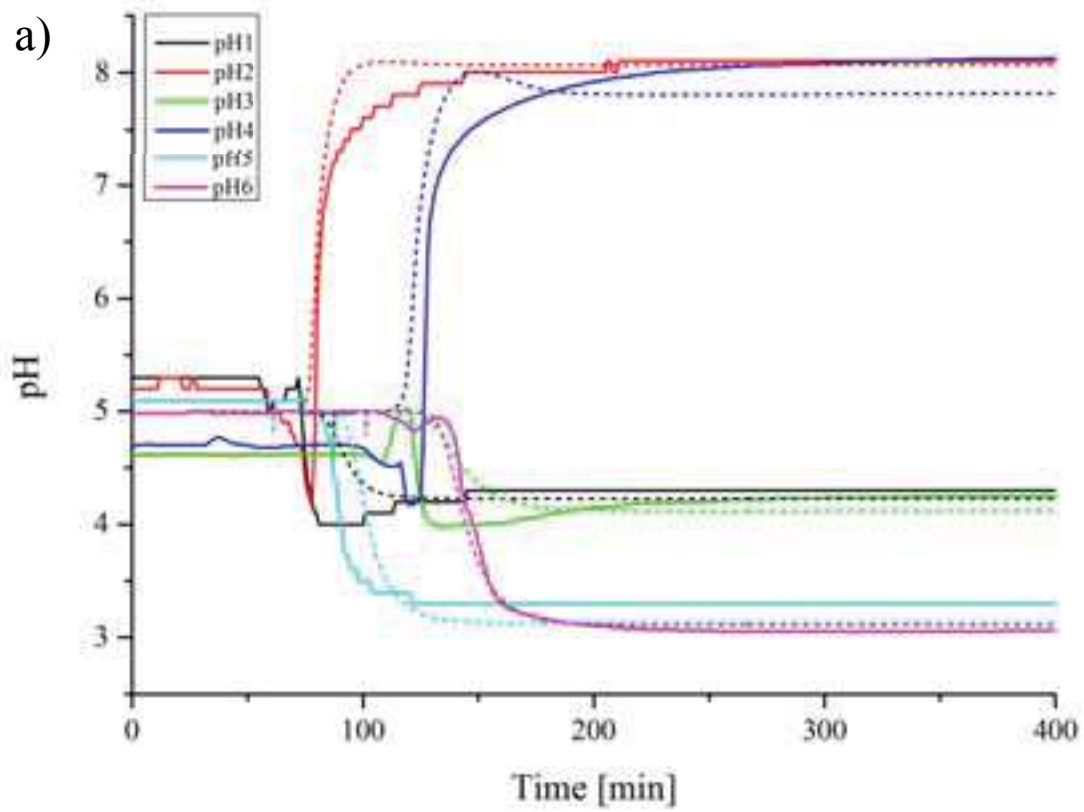
Figure 5.6 – pH experimental (continuous) and simulated (dashed) results for coarse (a) and fine (b) meshes for the Fe-Cr solid solution
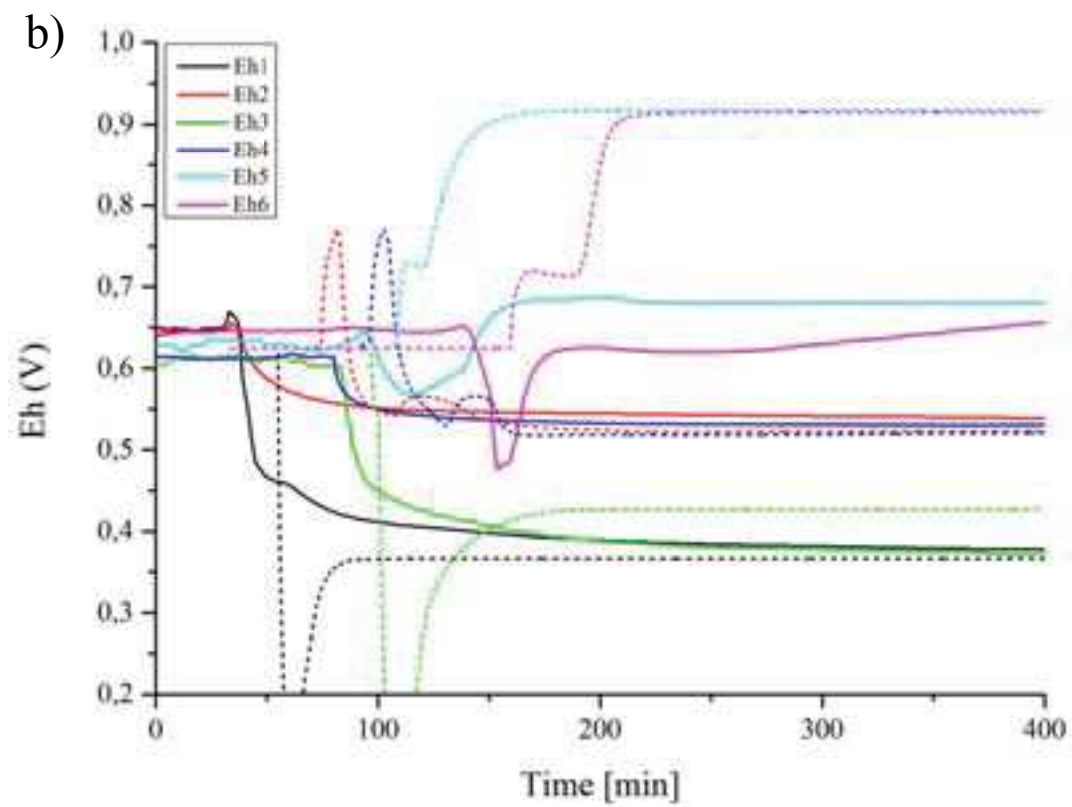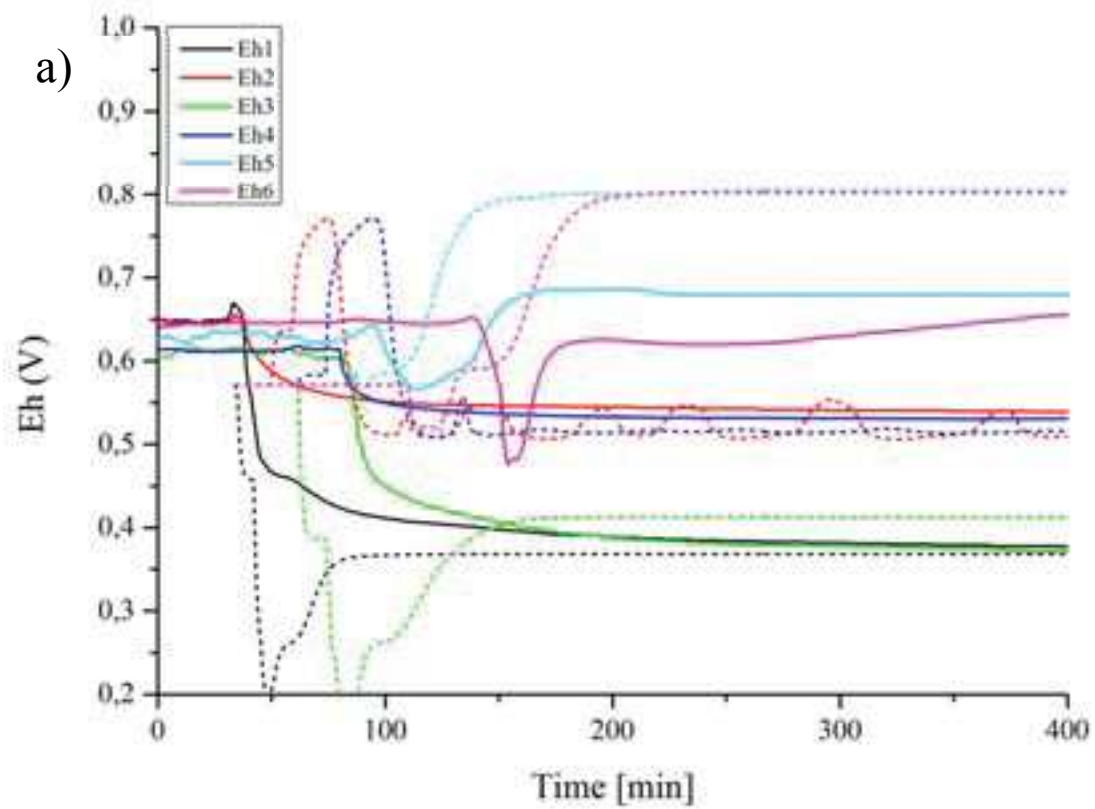
Figure 5.7 – Eh experimental (continuous) and simulated (dashed) results for coarse (a) and fine (b) meshes for the Fe-Cr solid solution

130

5.3 Conclusions about solid solutions

Throughout this chapter, the theoretical background of solid solutions' thermodynamics has been introduced, followed by a description of the possible ways to model solid solutions' thermodynamic equilibrium (and analogous states such as stoichiometric saturation) in a mass action law context. Two numerical examples were provided in order to test the implementation of the algorithm: a very simple batch precipitation of a $(Sr,Ca)CO_3$ solid solution formation and a more articulated reactive transport example including $(Fe,Cr)OOH$ precipitation. The batch experiment ensured that the algorithm is able to reproduce successfully a simulation obtained with PHREEQC. Beside the solid solutions' aspect, this experiment also tested the module capability to add reactants into a batch reactor, modifying total concentrations available for speciation ("titration module" in SPeCTr). The reactive transport simulation showed that i) the algorithm converges in numerical conditions different from the batch reactor ii) there is a satisfying degree of coherence between the numerical solutions and the experimental data although some inaccuracies remain iii) this type of interface problems can be potentially modeled with solid solutions. A discussion about the choice of equilibrium constants, transport parameters, porosity update algorithm goes beyond the scope of this Chapter although these parameters could provide better agreement between experiment and simulations.

It has to be kept in mind that the two examples do not ensure the capability to model every possible solid solution or prove to any extent the absence of limitations in the algorithm; therefore the importance of running as many benchmarks and problems as possible cannot be stressed enough.

It has abundantly been remarked that the theory behind kinetic models for solid solutions is not a well-established issue. Models exploiting the concept of solid solution to reproduce kinetic stable isotope fractionation are an extremely powerful and successful tool, but a careful use in terminology is mandatory to avoid the impression that the model could or should be extended to general solid solutions not containing isotopes of the same element. For example, there is no theoretical basis to extend to kinetic precipitation the two examples provided in this chapter. In order to stress this point of view, the numerical modeling of transition state theory (TST) modified on the basis of solid solutions is going was treated in Chapter 2.

Chapter 6 – Building SpeCTr, a reactive transport code

6.1 Coupling flow, transport and reaction

6.1.1 Governing equations

The simulation of transient and steady flow through a single continuum model responds to governing equations obtained through mass conservation and momentum equation (Darcy's law in a single continuum porous medium):

$$\begin{cases} \dfrac{\partial(\rho\phi)}{\partial t} + \nabla \cdot (\rho\mathbf{q}) = 0 \\ \mathbf{q} = -\mathbf{K}\nabla h \end{cases} \tag{6.1}$$

where $\mathbf{q}$ [L/T] is the Darcy flux, ρ [M^3/L^3] is the fluid density, ϕ [-] is the porosity, defined as the ratio between the volume of the pores and the volume of the porous medium, $\mathbf{K}$ is the hydraulic conductivity [L/T] tensor and h is the hydraulic head [L].

Combining mass action equation and Darcy's law, after a series of developments, a single equation function of the hydraulic head h can be reached, with s [L^{-1}] the specific storage coefficient:

$$s\frac{\partial h}{\partial t} - \nabla.\mathbf{K}\nabla h = 0 \tag{6.2}$$

Transport of *a single species i* in a single continuum model is described by a advection-diffusion/dispersion type partial differential equation (PDE) that determines the variations of concentration in space and time. When transport is not conservative, but *reactive*, a source term appears in the PDE, providing a link between transport and reactions:

$$\frac{\partial(\phi C)}{\partial t} + \nabla.(\mathbf{q}C - \mathbf{D}.\nabla C) = -S \tag{6.3}$$

$$\mathbf{D} = D_m\mathbf{I} + (\alpha_L - \alpha_T)\frac{\mathbf{q}\mathbf{q}}{|\mathbf{q}|} + \alpha_T|\mathbf{q}|\mathbf{I} \tag{6.4}$$

where ϕ [-] is the kinematic porosity, C [mol/L^3] is the concentration of the chemical species, $\mathbf{D}$ is the dispersion tensor [L^2/T], α_L, α_T are the longitudinal and transverse dispersivity [L], D_m is the pore

water diffusion coefficient [L^2/T], **I** the unit tensor; S [mol/L^3/T] is the reaction rate of a reaction causing production/consumption of species C; **q** [L/T] is the Darcy flux known from the solution of system (2.1). Transport operator is often referred to as $L = -\nabla.(\mathbf{q} + \mathbf{D}.\nabla)$ in the literature and equation (6.3) can be synthetized by:

$$\frac{\partial(\phi C)}{\partial t} - L(C) = -S \tag{6.5}$$

Analytical solutions for PDEs (6.2) and (6.3) are available exclusively for extremely simplified problems (i.e. van Genuchten and Wierenga 1976) and the use of numerical methods is mandatory. Numerical methods such as *finite differences* (Steefel and MacQuarrie 1996) or *finite elements* (Istok 1989) provide approximate solutions.

While flow equations (6.2) and reactive transport equations (6.3) can be solved independently, this is not the case for reaction and transport operators within equation (6.3). In fact, reaction rate S depends from concentration C brought from transport that is, in turn, dependent from the reaction rate. Equation (6.5) can be rewritten as:

$$\frac{\partial(\phi C)}{\partial t} - L(C) = -S(C) \tag{6.6}$$

Two different approaches exist to take this dependence into account: the first, one-step or global approach or global-implicit, is to solve *simultaneously* transport and reaction equations, that is to say equation (6.6) as it is; the other is the so-called Operator Splitting approach that consists into solving *subsequently* transport and reaction terms, splitting equation (6.6) in two. A number of studies have been performed in order to assess the superiority of one approach over the other (Yeh and Tripathi 1989; Saaltink et al. 2000; Saaltink et al. 2001; Fahs et al. 2008) and the debate in workshops is ongoing but the convenience of one methodology still has to be proven.

6.1.2 Global approach

Although it was made clear from the beginning that this work is conceived under an Operator Splitting approach (for a number of reasons and exigencies explained in Chapter I), a short presentation of one-step/Global Approach is proposed for the sake of completeness.

Global Approach consists in solving *simultaneously* transport and reaction operators. Several models were developed throughout years based on Global Approach (Valocchi et al. 1981; Lichtner 1985; Steefel and Lasaga 1994; Steefel and Yabusaki 1995; Saaltink et al. 1998; Saaltink et al. 2001; Kräutle

and Knabner 2005) and it is implemented in three over twelve analyzed codes by Steefel et al. (2015) both as an alternative (CrunchFlow, PFLOTRAN) or unique (MIN3P) coupling technique.

Within global approach, two variants exist to solve coupled systems (Yeh and Tripathi 1989; Fahs 2007): Direct Substitution Approach (DSA) and mixed Differential Algebraic Equations (DAE).

DAE approach consists in solving a system formed by differential equations of transport and algebraic, nonlinear equations describing reactions; DSA consists in substituting reaction equations directly into transport equations and solving the resulting system. Although further distinctions within global DSA exist (Fahs 2007), they go beyond the scope of this work. Despite alternatives exist, Global DSA is the approach usually employed in comparisons with Operator Splitting techniques (Saaltink et al. 2000; Saaltink et al. 2001; Steefel and MacQuarrie 1996; Fahs et al. 2008).

A basic explanation of Global implicit DSA is available in (Steefel and MacQuarrie 1996); adapting equation (6.6) to one species, one reaction, one dimensional flow, diffusion-reaction problem with constant porosity we obtain:

$$\frac{\partial C}{\partial t} - D\frac{\partial^2 C}{\partial x^2} = -S(C) \qquad (6.7)$$

According to Steefel and MacQuarrie (1996) the global implicit approach in finite differences for previous equations is:

$$\frac{C_v^{(n+1)} - C_v^{(n)}}{\Delta t} = \frac{C_{v-1}^{(n+1)} - 2C_v^{(n+1)} + 2C_{v+1}^{(n+1)}}{\Delta x^2} + S(C_v^{(n+1)}) \qquad (6.8)$$

where v, $v-1$, $v+1$ are the cells of the spatial discretization and n and $n+1$ are present and future instant. If the reaction term S is linear, a linear system can be written in the following form (Steefel and MacQuarrie 1996):

$$
\begin{aligned}
b_1 C_1^{(n+1)} + c_1 C_2^{(n+1)} &= d_1 \\
a_2 C_1^{(n+1)} + b_2 C_2^{(n+1)} + c_2 C_3^{(n+1)} &= d_2 \\
&\ldots \\
a_{N-1} C_{N-2}^{(n+1)} + b_{N-1} C_{N-1}^{(n+1)} + c_{N-1} C_N^{(n+1)} &= d_{N-1} \\
a_N C_{N-1}^{(n+1)} + b_N C_N^{(n+1)} &= d_N
\end{aligned}
\qquad (6.9)
$$

where N is the number of the cells of spatial discretization, a_v, b_v and c_v are the coefficients of the linear system and d_v is the right hand side. Although extending previous system to two or three dimensions implies a modest complication of the formulation, extending the approach to a

multicomponent and multi-species significantly increases the size of the matrix and the system to be solved becomes nonlinear (Steefel and MacQuarrie 1996; Steefel et al. 2015).

6.1.3 Operator splitting

Operator splitting approach consist in solving *sequentially* transport and chemistry operators, this implying that two algorithms have to be solved subsequently in the same code or that two codes have to be coupled and run together. Several reactive transport models were developed based on an operator splitting approach (Cederberg et al. 1985; Appelo and Willemsen 1987; Yeh and Tripathi 1991; Engesgaard and Kipp 1992; Simunek and Suarez 1994; Parkhurst et al. 1999; Xu et al. 1999; Saaltink et al. 2001; Carrayrou et al. 2004) and reactive modules designed for coupling keep being developed (Bea et al. 2009; Leal et al. 2014, 2015).

Two principal techniques exist to split transport and reaction operators: Sequential Non Iterative Approach (SNIA) and Sequential Iterative Approach (SIA). The difference between the two approaches is that SNIA solves separately transport and reaction but does not iterate between the two while SIA does (Saaltink et al. 2001).

Adapting the simplified example of equation (6.7) proposed by Steefel and MacQuarrie (1996), SNIA approach would solve at first transport equation:

$$\frac{dC}{dt} = D\frac{d^2C}{dx^2} \qquad (6.10)$$

Solution of equation (6.10) through numerical methods over the time interval $\Delta t = t^{n+1} - t^n$ provides a new concentration C^{trans} that is an intermediate step between C^n and C^{n+1}. The reaction step follows, integrating over *the same* the time step $\Delta t = t^{n+1} - t^n$ providing the final concentration C^{n+1}.

$$\frac{dC}{dt} = -S(C) \qquad (6.11)$$

This approach in based on the assumption that reactions take place only after that transport is completed and this approximation may generate coupling errors (Valocchi and Malmstead 1992).

An alternative to previous formulation (still within SNIA approach) is the so-called Strang splitting (Steefel and MacQuarrie 1996), where two transport steps are performed around a single reaction solution. Equations (6.10) is integrated over half the time step $\Delta t = t^{n+1} - t^n$, $\Delta t/2$ providing a concentration $C^{trans(1)}$. This first approximation is used as initial concentration for the integration of the reaction term (6.11) which is instead performed over the whole time step Δt.

$$\frac{C^{reac} - C^{trans(1)}}{\Delta t} = S(C) \tag{6.12}$$

A conclusive transport step is performed with the integration of (6.10) over $\Delta t/2$ that provides the evolution $C^{reac} \rightarrow C^{n+1}$.

Two non-iterative previous approaches tend to cause a coupling error. A more sophisticate approach is constituted by SIA, an iterative sequence of transport and reaction steps that continues until given a convergence criteria is satisfied. According to Steefel and MacQuarrie (1996), several different formulations of this approach have been proposed and their formulation is often confusing. The idea is that equation (6.7) is split in two "copies". In one "copy" the equation is solved with the reaction term considered as a source term (known). In the other "copy" of the equation, is the transport term that is considered a source term. Iterations continue until the two "copies" provide the same results.

$$\frac{C^{T(n+1),m+1} - C^{(n)}}{\Delta t} = L(C^{(n+1),m+1}) + S^m$$
$$\frac{C^{C(n+1),m+1} - C^{(n)}}{\Delta t} = L^m + S(C^{(n+1),m+1}) \tag{6.13}$$

where m is the index counting iterations within the computation of a single time step Δt, grey terms S^m and L^m are considered as source terms. At the iteration m+1, source terms are updated with their best approximation:

$$L^{m+1} = \frac{C^{T(n+1),m+1} - C^{(n)}}{\Delta t} - S^m$$
$$S^{m+1} = \frac{C^{C(n+1),m+1} - C^{(n)}}{\Delta t} - L^m \tag{6.14}$$

Iterations continue until concentrations computed with the two versions of equation (6.13) are close enough (some tolerance must be defined). Although SIA was intended as a compromise between the global-implicit and the operator splitting approaches in order to limit coupling errors (Carrayrou 2001; Saaltink et al. 1998, 2001; Kräutle and Knabner 2005), the approach may result in numerically inefficient (Saaltink et al. 2001) or instable (Engesgaard and Kipp 1992; Steefel and MacQuarrie 1996) behavior.

6.1.4 War of the approaches

The first work of comparison between Global Approach and Operator Splitting (Yeh and Tripathi 1989) was definitely favorable to Operator Splitting, pointing out the disproportionate computational effort required by Global Approach. This outcome was partly due to the still poor computational resources available at the time. More recent works are focused on establishing strengths and weaknesses of the two methods.

Strengths of Operator Splitting are: OS leads to the formation of smaller systems whose solution needs less memory (Yeh and Tripathi 1989; Saaltink et al. 2001; Kräutle and Knabner 2005) and it is easier to put in place (Saaltink et al. 2001); it allows the coupling of already existing codes and consequently the choice of specific numerical schemes for each operator (Valocchi and Malmstead 1992; Carrayrou et al. 2004); the modular aspect allows more flexibility and is more suited for parallelization (Yabusaki et al. 1998). On the other hand, although Global Approach results memory-consuming is more precise and does not introduce intrinsic errors dues to Operator Splitting (Carrayrou 2001; Saaltink et al. 1998, 2001; Kräutle and Knabner 2005); moreover it has quadratic convergence (Xu et al. 1999; Carrayrou 2001; Saaltink et al. 2001; Kräutle and Knabner 2005) and assures a lower number of iterations to converge.

6.1.5 Multicomponent reactive transport

Equations (6.3) to (6.13) are written for a generic chemical species, C. In case of multicomponent reactive transport, several chemical species C_i (i=I, Nc) are transported and expected to react.

We have already explained in Chapter 3 how a subset of those Nc species may describe the whole reaction network under the assumption of thermodynamic equilibrium. They go under the name of *components* or *primary species* and are usually indicated with symbol X_j.

At thermodynamic equilibrium, reactions are governed by two set of equations: mass conservation and mass action laws. Equations of mass conservation involve total concentrations T_j of a component X_j that is shared among species during speciation. In Chapter 4 it is also explained total concentrations T_j constitute the connection between thermodynamic equations and kinetic reactions.

Steefel and MacQuarry (1996) specify that, in order to reduce the number of equations, both SNIA and SIA algorithms can be written in terms of total concentrations instead that as functions of chemical species. Until now, no distinction was made between total dissolved concentration, T_j^d and total fixed concentration T_j^f. Whenever transport is taken into account a distinction is due. It is intuitive that total fixed concentrations won't be transported; therefore equation (6.6) takes the following form:

$$\frac{\partial(\phi T_j^d)}{\partial t} - L(T_j^d) = -S_j(\mathbf{X}(\mathbf{T})) \qquad (6.15)$$

137

where T_j^d is the dissolved total of primary species X_j, and S_j is the associated production/consumption rate, which depends from concentrations of primary species $\mathbf{X}$ (which, in turn, depend from available total concentrations $\mathbf{T}$). Decoupling equation (6.15) through Operator Splitting (SNIA) is the approach chosen for this work and it results in the following algorithm:

I)   Total dissolved concentrations are moved in the porous medium:

$$\frac{\partial(\phi T_j^d)}{\partial t} - L(T_j^d) = 0 \tag{6.16}$$

Equation (6.16) is solved for each primary species ($j=1,Nx$) and for each kinetic dissolved species, Cc_i^d. The equation is solved numerically over an interval Δt. In this work, transport equations are solved by code TRACES, that will be described in the following paragraphs. Solution of previous equations provides: $T_j^{d(n)} \rightarrow T_j^{d(trans)}$ and $Cc_j^{d(n)} \rightarrow Cc_j^{d(trans)}$.

II)   Totals available for chemical speciation that were updated by transport undergo transformations.

$$\frac{\partial(\phi T_j^d)}{\partial t} = -S_j(\mathbf{X(T)}) \tag{6.17}$$

Solution of equation (6.17) provides new values of dissolved totals, which may change according to kinetic reactions, but also following equilibrium precipitation or adsorption. Dissolved totals of a generic primary species X_j at instant t^{n+1} are then obtained: $T_j^{d(trans)} \rightarrow T_j^{d(n+1)}$; A coherent transformation occurs to fixed totals $T_j^{f(n)} \rightarrow T_j^{f(n+1)}$ and to kinetic species $Cc_j^{f(n)} \rightarrow Cc_j^{f(n+1)}$, $Cc_j^{d(trans)} \rightarrow Cc_j^{d(n+1)}$.

III)   Dissolved total concentrations and dissolved kinetic species are put into equation (6.16) and the cycle is repeated for a new $\Delta t = t^{n+2} - t^{n+1}$ continuing until $\sum \Delta t = t_{tot}$.

Some remarks: there is freedom over numerical methods applied to solve differential equations (6.2) ,(6.3) and their adaptations to particular problems, this is why most equations are written in their differential form and not in their discretized form. Discretization in time is usually carried out with

finite differences, while discretization in space may be carried through finite differences or finite elements. Discretization in time may as well be implicit or explicit (a short description of implicit and explicit methods is available in Chapter 4). It is useful to remind that the time step Δt over which transport equations and reaction equations are integrated is the same.

As anticipated, in this work the solution of conservative transport is carried out with the program TRACES whereas the reaction module developed through Chapters 3, 4 and 5 is used to solve chemical equations. The code for flow and conservative transport, TRACES, is presented in the following paragraphs.

6.2 TRACES

6.2.1 Code capabilities

TRACES (*Transport of ReACtive Elements in Subsurface* or, in its French version, *Transport RéActif de Contaminants dans les Eaux Souterraines*) is a computer program developed at the 'Laboratoire d'Hydrologie et de Géochimie de Strasbourg' of the University of Strasbourg.

TRACES allows transient or steady flow computations in 2D or 3D heterogeneous domains, although for 2D domains computations are restricted to confined aquifers. Parameters values required for flow computations are allowed to vary in space, as are boundary conditions. To each cell of the grid, a material property index is assigned, permitting simulations of highly heterogeneous domains.

Fluid and matrix properties, source terms and boundary conditions are also allowed to vary in time according to user-specified functions.

Concerning transport phenomena, TRACES is able to model advection, dispersion, diffusion phenomena. The code was initially intended as a reactive transport module and some basic models to take into account adsorption (linear, Freundlich, Langmuir isotherms), precipitation/dissolution and nuclides generation/degradation were included. Nevertheless, some implemented laws are empiric and such approach does not allow a comprehensive understanding of complex phenomena and interactions occurring in the porous medium (Steefel et al. 2005).

6.2.2 Numerical schemes

TRACES is based on *mixed* and *discontinuous* finite elements methods. These numerical methods ensure exact local mass balance, allow high parameter discontinuities between adjacent elements and treat full tensors without approximation. This last feature is of great interest, considering that most of the reactive transport codes analyzed by Steefel et al. (2015) work with diagonal tensors.

Mixed hybrid finite elements are employed to solve flow in the porous medium and dispersive/diffusive transport. Advective transport is solved by *discontinuous* Galerkin finite elements that generate no oscillations and limited numerical diffusion. Spatial discretization can be achieved through triangles or quadrangles for the 2D problems or through tetrahedrons, prisms, and hexahedrons for 3D problems. Time discretization scheme is explicit for advection, implicit for flow and diffusion/dispersion. We recall that an explicit time discretization implies that Courant number (or Courant-Friedrichs-Lewy number, *CFL*) criterion is fulfilled, i.e. (for 1D transport):

$$CFL = \frac{v\Delta t}{\Delta x} \leq 1.0 \tag{6.18}$$

Where v is the average pore water velocity $v = q / \phi$. The constraint expressed in equation (6.18) ensures that the mass of the solute cannot be moved further than one grid cell in a single time-step (Steefel and MacQuarrie 1996). Only fully implicit methods aren't subjected to this limitation.

Equation (6.18) may become a serious limitation whenever velocity becomes very high with respect to the cell size, for example when porosity is updated as a consequence of mineral precipitation or in the vicinity of a well. In the case variable porosity, ϕ may decrease to its threshold value, generating a disproportionate increase of v. To respect Courant-Friedrichs-Lewy condition the time-step must be reduced and may reach values that are unsustainable from a computational point of view.

Although an implicit discretization in time would be extremely helpful to handle changes in porosity or problems where transport is dominant, the advantage of this technique could be mitigated when solving reactive transport problems with Operator Splitting. In fact, when dealing with mass exchanges between the solid and dissolved phase, the time step required to reduce coupling errors could be inferior to the one imposed by the respect of Courant-Friedrichs-Lewy condition (Steefel 2009). The benchmark proposed in the following paragraphs is a clear example of the manifestation of this potential problem.

6.2.3 Coupling with reaction module

Some supplementary attention must be paid to the way of practically coupling transport and reaction modules. In the present work, transport is solved through finite elements, this meaning that the numerical solution of the equation provides a concentration for each node of the grid. On the other hand, the reaction module works with a single concentration characterizing one element (delimited by three/for nodes, according to the shape of the elements). This mechanism implies that concentrations at nodes must be averaged to provide a single value for the element.

The algorithm used to handle this transformation must be carefully verified since it can trigger oscillations in the solution. Simpler versions of the algorithm should be preferred to more sophisticated but less controllable alternatives. The version currently implemented algorithm is an arithmetic mean:

$$C_j^n = \sum_{i=1}^{Nodes} \frac{MTC(i,j)^n}{Nodes} \tag{6.19}$$

where MTC is the value at the node and i is its index for species C_j ($j = 1, Nx$). The algorithm used to distribute the concentration updated from the chemistry to the nodes is even more important. The current version of the algorithm is:

$$MTC(i,j)^{n+1} = MTC(i,j)^n + \left(C_j^{n+1} - C_j^n \right) \tag{6.20}$$

6.2.4 SpeCTr

The reactive transport code resulting from the coupling of the reaction and transport modules (connected through an operator splitting approach) will be referred to from now on as SpeCTr (*Spéciation Cinétique Transport* in French).

6.3 Validation: coupling and implementation of isotopes

6.3.1 Interest of validation

Although it is generally impossible to certify the absolute correctness of a computer program, the only way to detect potential malfunctions is through comparisons with analytical solutions, experimental data or numerical benchmarks. Analytical solutions (i.e. van Genuchten and Wierenga 1976) are available only for extremely simple problems; experimental data are subject to errors in their manipulations and various degrees of uncertainty; on the other hand, numerical benchmarks are well suited to test the behavior and characteristics of the code.

In this context, the interest was in testing: i) the quality of the coupling between the transport operator and the reaction operator ii) the effectiveness of the implementation of kinetic stable isotope fractionation in the reaction module iii) the reliability of SpeCTr in computing reaction networks that result in heavy systems of equations iv) the reliability of SpeCTr in simulating realistic geochemical scenarios.

Regarding point iii) and iv), it is interesting to point out that sometimes test-cases used as a basis for validations or comparisons are very simple from the computational point of view. Although this is necessary in the first stages of development (Calcite-Magnesite example for implementation of TST precipitation/dissolution law in the solver DASPK in Chapter 4 and $(Sr,Ca)CO_3$ solid solutions in Chapter 5) at some point it is necessary to introduce more complicated and realistic scenarios to test the code for what is meant to do, simulating realistic biogeochemical reaction networks.

The proper benchmark to address points i) to v) listed above is contained in Wanner et al. (2014) who provide benchmarks for Cr isotope fractionation obtained with four different mainstream programs (CrunchFlow, MIN3P, FLOTRAN, and TOUGHREACT) and based on experimental data from a dismissed industrial site in Switzerland (Wanner et al. 2012).

One of the conclusions in the work of Wanner et al. (2014) is that model to model comparison shows that the four codes are able to correctly describe the faith of Cr isotopes. As a consequence, a validation obtained with this benchmark would result in a serious assessment of the capabilities of code SpeCTr.

6.3.2 Presentation of the problem

The benchmarks presented in Wanner et al. (2014) describe Cr(VI) reduction to Cr(III). Cr(VI) is a carcinogenic compound that may result from industrial activity or from geogenic sources as well (Kotaś and Stasicka 2000). Cr(III), on the other hand, is less toxic and less soluble, a combination that makes reduction of Cr(VI) to Cr(III) an interesting solution for remediation of polluted sites; Wanner et al. (2014) describe Cr(VI) reduction through abiotic aqueous reaction with Fe^{2+}; they propose two versions of the benchmark: one that takes Cr fractionation into account and the other that doesn't. Cr(III) and its isotopes (^{52}Cr (more abundant) and ^{53}Cr (less abundant)) form minerals throughout non-fractioning precipitation.

6.3.2.1 Spatial discretization, flow characteristics and ground properties

The spatial discretization consists in a 1D problem solved along 800 meters. 800 subsequent square cells of 1 m^2 each (with an intrinsic thickness of 1 m) represent the domain. Porous medium is homogeneous with fixed porosity ϕ=0.17 and a constant flow throughout the domain has been fixed to q = 6.8870 10^{-6} m^3/s which corresponds to the 3.5 m/day of average velocity estimated on the field (Wanner et al. 2013).

Figure 6.1 – Schematization of spatial discretization in TRACES: although the domain is 1D, solution through finite elements requires surfaces. 800 square cells of 1m^2 each represent the domain.

Attention must be paid to TRACES input file: a negative value must be used as inflow condition in TRACES. To sum up, two flow boundary conditions were fixed: a Neumann boundary condition of q = 6.8870 10^{-6} m^3/s at the inlet and a Dirichlet boundary condition at the outlet (h=1.0 m, which is non-influent to the problem).

6.3.2.2 Boundary and initial conditions, transport parameters

Flow boundary conditions were described in previous paragraph but they are not the only ones required: transport boundary conditions must be fixed too. As it will be explained in the following paragraphs, the reaction network of this scenario can be described through 16 (or 18) primary species. For each primary species, a total concentration must be specified at the inlet, being this value

explicitly 0 mol/L if the primary species is absent. Total concentrations at the inlet (boundary conditions) are available in Table 1 as well as initial conditions. Initial and boundary conditions are different for Cl^- (this allowing the monitoring of a non-reactive tracer) and $Cr(VI)$ (the corresponding primary species is CrO_4^{2+}) is initially absent. Total initial concentrations are available together with boundary conditions in Table 1. When fractionation is not taken into account, the injected CrO_4^{2+} corresponds to the sum of $^{52}CrO_4^{2+}$ and $^{53}CrO_4^{2+}$ in Table 6.1.

	Initial conditions		Boundary conditions	
	pH	mol/L	pH	mol/L
H^+	6.2	$2.11124\ 10^{-4}$	6.2	$2.11124\ 10^{-4}$
	mg/L	mol/L	mg/L	mol/L
Na^+	4.7	$2.044385\ 10^{-4}$	4.7	$2.044385\ 10^{-4}$
K^+	0.9	$2.301890\ 10^{-5}$	0.9	$2.301890\ 10^{-5}$
Mg^{2+}	2.0	$8.228760\ 10^{-5}$	2.0	$8.228760\ 10^{-5}$
Ca^{2+}	13.58	$3.388393\ 10^{-4}$	13.58	$3.388393\ 10^{-4}$
Cl^-	**18.77**	**$5.294781\ 10^{-4}$**	**18.66**	**$5.263752\ 10^{-4}$**
SO_4^{2-}	8.85	$9.213376\ 10^{-5}$	8.85	$9.213376\ 10^{-5}$
NO_3^-	12.25	$1.975679\ 10^{-4}$	12.25	$1.975679\ 10^{-4}$
HCO_3^-	22.58	$3.700669\ 10^{-4}$	22.58	$3.700669\ 10^{-4}$
$^{52}CrO_4^{2-}$	**0**	**0**	**0.08**	**$1.39373917\ 10^{-6}$**
$^{53}CrO_4^{2-}$	**0**	**0**		**$1.58038813\ 10^{-7}$**
Fe^{2+}	0.01	$1.790671\ 10^{-7}$	0.01	$1.790671\ 10^{-7}$
Fe^{3+}	0	0	0	0
Na^+	0	0	0	0
SiO_2	0	0	0	0
Cr^{3+}	0	0	0	0
Al^{3+}	0	0	0	0

Table 6.1 – Initial and boundary conditions for the Cr Benchmark. They are identical with the exception of Cl^- and $Cr(VI)$ total concentrations. $Cr(VI)$ is initially absent and injected at the inlet.

Figure 6.2 – Cr(IV) under the form of CrO42- is absent in the domain, it is injected at the inlet and reduced to Cr(III) throughout the domain.

Transport equation (6.3) requires a diffusion/dispersion tensor **D** described in equation (6.4) ; a diffusion coefficient D_m, and a longitudinal (α_L) dispersivity coefficients are required *for each species* (transversal dispersivity (α_T) is not required in 1D problems). In this particular case no differences of coefficients between the species were imposed. Although in Wanner et al. (2014) longitudinal dispersivity α_L was set to 0, all employed numerical models engender numerical dispersion, which is quantified in $\alpha_L = 0.54$ m for CrunchFlow and TOUGHREACT and in $\alpha_L = 1$ m for MIN3P and FLOTRAN. Therefore, the benchmark will be tested with $\alpha_L = 0$ m and with values resulting from numerical dispersion in CrunchFlow and TOUGHREACT ($\alpha_L = 0.54$ m). The diffusion coefficient in water is set to the value D_m=1. 0 10^{-9} m^2/s.

6.3.2.3 Reaction network

From a chemical point of view, the test case involves *aqueous equilibrium* reactions, *kinetic homogeneous* reactions and *kinetic heterogeneous* (precipitation) reactions. Equilibrium reactions are resumed in Table 6.2: 52 (or 54) chemical species are described through 16 (or 18) primary species that generate, through mass action laws, 36 secondary species (this is the reason behind the necessity of defining the 16 (or 18) initial and boundary conditions for transported species in previous paragraph). There are indeed 36 equilibrium reactions taking place between the aqueous species, but they are not the only homogeneous reactions. Cr(VI) to Cr(III) reduction is described by an homogeneous kinetic reaction:

$$CrO_4^{2-} + 3Fe_{(aq)}^{2+} + 8H^+ = Cr^{3+} + 3Fe^{2+} + 4H_2O \qquad (6.21)$$
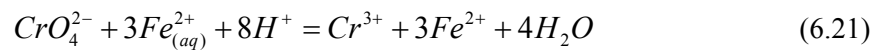
Two versions of reaction (6.21) exist when the two Cr isotopes are taken into account. One defines the kinetic reduction of $^{52}CrO_4^{2-}$ and the other defines the kinetic reduction of $^{53}CrO_4^{2-}$:

$$^{52}CrO_4^{2-} + 3Fe_{(aq)}^{2+} + 8H^+ = {}^{52}Cr^{3+} + 3Fe^{2+} + 4H_2O$$
$$^{53}CrO_4^{2-} + 3Fe_{(aq)}^{2+} + 8H^+ = {}^{53}Cr^{3+} + 3Fe^{2+} + 4H_2O \qquad (6.22)$$
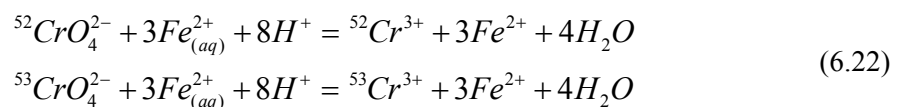
	H^+	H_2O	Cl^-	Na^+	K^+	Mg^{2+}	Fe^{2+}	Fe^{3+}	SO_4^{2-}	NO_3^-	HCO_3^-	Ca^{2+}	SiO_2	Al^{3+}	$LogK$
$NaOH$	-1	1	0	1	0	0	0	0	0	0	0	0	0	0	-14.799
AlO_2^-	-4	2	0	0	0	0	0	0	0	0	0	0	0	1	-22.199
AlO^+	-2	1	0	0	0	0	0	0	0	0	0	0	0	1	-10.343
$AloH^{2+}$	-1	1	0	0	0	0	0	0	0	0	0	0	0	1	-5
$HAlO_2$	-3	2	0	0	0	0	0	0	0	0	0	0	0	1	-15.604
CO_2	1	-1	0	0	0	0	0	0	0	0	1	0	0	0	6.341
CO_3^{2-}	-1	0	0	0	0	0	0	0	0	0	1	0	0	0	-10.325
$CaCO_3$	-1	0	0	0	0	0	0	0	0	0	1	1	0	0	-7.009
$CaHCO_3$	0	0	0	0	0	0	0	0	0	0	1	1	0	0	1.043
$CaOH^+$	-1	0	0	0	0	0	0	0	0	0	1	1	0	0	-12.384
$CaSO_4$	0	0	0	0	0	0	0	0	1	0	0	1	0	0	2.1
$HFeO_2^-$	-3	-2	0	0	0	0	1	0	0	0	0	0	0	0	-29.202
$FeCl^-$	0	0	1	0	0	0	1	0	0	0	0	0	0	0	-0.165
FeO^+	-2	1	0	0	0	0	0	1	0	0	0	0	0	0	-5.652
$FeCl^2$	0	0	2	0	0	0	1	0	0	0	0	0	0	0	-8.181
FeO	-2	1	0	0	0	0	1	0	0	0	0	0	0	0	-20.412
$FeOH^+$	-1	1	0	0	0	0	1	0	0	0	0	0	0	0	-9.315
FeO_2^-	-4	2	0	0	0	0	0	1	0	0	0	0	0	0	-21.618
$FeOH^{2+}$	-1	1	0	0	0	0	0	1	0	0	0	0	0	0	-2.205
$FeSO_4$	0	0	0	0	0	0	1	0	1	0	0	0	0	0	2.2
$FeSO_4^+$	0	0	0	0	0	0	0	1	1	0	0	0	0	0	1.917
$HFeO_2$	-3	2	0	0	0	0	0	1	0	0	0	0	0	0	-12.021
$FeCl^{2+}$	0	0	1	0	0	0	0	1	0	0	0	0	0	0	1.475
HNO_3	1	0	0	0	0	0	0	0	0	1	0	0	0	0	-1.308
H_2SO_4	2	0	0	0	0	0	0	0	1	0	0	0	0	0	-1.021
HSO_4^-	1	0	0	0	0	0	0	0	1	0	0	0	0	0	-1.975
$HSIO_3^-$	-1	1	0	0	0	0	0	0	0	0	0	0	1	0	-9.836
$KHSO_4$	1	0	0	0	1	0	0	0	1	0	0	0	0	0	-1.502
KSO_4^-	0	0	0	0	1	0	0	0	1	0	0	0	0	0	0.875
$MgCO_3$	-1	0	0	0	0	1	0	0	0	0	1	0	0	0	-7.365
$MgHCO_3^+$	0	0	0	0	0	1	0	0	0	0	1	0	0	0	1.033
$MgOH^+$	-1	1	0	0	0	1	0	0	0	0	0	0	0	0	-11.682
$MgSO_4$	0	0	0	0	0	1	0	0	1	0	0	0	0	0	2.22
$NaHCO_3$	0	0	0	1	0	0	0	0	0	0	1	0	0	0	0.149
$NaSO_4^-$	0	0	0	1	0	0	0	0	1	0	0	0	0	0	0.696
OH^-	-1	1	0	0	0	0	0	0	0	0	0	0	0	0	-13.991

Table 6.2 – Aqueous equilibrium reactions in the reaction network for the Cr fractionation benchmark.

Each version of equation (6.21) has its own kinetic formulation, resulting in Cr fractionation:

$$^{52}r = k \, T_{52CrO_4^{2-}}$$
$$^{53}r = k \, T_{53CrO_4^{2-}} \alpha^{53}Cr(III) / Cr(VI)$$

(6.23)

where α^{53}Cr(III)/Cr(VI) = 0.9966 in this work (Wanner et al. 2014). Five kinetic heterogeneous reactions (which are indeed six when the two Cr isotopes are studied separately) are taken into account too. They are resumed in Morel-type Table 3 and the associated constants and solubility products are listed in Table 4. All minerals follow a TST type kinetic law for precipitation/dissolution:

$$r = -k \, A_S \left(1 - \left(\frac{Q}{K_S} \right)^m \right)^n$$

(6.24)

where we remind r is the reaction rate [mol/T/ M_{H2O}], $A_s = A_m / \rho_w / \phi$ [L^2-min/M_{H2O}] is the reactive surface (A_m [L^2-min/ L^3] is the specific surface reported in Table 4, ρ_w [L^3/ M_{H2O}] is water density and ϕ [-] porosity), k is the kinetic constant [mol/T/L^2], Q [-] is the ion activity product, K_S [-] is the solubility product, n and m are two exponent taken here $m=1.0$, $n=1.0$. Please note that a minus appears in equation (6.24) with respect to previous versions of the TST reaction rate because a positive reaction rate is associated to precipitation. When the two Cr isotopes are taken into account, equation (6.24) is modified according to models presented in Druhan et al. (2013):

$$^{52}Cr(OH)_3 r = -k \, A_S \, x_{52} \left(1 - \left(\frac{Q}{^{52}K_S x_{52}} \right)^m \right)^n$$
$$^{53}Cr(OH)_3 r = -k \, A_S \, x_{53} \left(1 - \left(\frac{Q}{^{53}K_S x_{53}} \right)^m \right)^n$$

(6.25)

Where $^{52}K_S$ and $^{53}K_S$ are intended equal since no equilibrium fractionation is presumed in this reaction network and $x_{52} = [\, ^{52}Cr^{3+}] / T(Cr^{3+})$, $x_{53} = [^{52}Cr^{3+}] / T(Cr^{3+})$.

	H^+	H_2O	Cl^-	Na^+	K^+	Fe^{2+}	Fe^{3+}	SO_4^{2-}	HCO_3^-	Cr^{3+}	$^{52}Cr^{3+}$	$^{53}Cr^{3+}$	SiO_2	Al^{3+}
$CO_{2(s)}$	1	-1	0	0	0	0	0	0	1	0	0	0	0	0
$Cr(OH)_3$	-3	3	0	0	0	0	0	0	0	1	0	0	0	0
$^{52}Cr(OH)_3$	-3	3	0	0	0	0	0	0	0	0	1	0	0	0
$^{53}Cr(OH)_3$	-3	3	0	0	0	0	0	0	0	0	0	1	0	0
Chamosite	-10	7	0	0	0	2	0	0	0	0	0	0	1	2
Quartz	0	0	0	0	0	0	0	0	0	0	0	0	1	0
Annite	-10	6	0	0	1	3	0	0	0	0	0	0	3	1

Table 6.3 – Morel's table for kinetic minerals for the Cr fractionation benchmark.

	Formula	Molar Volume (m^3min/mol)	$LogK_S$ (25°C)	LogKc(mol/ KgH2o/s)	A_m (m^2min/m^3m edium)
$CO_{2(s)}$	CO_2	1.0	-9.5	-4	1
$Cr(OH)_3$	$Cr(OH)_3$	29.09	9.350	-4	1
$^{52}Cr(OH)_3$	$^{52}Cr(OH)_3$	29.09	9.350	-8	1
$^{53}Cr(OH)_3$	$^{53}Cr(OH)_3$	29.09	9.350	-8	1
Chamosite	$Fe_2Al_2SiO_5(OH)_4$	106.20	32.832	-12	1
Quartz	SiO_2	22.69	-3.732	-13.4	1
Annite	$KFe_3AlSI_3O_{10}(OH)_2$	154.32	29.453	-9.5	1

Table 6.4 – For each mineral: formula, molar volume, logarithm of the solubility product, logarithm of the kinetic constant, specific surface.

6.3.2.4 Considerations about Courant number

As explained before, TRACES adopts an explicit time discretization that requires a maximum CFL (Courant-Friedrichs-Lewy) number of 1.0 (equation (6.18)). This constraint guarantees that a molecule present in cell 1 will travel at most as far as in cell 2 during the time step and won't have the time to reach cell 3. This is a condition imposed to avoid oscillations in explicit schemes and is only related to transport (reactive but also conservative). At the same time, time stepping has an impact on operator splitting errors and it may happen that a solution, to be acceptable, requires a time step lower than the one imposed by the CFL condition. Although both constraints involve the time step, they are not the same thing and there is no theoretical connection between CFL number and operator splitting errors. In CrunchFlow technical notes (Steefel 2009), it is reported that for OS3D the default initial time step corresponds to a CFL=0.5 and that operator splitting errors appear to reach a minimum for time step corresponding to a CFL=0.2. Considering the dependence of operator splitting error from time stepping, the solution of the benchmark has been repeated with several different time steps (which of course correspond to different Courant numbers).

6.3.3 Results of numerical simulations: SpeCTr

6.3.3.1 Results: $\Delta t(CFL)$, $\alpha_L = 0$ m, no Cr fractionation

The very first simulation doesn't take Cr fractionation into account. Only one primary species represents Cr(VI), CrO_4^{2-}, and only one primary species represents Cr(III), Cr^{3+}, for a total of 52 species (16 primary species of components, see Table 6.2). The simulation was performed with the maximum time step allowed by the Courant-Friedrichs-Lewy condition (CFL=1.0) and with no dispersion. Results for conservative tracer Cl^- are reported in Figure 6.3, results for major elements are reported in Figure 6.4. Spatial distribution of Cr(VI), Cr(III) and solid Cr(OH)3 after 1000 days are reported in Figure 6.5, Figure 6.6 and Figure 6.7 respectively. Concentrations computed with SpeCTr (generally reported with continuous lines) are confronted with those obtained with FLOTRAN (reported with squares), available in the supplementary material of Wanner et al. (2014). Curves are in very good agreement with published results (Wanner et al. 2014) and no further reduction of the time step seems necessary: the time step corresponding to CFL=1.0 did not introduce major or evident errors, especially for Cr^{3+} (that is involved in precipitation) and in Cr(OH)3 (that is the mineral associated to Cr^{3+} precipitation).
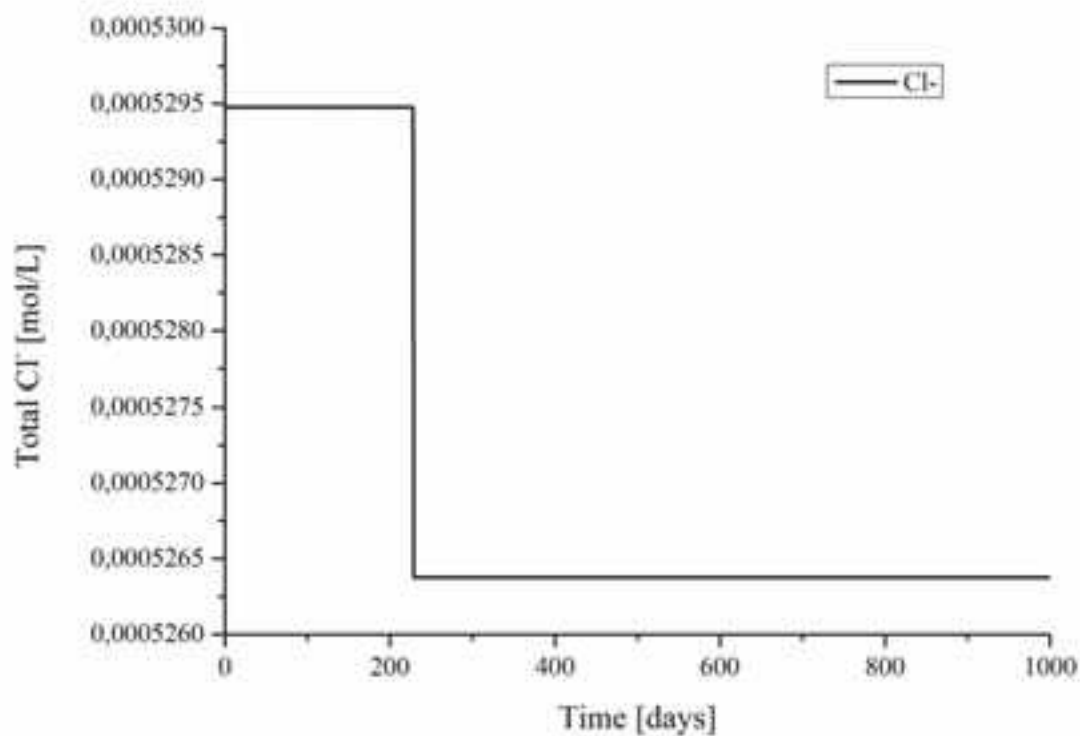
Figure 6.3 – Breakthrough curve of tracer Cl- obtained with SpeCTr at x=800 m, α_L = 0.0 m.
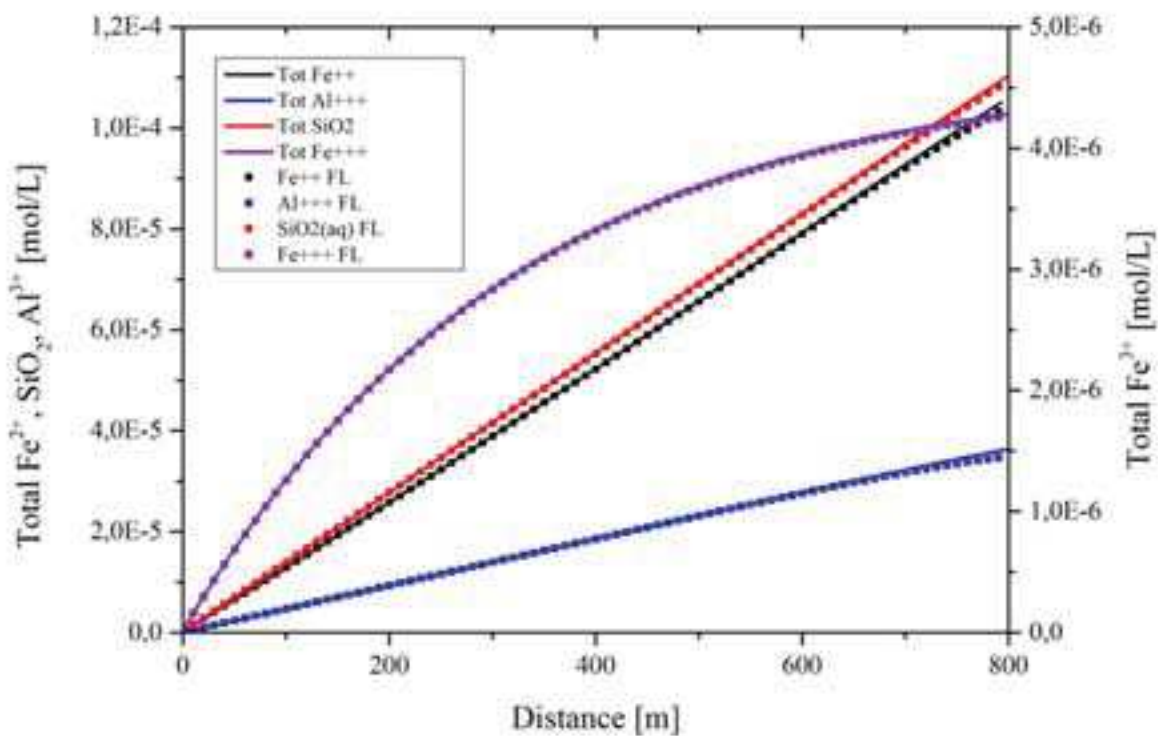
Figure 6.4 – Comparison between total concentrations of Fe^{2+}, Al^{3+}, SiO_2 and Fe^{3+} obtained with SpeCTr (continuous lines) and FLOTRAN (squares).
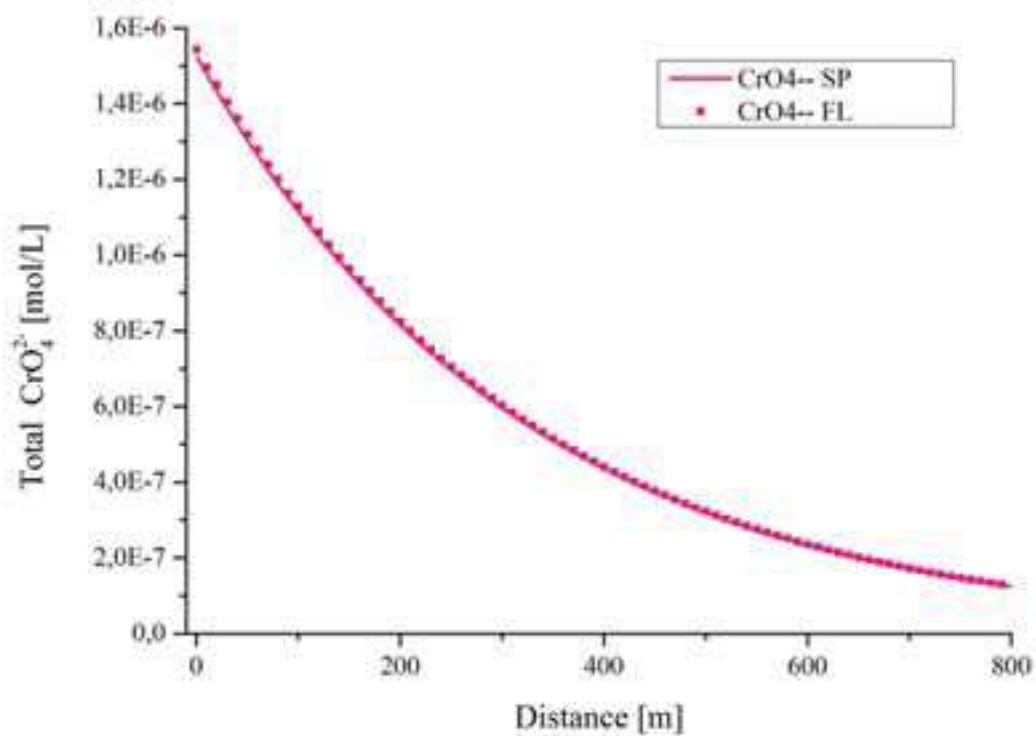
Figure 6.5 – Cr(VI) concentrations with SpeCTr (continuous line) and FLOTRAN (squares).
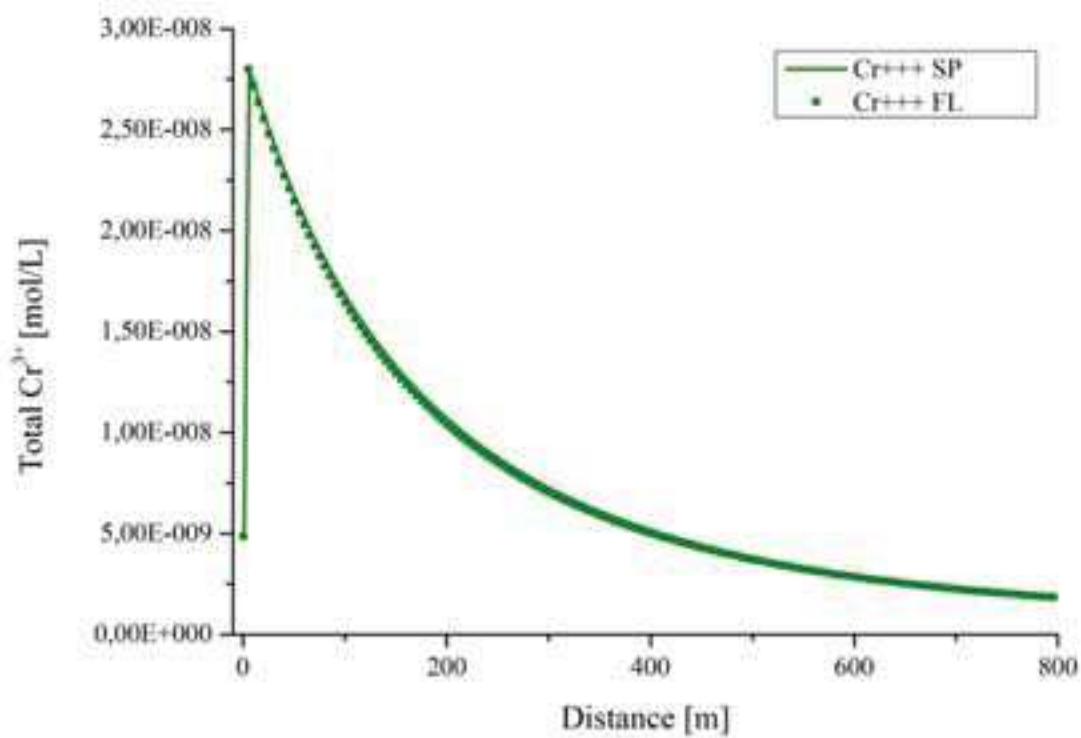
Figure 6.6 – Cr(III) concentrations with SpeCTr (continuous line) and FLOTRAN (squares).
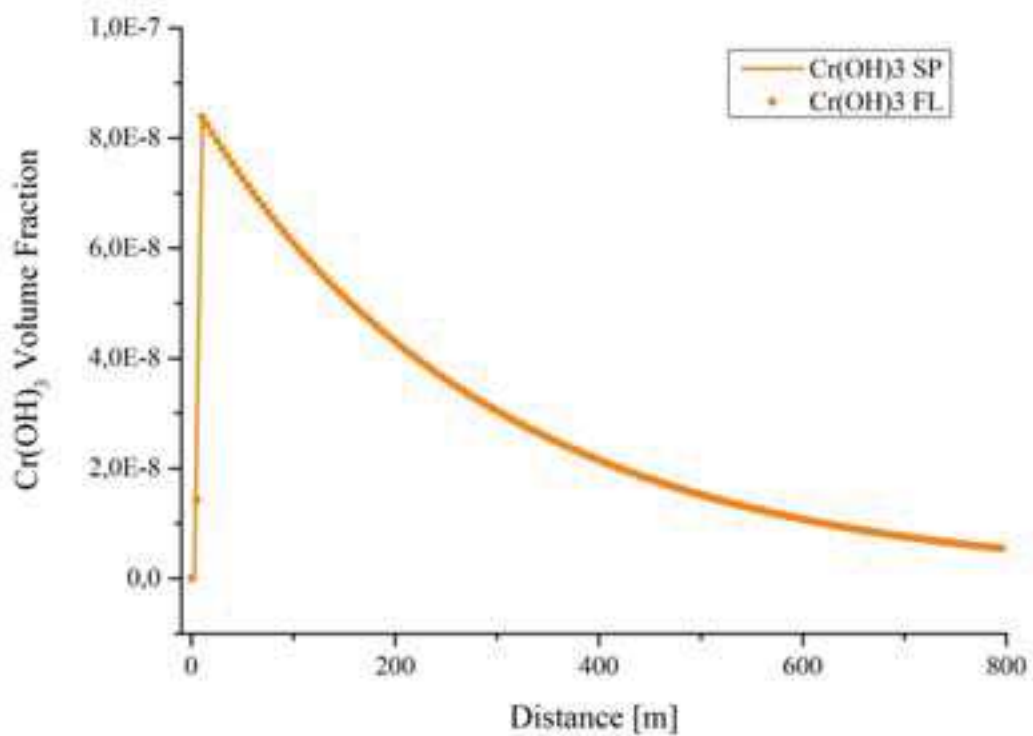
Figure 6.7 – Cr(OH)3 volume fraction with SpeCTr (continuous line) and FLOTRAN (squares).

6.3.3.2 Results: Δt(CFL=1), αL = 0 m, Cr fractionation

In this simulation, Cr fractionation is taken into account. The reaction network involves then 54 chemical species, described through 18 components or primary species. Reaction (6.21) for total Cr is substituted by two reactions that account separately for ^{52}Cr and ^{53}Cr. Precipitation of Cr(OH)$_3$ is also treated according to the model of Druhan (2013), and equations (6.25) represent the reaction rates of the end-members of what is defined a solid solution (the problem of whether the expression solid solution is pertinent was addressed in Chapter 5). Reaction network and minerals' composition are reported in Table 6.3 and Table 6.4.

Dispersivity coefficient is still fixed at $α_L = 0$ m and simulations were performed with the time step corresponding to a Courant number equal to 1.0. Concentration of tracer Cl- and major elements remain the same as in Figure 6.3 and Figure 6.4 of previous paragraph and there is no interest in reporting them again. On the contrary, in this simulations there are two curves corresponding to the two isotopes ^{52}Cr and ^{53}Cr for both Cr(VI) and Cr(III). Concentrations are reported in Figure 6.8 for Cr(VI) and in Figure 6.9 for (Cr(III)). Results seem, at least at first, in quite good agreement with those of FLOTRAN (Wanner et al. 2014).
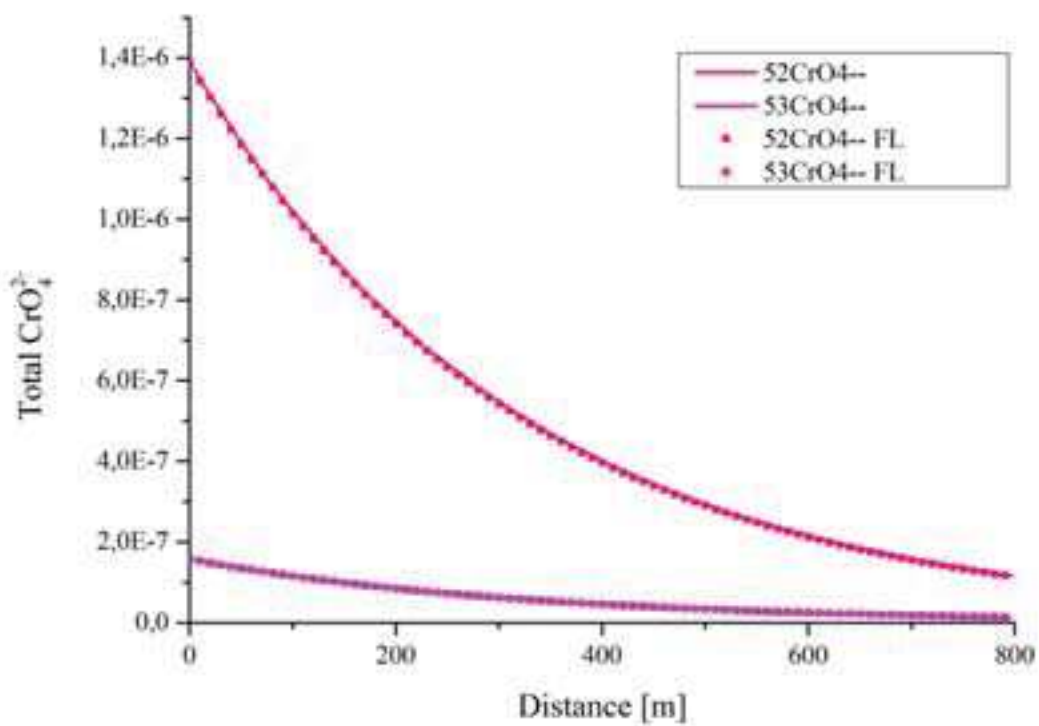
Figure 6.8 – Cr(VI): $^{52}CrO_4^{2-}$ and $^{53}CrO_4^{2-}$ with SpeCTr (continuous line) and FLOTRAN (squares).
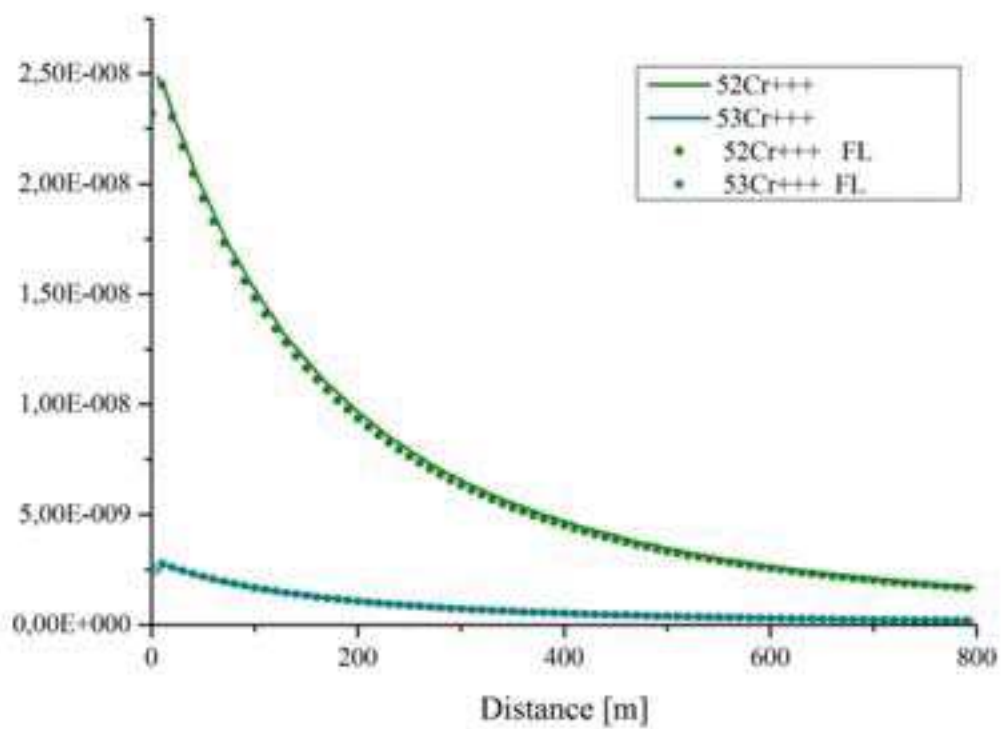
Figure 6.9 – Cr(III): $^{52}Cr^{3+}$ and $^{53}Cr^{3+}$ with SpeCTr (continuous line) and FLOTRAN (squares).
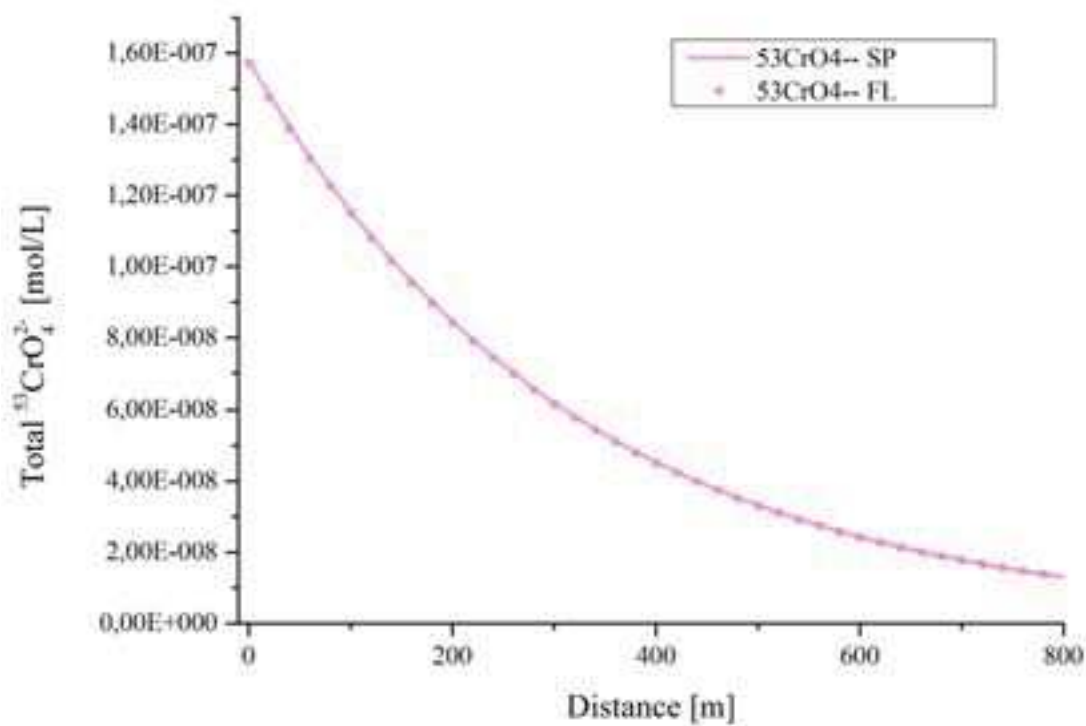
Figure 6.10 – Cr(III): $^{53}CrO_4^{2-}$ with SpeCTr (continuous line) and FLOTRAN (squares).
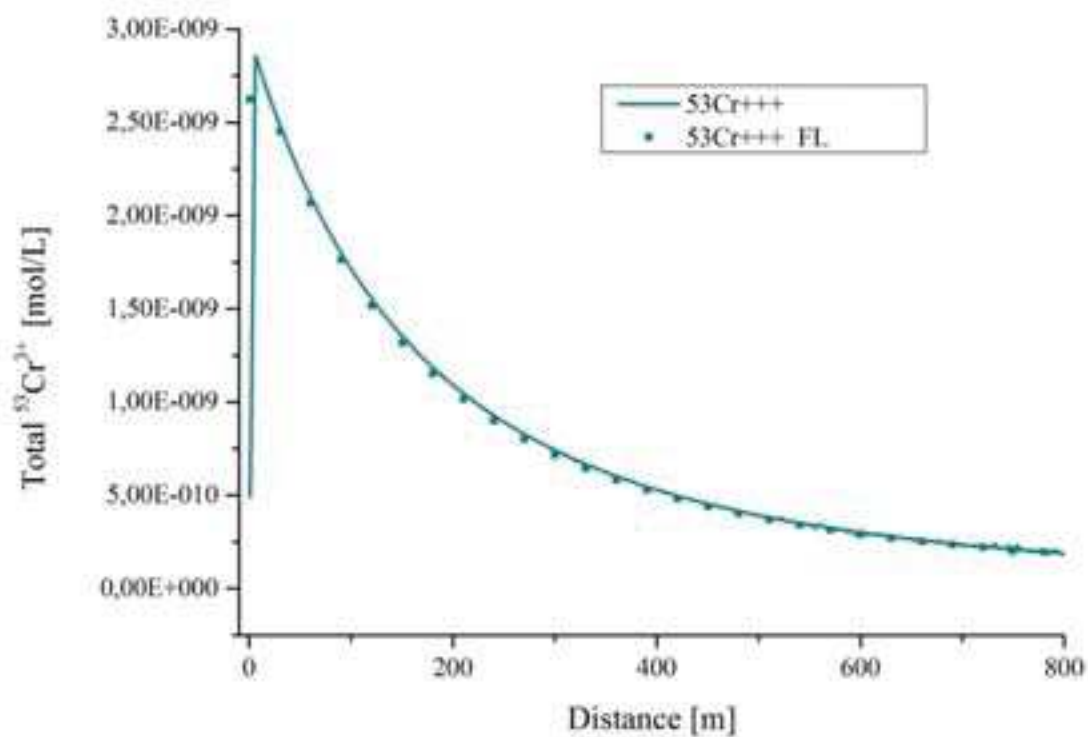
Figure 6.11 – Cr(III): $^{53}Cr^{3+}$ with SpeCTr (continuous line) and FLOTRAN (squares).

Although Figures 6.8 and 6.9 show good agreement between SpeCTr results and those of the benchmark, a closer look to the rare isotope curves shows some small irregularities (Figure 6.11) when $^{53}Cr^{3+}$ goes below the threshold of 5 10^{-10}. These irregularities are partly at the origin of disastrous results obtained during computation of the isotopic *delta* (δ) of ^{52}Cr and ^{53}Cr. We remind that isotopic delta is computed as follows:

$$\delta^{53}Cr_{SRM979} = \frac{R(^{53}Cr / ^{53}Cr)_{model}}{R(^{53}Cr / ^{53}Cr)_{SRM979}} - 1 \tag{6.26}$$

where $R(^{53}Cr/^{52}Cr)_{model}$ is the computed isotopic ratio and $R(^{53}Cr/^{52}Cr)_{SRM979}$ is the isotopic ratio from a standard reference (in Wanner et al. (2014) $R(^{53}Cr/^{52}Cr)_{SRM979} = 0.11339$).

$\delta^{53}Cr$ expressed in ‰ obtained with SPeCTr is reported in Figure 12 (Cr(VI)) and 13 (Cr(III)). Oscillations are present for both Cr(VI) and Cr(III) although the amplitude of oscillations of $\delta^{53}Cr(III)$ is orders of magnitude higher. They increase at around 300 m from the origin for Cr(III), when $^{53}Cr^{3+}$ concentrations go below 1 10^{-9} and become huge in correspondence of irregularities detected in the last part of the curve depicted in Figure 6.11.
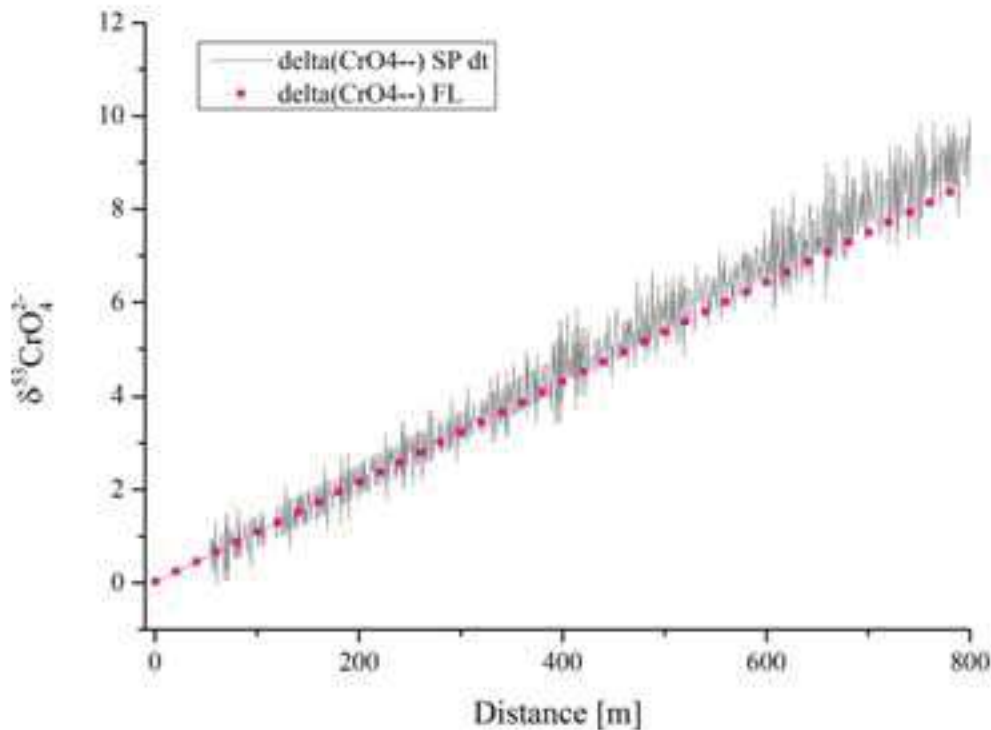
Figure 6.12 – $\delta^{53}Cr(VI)$ with SpeCTr (grey continuous line) and FLOTRAN (pink squares).
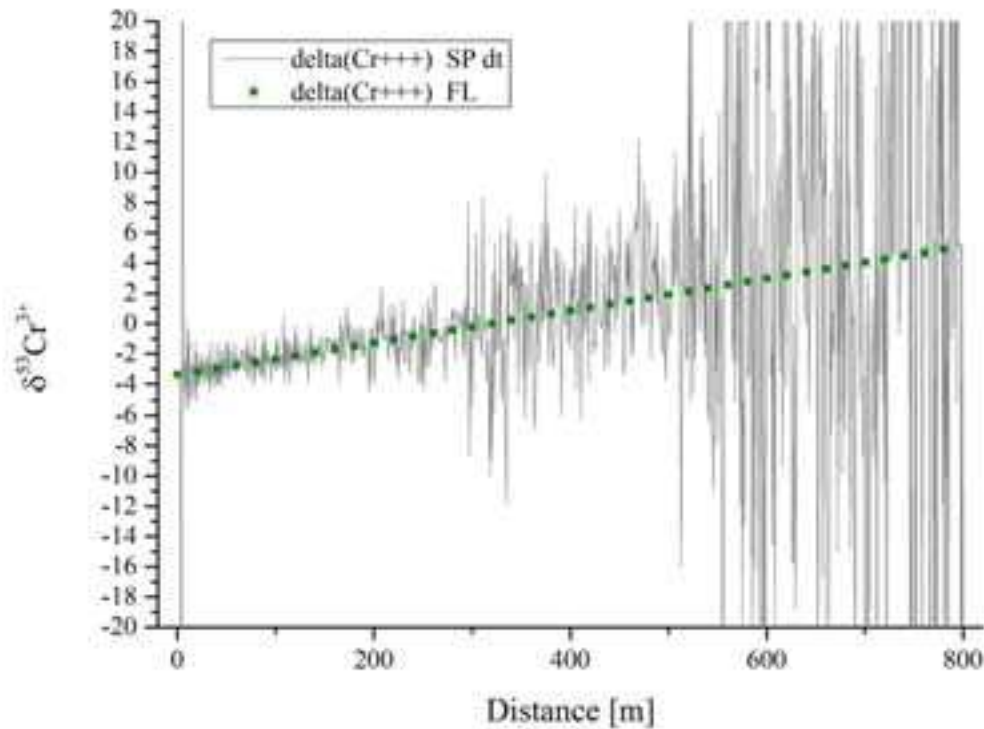
Figure 6.13 – δ^{53}Cr(III) with SpeCTr (grey continuous line) and FLOTRAN (green squares).

Possible reasons of the irregularities detected for very low concentrations of ^{53}Cr^{3+} (Figure 6.11) and oscillations of the isotopic δ^{53}Cr are: i) error due to operator splitting and excessive time step length ii) sharp fronts obtained thanks to finite elements with $\alpha_L = 0$ are challenging when transport and reaction are coupled iii) at low concentrations the chemical solver approaches its limits and is not able to guarantee accurate solutions iv) a combination of the previous.

The most immediate strategies to exclude liabilities of reaction module are: i) lowering the time step length ii) increasing values of longitudinal dispersion to $\alpha_L = 0.54$, $\alpha_L = 1.0$ (corresponding to numerical dispersion detected in CrunchFlow and TOUGHREACT, MIN3P and FLOTRAN respectively (Wanner et al. 2014). Other, more time-consuming strategies would be: iii) using an alternative numerical method to solve the mix of kinetic and equilibrium reactions (the explicit solver already available) iv) using another solver for transport v) a combination of the previous.

In the following paragraphs, the fastest strategies to put in place (increasing the time step and/or the dispersion) are put in place.

Simulation presented in paragraph 6.3.3.2 was repeated with a reduced time-step: the time step Δt imposed by CFL condition was divided by a factor 5 (Δt / 5) keeping the value of longitudinal dispersivity to $\alpha_L = 0$.

Figure 6.14 shows that the curve of Cr(III) is almost perfectly smooth (a nearly invisible imperfection is present at around 200 m corresponding to a concentration of $1 \cdot 10^{-9}$ mol) and that the oscillations in the last part of the curve visible in Figure 6.11 have disappeared. Figure 6.15 shows the $\delta^{53}Cr$ expressed in ‰: the improvement with respect to the $\delta^{53}Cr$ computed with a time step five times bigger is striking. $\delta^{53}Cr(VI)$ is perfectly superposed to FLOTRAN results, while $\delta^{53}Cr(III)$ still shows some oscillations. The most important oscillation in Figure 6.15 appears at around 200 m, in correspondence of the imperfection in Figure 6.14. While the oscillations around x = 0 m are explicable with the proximity to boundary conditions (Cr starts to precipitate), the reason of the presence of an imperfection at x = 200 m (or between 500 and 600 m to a lesser extent) is not explicable.

These results clearly demonstrate the impact of operator splitting errors on the computation of isotopic delta, showing that a meaningless isotopic delta can be obtained even starting from concentrations that seem acceptable.
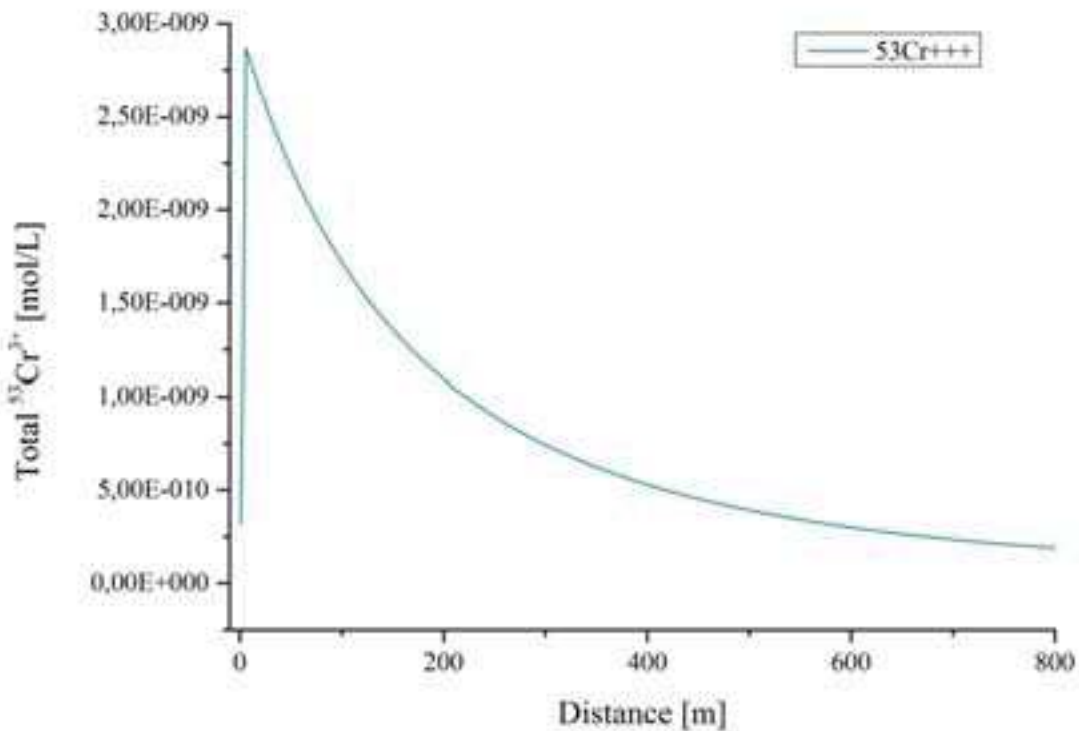
Figure 6.14 – Cr(III): $^{53}Cr^{3+}$ with SpeCTr (continuous line), transport time-step Δt / 5, and $\alpha_L = 0$.
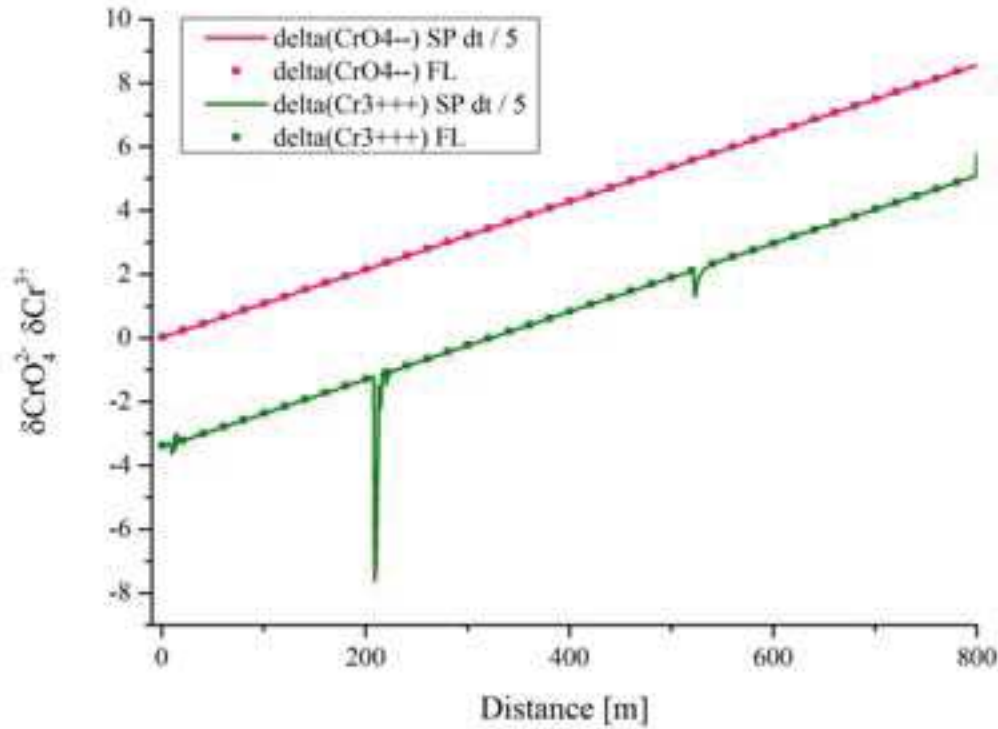
Figure 6.15 – δ^{53}Cr(VI) (pink) and δ^{53}Cr(III) (green) with SpeCTr (continuous lines) and FLOTRAN (squares), transport time-step Δt / 5, α_L = 0 m.

6.3.3.2 Results: Δt (CFL=1), α_L = 1.0 m, Cr fractionation

In order to gain some more insight on the oscillations reported in isotopic delta δ^{53}Cr, a simulation was performed with a non-zero value of longitudinal dispersivity (α_L = 1.0 m), keeping Δt to its original value (CFL=1.0). Figure 6.16 shows the transformation of the curves of conservative tracer Cl⁻ when longitudinal dispersivity moves from 0 to 1 m. We remind that α_L = 1.0 m is the value that matches numerical dispersion generated by finite differences in codes MIN3P and FLOTRAN.

Imposing α_L = 1.0 has some impact on the results of δ^{53}Cr, although it seems to modify the oscillations instead of eliminating them as the reduction of the time step did. Amplitude of δ^{53}Cr(VI) oscillations (see Figure 6.17) is slightly reduced but some kind of deviation to higher values of the isotopic delta seem to appear at 500 m. On the other hand, δ^{53}Cr(VI) oscillations are somehow worsened (see Figure 6.18), especially with respect to the first 300 m of Figure 6.13.

A partial conclusion is that, although changes in dispersivity modify the oscillations, the absence of dispersion is certainly not their cause. This information is really valuable because it allows to fully exploiting the characteristic of modeling sharp fronts of discontinuous Galerkin finite elements.
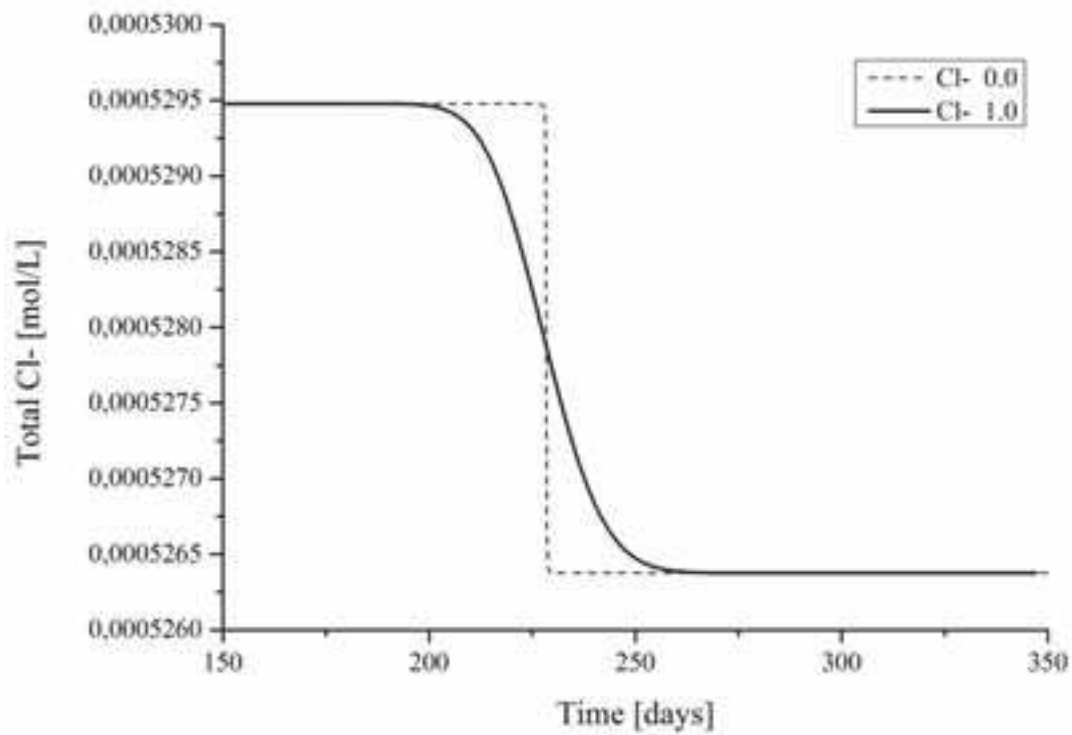
Figure 6.16 – Breakthrough curve of tracer Cl⁻ obtained with SpeCTr at x=800 m, α_L = 1.0 m (continuous) and α_L = 0.0 (dashed).
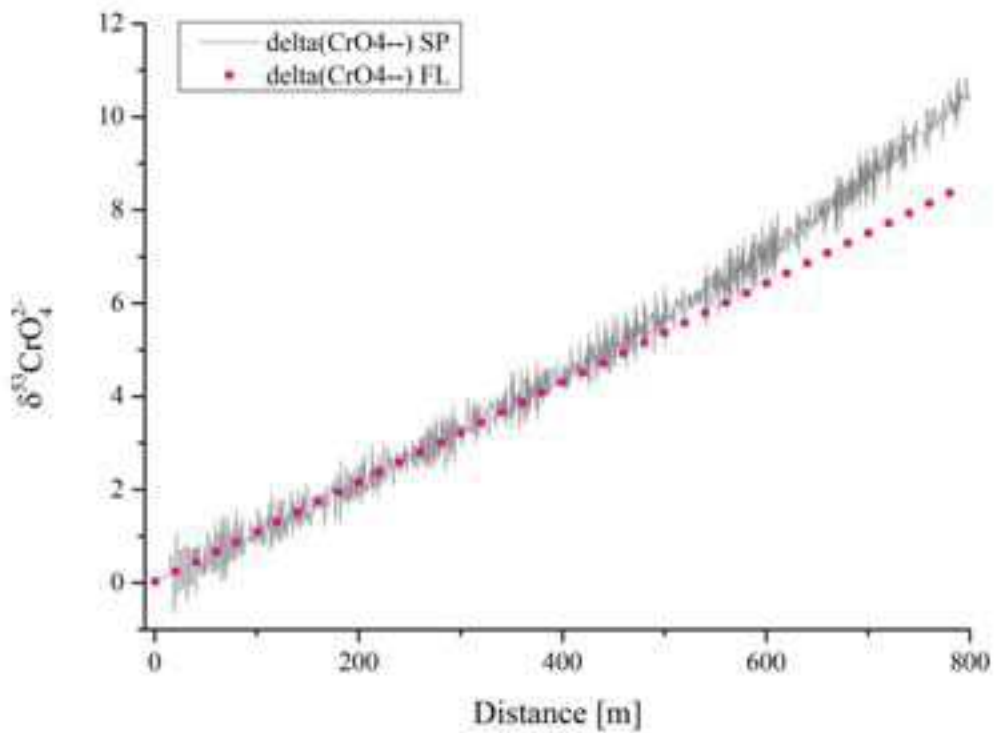
Figure 6.17 – δ^{53}Cr(VI) with SpeCTr (grey continuous) and FLOTRAN (pink squares), α_L = 1.0 m.
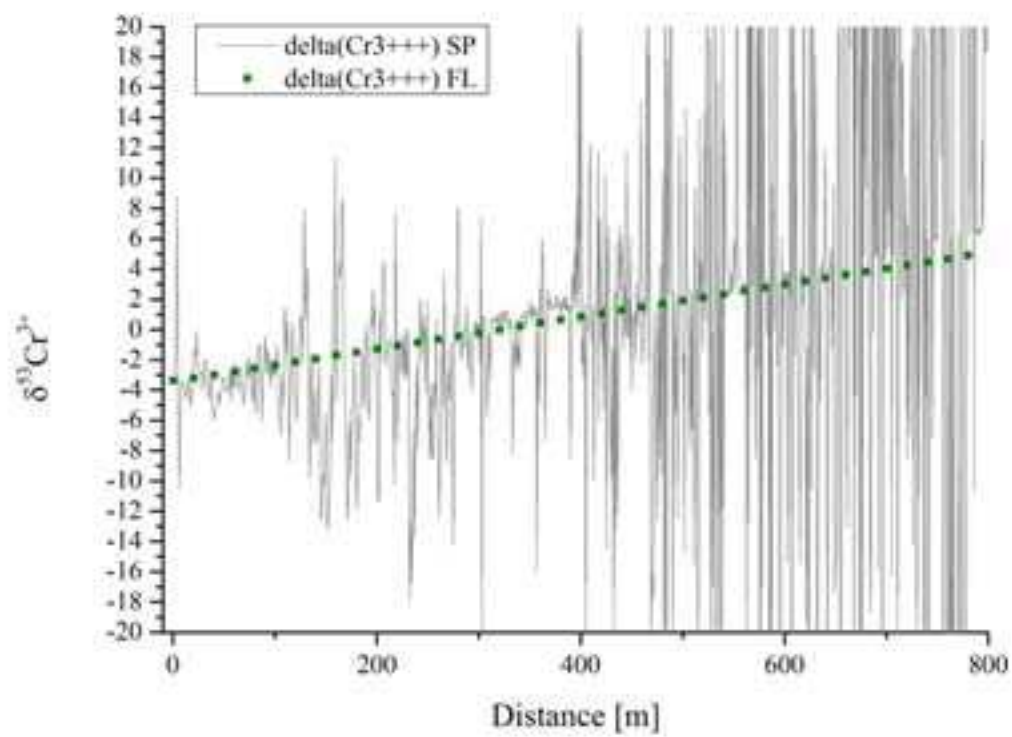
Figure 6.18 – $\delta^{53}Cr(III)$ with SpeCTr (grey continuous) and FLOTRAN (green squares), $\alpha_L = 1.0$ m.

6.3.3.3 Results: reduced time step, $\alpha_L = 0.54$ m, Cr fractionation

Another series of simulations was performed with time steps $\Delta t / 5$, $\Delta t / 10$, $\Delta t / 25$, corresponding to CFL numbers ranging from 0.2 to 0.04 and nonzero dispersion coefficient in order to test the combined effect. These simulations were performed with a dispersivity coefficient $\alpha_L = 0.54$, the value corresponding to numerical dispersion in CrunchFlow and TOUGHREACT. This value is intermediate with respect to previous two ($\alpha_L = 0$, $\alpha_L = 1$) and its effect on Cl breakthrough curve is reported in Figure 6.19.
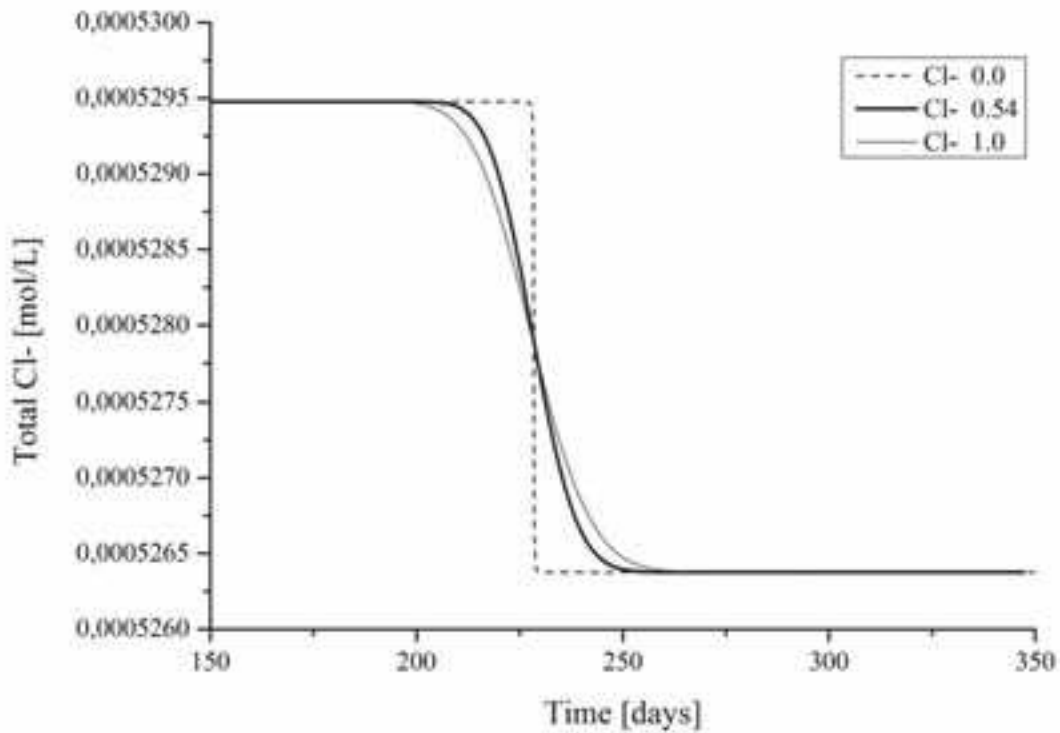
Figure 6.19 –Breakthrough curve of tracer Cl obtained with SpeCTr at x=800 m, $\alpha_L = 1.0$ m (continuous line), $\alpha_L = 0.54$ m (continuous thick line), and $\alpha_L = 0$ (dashed line).

Figure 20 shows the $\delta^{53}Cr$ expressed in ‰ for a time-step $\Delta t / 5$ (CFL=0.2), which is again an obvious improvement with respect to $\delta^{53}Cr$ computed with Δt and a slight improvement to $\delta^{53}Cr$ computed with $\Delta t / 5$ and $\alpha_L = 0$. To further confirmation that the oscillations of $\delta^{53}Cr$ are due to excessive amplitude of the time-step, simulations with $\Delta t / 10$ and $\Delta t / 25$ were also performed; Figure 6.21 shows values of $\delta^{53}Cr(III)$ throughout the domain. Oscillations at the beginning of the domain completely disappear at $\Delta t / 25$ while oscillations between 500 m and 600 m persist. Figure 6.22 shows that oscillations are translated (they occur later in space) and somehow smoothed by the reduction of the time-stepping.
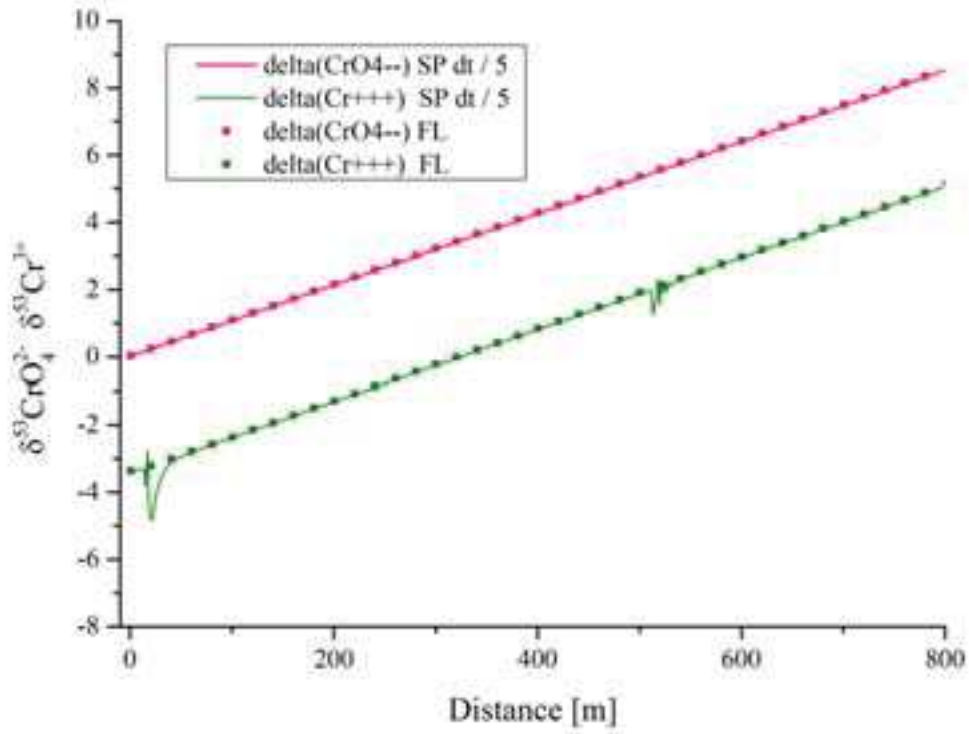
Figure 6.20 – $\delta^{53}Cr(VI)$ and $\delta^{53}Cr(III)$ with SpeCTr (continuous line) and FLOTRAN (squares), transport time-step $\Delta t / 5$, α_L=0.54 m
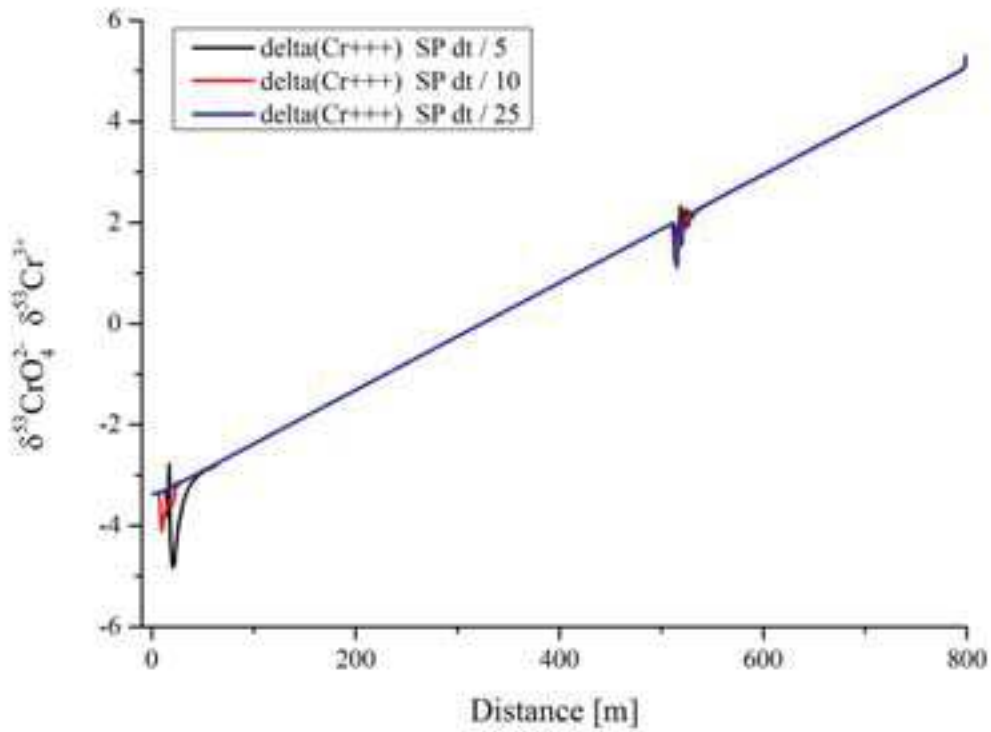
Figure 6.21 – $\delta^{53}Cr(III)$ for transport time-step $\Delta t / 5$ (black), $\Delta t / 10$ (red), $\Delta t / 25$ (blue) all computed with SpeCTr, α_L=0.54 m.
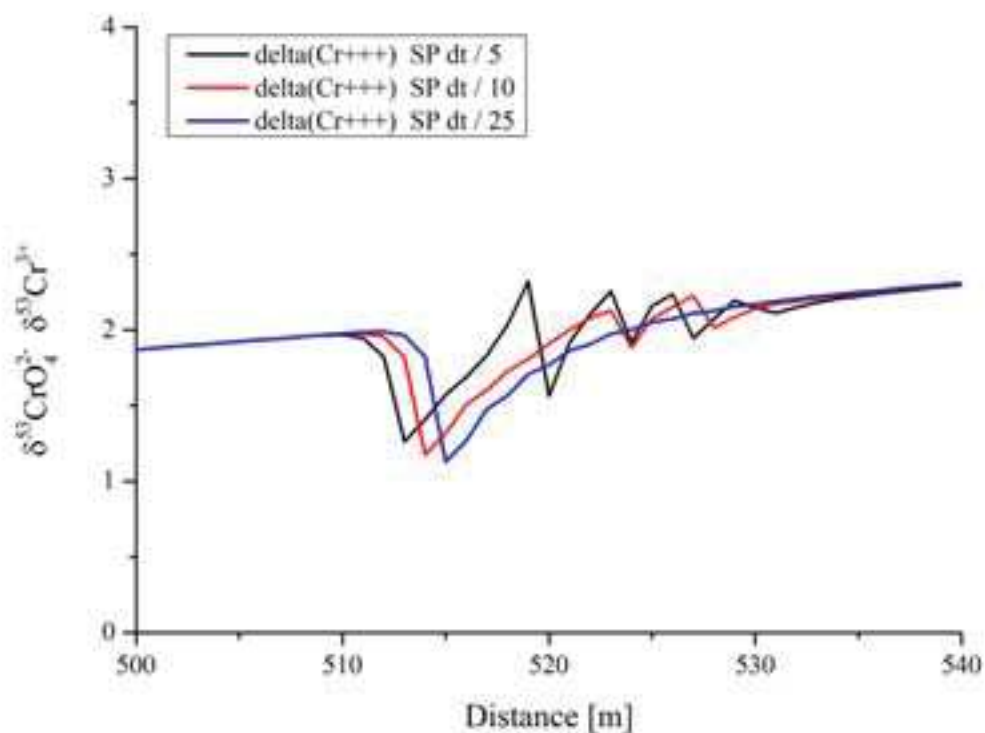
Figure 6.22 – δ^{53}Cr(III) for transport time-step $\Delta t / 5$ (black), $\Delta t / 10$ (red), $\Delta t / 25$ (blue) all computed with SpeCTr, zoom between 500 m and 540 m.

The position and amplitude of oscillations of δ^{53}Cr(III) changes with the value longitudinal dispersivity and is impossible to individuate a trend (oscillations do not systematically increase or decrease with longitudinal dispersivity). Considered that the porous medium is homogeneous and that precipitation of Cr(OH)3 occurs all along the domain, reasons for the oscillations are also hard to explain geochemically.

6.4 Conclusions about SpeCTr validation

Results presented in this chapter show that the implementation of isotopes implies working with increasingly low concentrations, thus leaving virtually no place for numerical errors. In fact, solutions that could be considered successful if computations were limited to major elements (or even for elements at low concentrations, around an order of magnitude of 10^{-10}) may still be considered a failure when computing isotopic ratios or isotopic delta.

Reduction of the time step resulted crucial to obtain useful curves of isotopic delta (δ); although some inaccuracies remained in one of the computed isotopic delta, results can be considered quite satisfactory. Further reductions of the time step reduced oscillations but did not eradicate them; therefore the increase in the computational time generated by excessively small time steps is not justified.

Introducing longitudinal dispersion had an ambiguous impact on results. It brought some benefice to the regularity of one isotopic delta but at the same time worsened the other when introduced while computing with the maximum time step. While working with a reduced time step, the introduction of longitudinal dispersivity smoothed some of the oscillations and slightly increased others. The hypothesis that extremely sharp fronts may be at the origin of oscillations was definitely excluded.

The fact that such important oscillations were cleaned up with the sole reduction of the transport time-step partially cleared the reputation of the chemical solver, proving that it is not the principal cause of delta oscillations and that it can properly handle low concentrations. Also, the subroutine handling the passage between finite elements node concentrations to a mean value to be used in the reaction module was proved not responsible for the oscillations.

Although it didn't minimize errors, performing the simulation with a time step five times smaller than the one imposed by the CFL condition constitutes the best compromise between the quality of the results and the computational cost. This time step corresponds to a CFL = 0.2, which is the same recommended in CrunchFlow technical note.

Chapter 7 – Application of SpeCTr: modeling Calcite dissolution & precipitation

This chapter is dedicated to the application of SPeCTr to reactive transport problems involving Calcite dissolution and precipitation.

Calcite dissolution is modeled in relation to column and batch experiments performed in the context of A. Buissonnié's Ph.D. work that resulted in a paper submitted to *Chemical Geology* (Bouissonnié et al, 2018). In the paper, a series of pseudo-2D simulations are performed with SPeCTr in order to model experimental results of Calcite dissolution rate. Simulations were repeated with different models for reaction rates (classical Transition State Theory or TST and the stepwave model SWM (Lasaga and Luttge (2001), Gruber et al (2014)) and with different values of transport parameters. The details about the setup of the experiment, the different models implemented in SpeCTr for reaction rates, flow and transport parameters are reported in Bouissonnié et al. (2018) that included in this work as section 7.1. In section 7.2 is reported the preparatory work for Bouissonnié et al. (2018) including simulations with different mesh sizes and different time-stepping in order to avoid dependencies of the results from spatial and time discretization.

Calcite precipitation was explored through the simulations of experimental results of calcite precipitation caused by mixing at the interface of two potentially reactive solutions (Katz et al., 2009). In Katz et al. (2009), experimental results were accompanied by 2D numerical simulations in heterogeneous porous medium performed with the code Retraso (Saaltink et al. 2004). Simulations carried out with Retraso were performed with SPeCTr in order to assess similitudes and differences with the results in Katz et al (2009). Results of simulations (equilibrium and kinetic precipitation, constant and variable porosity) are reported in section 7.3.

7.1 From mixed flow reactor to column experiments and modeling: upscaling of calcite dissolution rate

Arnaud Bouissonnié, Damien Daval, Marianna Marinoni, Philippe Ackerer
Laboratoire d'Hydrologie et de Géochimie de Strasbourg, Université de Strasbourg /EOST-CNRS
UMR 7517, 1 Rue Blessig, 67084 Strasbourg, France

7.1.1 Abstract

The objective of this work was to assess the extent to which calcite dissolution rate ($R_{calcite}$) measured at controlled saturation state in mixed flow set-ups could be upscaled to column experiments, where the solution composition was variable in space and time. The dissolution rate of the {104} calcite face was investigated in mixed flow reactor set-ups at room temperature and pH 8. Various saturation conditions were studied by changing the composition of the inlet solution, enabling to determine an empirical relation between $R_{calcite}$ and the Gibbs free energy of calcite dissolution (ΔG) by measuring the surface topography with vertical scanning interferometry (VSI). The prevalent dissolution mode (i.e., etch pit nucleation or homogeneous surface retreat) was assessed with the same method. A dramatic decrease of the dissolution rate was observed for $-8 < \Delta G < -3$ kJ/mol, correlated with a switch in the dissolution regime (inhibition of etch pit nucleation). The resulting $R_{calcite}$-ΔG relation, which is at odds with that derived from the transition state theory (TST), was successfully fitted using the stepwave model (SWM). These experiments were supplemented with plug-flow column experiments, consisting of a chemically inert porous medium and oriented rhombohedral calcite single-crystals (0.4×0.4 cm²) regularly distributed in the column. The dissolution rates of calcite single crystals all along the column were retrieved using VSI on the recovered crystals at the end of the experiments. These latter experiments were compared with 1D and 2D reactive transport simulations, using either the TST- or the SWM-derived rate equation determined from our mixed-flow reactor experiments. The reactive transport simulations revealed that (i) 1D-simulations overestimate the dissolution rate of upstream and downstream calcite faces by a ~3- and ~20-fold factor, (ii) 2D-simulations satisfactorily reproduce the dissolution rates of all faces without any fitting parameter, within experimental uncertainties and (iii) both models slightly overestimate the steady-state concentration of calcium at the outlet of the column. Overall, this study can be considered as one of the multiple intermediate steps between chemostatic experiments and field measurements to assess the validity of the classical bottom-up upscaling approach. It also provides insights into our ability to model fluid flow and solution composition in the vicinity of dissolving single crystals.

7.1.2 Introduction

Considerable advances concerning our understanding of chemical weathering processes and their impact on water chemistry or Earth's climate occurred over the last decades. Various processes impact weathering, but one of the most significant is the chemical weathering (dissolution or precipitation) of minerals. The kinetics of these reactions contribute to (bio)geochemical cycles as important as the C cycle, as the chemical weathering of silicate and carbonate minerals represents a net sink for CO_2 over long (Berner, 1990) and short (Beaulieu et al., 2012) timescales, respectively. As a consequence, a significant body of experimental and theoretical studies was dedicated to the development of kinetic rate laws of mineral dissolution and precipitation (Brantley and Olsen, 2014). However, bridging the gap between laboratory experiments and field data remains an elusive goal, as mineral dissolution/precipitation rates measured in laboratory generally remain orders of magnitude greater than those measured in the field (Fischer et al., 2014; White and Brantley, 2003). A common way to circumvent this upscaling issue consists in tuning several modeling parameters (e.g., Aradóttir et al., 2012; Montes-H et al., 2005), albeit this strategy is not devoid of risks, since it does not account for the mechanistic origins of the so-called "field-lab" discrepancy.

Several non-exclusive explanations have been proposed to account for such discrepancies, which can be divided into intrinsic and extrinsic and factors (White and Brantley, 2003). Intrinsic factors are related to the physicochemical properties of the reacting mineral itself, such as the density of line defects (e.g., screw dislocations) outcropping at the mineral surface (Fischer et al., 2012; Macinnis and Brantley, 1992; MacInnis and Brantley, 1993; Pollet-Villard et al., 2016b; Smith et al., 2013; Teng, 2004), which represent favorable surface energy sites that promote the nucleation of etch pits (Lasaga and Blum, 1986; Pollet-Villard et al., 2016b), or the distribution of crystal morphologies, which results in a wide range of crystal reactivity due to dissolution anisotropy (Daval et al., 2013; Godinho et al., 2012; Pollet-Villard et al., 2016a; Smith et al., 2013). Extrinsic factors encompass all processes and parameters that are not derived from the nature of the dissolving mineral, such as the microbial activity or the chemical composition of the aqueous phase and in particular, the saturation state of the solution with respect to the considered mineral (Schott et al., 2009; Smith et al., 2013; Teng, 2004). In that respect, it has been suggested that the effect of the driving force of the reaction (i.e., the Gibbs free energy of reaction, ΔG) on the dissolution rate (R), often implemented in reactive transport codes by using a relation derived from the transition state theory (TST; Eyring, 1935; Lasaga, 1995), fails to account for the actual R–ΔG relations (e.g., Burch et al., 1993; Lasaga and Luttge, 2001; Pollet-Villard et al., 2016a; Smith et al., 2013), and that the use of alternative relations such as the stepwave model (Lasaga and Luttge, 2001) helped to improve the agreement between modeled and measured weathering rates (Maher et al., 2009). Hence, a possible improvement of the reliability of reactive transport simulations (at least partly) relies on the implementation of the actual dependence of mineral dissolution rates on the solution saturation state.

Closely related to the issue of R–ΔG relations, other critical extrinsic factors that may contribute to bridging the gap between laboratory- and field-derived chemical weathering rates are the knowledge of the local fluid composition surrounding the dissolving minerals that impacts their dissolution rates (Molins et al., 2014; Noiriel and Daval, 2017), and the existence of diffusive boundary layers (Ruiz-Agudo et al., 2016).

In general, flow and solute transport in a porous material are modelled at the scale of a representative elementary volume (REV) where the porous material is described as continuous. Depending on the spatial discretization of the domain (1D to 3D, size of the control volume used to compute the numerical solution), the computation of the fluid velocity will show different kinds of variability. Conversely, at the pore scale, flow paths are complex and might have a significant impact on the reactivity of a given geological formation. In that respect, the use of geochemical models in a simplified 1D geometry (e.g., WITCH; Godderis et al., 2006) allows for fast computation, but may miss important issues related to the complex fluid velocity around minerals and to the mixing due to lateral dispersion/diffusion in case of concentration gradients.

The objective of this work was to quantify the dissolution rate of calcite using mixed flow reactor (MFR) experiments performed on cleaved and polished {104} calcite surfaces and to use the corresponding model and parameters to evaluate the dissolution of calcite under different flow conditions, i.e. in a column filled with porous inert material. The key question that we aimed to tackle can be summarized as follows: can we use the dissolution rate law defined by experiments performed in MFR without porous material and in turbulent flow conditions to model the dissolution rate of calcite measured in a column filled with porous material under laminar flow and in cylindrical configuration? Furthermore, because column experiments are usually described in one dimension, we also analyzed the effects of this additional simplification on the modelling of the dissolution processes. This comparison can be considered as one of the many intermediate steps between chemostatic experiments and field tests to assess the validity of the classical bottom-up upscaling approach (see e.g. Galeczka et al., 2014; Molins et al., 2014 for similar attempts). It also provides insights into our ability to model fluid flow and solution composition in the vicinity of dissolving single crystals.

7.1.3 Materials and experimental methods

7.1.3.1 Sample preparations

A decimeter-sized calcite sample (see Table 1 for chemical composition) optically transparent coming from the Massif des Ecrins (Alpes, France) was cleaved following the natural {104} calcite plane to obtain several single crystals of calcite with a size ranging from 0.3 to 0.6 cm. The crystallographic orientation was verified over the entire surface of each sample using electron backscatter diffraction (EBSD) on a Tescan Vega 2 scanning electron microscope (SEM). Each sample was subsequently

polished down to the nanometer-scale in aqueous solution saturated with respect to calcite to avoid etching of the surface through a multi-step abrasive sequence. The obtained samples had a similar initial average arithmetic roughness (Ra), defined as the arithmetic average of the absolute values of the roughness profile, ranging between 43 and 100 nm, enabling us to minimize the effect on the dissolution rate of various step densities on the mineral surfaces. This initial roughness parameter was measured on 350×85 μm² images collected using vertical scanning interferometry (VSI, see below).

Two types of experiments were conducted: mixed-flow reactor experiments and a flow-through column experiment. Regarding mixed-flow reactor experiments, only one face was polished whereas for the column experiment, both the front (upstream) and back (downstream) faces of each crystal were polished (see sections 2.3 and 2.4).

Finally, for each sample, a portion of the surface was masked with either RTV glue or CrystalBond^{TM} (CB) for mixed flow or column experiments, respectively. This protocol allowed for preventing interactions between the portion of the mineral underneath the mask and the fluid and thus, to maintain a non-reacted surface to measure the height difference between the masked and unmasked portions (that is, the dissolution rate) using VSI.

7.1.3.2 Aqueous solution preparations

Reagent-grade NaCl, $NaHCO_3$ and $CaCl_2$ were added to ultra-pure water (18 MΩ.cm) in different concentrations similar to Smith et al. (2013): 5.85 g/L of NaCl were added to fix the ionic strength to approximately 0.1 molal. The addition of 0.086 g/L of $NaHCO_3$ enabled to fix the alkalinity, and various concentrations of $CaCl_2$ were used to vary the saturation index of the solution with respect to calcite (see Table 2). Before experiments, the solutions were left at rest during a day to allow the equilibration with atmospheric CO_2. Measured pH of these solutions were equal to 8.0 ± 0.1.

7.1.3.3 Mixed flow reactor experiments

Classical mixed-flow reactor experiments such as described in e.g. Pokrovsky and Schott (2000) were conducted on calcite single crystals as a function of the solution saturation state. In brief, a 50mL Teflon reactor containing the single-faced polished calcite samples placed on a Teflon tripod and a Teflon-coated stir bar was connected with Tygon tubing to a Gilson Minipuls 3 peristaltic pump running at a constant flow rate (0.25 mL/min). The aqueous solution at the outlet of the reactor was regularly sampled for pH and calcium measurements. All experiments were run for 7 to 9 days in an air-conditioned room at 22±1 °C. The experimental apparatus is illustrated in Figure 7.1a.

7.1.3.4 Column experiment

To investigate the effects of the velocity variability at the calcite surface, of the mixing through dispersion and more generally, of the role of aqueous concentration gradient, a column experiment was performed (Figure 7.1b). A 15 cm-long and 3.75 cm in diameter column was filled with inert zirconia beads (yttria stabilized, 1 mm in diameter, American Elements®), which resulted in an idealized inert porous medium with 38% porosity. Eight partially masked samples of rhombohedral calcite polished on their two opposite {104} surfaces were placed horizontally every 1.5 cm in the mean flow direction. The solution (5.83 g/L of NaCl, 0.0812g/L of $NaHCO_3$) was injected at the bottom of the column at a flow rate of 0.25 mL/min via a Gilson Minipuls 3 peristaltic pump. The outlet solution was regularly sampled for pH and Ca^{2+} concentration measurements. The experiment was run in an air-conditioned room at 22±1 °C during 10 days.

7.1.3.5 Aqueous sample analyses and thermodynamic calculations

The experiments were regularly sampled for pH measurements and chemical analyses. Calcium concentration was determined from inductively coupled plasma atomic emission SPeCTroscopy (ICP-AES) data acquired with a ThermoICAP 6000 Series apparatus. The measured aqueous concentration of Ca^{2+} together with the known concentrations of the chemical reagents introduced in the inlet solution were implemented in the CHESS code (van der Lee and De Windt, 2002) to calculate the in situ pH and saturation indices with respect to calcite dissolution. Activity coefficients for aqueous species were calculated using the Davies equation.

7.1.3.6 Determination of calcite dissolution rate

Average changes in height measured by VSI (Zygo NewView 7300) between the unreacted reference surface and the reacted mineral surface allowed for the determination of the nanoscale dissolution rate of the specific face following (e.g., Smith et al., 2013):

$$R = \frac{\Delta h}{\Delta t} \frac{1}{V_m} \qquad (7.1)$$

where R is the dissolution rate (mol/m²$_{min}$/s), Δh is the average height difference (m) between the reacted and the non-reacted surface, Δt is the experiment time (s) and V_m is the molar volume of calcite (m³/mol). The data were analyzed with the Metropro software (stitch7k application).

Elements	Loss 1000°C %	CaO %	MgO ‰	MnO ‰	Sr ppm
Calcite	42.3	57.2	2	0.08	475

Table 7.1. Chemical composition of calcite used in experiments. Concentrations are determined from 3g of calcite by loss on ignition and alkaline fusion.

Experiment	NaCl (g/L)	NaHCO3 (g/L)	CaCl2 (g/L)	Ω
Stirred-reactor	5.8	0.087	0	0
Stirred-reactor	6.1	0.086	0.014	0.054
Stirred-reactor	5.8	0.085	0.028	0.11
Stirred-reactor	5.8	0.086	0.05	0.201
Stirred-reactor	5.9	0.09	0.07	0.24
Stirred-reactor	5.8	0.084	0.09	0.31
Stirred-reactor	5.8	0.087	0.12	0.45
Stirred-reactor	5.9	0.084	0.15	0.49
Stirred-reactor	5.8	0.086	0.2	0.67
Stirred-reactor	5.8	0.086	0.25	0.8
Column	5.8	0.081	0	0

Table 7.2. Concentration of reagent grade NaCl, NaHCO$_3$ and CaCl$_2$ added in solution. The corresponding values of saturation index (Ω) calculated using Chess code van der Lee and De Windt, are also reported

	H+	H2O	HCO3-	Cl-	Na+	Ca++	Log(K)
CaOH+	-1	1	0	0	0	1	-12.83
CaCl+	0	0	0	1	0	1	-0.70
CaHCO3+	0	0	1	0	0	1	1.05
NaCO3-	-1	0	1	0	1	0	-9.81
NaHCO3	0	0	1	0	1	0	0.15
NaCl(aq)	0	0	0	1	1	0	-0.78
CaCO3(aq)	-1	0	1	0	0	1	-7.01
CaCl2(aq)	0	0	0	2	0	1	-0.64
NaOH(aq)	-1	1	0	0	1	0	-14.79
HCl(aq)	1	0	0	1	0	0	-0.67
CO2(aq)	1	-1	1	0	0	0	6.34
CO3--	-1	0	1	0	0	0	-10.33
OH-	-1	1	0	0	0	0	-13.99

Table 7.3. Aqueous complexation reactions and corresponding thermodynamic parameters log(K). The numbers refer to the stoichiometric coefficients of the species in the considered reactions (positive values for reactants). Notice that the equilibrium constant K is intended as: $C_i = K_i \prod_{j}^{Nx} X_j^{V_{ij}}$
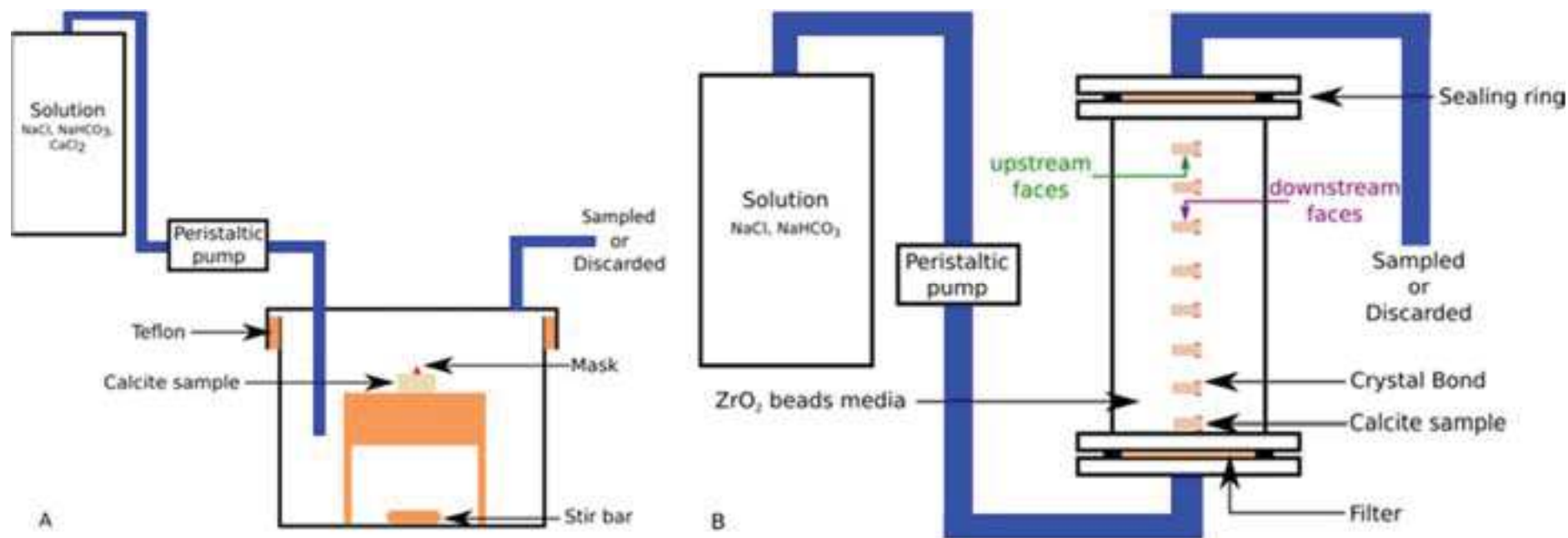
Figure 7.1. A. Sketch of the experimental apparatus for mixed flow reactor experiments. A solution with a fixed chemical composition is injected via a peristaltic pump in a continuously stirred reactor. A sample of masked calcite is placed over a Teflon tripod in the reactor. The solution at the outlet of the reactor is either discarded or sampled. B. Sketch of the experimental apparatus of the column experiment. The solution is injected at the bottom of the column via a peristaltic pump with a flow rate of 0.25 mL/min. The column is filled with zirconia beads to mimic an ideal porous media with 38% porosity. Calcite sample are placed every 1.5 cm in the column and are masked with CrystalBondTM on each side of the crystal surface with (104) orientation. The column is 15 cm-long and 3.75 cm in diameter.

7.1.4 Mathematical modeling of flow and reactive transport for the column experiments

The flow was assumed to be at steady state and the corresponding mathematical model is given by:

$$\begin{cases} \nabla \cdot \mathbf{q} = 0 \\ \mathbf{q} = -\nabla \cdot \mathbf{K}\nabla h \end{cases} \tag{7.2}$$

where $\mathbf{q}$ (m/s) is the Darcy flux, $\mathbf{K}$ is the hydraulic conductivity tensor (m/s) and h the hydraulic head (m). A constant flux (Neumann condition) was prescribed at the column inlet whereas a constant hydraulic head (Dirichlet condition) was set at the column outlet. It is worth to notice that under these boundary conditions and considering the column as homogeneous, it is not necessary to determine the exact value of the hydraulic conductivity to compute the fluid velocities.

The mathematical model used to simulate the reactive solute transport was the classical reaction-dispersion-advection equation defined by:

$$\begin{cases} \dfrac{\partial(\phi C_i)}{\partial t} + \nabla.(\mathbf{q}C_i - \mathbf{D}.\nabla C_i) = -\left(\sum_{j=1}^{Nr} v_{ij}r_j + \sum_{m=1}^{Nm} v_{im}r_m \right) \\ \mathbf{D} = D_m\mathbf{I} + (\alpha_L - \alpha_T)\mathbf{q}\mathbf{q}/|\mathbf{q}| + \alpha_T|\mathbf{q}|\mathbf{I} \end{cases} \tag{7.3}$$

Where ϕ [-] is the kinematic porosity, C_i ($mol/m^3/s$) is the concentration of the ith primary species, $\mathbf{D}$ is the dispersion tensor [m^2/s], α_L, α_T the longitudinal and transverse dispersivity [m], D_m the pore water diffusion coefficient [m^2s^{-1}], $\mathbf{I}$ the unit tensor; r_j [$mol/m^3/s$] and r_m [$mol/m^3/s$] are the homogeneous (aqueous phase) and heterogeneous (mineral) reaction rates, respectively; v stands for the stoichiometric reaction coefficients [-].

The solute concentrations were prescribed at the column inlet and the dispersive flux is neglected at the column outlet.

Both partial differential equations were solved using our own numerical code, SpeCTr (Carrayrou et al., 2010, Marinoni et al., 2017) which was verified by comparisons with different existing codes like CrunchFlow (Steefel, 2009), a widely used reactive transport code to model geochemical reactions (e.g. Knauss et al., 2005; Dontsova et al., 2009; Molins et al., 2014). The speciation was treated using the extended Debye-Hückel equation for activity coefficients calculation, equations of mass conservation and combination of laws of mass actions for the various considered species and chemical reactions, respectively. The CHESS code (van der Lee and De Windt, 2002) was used to determine all possible aqueous species considering the different solutes added to the column inlet solution (Table 7.2) and solutes provided by the calcium dissolution (Table 7.3).

173

The calcite dissolution rate ($r_{calcite}$) [mol/s/m^3] r_m in equation (7.3) was computed using either a first order transition state theory (TST) formulation (Lasaga, 1981) or using a stepwave model (SWM) formulation suggested by Lasaga and Luttge (2001) and modified after Gruber et al. (2014). The TST formulation is defined by:

$$^{Calcite}r = k\left(1 - e^{\frac{\Delta G_r}{R_g T}}\right) = k\,A_S\left(1 - \Omega\right) \qquad (7.4)$$

where A_S is the reactive surface area of the mineral (m$^2_{min}$/m^3) which is computed as a function of the size of grid cells and porosity, k is the rate constant [mol/m$^2_{min}$/s], ΔG_r [J/mol] is the Gibbs free energy of the reaction, R_g [J/K/mol] is the gas constant, T is the temperature [K] and Ω is the saturation index (ion activity product Q over solubility product K_S) of the solution with respect to calcite. The SWM formulation can be written as follows (Gruber et al., 2014):

$$\begin{cases} ^{Calcite}r = A_s k_1 \left(1 - e^{\Delta G_r / R_g T}\right) \tanh\left(\frac{B}{f(\Delta G)}\right) f\left(\Delta G_{crit}\right) + A_s k_2 \left(1 - e^{\Delta G_r / R_g T}\right) \\ f\left(\Delta G\right) = 1 - \dfrac{1 - e^{\Delta G_{crit} / R_g T}}{1 - e^{\Delta G_r / R_g T}} \end{cases} \qquad (7.5)$$

where A_s is again the reactive surface area of the mineral (m$^2_{min}$/m^3), k_1 and k_2 are the rate constants [mol/m$^2_{min}$/s], ΔG_{crit} is the Gibbs free energy that is required to form etch pits and B [-] is a constant that depends on surface diffusion distance. Note that for each formulation (TST or SWM), no specific dependence of the dissolution rate on pH was implemented, as calcite dissolution rate is essentially pH-independent in the pH range investigated here (Brantley and Olsen, 2014).

Since the porous medium in the column is chemically inert (except calcite crystals) and the dissolution of calcite results in a tiny modification of calcite dimensions (surface retreat of a few micrometers at the most), the change of porosity and permeability was not considered.

Flow and transport equations in SpeCTr are solved using mixed finite elements for flow and a combination of discontinuous-mixed finite elements for the transport equation (Siegel et al., 1997; Younes et al., 2010). This combination allowed accurate simulations of sharp solute fronts without excessive numerical dispersion. The equilibrium reactions were solved using a constraint Newton-Raphson method (Marinoni et al., 2017) and the solver DASPK for the kinetic reactions (Brown et al., 1994). The spatial discretization for both 1D and 2D simulations was set to 1 mm after preliminary runs performed to define the optimal spatial discretization. For the 1D simulation, the reactive mineral

CaCO$_3$(s) was discretized by two grid cells, representing the two faces of each crystal. For the 2D simulation, the grid cells were square and the calcite crystals were described by 4 impermeable cells.

7.1.5 Results and discussion

7.1.5.1 Mixed-flow reactor experiments
7.1.5.1.a Etching and etch pits morphology

In order to understand the role of saturation on the dissolution rate and on the specific topographic patterns of the {104} calcite face, experiments have been run under a large range of saturation indices (Ω) ranging from ~0 to 0.8. The aqueous conditions were purposely similar to those chosen by Smith et al. (2013), as they were well suited for VSI investigations. Note however that a wider range of Ω values were investigated (using vertical scanning interferometry) in the present study, in order to better refine the R- Ω relation at low Ω values.
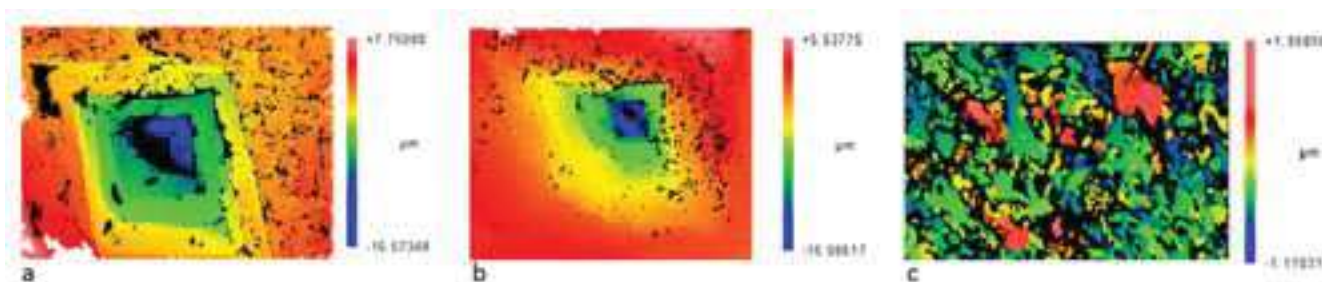
Figure 7.2 - Typical dissolution patterns observed with VSI on sample surfaces after dissolution. The images were acquired on samples reacted at (a) Ω = 0.02, (b) Ω = 0.20, and (c) Ω = 0.67. These images show that etch pits vary from (a) rhombohedral to (b) triangular shape and are not visible for Ω > 0.3. Field of view: 100 μm× 70 μm.

VSI images of the surface of the dissolved samples are characterized by an evolution of the dissolution patterns: while for low saturation indices ($0 \leq \Omega \leq 0.31$), the surface was dominated by the formation of etch pits (Figure 7.2a and b), at higher Ω values ($0.31< \Omega \leq 0.80$), the dissolution was homogeneous and weaker all over the mineral surface (Figure 7.2c). This transition of dissolution mode occurred at $\Omega \approx$ 0.3-0.4. This result is in reasonable agreement with previous studies, which reported pitted surfaces for Ω values ranging between ~0 and 0.4 (Smith et al., 2013 and Teng, 2004). Because in the present study data have not been collected for $0.31 < \Omega < 0.45$, the presence of pits for Ω values as high as ~0.4 cannot be excluded.

Similar transitions from deeply pitted surfaces to more homogeneous topography have been previously documented for carbonates (e.g. Arvidson et al., 2003; Teng, 2004; Vinson and Lüttge, 2005; Xu et al., 2012) and other minerals (Beig and Luttge, 2006; Burch et al., 1993; Hellmann and Tisserand,

2006; Pollet-Villard et al., 2016a). These transitions were explained by the existence of a critical Gibbs free energy value (ΔG_{crit}), above which the opening of etch pits is no longer spontaneous, resulting in a homogeneous dissolution all over the mineral surface. Lasaga and Blum (1986) showed that a basic expression for calculating the numerical value of ΔG_{crit} at screw dislocations can be written as follows:

$$\Delta G_{crit} = \frac{-2\pi^2\sigma^2 V_m}{\mu b^2} \tag{7.6}$$

where σ is the surface free energy (J/m²), V_m is the molar volume (m³/mol), μ is the bulk shear modulus (Pa), and b is the length of the Burgers vector of the dislocation (m). Considering the range of acceptable values reported respectively by Fernandez-Martinez et al. (2012), Dvorkin et al. (2014) and Goetze and Kohlstedt (1977) for σ, μ and b allows one to calculate the corresponding range of ΔG_{crit} (Figure 7.3), which varies between -0.26 and -2.88 kJ/mol (i.e. $0.31 < \Omega < 0.90$). These values are in reasonable agreements with the saturation index of the solution for which etch pit are no longer observed ($0.31 \leq \Omega < 0.45$).
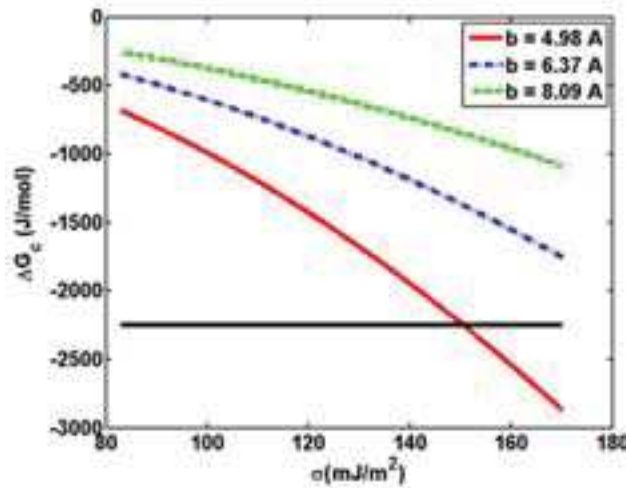
Figure 7.3 - Variation of the critical Gibbs free energy of etch pit nucleation as a function of surface free energy. Each curve represents one Burgers vectors. Note that ΔG_{crit} varies from -260 to -2880 J/mol, depending on the values of b and σ that are considered. Notice that the ΔG_{crit} revealed in this study is compatible with one Burgers vector only (the shortest one).

The surface of the samples after dissolution at low saturation ($\Omega \leq 0.2$-0.3) were characterized by different etch pit geometry. When $\Omega \approx 0$, etch pits were mostly rhombohedral, while the increase in saturation ($\Omega \approx 0.1$-0.2) led to etch pits becoming triangular (Figure 7.2). These observations are in agreement with several studies (Smith et al., 2013; Teng, 2004; Xu et al., 2012). The change in pit morphology from rhombohedral to triangular shape has been discussed by Xu and Higgins (2011). Curvilinear shapes on acute-acute corners of pit kinks were proposed to stem from the preferential

occurrence of a backward reaction on these sites. The kink detachment rate at the acute-acute site would also be significantly reduced compare to that of obtuse-acute kink sites.

Interestingly, we also observed that etch pit morphology changed from rhombohedral at the top of the pits to triangular at the bottom (Figure 7.2a). This observation may imply that a chemical aqueous gradient developed along the etch pits depth, which might have limited the deepening of the pits.

7.1.5.1.b R-Ω and R-ΔG relationships as determined from VSI measurements

Dissolution rates from mixed flow reactor experiments are plotted as a function of the saturation index in Figure 7.4a, together with those previously reported by Smith et al. (2013) over a narrower range of Ω values for the same {104} cleavage plane. The figure illustrates the good agreement between both datasets despite differences in the experimental protocols (flow-through versus batch experiments). For low saturation indices (i.e., $\Omega \leq 0.45$), the dissolution rate decreases sharply from 5.2×10^{-7} mol/m$^2_{min}$/s to 1.8×10^{-8} mol/m$^2_{min}$/s. For $\Omega \geq 0.45$, the dependence of the dissolution rate on solution saturation is less pronounced, ranging from 1.8×10^{-8} mol/m$^2_{min}$/s ($\Omega = 0.45$) to 5.6×10^{-9} mol/m$^2_{min}$/s ($\Omega = 0.80$). As emphasized by Smith et al. (2013), a simple linear function between R and Ω, such as expected from the transition state theory (equation (7.4)) cannot account for the measured R-Ω relation.
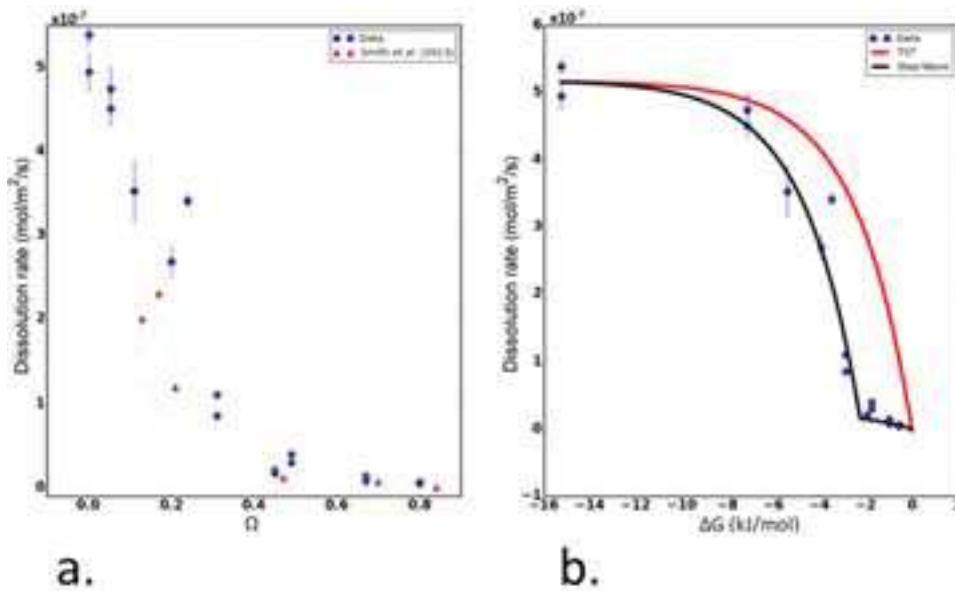
Figure 7.4 - a. Relations between R and Ω. A sharp decrease is observed over the range $0 < \Omega < 0.45$. Below this value, the dissolution rate is mostly controlled by etch pitting while for $\Omega > 0.45$, the dissolution is homogeneous over the entire surface of the samples.. b. Relation between R and ΔG. The stepwaves model is represented by the black line and the TST by the red line. Parameters used to fit the data with the SWM are listed in Table 7.5.

The existence of a non-TST relationship is even more obvious when the data are compared to the TST-curve as a function of ΔG (Figure 7.4b). As previously discussed by Xu et al. (2012), this non-TST behavior can be fitted using more complex empirical relations such as parallel rate laws. In the present study, the relation derived from the stepwave model (SWM; Gruber et al., 2014; Lasaga and Luttge, 2001) was preferred. This relation (equation (7.5)) is based on the sum of two independent terms: the first term of the equation results from the theoretical formulation of the defect-generated dissolution stepwave model, which prevails at far-from-equilibrium conditions (Lasaga and Luttge, 2001). The second term of the equation is a simple TST term, which accounts for the dependence of the dissolution rate on ΔG when the nucleation of dislocation etch pits is no longer spontaneous. The mechanistic switch between the two dissolution modes occurs at $\Delta G = \Delta G_{crit}$. The values of the different parameters used in the SWM-relation, determined by fitting the data points, are listed in Table 7.5. Interestingly, the fitted value of ΔG_{crit} (-2.25 kJ/mol) fell within the range of possible theoretical ΔG_{crit} values determined above ($-0.26 \geq \Delta G_{crit} \geq -2.88$ kJ), which is in excellent agreement with the ΔG range where etch pits were no longer observed experimentally ($0.31 \leq \Omega < 0.45$; i.e. $-1.96 \geq \Delta G_{crit} > -2.87$ kJ).

The choice of using the SWM-relation in this study rather than an empirical parallel rate law (Xu et al., 2012) was motivated by the mechanistic approach of this model. However, this model misses a possibly important point in its construction: the multiplicity of ΔG_{crit} values. Indeed, a single ΔG_{crit} value is required in equation (7.5), which corresponds to the length of a single Burgers vector, whereas dislocations with various Burgers vector orientations can outcrop at the {104} calcite face (Figure 7.3). Therefore, the model fails to take into account the variety of Burgers vector orientations of the dislocations, while some of them may remain active sources of etch pits for $\Delta G_{crit} > -2.25$ kJ/mol. As a consequence, for calcite samples having a wide range of dislocation orientations, the actual dissolution rate in the vicinity of the ΔG_{crit} determined in the present study may be higher than that calculated using our set of parameters.

7.1.5.2 Column experiment

Column experiments represent one of the several intermediate steps in an upscaling exercise, which could possibly help to understand the differences of mineral dissolution rates between field and laboratory (Salehikhoo et al., 2013). Indeed, while mineral dissolution in mixed flow reactors occurs in a chemically homogeneous solution, column experiments reveal the importance of flow and dispersion (longitudinal and lateral) due to the porous material. In this section, dissolution rates obtained by a column experiment are presented and linked to etch pit morphologies. This link is then discussed regarding results obtained in mixed flow reactor experiments. The column experiment lasted 10 days and we assume that steady state was reached because the calcium concentration at the column outlet remained constant since the second day of experiment.

Dissolution rates determined by VSI measurements are shown in Figure 7.5. Two distinct behaviors are visible, with upstream-faces dissolving systematically faster than the downstream-faces (upstream and downstream with respect to the flow direction). Furthermore, the evolution of the dissolution rate of upstream-faces along the column behaves differently from those of downstream-faces: while for upstream-faces, the dissolution rate decreases steadily along the column prior to reaching a plateau, the dissolution rate of downstream-faces remains relatively constant ($R \sim 8.33 \times 10^{-9}$ mol/m²$_{min}$/s). For upstream faces, a rate decrease, from 7.31×10^{-8} mol/m²$_{min}$/s to 3.72×10^{-8} mol/m²$_{min}$/s, is observed up to the forth mineral from which it became nearly constant.
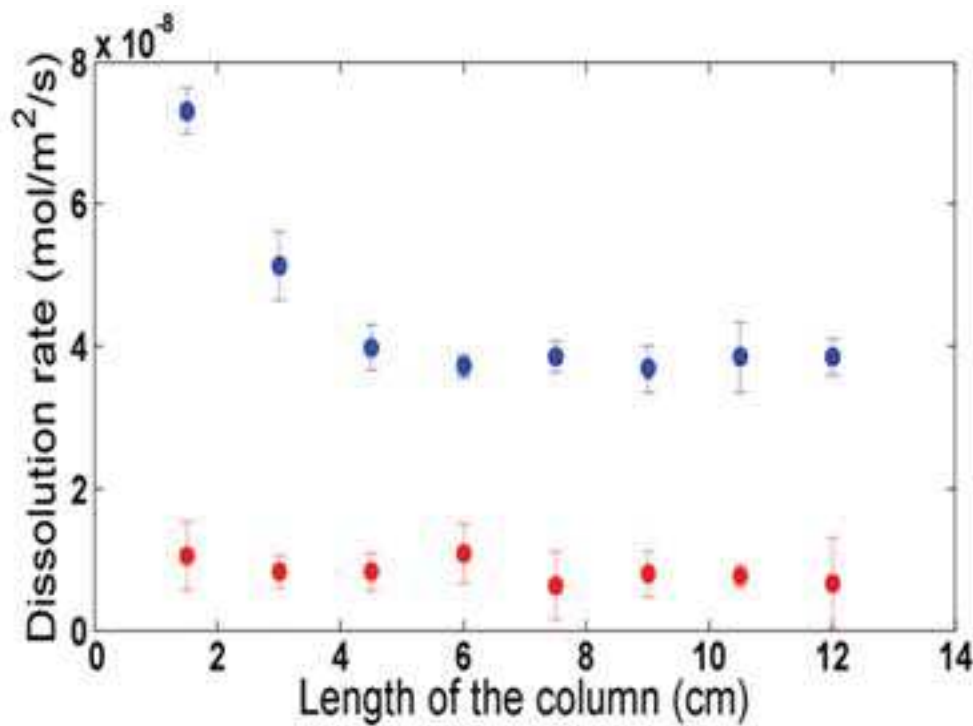
Figure 7.5 - Variation of the dissolution rate of the {104} faces in the column, calculated after 10 days of experiment. Blue and red symbols were used to depict the dissolution rate of upstream- and downstream-faces, respectively.

Qualitatively, these differences between upstream-faces and downstream-faces may be explained by the evolution of the saturation state in the vicinity of the calcite surface. Figure 7.6a represents a schematic view of the transport along a path line. Due to laminar flow conditions, the velocity magnitude at both sides of the crystal (upstream and downstream) is the same for the same x location and for the eight crystals placed in the column (assuming here that the errors due to the lateral crystal positioning and to the location of column's inflow and outflow can be neglected). At the column inlet,

the concentration of Ca^{2+} of the injected solution is equal to zero. At steady state, the concentration at location C1 represents the average concentration due to dissolution and transport (advection and dispersion) fluxes. Along the crystal, concentration changes (as the saturation index) are due to dissolution and lateral dispersion. Assuming that the dissolution flux is greater that the lateral dispersive-diffusive flux, the concentration increases from location C1 to C2; this explains the differences between the upstream and downstream dissolution rates. The concentration decreases from C2 to C3 due to lateral dispersion-diffusion, which explains the higher dissolution rate of the upstream face compared to the dissolution rate of the previous downstream face. Moreover, because the concentration in C2 is higher than in C1, the dissolution rate between two successive upstream faces decreases. However, the dispersion process depends on the concentration gradient and this effect diminishes with the distance, which explains that the dissolution rates between successive upstream faces remain constant after the fourth crystal. Finally, the average concentration at the downstream faces is more or less the same for each crystal (same dissolution rate).

Overall, these results suggest that accounting for the modification of the fluid flow direction and velocity in the vicinity of the crystals, as well as accounting for the dispersion between two consecutive crystals will be central to accurately model calcite reactivity all along the column.

7.1.5.2.b Etch pit morphology

As emphasized in section 3.1.1, etch pit morphologies strongly depend on the saturation index of the solution that contacts the dissolving surface. A triple bijective link between etch pit morphologies, solution composition and crystal dissolution rates may be a clue to determine dissolution rates in the field or the chemical composition of the reactive solution, directly from mineral surface analyses (Berner et al., 1980; Velbel, 2009). However, the strong discrepancies between dissolution rates measured in the field and in the laboratory indirectly suggest that differences may exist in the etching patterns observed in the laboratory and those observed in the field.

Overall, all crystals in the column (both upstream and downstream faces) recovered after ten days of dissolution exhibited triangular etch pits. In addition, upstream faces of the first two crystals contained also some rhombohedral pits. As opposed to the rhombohedral pits observed in mixed flow reactor experiments, the rhombohedral pits observed on these faces are almost flat (possibly resulting from point defects such as foreign ions, or to the outcrop of edge dislocations (Lee and Parsons, 1997; Figure 7.7). Considering the qualitative relation between solution saturation state and pit morphology discussed in section 4.1.1, the theoretical fluid saturation state at these specific mineral-water interfaces may have ranged between 0 and 0.3-0.45. These values correspond to a dissolution rate ranging between 5.2×10^{-7} mol/m²$_{min}$/s and 1.8×10^{-8} mol/m²$_{min}$/s.
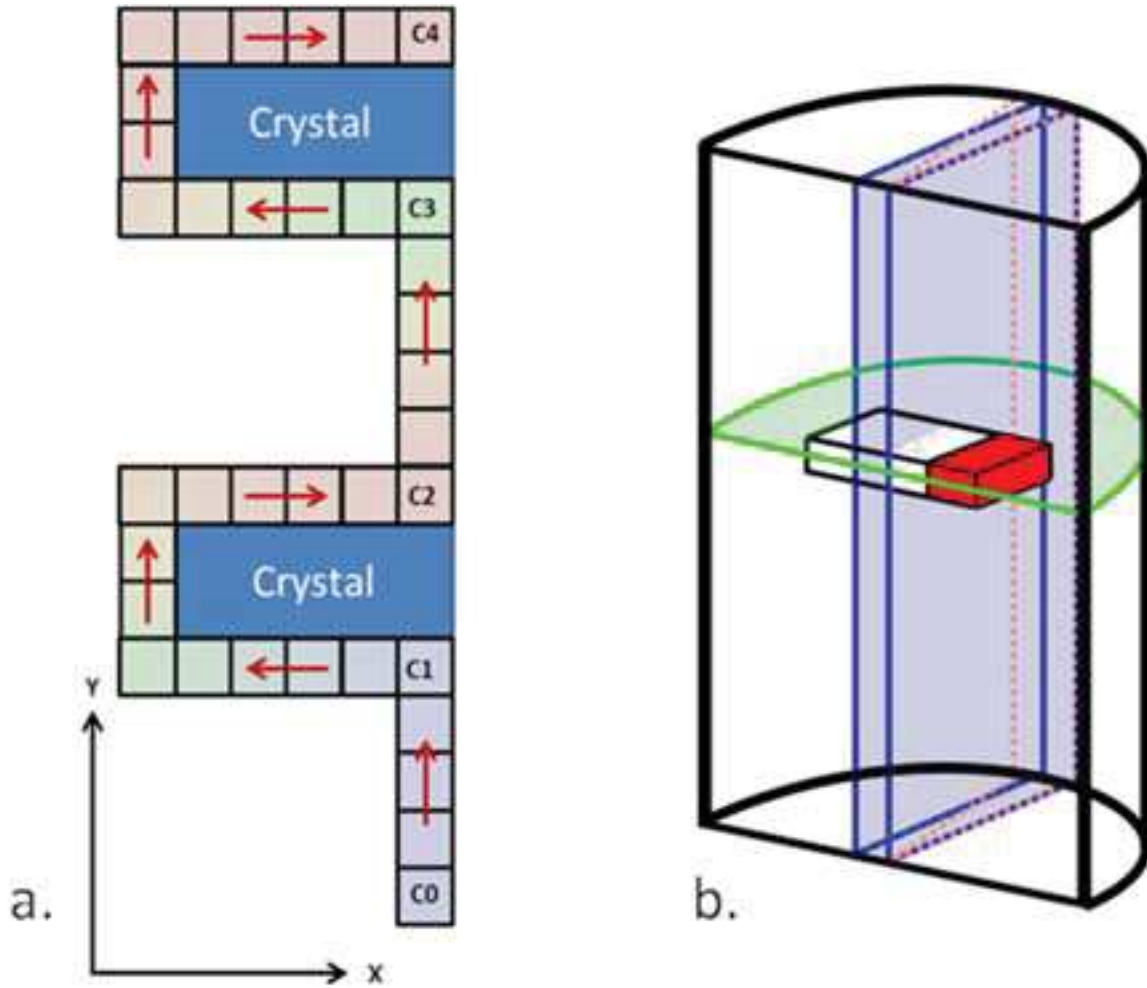
Figure 7.6 - a. Scheme of a flow path along the crystals in the column experiment. Colors represent the evolution of the calcium concentration along this path. The color gradient from blue to red stands for low to high concentrations, respectively. b. Scheme of a half-section of the column. Blue planes represent the conceptual thickness considered in the 2D model. Then, the crystal is not considered in its entirety. The red part represents the mask on the crystal surface. The green plane represents the separation between two elements considered in the 1D model. Finally, salmon lines represent the best width that should have been considered for the best agreement between model and experiment.

7.1.5.2c Comparison of the mean dissolution rates retrieved with VSI to those inferred from pit morphology

While the range of calcite dissolution rates inferred from etch pit morphologies (from 5.2×10^{-7} mol/m²$_{min}$/s to 1.8×10^{-8} mol/m²$_{min}$/s) is in reasonable agreement with the mean dissolution rate calculated from VSI measurements for upstream faces (from 7.31×10^{-8} mol/m²$_{min}$/s to 3.72×10^{-8} mol/m²$_{min}$/s), this method overestimates the mean calcite dissolution rate of downstream faces by more than a two-fold factor ($\geq 1.8 \times 10^{-8}$ mol/m²$_{min}$/s vs. ~8.33×10^{-9} mol/m²/s). In addition, the occurrence

of pits on upstream-faces is consistent with the observations from mixed flow reactor experiments, whereas the mean dissolution rate of downstream faces is not compatible with the spontaneous nucleation of triangular pits. Below, we briefly discuss some tentative explanations that might contribute to resolve this apparent paradox, namely:

(i) etch pits represented relict structures inherited from the early stage of the experiment, while the saturation state was still lower than 0.45;

(ii) A direct effect of the porous medium (and in particular, the contact between zirconia beads and mineral surfaces), which may exert an inhibiting role on the dissolution kinetics;

(iii) the hydrodynamics of the solution (turbulent in mixed flow reactor experiments vs. laminar in the column experiment) may control the relation between etch pit morphology, R and Ω beyond the simple development of compositional gradients in the fluid contacting the mineral surface. With respect to (i), as the column experiment was initiated in a Ca-free solution, the early nucleation of etch pits could have occurred on the (upstream and downstream) faces of all crystals. While this process may explain the observation of triangular etch pits on faces that were supposedly in contact with a solution close to calcite saturation, it does not explain why such etch pits did not contribute to raise the dissolution rate, as expected from the dissolution mechanism discussed in section 3.1.2 (see also Beig and Luttge (2006), who evidenced enhanced dissolution rates of pre-treated albite powders, even at close-to-equilibrium conditions).
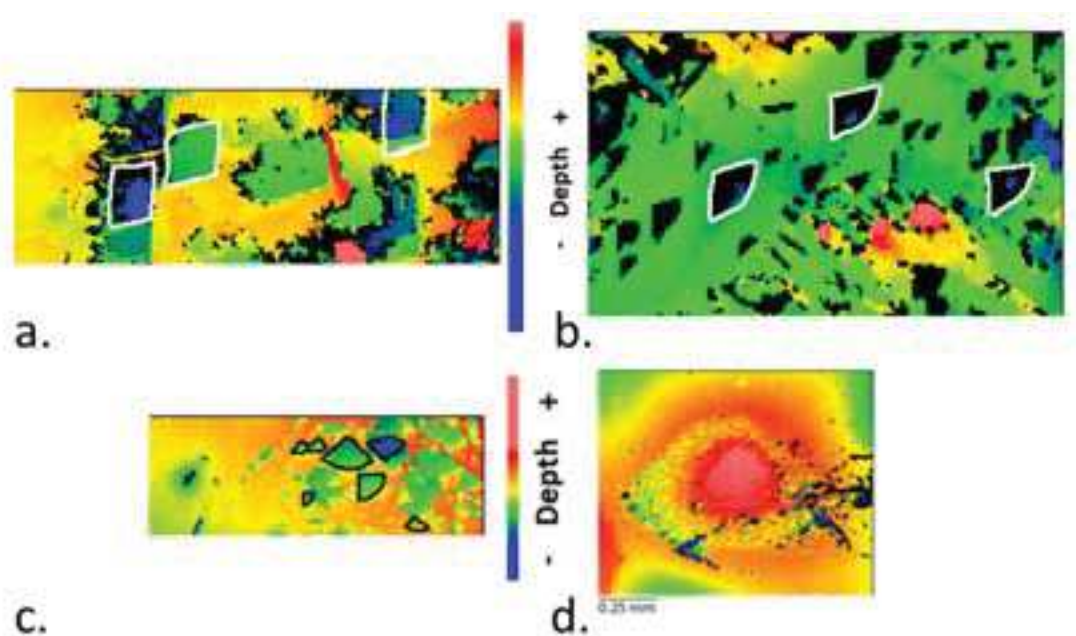
Figure 7.7 - Typical features observed on upstream and downstream faces of calcite crystals in the column experiment. a. Rhombohedral pits observed on the two first upstream faces. b. Triangular pits observed on upstream faces. c. Triangular pits observed on downstream faces. d. The circular area in red is likely due to the contact between mineral surface and zirconia beads, which creates a non-wetted surface.

The subsequent explanation (ii) is suggested by the observation of circular zones on the mineral surface with a mean height close to that of the reference surface (Figure 7.7). These zones were present on all mineral surfaces and are undoubtedly due to the contact between mineral surface and zirconia beads. These contacts may have played a role equivalent to that of the masks we applied on the surface, and one could wonder the extent to which an elevated density of such additional masks could impede the propagation of step-waves at the calcite surface, eventually playing a role similar to that of step bunches or macrosteps, which ultimately result in a significant reduction of local dissolution rates (Saldi et al., 2017; Smith et al., 2013). In that sense, the relation between etch pit morphology, R and Ω would not hold because R is lowered by the inhibiting role of zirconia beads.

The last explanation (iii) is supported by studies that showed that the effect of the fluid hydrodynamics goes beyond the simple development of a diffusion boundary layer (DBL), which drives the interfacial solution towards higher Ω values and may lead to a transport-controlled process (Molins et al., 2014; Noiriel and Daval, 2017; Ruiz-Agudo et al., 2016). It has been further suggested that the laminar flow on mineral surfaces may lead to a reversible change in surface charge and a modification of the surface potential (Lis et al., 2014), which ultimately affect the dissolution rate. If this explanation prevails, the results obtained from mixed flow reactor experiments may not directly apply to modeling the column experiment, and more generally questions the conceptual bases of the upscaling approach of water-rock interactions developed over the last three decades. The extent to which this mechanism is detrimental to the modeling of calcite dissolution in the column experiment is discussed in the next section, by means of reactive transport simulations.

7.1.5.3 Modeled dissolution rates using 2D reactive transport simulations of the column experiment

2D-models represent an efficient way to describe the hydrodynamics inside the column, and hence, to represent the complexity of the flow, which is not possible with 1D models. They also allow for the implementation of all the transversal mixing processes due to transverse dispersion and diffusion.

A rigorous modelling of the column geometry (cylinder) would be a half of the cylinder's section due to symmetry (rectangular parparallelepiped crystals centered in a cylinder with Crystalbound[TM] on one side – see Figure 6b). To avoid excessive computational effort, the simulations are performed on a 2D domain representing one vertical centered slice of the column.

The simulations were run without adjustment of any boundary conditions and/or model parameter. The only unknown parameters are dispersivities. The longitudinal dispersivity was assumed to be equal to the average grain size and the transverse dispersivity is set to $1/10^{th}$ of the longitudinal dispersivity, which are usual values for the simulation of solute transport in homogeneous porous media (Ballarini et al., 2012; Maina et al., 2017). We also analyzed the effect of the uncertainty on the dispersivities by using values ten times greater. Although the mixed flow reactor experiments showed that the stepwave model better describes the relationship between the dissolution rate and the saturation index, the

transition state theory was also used as an alternative dissolution rate model, as TST-based rate laws are commonly implemented into most reactive transport codes. This will allow us to discuss some potential limitations of using TST-based rate equations for modeling purposes. Chemical reactions and chemical parameters are summarized in Table 7.3 and the transport parameters are summarized in Table 7.4.

SpeCTr allows for the computation of the dissolved mass for each grid cell. To assess the reliability of our modelling, the cumulated dissolved mass computed for each upstream and downstream crystal face was compared to the dissolved mass measured by VSI on the corresponding faces at the end of the experiment. This local validation of the model was completed by a more global validation based on the comparison between measured and computed Ca^{2+} concentration at the column outlet (see section 4.5).

Parameters	$\phi(-)$	α_L (m)	α_T (m)	$D_m(m^2/s)$
	0.380	10^{-3}-10^{-2}	10^{-4}-10^{-3}	0.3×10^{-9}

Table 7.4 - Transport parameter values.

	H+	H2O	HCO3-	Cl-	Na+	Ca++	ΔG_{crit}	k_1	k_2	B
Calcite	1	0	1	0	0	1	-2248.6	$1.08\ 10^{-6}$	$2.58\ 10^{-8}$	4.27

Table 7.5 - Dissolution reaction and kinetic parameters of the mineral reaction (see reaction rate equation (7.5)).

Simulation results using SWM are depicted in Figure 7.8a. The agreement between modelled and measured dissolution rates is within the range of both experimental and numerical uncertainties, except for the upstream face of the crystal located close to the outlet (computed R between 1.5×10^{-8} and 3.3×10^{-8} mol/m²$_{min}$/s and measured R between 3.6×10^{-8} and 4.1×10^{-8} mol/m²$_{min}$/s). The model further confirms the decrease of the dissolution rates for both faces of each crystal from the column inlet to its outlet. It also shows the sensitivity of the dissolution processes to the mixing conditions, i.e., dispersion/diffusion, as discussed in section 4.2. The highest dissolution rates were obtained with the highest dispersivity values. For each crystal, the change in dispersion values resulted in the same dissolution rate variations for the upstream faces. This was not the case for the downstream faces, where the dispersion changes led to a decreasing variation of the dissolution rates with the distance to the column inlet. This may be explained by the concentration gradients, which are higher close to the inlet compared to the outlet.

Quite unexpectedly, the agreement between measured and computed dissolution rates using the TST model was similar to that obtained using the stepwave model for upstream faces, except for the two

first crystals (Figure 7.8b). Conversely, the simulations performed using the TST rate law generally overestimate the reactivity of downstream faces. Taken together, these results illustrate that in the specific case of this set-up, the outputs of the simulation are more impacted by the uncertainty related to the transport parameters (i.e., dispersivity/diffusion) than to the choice of the rate law. This may be related to a dissolution regime where the increment of solutes released from the crystals is no longer enough to result in a drastic change in the saturation state from one crystal to the next, so that the whole system is fixed at a dissolution regime set by the absolute dissolution rate of calcite, regardless of the rate law that was used to model the experiment.
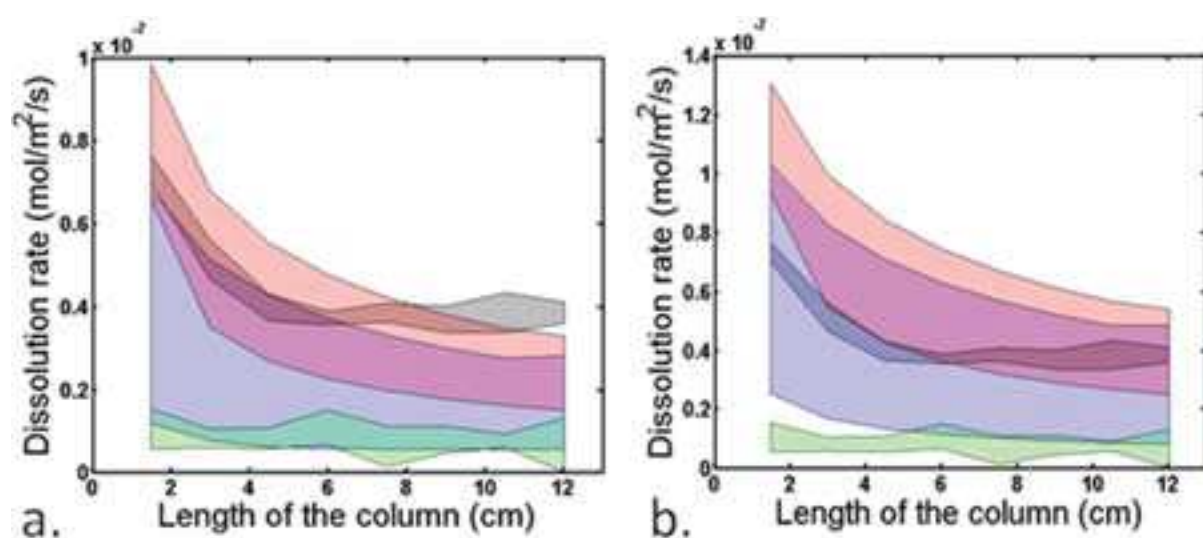
Figure 7.8 - Outputs of the 2D simulations using SWM (a) and TST (b) rate laws. The grey and green areas depict the experimental data for the upstream and downstream faces, respectively, together wither associated uncertainties. The red and blue areas are modeled predictions for upstream and downstream faces, respectively, for dispersivity varying between 1 mm and 10 mm.

7.1.5.4 Modeled dissolution rates: 1D versus 2D simulations.

In this section, as for the 2D model, a 1D model was used to study the geochemical evolution of the column experiment. One dimensional simulations are the most commonly used to model geological processes such as pedogenesis (e.g. Maher et al., 2009; Schott et al., 2012) and water-rock interactions at the catchment scale (e.g. Godderis et al., 2006; Lucas et al., 2017) and in aquifers (Vital et al., 2018). The same chemical reactions, flow and transport parameters as in the 2D simulations were used to run the 1D simulations, with the aim to decipher whether such simulations already provided satisfactory agreement with the experimental results.

Figure 7.9 shows the modeled dissolution rates for the calcite upstream and downstream faces. The first striking result is that TST- and SWM-based simulations provide similar results, while

significantly overestimating the dissolution rate of upstream and especially downstream faces (by a factor of ~3 to 19 for the first crystal and by a factor of ~5 to 29 for the last one, regarding upstream and downstream faces, respectively). This result can be ascribed to the velocity magnitude, which is constant for the 1D simulation and is very low at the crystal/porous medium interface for the 2D simulations. The higher velocity in the 1D simulation leads to lower saturation indices close to the crystal and demonstrates the little interest of 1D simulation for kinetic dissolutions when the fluid velocity is an important component of the solute transport. In addition, a fundamental assumption of 1D-simulations is that the solid matrix is homogeneously distributed in an elementary cell, so that the solution composition is also homogeneous in each cell. This condition is not met here. It results from these two explanations that the computed solution composition in the column is always far-from-equilibrium, where the TST and the SWM predict similar dissolution rates (Figure 7.4).

Secondly, while dissolution rates decrease with the distance to the column inlet, there are no significant differences between upstream and downstream faces of a same crystal. This result means that the saturation index of the solution contacting the downstream face is not sufficiently different from the saturation index of the solution that contacts the upstream face of the same crystal. This difference between the 2D and 1D simulations is a direct consequence of the space discretization. Indeed, in the 2D-simulations, the circulation of the solution around the crystal results in a gradual increase in calcium concentration in the cells in contact with the crystal surface, because of calcite dissolution. The corresponding increase of the saturation index results in a dramatic decrease of the dissolution rate of the downstream faces compared to the upstream faces. Conversely, in the 1D-simulations, this gradual loading does not occur since the surface area of one face is considered to be homogeneously distributed into the cell. The difference of saturation index between upstream and downstream faces is thus weaker than it is for the 2D simulations.

Finally, the third significant difference between the 2D and 1D simulation is the sensitivity to transverse mixing, which cannot be taken into account in the 1D computation. Overall, these results show that the saturation state of the fluid in the vicinity of the calcite crystal is not satisfactorily modeled in a 1D geometry. The lack of agreement between the simulations and the observations most likely originates from an improper definition of the spatial representation of the mineral inside the column and/or the need of effective (upscaled) parameters for the 1D-simulations.

While the failure of the 1D-simulations to account for the measured calcite dissolution rates may be attributed to the specific configuration of the column experiment (heterogeneous distribution of highly reactive minerals submitted to dissolution at relatively high fluid flow), it is noteworthy that this case is often met in aquifers (Vital et al., 2018) or in soil profiles (Godderis et al., 2006), where the dissolution of trace minerals disseminated in the bedrock was suggested to have a first order impact on the concentration of major elements in the soil horizons. For instance, Godderis et al. (2006) proposed that the dissolution of apatite was the main contributor to the dissolved concentration of calcium in the spring collector of the Strengbach catchment (Vosges massif, France)). In that sense, our study

suggests that 1D models may significantly overestimate the reactivity of such phases for various geological settings.
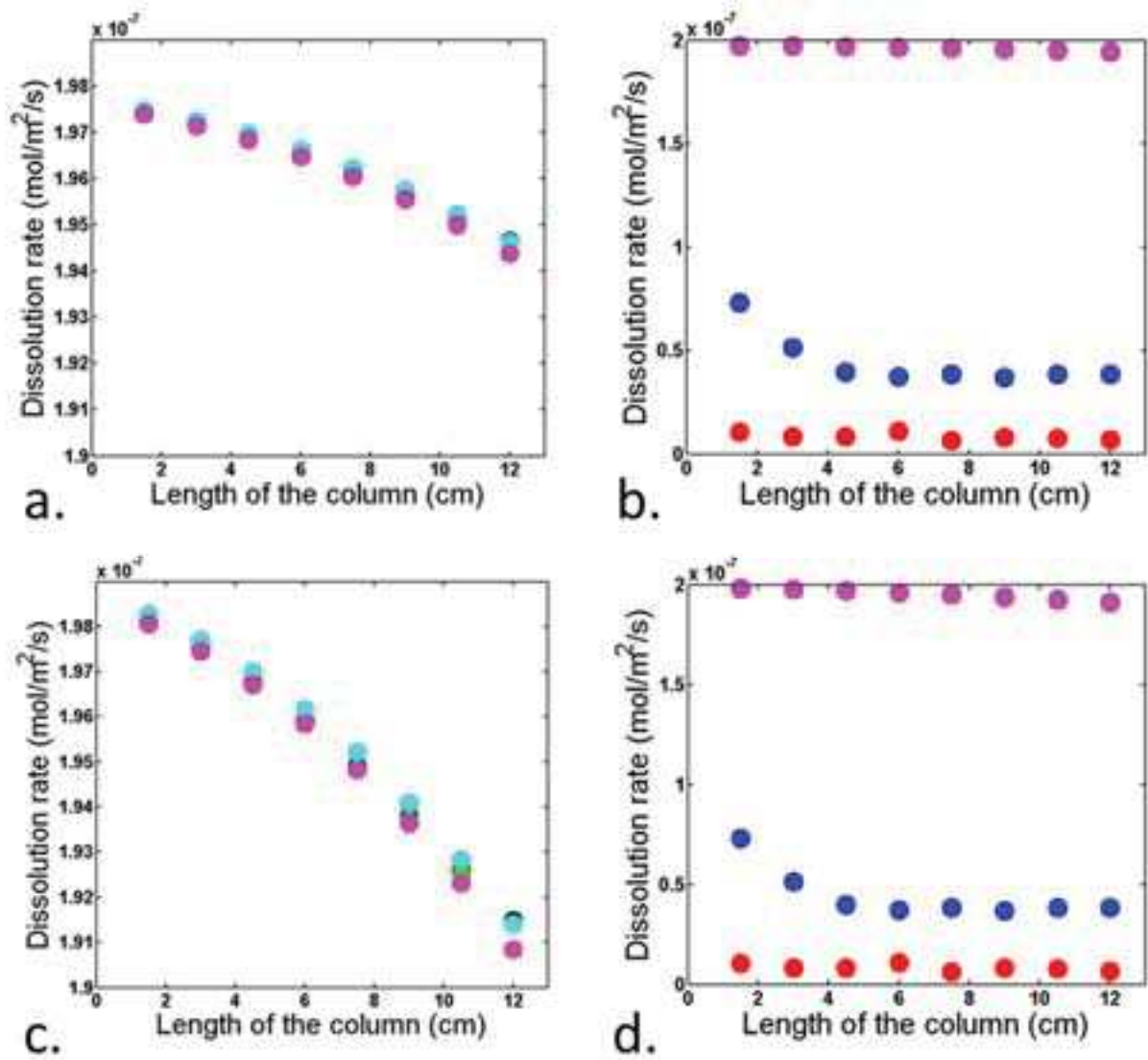
Figure 7.9 - Results from the 1D model. a. Results based on a TST- dissolution rate law and dispersivity values of 1 mm and 10 mm. b. Results using TST compared to experimental data. c. Results a dissolution rate law based on SMW, and dispersivity values of 1 mm and 10 mm. d. Results using SWM compared to experimental data. In all cases, black and cyan points represent modeled dissolution rates of upstream faces and green and magenta points, the modeled dissolution rates of downstream faces for dispersivity values of 10 mm and 1 mm, respectively. The blue points depict the measured upstream faces dissolution rates. The red points depict the measured downstream faces dissolution rates.

A proper estimation of dissolution rates in the column represents a major issue for mineralogical concerns or for the lifetime of a mineral in natural environment (the longer a mineral is present in the system, the greater its contribution to the geochemical evolution of the solutions), but this does not reflect all the possible highlights that a column experiment can provide. Indeed, another concern at a large scale is the evolution through time of the elemental concentration at the outlet of a system (soil, catchment…).

During the run of the column experiment, the solution was regularly sampled at the outlet of the column. These samples have surprisingly shown a significant initial calcium concentration followed by a decrease of the concentration at the very beginning of the experiment (Figure 7.10). This initial value and the decrease might be explained by the column's filling procedure. The column was filled under dry conditions to avoid dissolution before water injection and the calcite samples were deposited using a clamp. This clamp possibly damages the crystal samples and leads to the production of fines When the injection of the solution started, these particles started to be dissolved but also pulled away towards the outlet of the column.

This assumption was checked by adding calcium as initial condition in some cells of the numerical grids. This represents the only scaling parameter in this study. The number of cells that contain calcium was chosen in order to match the calcium concentration measured in the first collected sample, after the outflow of a volume of solution (Vs) equivalent to 1.67×10^{-1} pore volume (V_p). A good match is obtained by setting an initial calcium concentration of 5.29×10^{-4} mol/L over the last 2.5 cm of the column (corresponding to 2 mg of calcite powder distributed in this part of the column). Importantly, it was verified that adding this initial concentration did not impact the outputs of the simulations, neither in terms of the steady-state concentration of Ca at the outlet, nor in terms of mean dissolution rates retrieved for each crystal face.

Figure 7.10 shows the evolution of the experimental and modeled calcium concentrations over time at the outlet of the column. Over this time period, only two samples have been collected. At the beginning of the experiment, the Ca concentration was 5.29×10^{-4} mol/L. This concentration decreased rapidly to 1.80×10^{-4} mol/L after 1.67×10^{-1} V_p and finally reaches a steady-state with a concentration of 1.25×10^{-5} mol/L. Note that, for the last datum, the calcium could have been considered as a trace element because of its weak concentration, resulting in a high ICP-AES measurement error (20%).

2D and 1D simulations shown in Fig 7.10 were performed with both TST and SWM dissolution rate laws. For the simulations conducted with a 1 mm dispersivity, the concentration remains constant for $V_s \leq 5.16 \times 10^{-2}$ V_p, and decreases rapidly to reach a minimum before increasing slightly to a constant value for V_s close to 1 V_p.

This minimum represents the outflow volume of solution after which the initial calcium concentration is balanced with the calcium plume resulting from calcite dissolution. The increase of dispersivity to 10 mm led to a more smeared concentration variation. The steady state concentration values are different for the two values of dispersivity for the 2D configuration compared to the 1D configuration. For the 2D configuration, the most likely dispersivity value (1 mm) led to a better estimate of the measured steady state concentration. The steady state is obtained for V_s close to 1 V_p for almost all simulations, except for the one run using TST and a dispersivity of 10 mm, where the steady state is reached for $V_s = 1.75$ V_p. At steady state, the measured concentration was equal to 1.25×10^{-5} mol/L and the simulated concentration for a dispersivity of 1 mm and the SWM rate law was 3.36×10^{-5} mol/L for the 2D configuration and 2.27×10^{-5} mol/L for the 1D geometry. This better match between measured and computed concentrations for the 1D configuration is in contradiction with the simulation of the dissolution where the 2D configuration outperformed the 1D configuration. This apparent paradox is discussed in section 4.6.2.
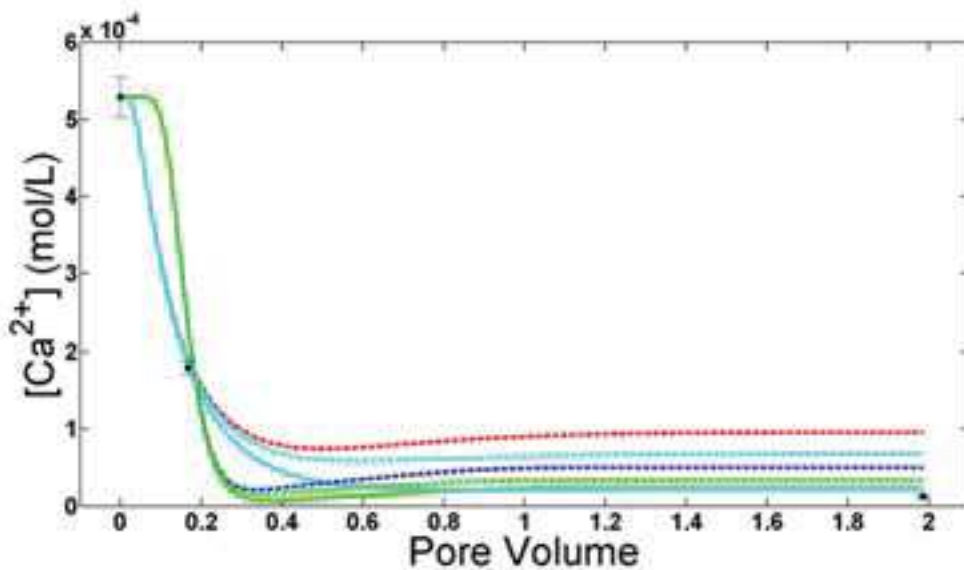
Figure 7.10 - Evolution of the calcium concentration as a function of the outlet solution volume. The decrease at the beginning of the experiment corresponds to dissolved calcite fines resulting from the preparation step of the column. Dashed lines correspond to 2D simulations and solid lines to 1D simulations. Blue and red correspond to simulations using TST as dissolution rate law and dipersivity of 1 mm and 10 mm respectively. Green and cyan lines correspond to simulations using SWM as dissolution rate law and dispersivity of 1 mm and 10 mm respectively. Black points are ICP measurements. Notice that the last ICP point correspond to the calcium concentration at steady state but it was measured at 4.3 pore volume.

7.1.5.6 1D and 2D-reactive transport simulations of the column experiment: overview and perspectives

7.1.5.6a Mineralogical considerations

Overall, the simulations conducted using the SWM-based rate law have provided a better agreement with the measured dissolution rates than the simulations run with a TST-based rate law. However, it is striking that the greatest improvement was obtained using 2D-reactive transport models instead of 1D-simulations. In spite of this improvement, it is clear that we were unable to obtain a perfect match between the simulations and the model using an *ab initio* approach, even with 2D-simulations implemented with SWM. Because these latter simulations provided the best agreement between the model outputs and the data, the discussion below is mainly based on the results of these simulations:

A first important point to emphasize is that the dissolution of each crystal is not independent of the dissolution of the others. In particular, the entire system is primarily driven by the dissolution rate (and therefore the dissolution rate law) of the upstream face of the first crystal.

Regarding the downstream faces, the strong dependence of their dissolution rates on the transverse dispersivity allows for a fine tuning of this parameter. For homogeneous porous media, the usual value of longitudinal dispersivity is equal to the mean grain size and the transverse dispersivity is set to $1/10^{th}$ of the longitudinal dispersivity (Ballarini et al., 2012; Maina et al., 2017). Using a longitudinal dispersivity of 1 mm provided an excellent agreement between the modeled and measured dissolution rates of downstream faces. However, it results in a greater underestimation of the dissolution rates of all upstream faces. As suggested by Beig and Luttge (2006), the measured dissolution rates might be greater than expected from the simulations because of the early formation of etch pits, which might have remained active even when the solution composition exceeded ΔG_{crit}, resulting in enhanced dissolution rates. Knowing that these models do not take into account the mineral surface's history, they would ultimately result in underestimations of the dissolution rates.

7.1.5.6.b Calcium breakthrough

Considering the calcium breakthrough curve, the 1D simulation allowed for a better agreement with experimental data than the 2D simulation. This paradox could be explained by the domain considered in the 2D case. The 2D model considers a projection of the cylinder on a plane of a prescribed thickness. Therefore, the 2D geometry does not allow for a detailed representation of the velocity variations, and the radial dispersion is hampered in the 2D geometry compared to the 3D. Furthermore, the concentration at the column outlet is a flux weighted concentration where the fluxes with very low calcium concentration (close to the column limits) are overestimated in the 2D configuration.

Despite the better agreement between the 1D simulation and experiment ($C_{1D} = 1.8 \times C_{exp}$), there is no significant difference between the 2D simulation and experiment ($C_{2D} = 1.5 \times C_{1D} = 2.7 \times C_{exp}$; i.e. less than an order of magnitude). Considering that the difference in terms of mineral reactivity is much bigger in the 1D simulations than in the 2D simulations, these latter simulations remain, overall, much more satisfactory to model the dissolution rate of fairly reactive solids disseminated in a porous medium.

7.1.5 Conclusion

In this study, the dissolution rate model developed and parameterized with mixed flow reactors has been quite successfully applied to simulate a column experiment without any calibration of the parameters involved in this model.

Under our experimental conditions and set-ups, calcite dissolution considered in a mixed flow reactor and in a column highlighted the follow results:

1. In agreement with several studies, the experiments conducted in mixed-flow reactors demonstrated that a simple TST-based equation cannot capture the R-Ω relation followed by the (104) face, whereas a strong relation between the saturation index, the nucleation of etch pits and the dissolution kinetics was observed. The stepwave model proposed by Lasaga and Luttge (2001) was found to accurately describe the dissolution of the (104) face. However, depending on the saturations, the difference between both models can be negligible.

2. The face orientation of the crystal with respect to the flow (upstream or downstream) significantly impacts the dissolution of the crystal. Upstream faces dissolved more rapidly than downstream faces.

3. The effects of the face orientation are due to a balance between the calcium flux resulting from dissolution and the transported flux due to advection and dispersion/diffusion.

4. Both transport fluxes play an important role in the dissolution: advection with low velocities around the crystal compared to the average water velocity and transverse dispersion/diffusion that reduces the concentration in the streamline that follows the crystals.

Overall, this study emphasized that 1D-reactive transport simulations may be improper to model the dissolution rate of fast dissolving trace minerals because neither the flow field variability nor the transverse mixing can be taken into account. Therefore, 1D simulations would require modifications of the parameters (at least) to describe the dissolution processes within a 1D geometry. These results show that the upscaling from mixed flow reactor to the column scale is possible if the geometry of the system is properly described.

7.2 Preparing Calcite dissolution rate modeling

In the following paragraphs is reported the preparatory work for Bouissonnié et al. (2018, submitted to *Chemical Geology*), concerning the adaptation of the code to model the experiment and the choices of spatial and time discretization. In order to compute the reactive surface as a function of the mesh size, a model is proposed in paragraph 7.2.1. All the results presented in previous paragraphs were obtained with a 5668 elements mesh, representing the diametric section of the column, parallel to the main side of the crystals (see Figure 11). Elements are square and 1mm size. Considering the symmetry of the mesh, preliminary studies over time and spatial discretization were performed over only half of the column (see section 7.2.2).
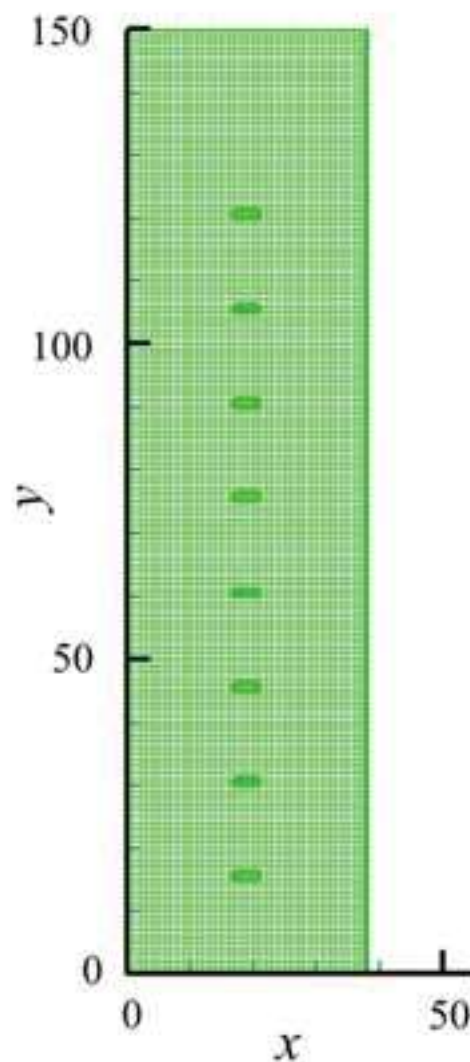
Figure 7.11 – Mesh used for simulation in Bouissonnié et al (2018). The 5668 elements are square and 1mm side.

7.2.1 Computation of reactive surface area for TST and SWM models

Two different models were implemented in the code for the simulation of Calcite crystals dissolution: the popular TST dissolution rate (equation (7.4)), which is available in most codes, and SWM dissolution rate (equation (7.5)). Both models require the presence of a reactive surface area A_s [L^2-min/M_{H2O}] to connect the evolution of the mineral with the solution. The value of A_s can be computed on the basis of porosity and values of specific surface extracted from literature, such as in Wanner et al. (2015). Nevertheless, in order to guarantee a better representation of the experiment, the reactive surface area was computed as a function of the size of the element in this work. Figure 7.12 shows elements in contact with one crystal in Figure 7.11 or 7.13 (the system of reference is the same as Figures 7.11 and 7.13).

For a single element, the surface of the mineral exposed to the flux (red shadow in Figure 7.12) can be computed as $\Delta X \times \Delta Z$ [L^2]. At the same time, given ϕ the porosity of the medium, the volume of water contained in the cell is $V_w = \Delta X \times \Delta Y \times \Delta Z \times \phi$ [L^3]. Since the interest is in obtaining a parameter measured in [L^2_{min}/M_{H2O}], the following formula for the computation of A_s is proposed:

$$A_S = \frac{\Delta X \Delta Z}{\Delta X \Delta Y \Delta Z \phi \rho_{H_2O}} \frac{\left[L^2_{min} \right]}{\left[L^3 \right]} \frac{\left[L^3 \right]}{\left[M_{H_2O} \right]} = \frac{\Delta X}{\Delta X \Delta Y \phi \rho_{H_2O}} \frac{\left[L^2_{min} \right]}{\left[M_{H_2O} \right]} \tag{7.7}$$

It is worth reminding that in SpeCTr the coherence of space and time units is a responsibility of the user and an effort is required to make sure that constants (for example water density ρ) are expressed in their correct units. The same is true for kinetic constants [mol/T] in equations (7.4) and (7.5), they must be expressed in the time unit adopted in the problem.
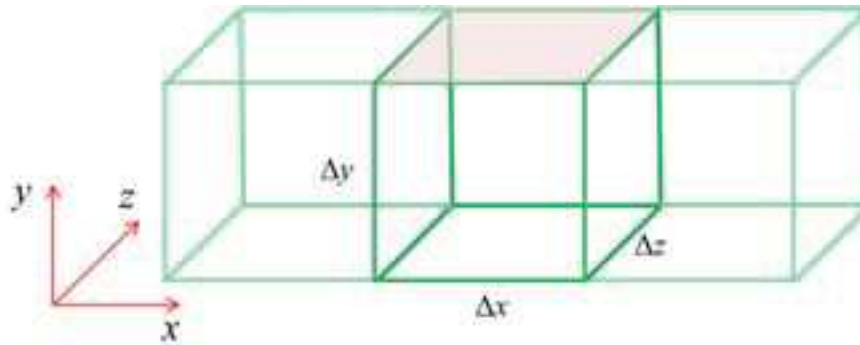
Figure 7.12 – Schema of an element of the mesh in Figure 7.11 (or 7.13) in contact with the Calcite crystal (red shadow), coordinates are reported as in Figure 7.11 (or 7.13).

7.2.2 Time and spatial discretization

The symmetric nature of the mesh in Figure 7.11 allowed testing the size of elements and time stepping only over half of the column section (see Figures 7.12 and 7.15). Figure 7.6a shows that Calcite crystals were considered, as impervious from a flow point of view, i.e. as holes in the mesh. Figure 7.13 shows the 1mm side elements mesh used to describe the half-column section. From a chemical point of view, Calcite was made available to dissolve in the elements surrounding holes (for example, for the first crystal: in Figure 7.13, elements 281-285 on the upstream face and their homologs on the downstream face). In order to avoid possible dependencies of results from time or spatial discretization, two meshes were tested (one with 2810 elements 1 mm side and the other with 11240 elements 0.5 mm side) and tests were performed with different time step sizes.
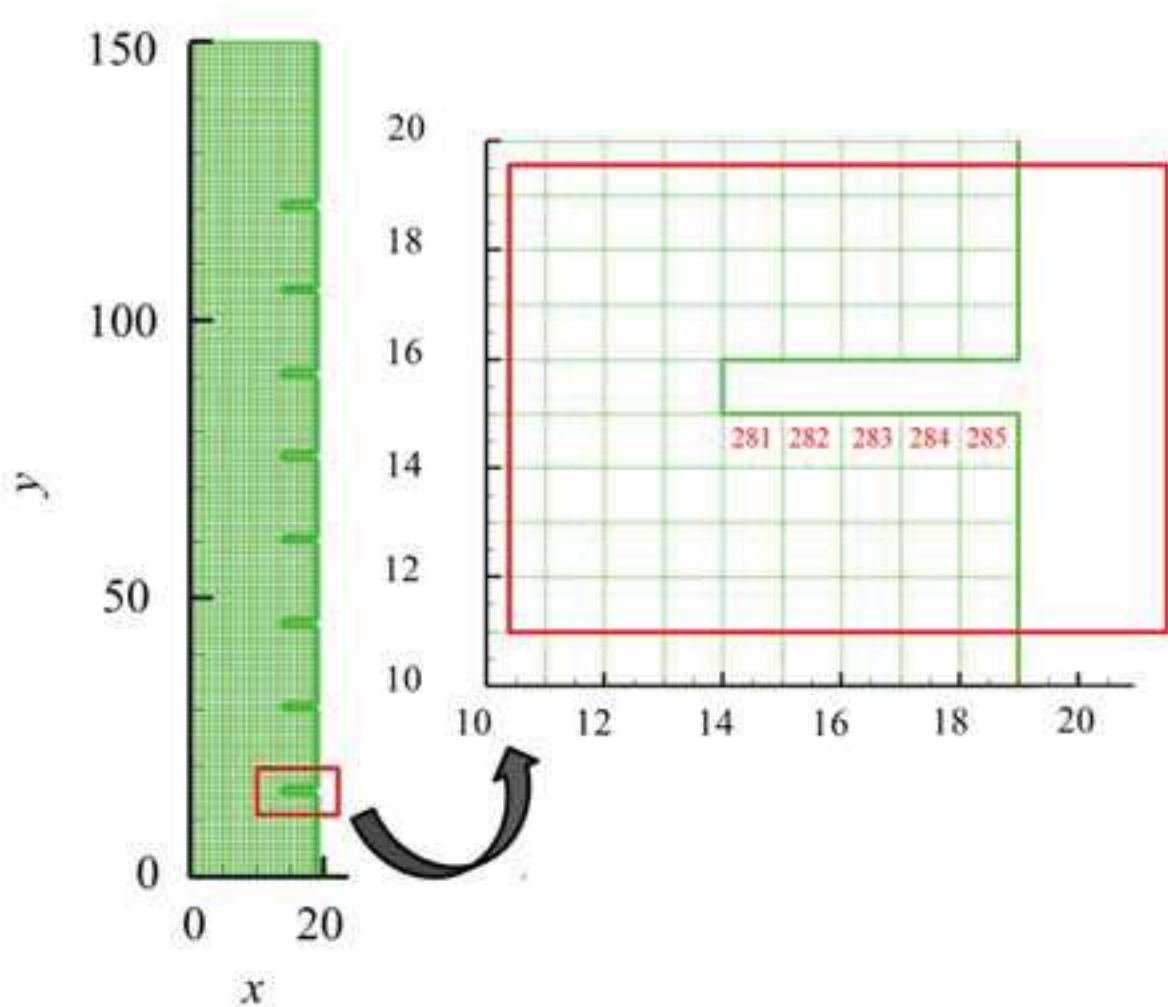
Figure 7.13 – The 2810 elements mesh used for testing time discretization for the simulations in Bouissonnié et al. (2018). The size of elements (1 mm^2) was confirmed after a comparison of the results obtained with a finer grid.

194

The experiment was carried in a column of 150 mm height and 18 mm radius, filled with non-reactive glass beads and containing eight Calcite ($CaCO_3$) crystals; a constant flow ($v=3.77 \cdot 10^{-3}$ [mm/s]) was imposed in the column (direction $y=0$ to $y=150$) engendering Calcite dissolution.

Simulations were run only for the following combination of models and parameters: $\alpha_L=10$ mm, $\alpha_T=1$ mm, $D_0=10^{-4}$, TST dissolution model (assuming that TST and SWM models for calcite dissolution behave accordingly), reactive surface dependent from the mesh-size as in equation (7.7). Flow, transport and TST parameters used in the simulations are resumed in Table 7.6, while the reaction network is the same presented in Table 7.3.

Parameter	Value	Unit
Porosity ϕ	0.38	[-]
Conductivity	100	[mm/s]
V_y	$3.77 \cdot 10^{-3}$	[mm/s])
α_L	10	[mm]
α_T	1	[mm]
D	10^{-4}	[mm^2/s]
K_{eq}	1.8487	[-]
K_{kin}	$5.2 \cdot 10^{-7}$	[mol/m^2/s]

Table 7.6 – Main parameters for preparatory simulations.

Tests were performed at first using the 1 mm size elements grid. The time step size computed to respect CFL condition was progressively reduced, initially divided by a factor 5 and subsequently by a factor 10. Concentrations of total Ca^{2+} were monitored at the upstream elements of the first Calcite crystal, which is considered the most critical position since it's the closest to boundary conditions. Elements representing the upstream face (the direction of the flow is from $y=0$ to $y=150$) of the first Calcite crystal are 281-285 (see Figure 13).

Important and systematic reductions of concentrations appear in Figure 14 when moving from the step size required by CFL condition to a fifth of its value. Differences are more important far from the column axes. Moving from dt/5 to dt/10 causes a modest reduction of concentrations (see Figure 15) which remains more important far from the column axis.
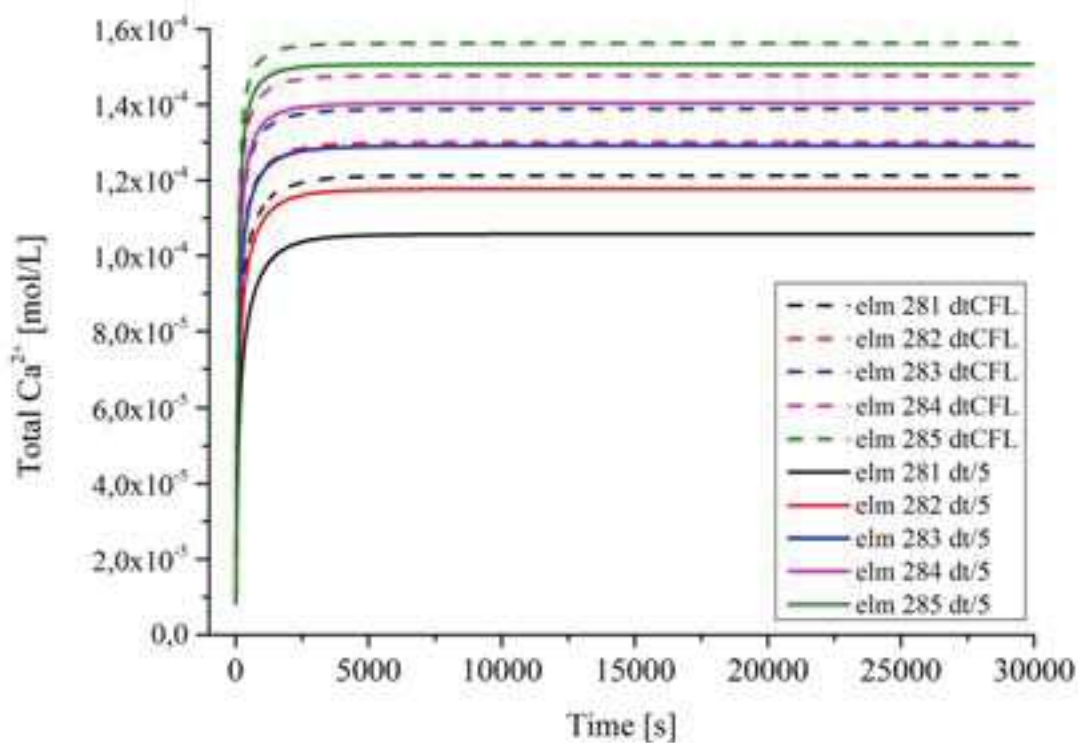
Figure 7.14 – Total dissolved Ca^{2+} concentrations at upstream faces of first crystal obtained with dtCFL and dt/5 (dtCFL divided by a factor 5).
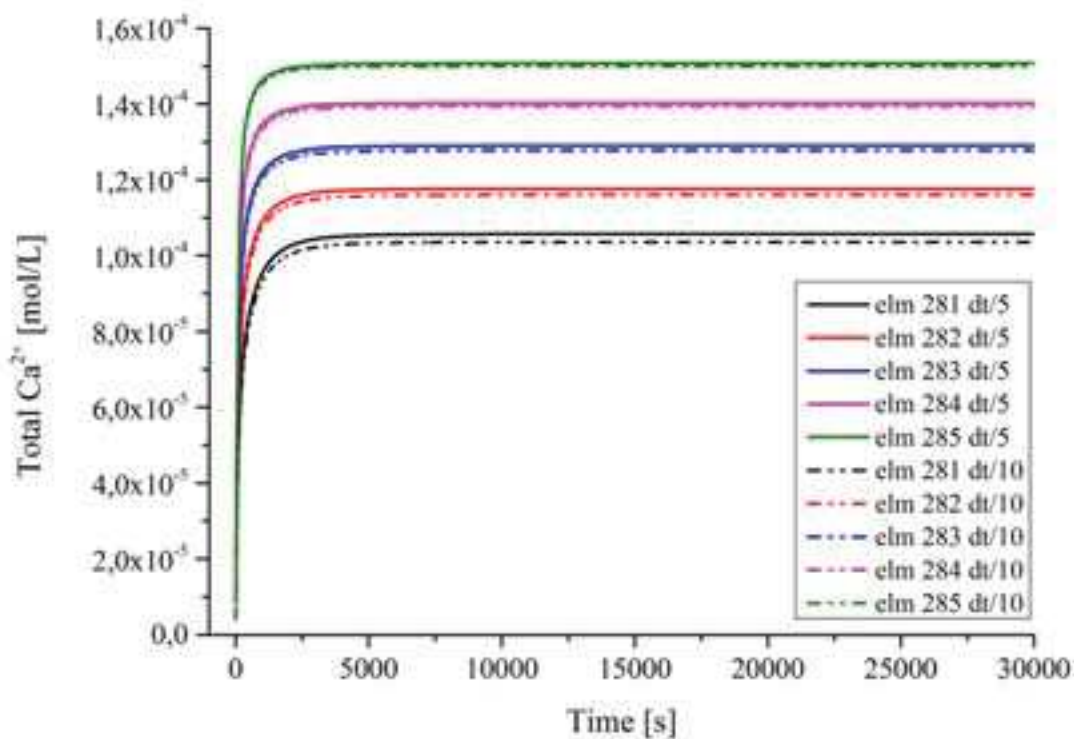
Figure 7.15 – Total dissolved Ca^{2+} concentrations at upstream faces of first crystal obtained with dtCFL and dt/10 (dtCFL divided by a factor 10).

In order to avoid dependencies of the solution from the spatial discretization, a simulation was run with a finer mesh (around 11000 elements, 0.5 mm side; see Figure 7.16) and a time step of dt/5. Concentrations were monitored at the elements closest to the column axis, since only in those elements the retreat of the crystal was compared to experimental data. For the upstream face of first crystal, the element of interest is element 285. Figures 7.17 and 7.18 show the total dissolved Ca^{2+} concentrations at crystals while Figure 7.19 shows it at the outlet; the concentration at the outlet is the result of a mean over the outlet elements (*x=0* to *x=18, y=150*) computed taking fluxes into account.
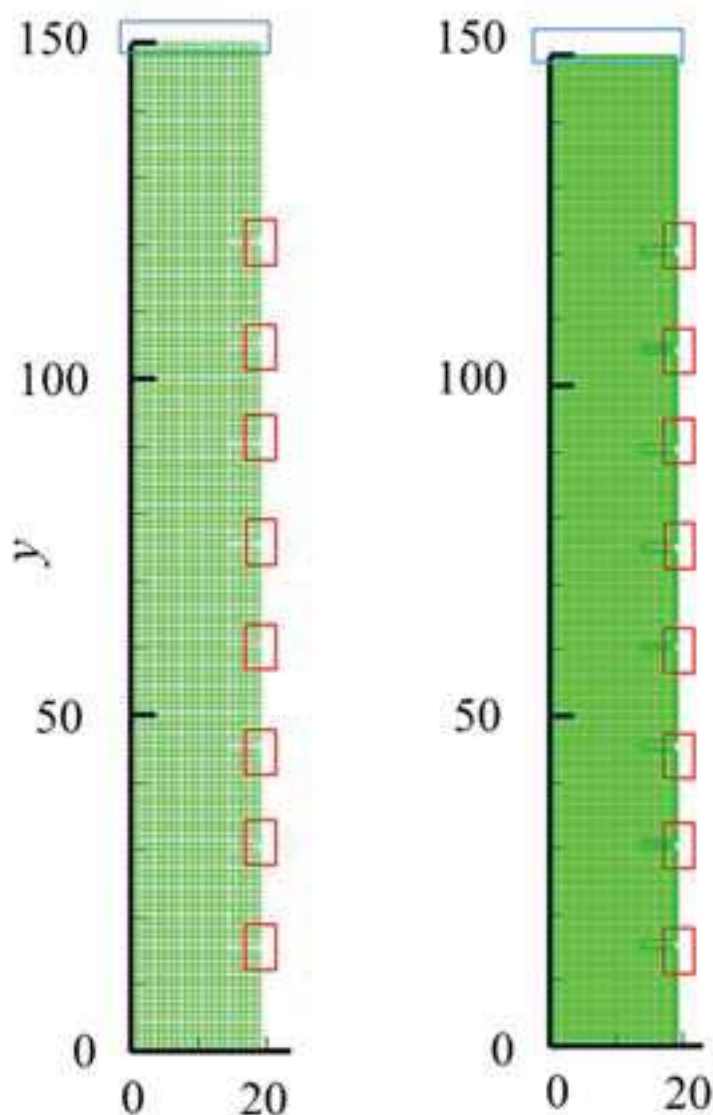
Figure 7.16 – The coarse mesh (2810 elements, 1 mm side) on the left and the fine mesh (11240 elements, 0.5 mm side) on the right. Red rectangles highlight the portions of the crystals that were monitored; in the blue rectangles, the outlets.
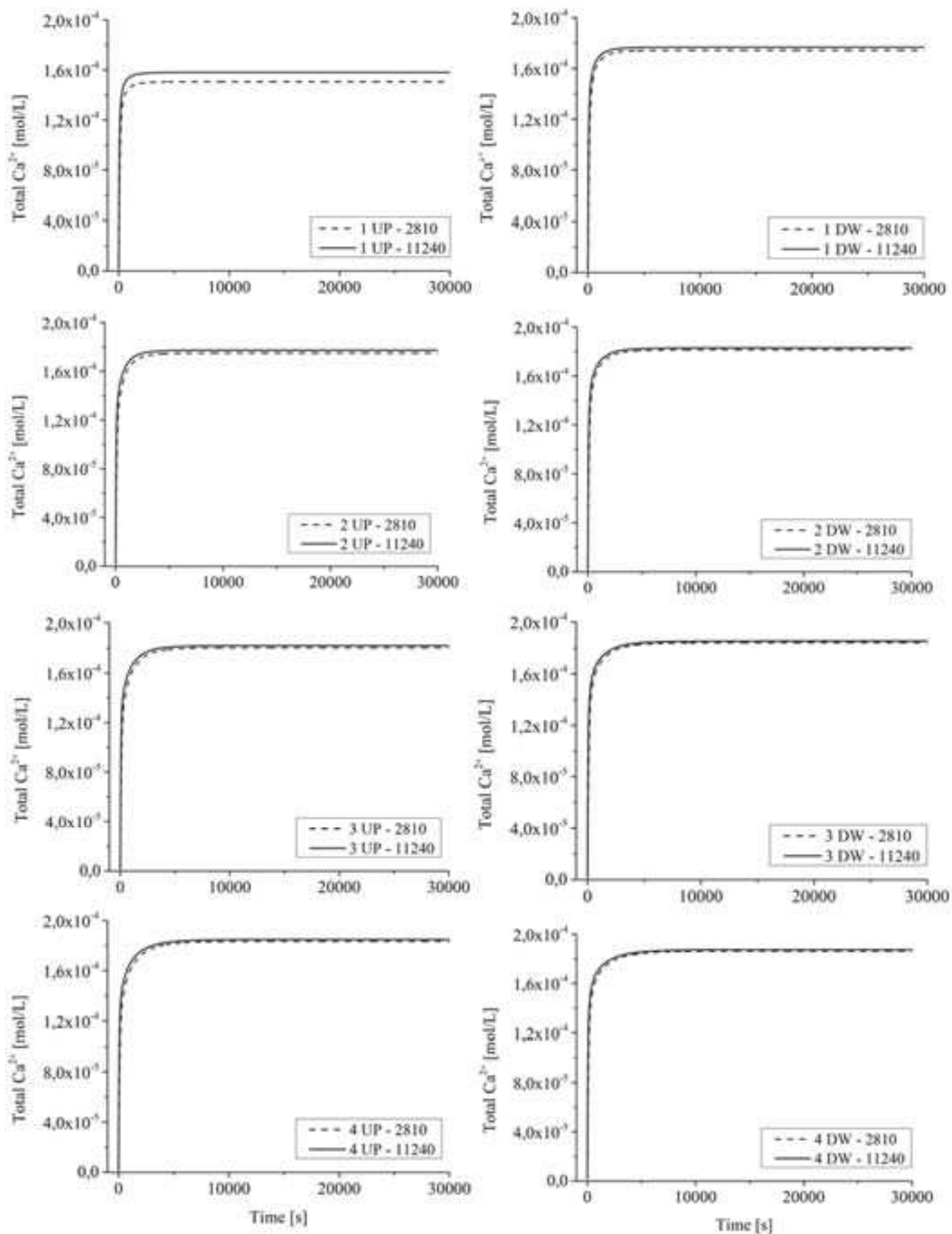
Figure 7.17 – Total dissolved Ca^{2+} concentrations at crystals obtained with coarse (dashed) and fine (continuous) mesh.
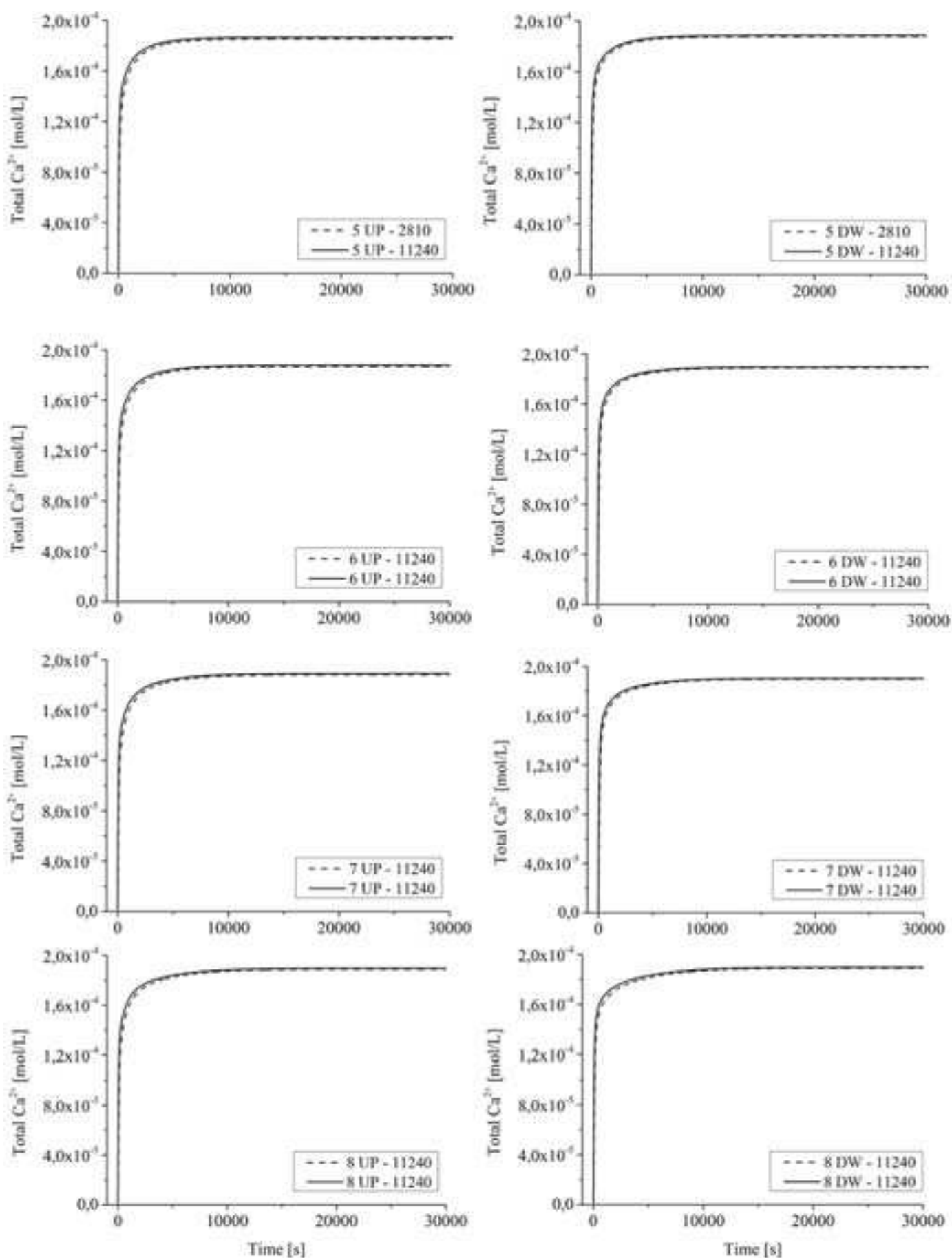
Figure 7.18 – Total dissolved Ca^{2+} concentrations at crystals obtained with coarse (dashed) and fine (continuous) mesh.

Results obtained with the two meshes are in good agreement although small differences exist. Most important discrepancies appear at the first crystal, confirming the hypothesis that the crystal closer to the boundary conditions is the more exposed to time and spatial discretization dependencies. Results in Figures 7.17, 7.18, 7.19 also confirm that equation (7.7) is independent of the mesh size, as predictable from some basic mathematical considerations. Although there is an effect of the spatial discretization, it is minimal and it doesn't justify the use of the 0.5 mm elements grid.

Concerning time discretization, although the difference between concentrations computed with dt/5 and dt/10 is around 2%for element 281, the direct interest is over element 285 (the retreat of the crystal was compared to experimental data only at central elements of the crystal), which shows an error of about 0.7%. Moreover, differences are expected to lower proceeding in the y direction (as happens for spatial discretization in Figures 7.17 and 7.18), therefore the use of dt/5 is justified. For this reason, all simulations in Bouissonnié et al. (2018, submitted) are run with a transport time step five times smaller than the required CFL condition.
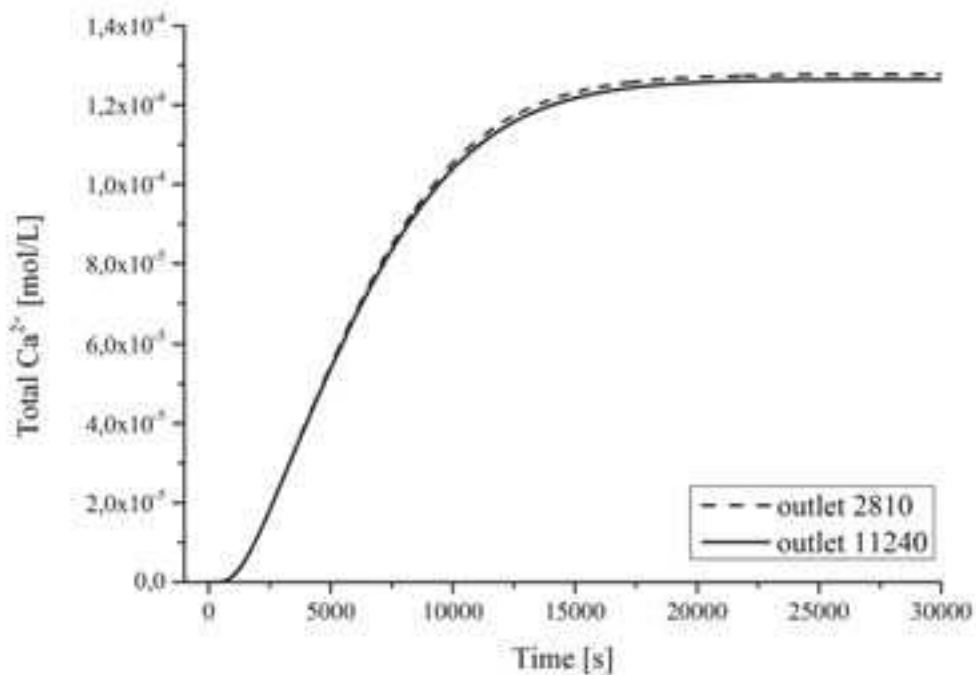
Figure 7.19 – Total dissolved Ca^{2+} concentrations at the outlet obtained with coarse (dashed) and fine (continuous) mesh.

7.3 Mixing induced CaCO₃ precipitation

7.3.1 Presentation of the test case

The test case presented in the next paragraphs was published by Katz et al. (2009) in a comprehensive experimental and numerical study regarding mixed induced precipitation of Calcite. The original work included both conservative and reactive transport modeling in homogeneous and heterogeneous media. Conservative transport experiments reported in Katz et al. (2009) were also used as a basis for global sensitivity analysis (Fajraoui et al. 2009); in this work, the interest is focused on the reactive transport experiment in a heterogeneous medium, which will be modeled with SpeCTr. The importance of solving as many problems as possible cannot be stressed enough if the purpose is to provide a reliable code for realistic geochemical simulations. In this particular case, SpeCTr will be confronted with the modifications of physical modifications of the porous medium following the precipitation of a solid phase.
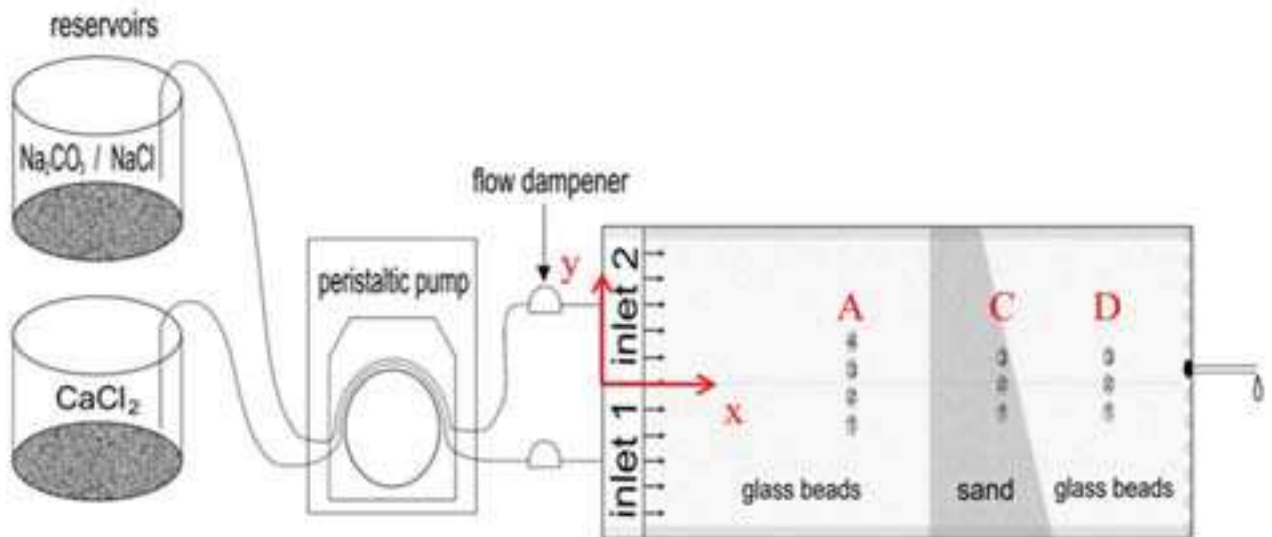
Figure 7.20 – Experimental setup for the reactive transport experiment in heterogeneous porous medium (Katz et al. 2009).

The experimental setup for reactive transport in heterogeneous medium (Katz et al. 2009) is shown in Figure 7.20. Laboratory experiment consisted in injecting two potentially reactive solutions (calcium chloride, $CaCl_2$, and sodium carbonate, Na_2CO_3) with a parallel flow, triggering Calcite ($CaCO_3$) precipitation at the interface. The dimensions of the flow cell are $x=25$ cm, $y=10$ cm, and $z=0.8$ cm. Two different porous media constitute the heterogeneous domain. The majority of the domain is filled with 1 mm glass beads, while 0.532 mm sand grains fill a trapezoidal section of coordinates: $x=14$, $y=-5$; $x=21.25, y=-5$; $x=14, y=5$; $x=15.25$, $y=5$ (see Figure 7.2). Calcium chloride ($CaCl_2$) solution is injected through inlet 1, that goes from ($x=0, y=0$) to ($x=0, y=-5$); sodium carbonate (Na_2CO_3) is

injected at inlet 2, that goes from ($x=0,y=0$) to ($x=0,y=5$). There are three series of sampling ports over the domain, named A(1-4), C(1-3) and D(1-3) (see Table 7.7 for the exact location). Total Calcium (Ca^{2+}) concentrations were measured throughout time at sampling ports and subsequently confronted with simulated values obtained with code RETRASO, (Saaltink et al. 2004).

	A1	A2	A3	A4	C1	C2	C3	D1	D2	D3
x	11.4	11.4	11.4	11.4	17.4	17.4	17.4	21.4	21.4	21.4
y	-1.5	-0.5	0.5	1.5	-1	0	1	-1	0	1

Table 7.7 – Coordinates of sampling ports [cm].

7.3.1.1 Spatial discretization, flow characteristics and ground properties

The domain was discretized by a mesh composed of around 17000 triangular elements (see Figure 7.21). Glass beads that fill the majority of the domain have an estimated porosity of 0.375 [-] and permeability of 1.12 10^{-9} [m^2]; the sand filling the trapezoidal area has a porosity of 0.32 [-] and permeability of 2.31 10^{-10} [m^2] (Fajraoui et al. 2011). Previous values of permeability result in values of hydraulic conductivity of 67.2 [cm/min] and 13.8 [cm/min] for respectively glass beads and sand grains. Neuman conditions were imposed at the inlet, with a constant flow varying slightly between inlet 1 and inlet 2 in order to account for a non-uniform distribution of the flow rate (Fajraoui et al. 2011): v=0.15870 [cm/min] at inlet 2 and v=0.14130 [cm/min] at inlet 1). A Dirichlet boundary condition was imposed at the outlet (h=1 [cm]).
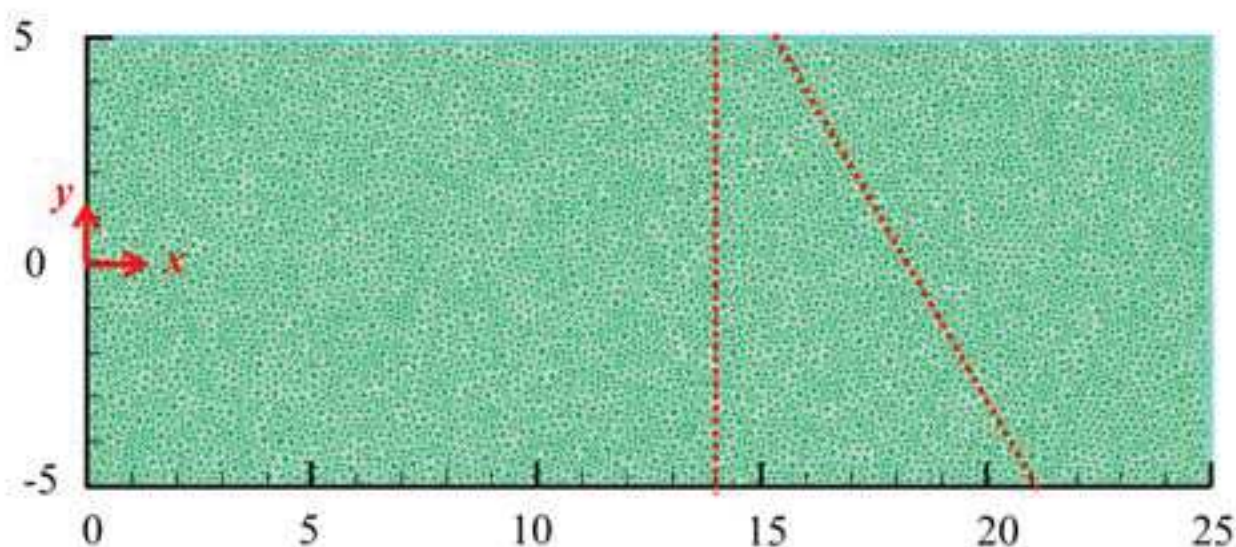
Figure 7.21 – Spatial discretization of the domain with triangular elements; red dashed lines emphasize the zone at lower porosity.

As explained in Katz et al (2009), the heterogeneous porous medium is initially saturated with a NaCl solution at 5 g/kg-water equilibrated with ambient air. Throughout the duration of the experiment, two solutions are injected at the inlet (both at 5 g/kg-water, equilibrated with ambient air): $CaCl_2$ at inlet 1 and Na_2CO_3 at inlet 2. Equilibration with ambient air was computed with CHESS (Van der Lee 1998) model.

Six total dissolved concentrations (corresponding to the six primary species chosen to represent the reaction network) are transported throughout the domain. Initial and boundary conditions for each of the six elements are listed in Table 7.8.

	Initial Conditions	*Boundary Conditions* Inlet 1	*Boundary Conditions* Inlet 2
	mol/L	mol/L	mol/L
H^+	$1.29031 \ 10^{-5}$	$1.26957 \ 10^{-5}$	$5.67332 \ 10^{-3}$
H_2O	55.5	55.5	55.5
HCO_3^-	$1.29137 \ 10^{-5}$	$1.23807 \ 10^{-5}$	$4.71865 \ 10^{-2}$
Cl^-	$9.01901 \ 10^{-2}$	$9.01000 \ 10^{-2}$	$9.98000 \ 10^{-2}$
Na^+	$9.01901 \ 10^{-2}$	0.0	$9.43497 \ 10^{-2}$
Ca^{2+}	0.0	$4.50505 \ 10^{-2}$	0.0

Table 7.8 – Initial and boundary conditions obtained with CHESS.

In the portion of the domain occupied by glass beads, longitudinal dispersivity (α_L) is set to 0.1 cm (corresponding to glass beads diameter) and transverse dispersivity (α_T) is set to 0.01 cm ($\alpha_T = \alpha_L /10$) for each chemical species. In the portion of the domain occupied by sand α_L is set to 0.05 cm (as sand mean grain diameter) and α_T is set to 0.005 cm ($\alpha_T = \alpha_L /10$) for each chemical species. Diffusion coefficients for chemical species *in the porous medium* are set to $6 \ 10^{-5}$ [cm^2/min] (corresponding to a diffusion coefficient *in water* of $1 \ 10^{-9}$ [m^2/s]) for every chemical species in both the glass beads and sand portions of the domain.

7.3.1.3 Reaction network

The equilibration with ambient air of the three solutions (NaCl, $CaCl_2$, Na_2CO_3) performed with CHESS provided a reaction network of 19 species that can be described through 6 primary species (*tableau* de Morel reported in Table 7.9) and 13 mass action laws. Equilibrium constants linking

primary to secondary species are also reported in Table 7.9. Pay attention to the fact that in SpeCTr equilibrium constant is intended as: $C_i = K_i \prod_{j}^{N_x} X_j^{V_{ij}}$.

	H^+	H_2O	HCO_3^-	Cl^-	Na^+	Ca^{2+}	$Log_{10} K$
$CaOH^+$	-1	1	0	0	0	1	-12.834
$CaCl^+$	0	0	0	1	0	1	-0.6956
$CaHCO_3^+$	0	0	1	0	0	1	1.0467
$NaCO_3^-$	-1	0	1	0	1	0	-9.8144
$NaHCO_3$	0	0	1	0	1	0	0.1541
$NaCl$	0	0	0	1	1	0	-0.777
$CaCO_3$	-1	0	1	0	0	1	-7.009
$CaCl_2$	0	0	0	2	0	1	-0.643
$NaOH$	-1	1	0	0	1	0	-14.795
HCl	1	0	0	1	0	0	-0.67
CO_2	1	-1	1	0	0	0	6.341
CO_3^{2-}	-1	0	1	0	0	0	-10.329
OH^-	-1	1	0	0	0	0	-13.991

Table 7.9 – Aqueous equilibrium reactions in the reaction network.

Precipitation at the interface of the two solutions was modeled in Katz et al. (2011) according to the assumption of thermodynamic equilibrium. We recall that under this assumption, the solution is saturated when in equation (7.8) SI $\geq$ 1; when the solution is saturated, a solid phase is allowed to form to bring equation (7.8) to SI = 1.

$$SI_i = K_{pi} \prod_{N_x} \{X_j\}^{a_{i,j}} \qquad (7.8)$$

where constant K_{pi} is the inverse of the solubility product K_s and was set to Log_{10} $Kpi(CaCO_3)$ = -1.8487. An alternative to the model of thermodynamic equilibrium is the kinetic precipitation of the Calcite, according to the TST model as presented in Chapters 4, 6 and 7.

$$^{CaCO_3}r = -k \, A_S \left(1 - \frac{Q}{K_S}\right)^n \qquad (7.9)$$

Where As is the reactive surface, k is the kinetic constant and K_S is the solubility product (Log_{10} $Ks(CaCO_3)$ = 1.8487, k=3.12 10^{-5} mol/min).

7.3.1.4 Algorithms for porosity changes

A consequence of Calcite precipitation is clogging of the pores, which of course causes a variation in porosity. In Katz et al. (2009), porosity is updated as a function of the number of mineral moles:

$$\frac{\partial \phi}{\partial t} = -\sum_m V_m \frac{\partial m_m}{\partial t} \tag{7.10}$$

where m_m is the number of moles of mineral m and V_m is its molar volume. In Katz et al (2009) m_m is computed at nodes, while porosity is required at elements, this implying some sort of conversion between nodes and elements. The change in pore volume with RETRASO is computed at nodes:

$$\Delta V_p(node_i) = -\sum_{m=1}^{Nm} V(cell_i)\Delta m_m(cell_i)v_m \tag{7.11}$$

where *V(cell)* is the volume related to node i, *Δm* is the variation of moles per volume of porous medium. The further conversion from cell to element can be found in Katz et al (2009). What is interesting here is the system for porosity update. In SpeCTr, until now, a linear variation of porosity is implemented:

$$\phi_{new} = \phi_{old}\left(\frac{1 + V_{m-old}}{1 + V_{m-new}}\right) \tag{7.12}$$

where:

$$
\begin{aligned}
V_{old} &= \sum_m Cp_{m-old}v_m \\
V_{new} &= \sum_m Cp_{m-new}v_m
\end{aligned}
\tag{7.13}
$$

Equation (7.13) is written for equilibrium equations and *Cp* can be substituted with *Cc* for kinetic minerals. Following porosity update, permeability is changed according to (Cochepin et al. 2008):

$$k = k_{old}\left(\frac{\phi}{\phi_{old}}\right)^3 \tag{7.14}$$

Diffusion is updated according to the model (Cochepin et al. 2008):

$$D = D_m\,\phi^{cem} \tag{7.15}$$

where D is the Diffusion coefficient in the porous medium, D_m is the diffusion coefficient in water , ϕ is porosity and *cem* is the cementation exponent.

7.3.2 Results of numerical simulations: SPeCTr

7.3.2.1 Results: constant porosity – equilibrium and kinetic CaCO₃ precipitation

In order to evaluate the impact of porosity changes, two preliminary simulations were run with constant porosity. In one simulation, precipitation of $CaCO_3$ is modeled at thermodynamic equilibrium while in the other, precipitation of Calcite is considered kinetic (laws and constants are defined in paragraph 7.3.1.3). Chronological evolutions of total dissolved Ca^{2+} at sampling ports A, C and D are reported in Figures 7.22 to 7.31. Two experiments were performed (Katz et al. 2009) therefore two series of experimental concentrations are represented in the following figures (black squares and red rounds). Simulations published in Katz et al. (2009) for the heterogeneous reactive transport experiment are reported in green continuous line. Calcium evolution curves obtained with SpeCTr are reported in blue: a blue continuous line shows results obtained with equilibrium precipitation of Calcite, a blue dashed line shows results of kinetic precipitation. A black dashed line shows the total Calcium concentration injected at inlet 1. It should be kept in mind that sampling ports are numbered from the lowest (with reference to y axis) to the highest.

Figure 7.22 – Time evolution of total Calcium concentration at sampling port A1. Red rounds and black dots represent experimental data; green continuous line represented the simulation in Katz et al (2009); black dashed line corresponds to the concentration at inlet 1; blue curves represent SpeCTr simulations for equilibrium (continuous) and kinetic (dashed) Calcite precipitation.

Figure 7.23 – Time evolution of total Calcium concentration at sampling port A2 (legend in Figure 7.22).

Figure 7.24 – Time evolution of Total Calcium concentration at sampling port A3 (legend in Figure 7.22).

Figure 7.25 – Time evolution of Total Calcium concentration at sampling port A4 (legend in Figure 7.22).

Figure 7.26 – Time evolution of Total Calcium concentration at sampling port C1 (legend in Figure 7.22).

Figure 7.27 – Time evolution of Total Calcium concentration at sampling port C2 (legend in Figure 7.22).

Figure 7.28 – Time evolution of Total Calcium concentration at sampling port C3 (legend in Figure 7.22).

Figure 7.29 – Time evolution of Total Calcium concentration at sampling port D1 (legend in Figure 7.22).

Figure 7.30 – Time evolution of Total Calcium concentration at sampling port D2 (legend in Figure 7.22).

Figure 7.31 – Time evolution of Total Calcium concentration at sampling port D3 (legend in Figure 7.22).

At sampling ports outside the precipitation zone or at its lower boundary (A1, C1 and D1, see Figure 7.32 and 7.33) experimental values reach the initial total Ca^{2+} concentrations or a slightly inferior value (sampling port C2). SpeCTr simulations reproduce this behavior correctly with both equilibrium and kinetic Calcite precipitation. Differences between results of equilibrium and kinetic Calcite precipitation increase with their distance from the *reservoir* of Ca^{2+} (that is the red zone in Figure 7.32). At sampling ports C3 and D2 (which appear to be in the green stripe in Figure 7.32 b) and c)) the difference between the equilibrium and kinetic curves becomes distinguishable. The difference between the results of the two types of simulations becomes huge at sampling ports A4 and D3. Total dissolved Calcium concentration is systematically higher for kinetic simulation, which is coherent with the fact that less Ca^{2+} is retired in the solid phase.

Generally, results from equilibrium simulation seem to better reproduce the time evolution of total Calcium concentration, which is rarely very different from measured values (with the exception of port D3). SpeCTr simulations seem to better fit experimental data with respect to those published in Katz et al. (2011), although this is probably due to more appropriate values of dispersivity and diffusion applied. From Figures 7.22 to 7.31 it is also evident that when no porosity changes are taken into account, once a stable value of total Ca^{2+} is reached there is no further evolution of its concentration: a perfect asymptote is reached. Experimental data show a clear evolution in time with values that tend to increase (sampling ports A2, A3, C3, D2) or decrease (sampling port A4) which simulations in Katz et al. (2009) are capable to reproduce qualitatively (though not quantitatively).
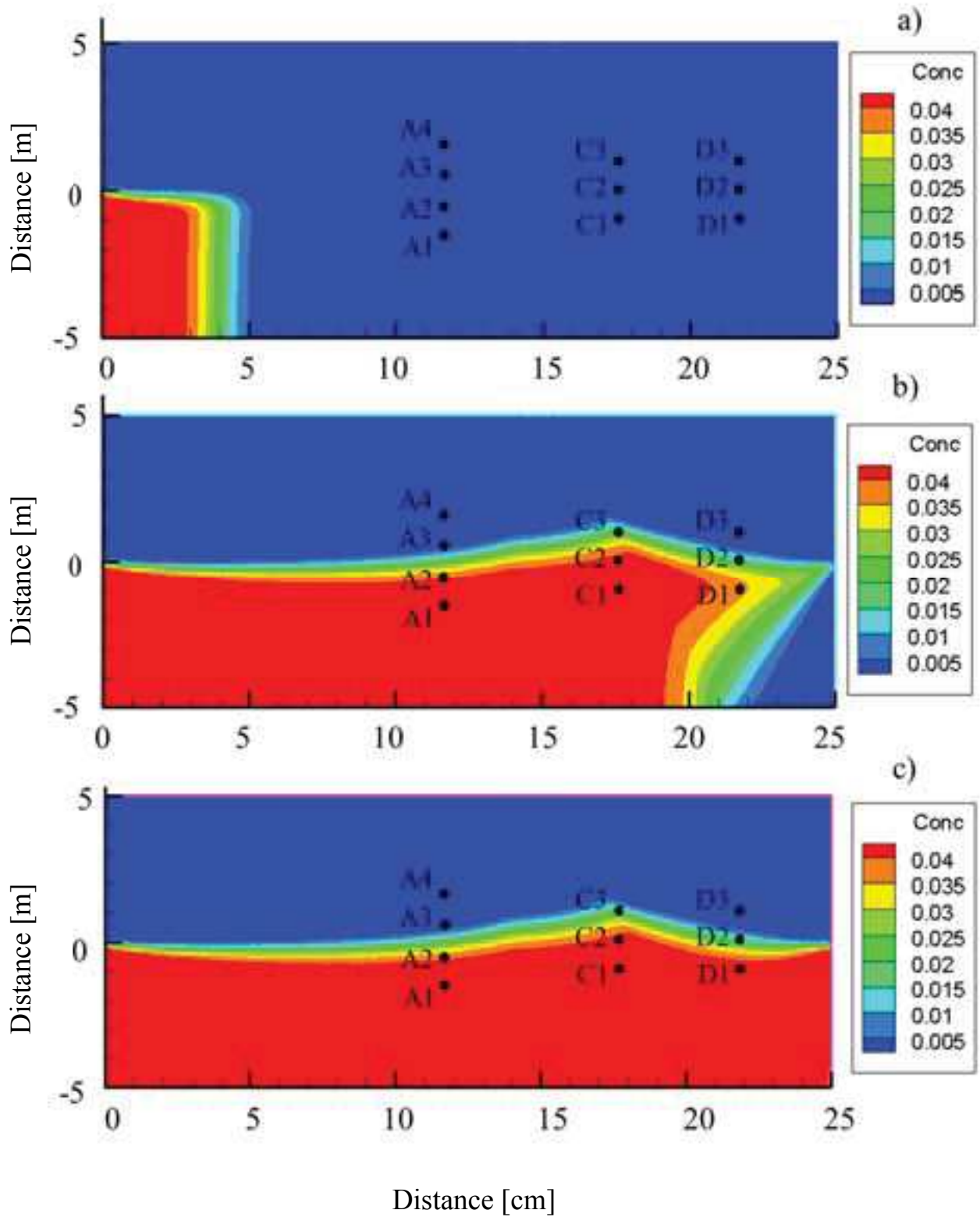
Figure 7.32 – Time evolution of Total Calcium concentration after 10 minutes (a), 60 minutes (b) and 120 minutes (c) for CaCO$_3$ equilibrium precipitation [mol/L].
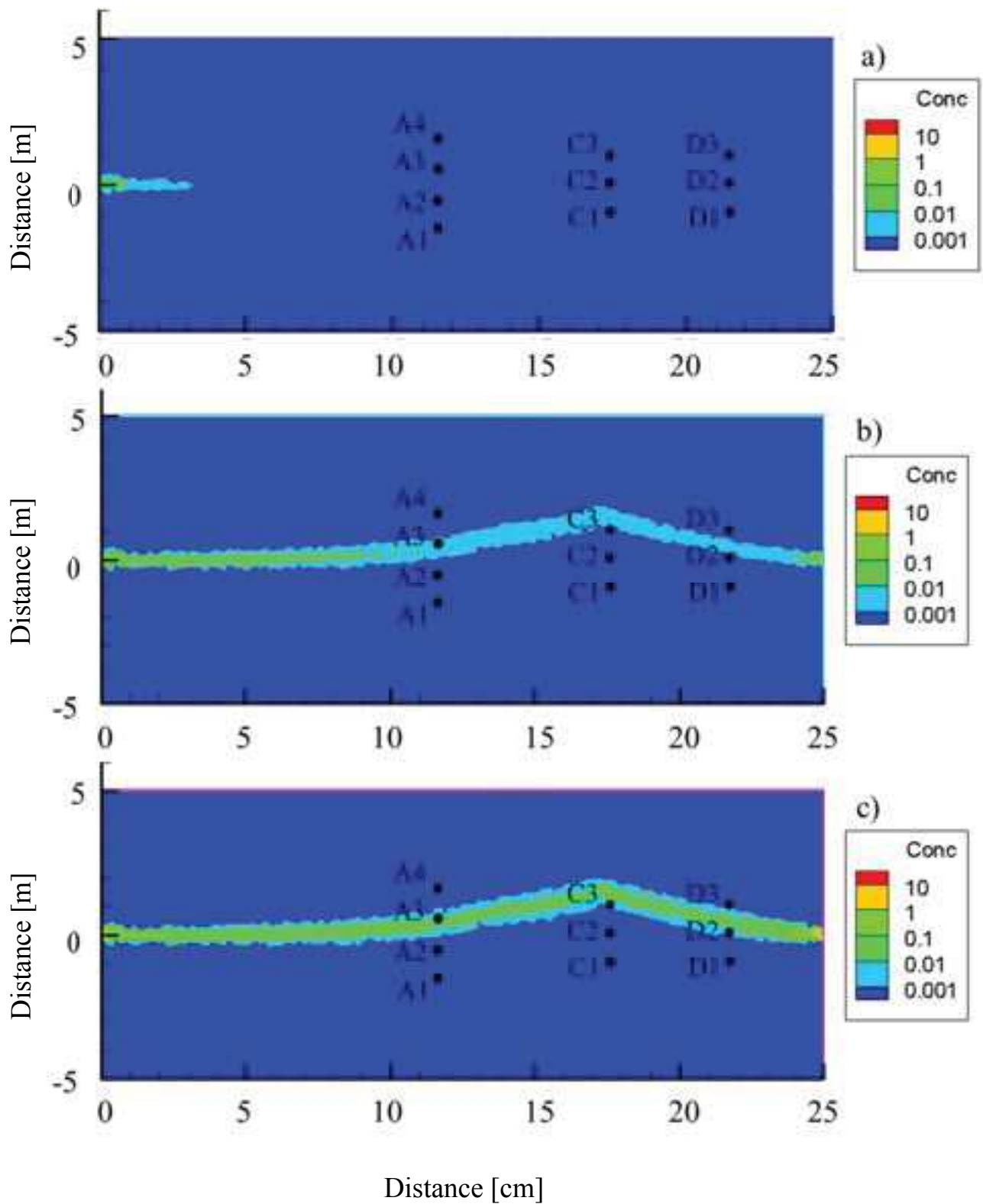
Figure 7.33 – Time evolution Calcite concentration after 10 minutes (a), 60 minutes (b) and 120 minutes (c) for CaCO$_3$ equilibrium precipitation [mol/L].
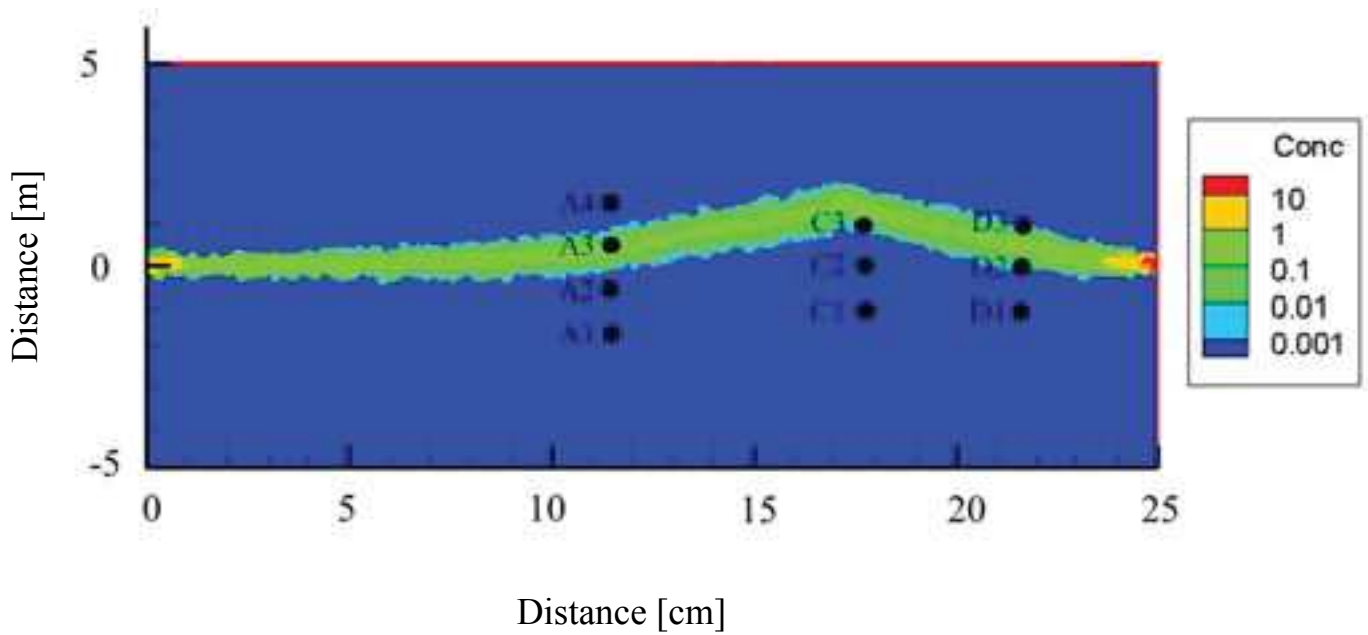
Figure 7.34 – Spatial distribution of Calcite after 12h for CaCO$_3$ equilibrium precipitation [mol/L] with SpeCTr.
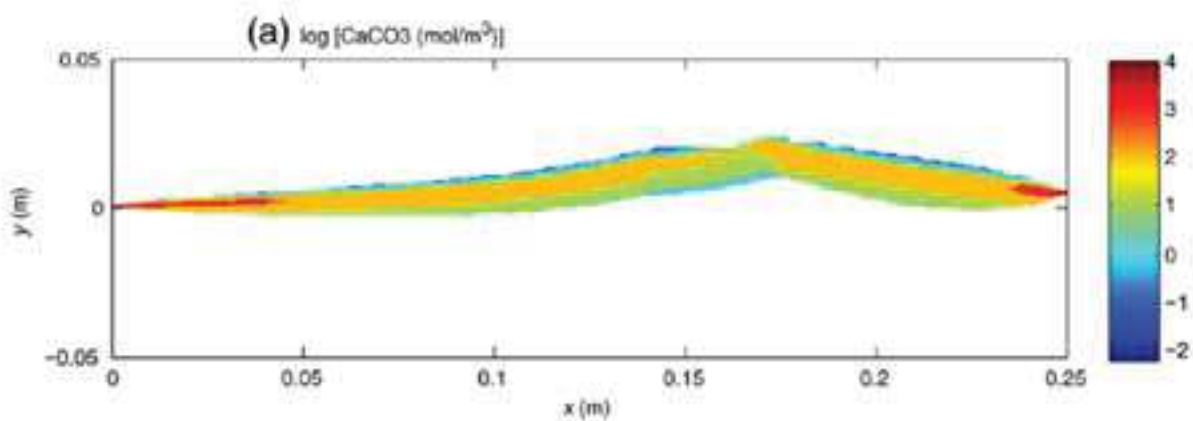
Figure 7.35 – Spatial distribution of Calcite after 11h for CaCO$_3$ equilibrium precipitation [mol/m^3] with RETRASO (Katz et al. 2009).

Although a quantitative comparison of Figures 7.34 and 7.35 is not possible (the units in which results are expressed are different, the duration of the simulations are different), qualitatively the two simulations are in agreement. Calcite precipitation is concentrated at the outlet and at the interface of inlet 1 and inlet 2 in the two cases although precipitation is less pronounced at the inlet in SpeCTr simulation. Moreover, the reduction in precipitation that characterizes the entering in the region at lower porosity is not significant in SpeCTr simulations.

Results obtained with equilibrium precipitation of $CaCO_3$ and variable porosity are presented in this paragraph. The algorithm used to update porosity (and consequently permeability and diffusion in the porous medium) is presented in paragraph § 7.3.1.4. Results are presented in Figure 7.36 to 7.45 with a blue line and symbol + . It is worth remembering that red circles and black squares represent experimental results and green line simulations performed with RETRASO. Blue continuous lines represent SpeCTr results with constant porosity. Once again, sampling ports below the precipitation zone (A1, C1, and D1) are immune to changes in the chemistry of the system. At ports A2, C2, and D2 concentrations are slightly superior to the constant porosity simulations. The same is true for A3, A4, C3, D3. If in the case of A4 and C3 this behavior represents an improvement of the results, this is certainly not the case for D3. What is evident is that the simulation does not (except for sampling port A4, see Figure 7.40) reproduce augmentations or reductions of concentrations dues to porosity changes. This may due to the fact that porosity was set to a minimum value of 0.1 in order to keep the computational cost of simulations reasonable (CFL Criterion has to be fulfilled).
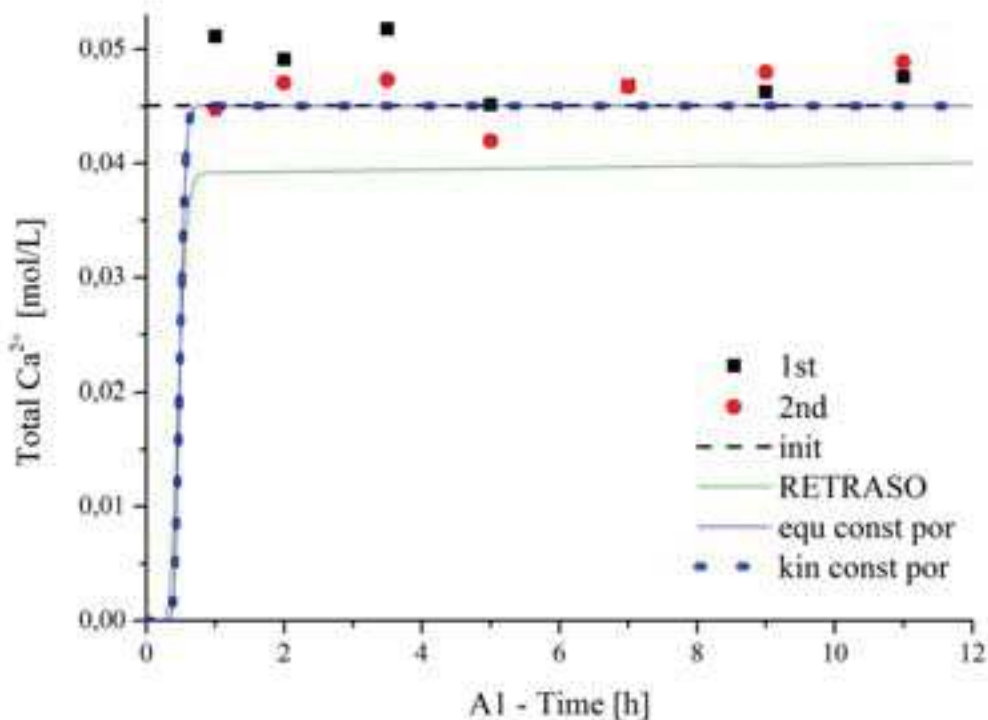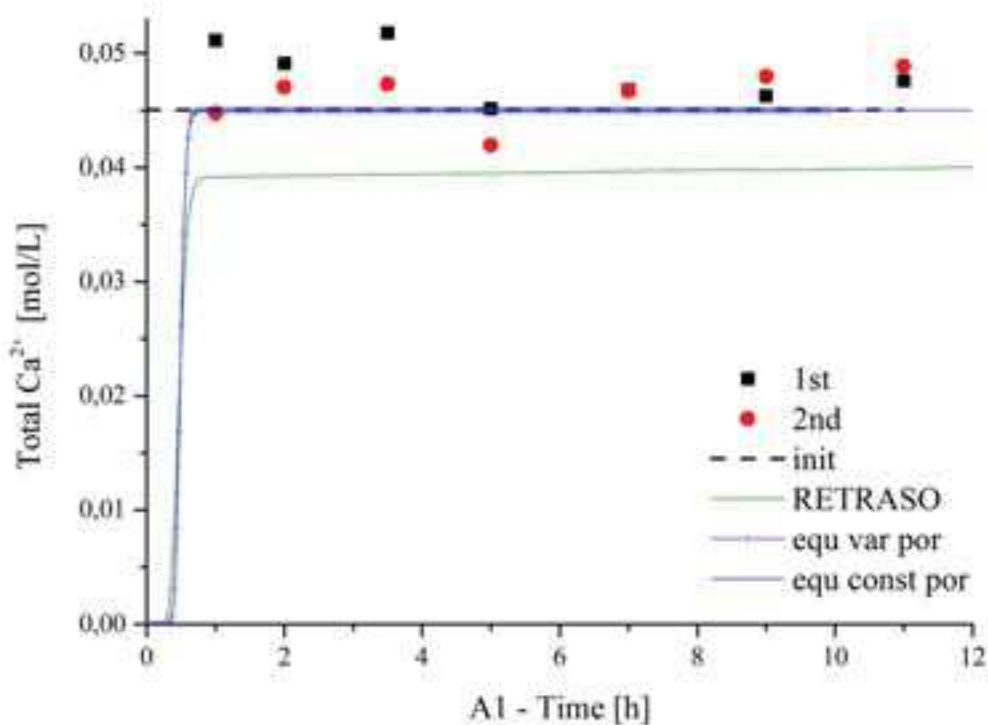

Figure 7.36 – Time evolution of total Calcium concentration at sampling port A1. Red rounds and black dots represent experimental data; green continuous line represented the simulation in Katz et al (2009); black dashed line corresponds to the concentration at inlet 1; blue curves represent SpeCTr simulations for equilibrium Calcite precipitation with constant (continuous) and variable (continuous +) porosity.
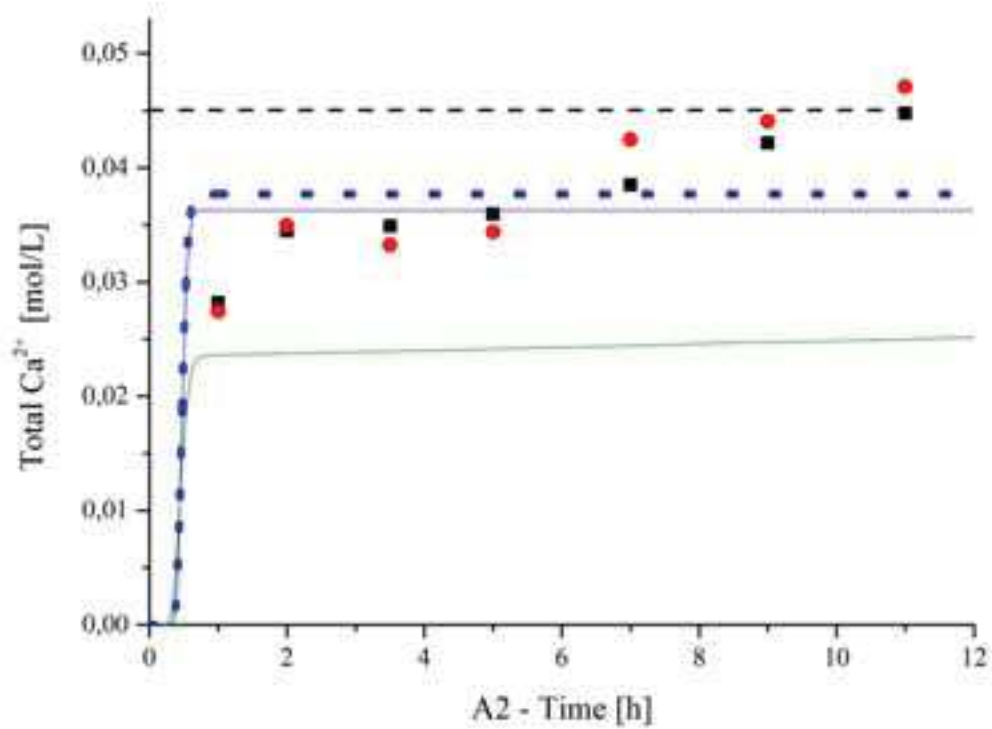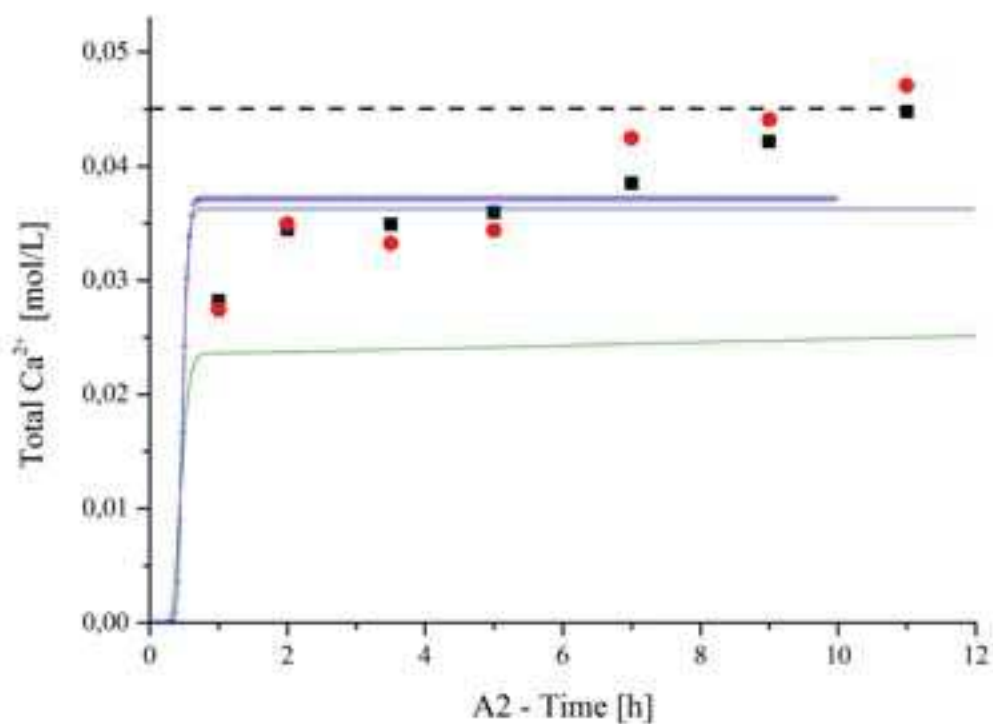
Figure 7.37 – Time evolution of Total Calcium concentration at sampling port A2 (legend in Figure 7.36).
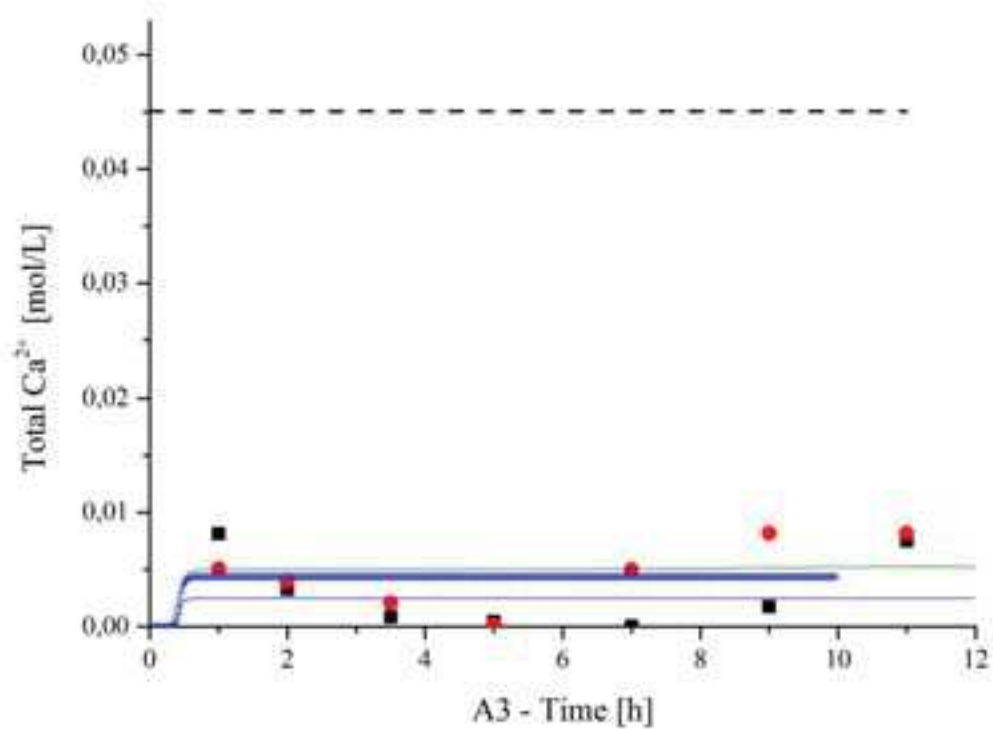
Figure 7.38 – Time evolution of Total Calcium concentration at sampling port A3 (legend in Figure 7.36).
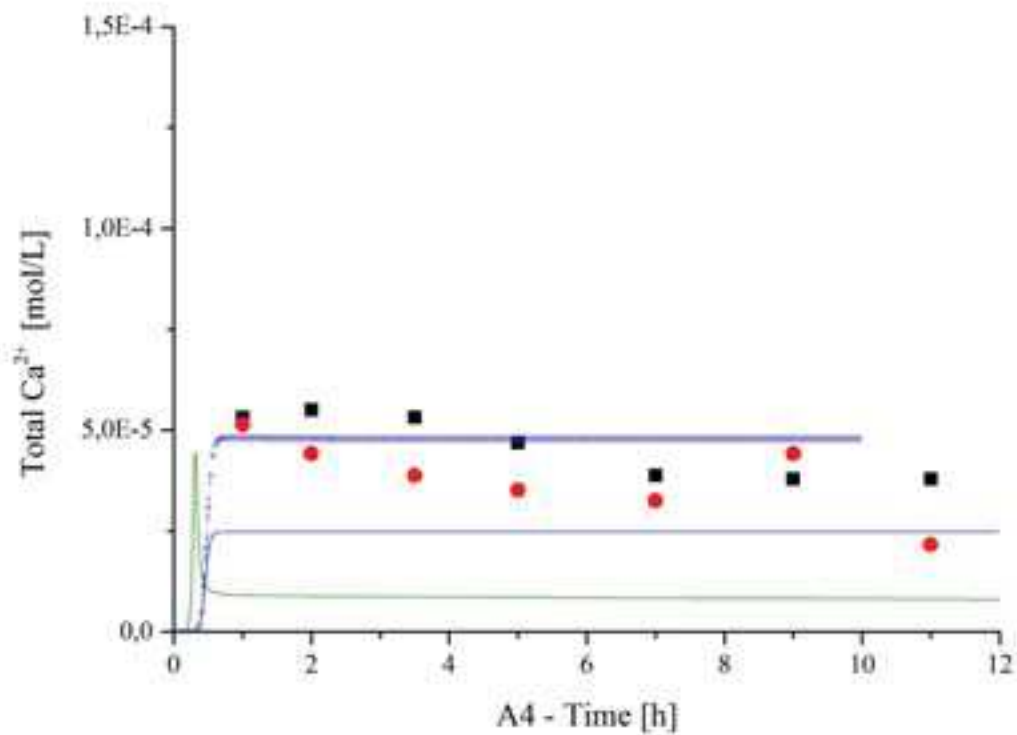
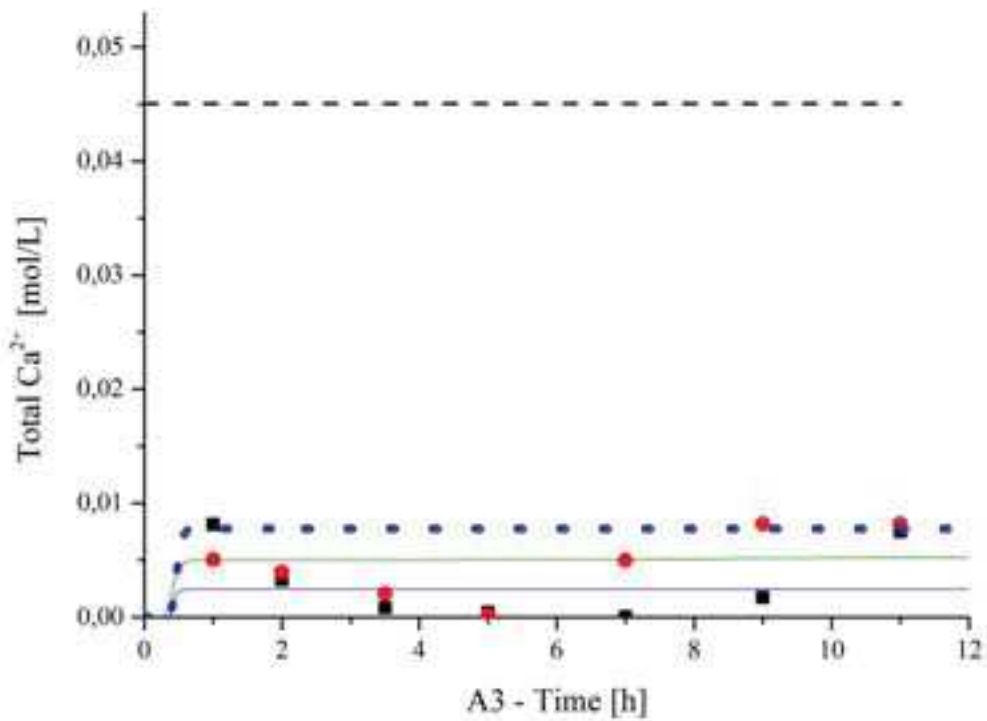Figure 7.39 – Time evolution of Total Calcium concentration at sampling port A4 (legend in Figure 7.36).
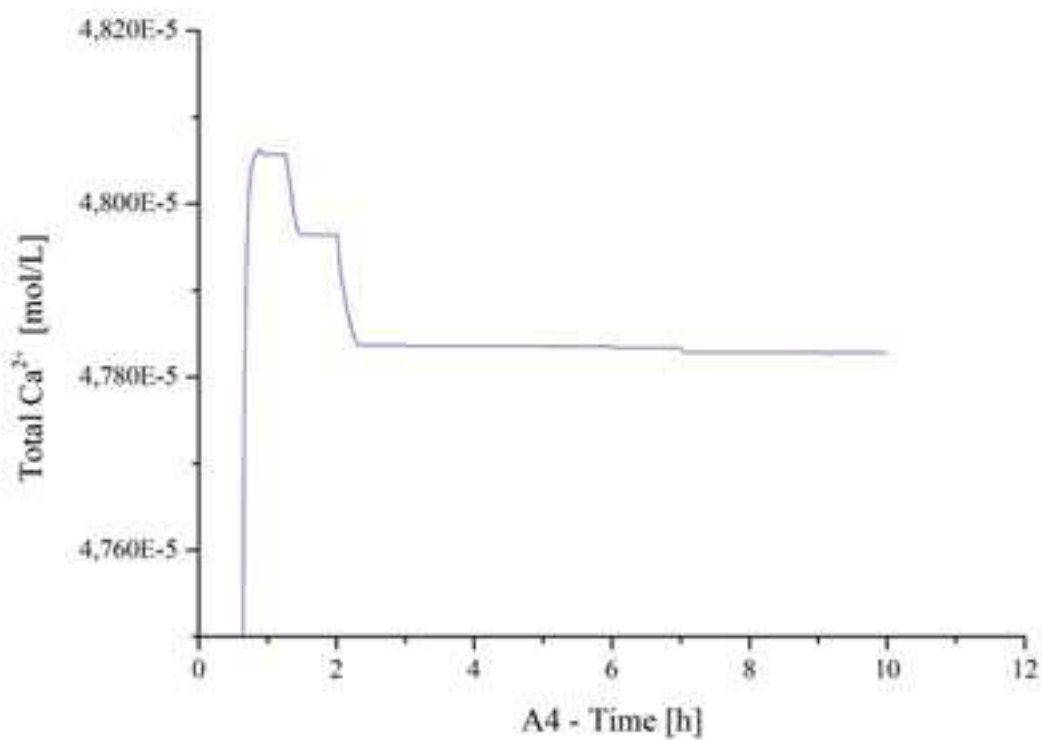
Figure 7.40 – Time evolution of Total Calcium concentration at sampling port A4 (legend in Figure 7.36).
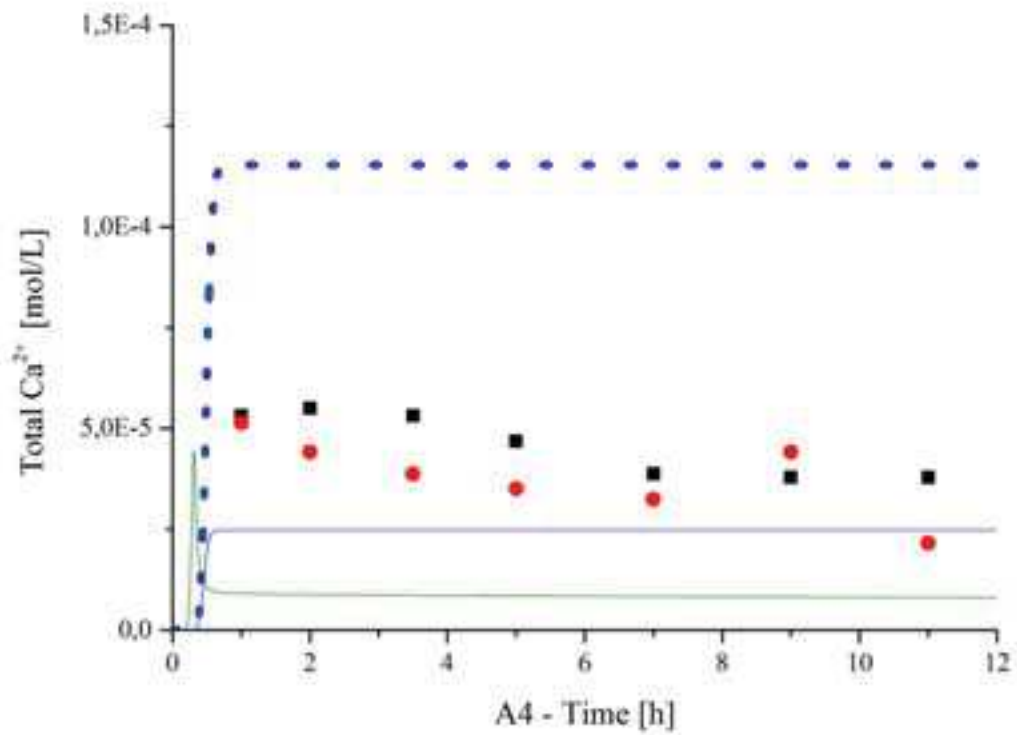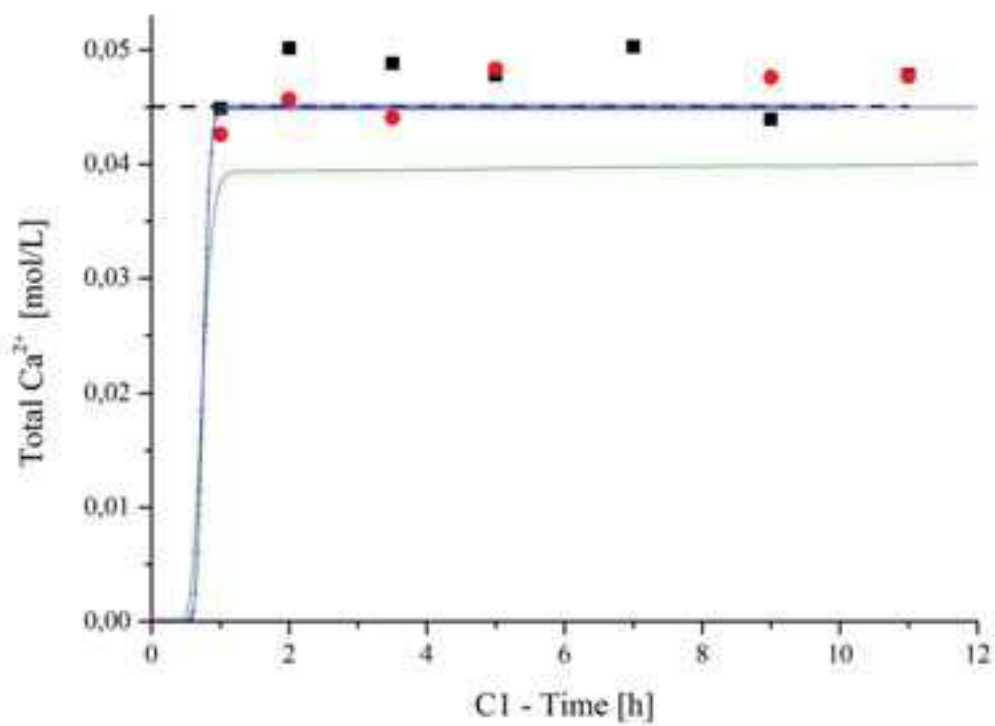
Figure 7.41 – Time evolution of Total Calcium concentration at sampling port C1 (legend in Figure 7.36).
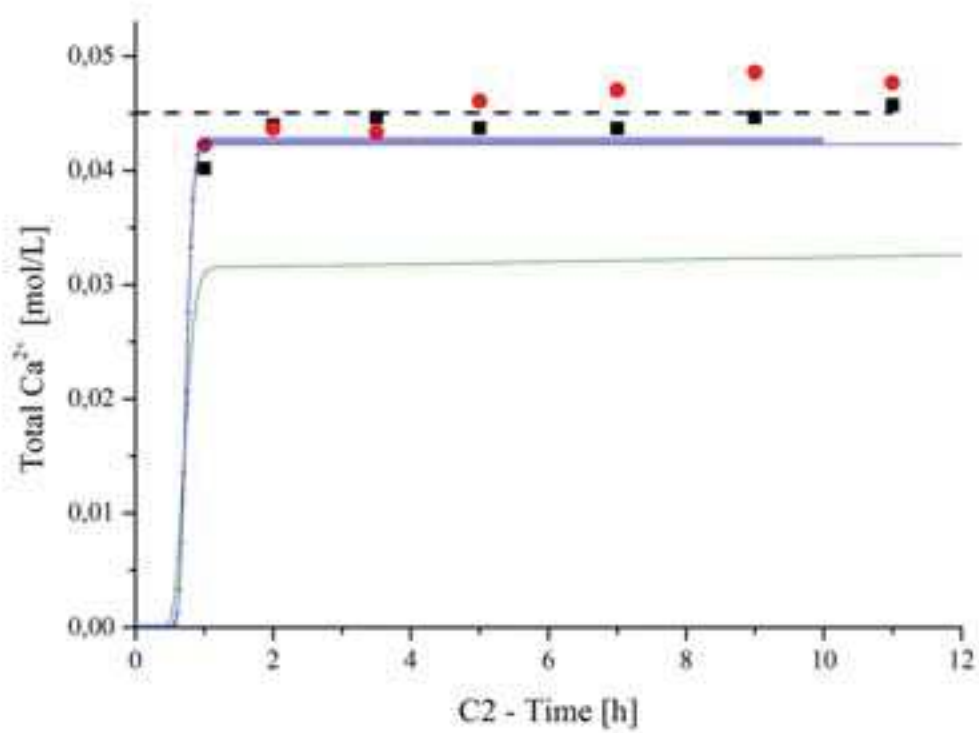
Figure 7.42 – Time evolution of Total Calcium concentration at sampling port C2 (legend in Figure 7.36).
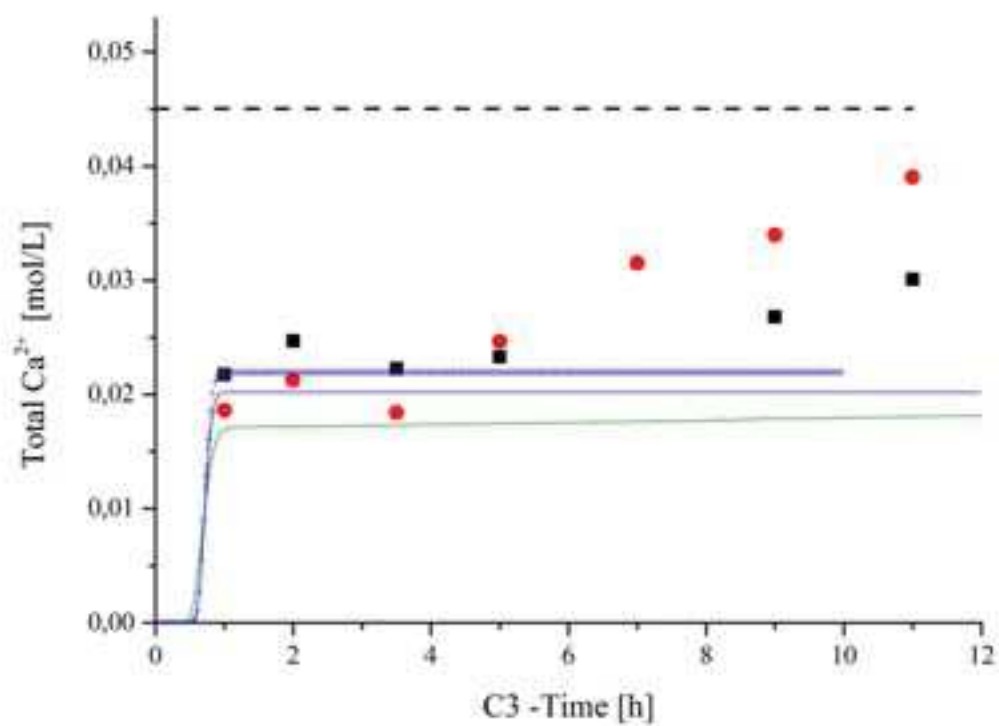
Figure 7.43 – Time evolution of Total Calcium concentration at sampling port C3 (legend in Figure 7.36).
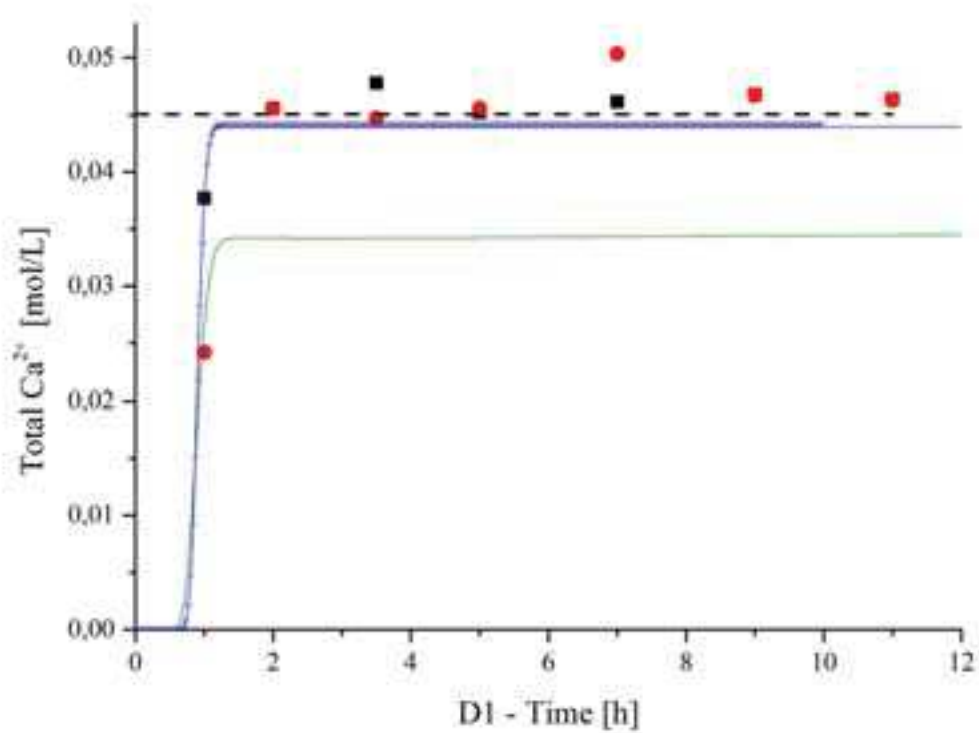
Figure 7.44 – Time evolution of Total Calcium concentration at sampling port D1 (legend in Figure 7.36).
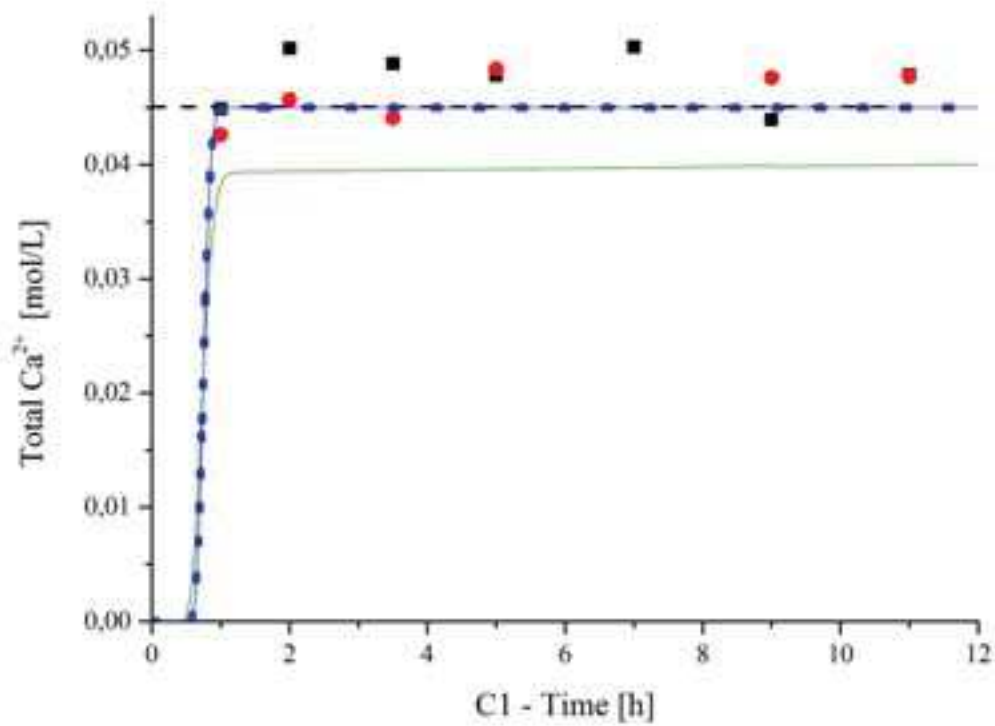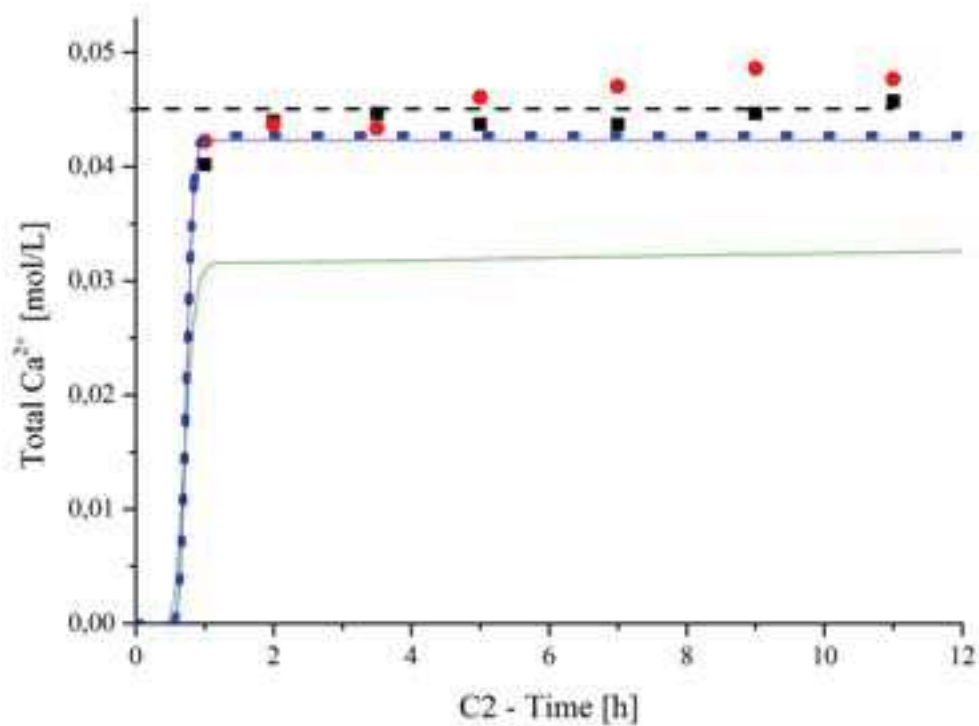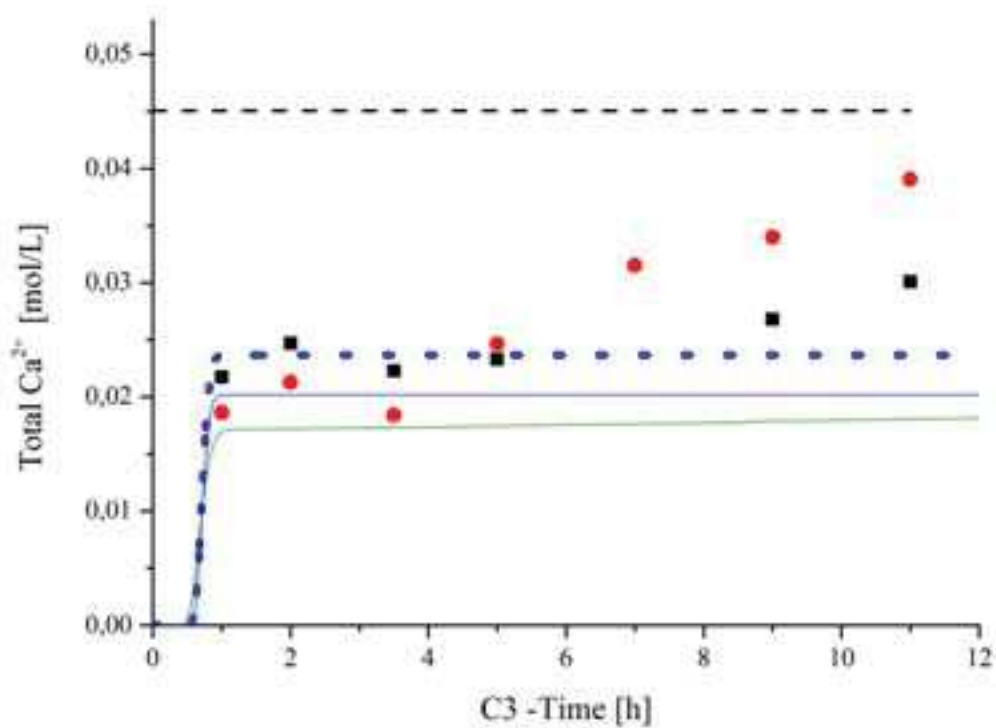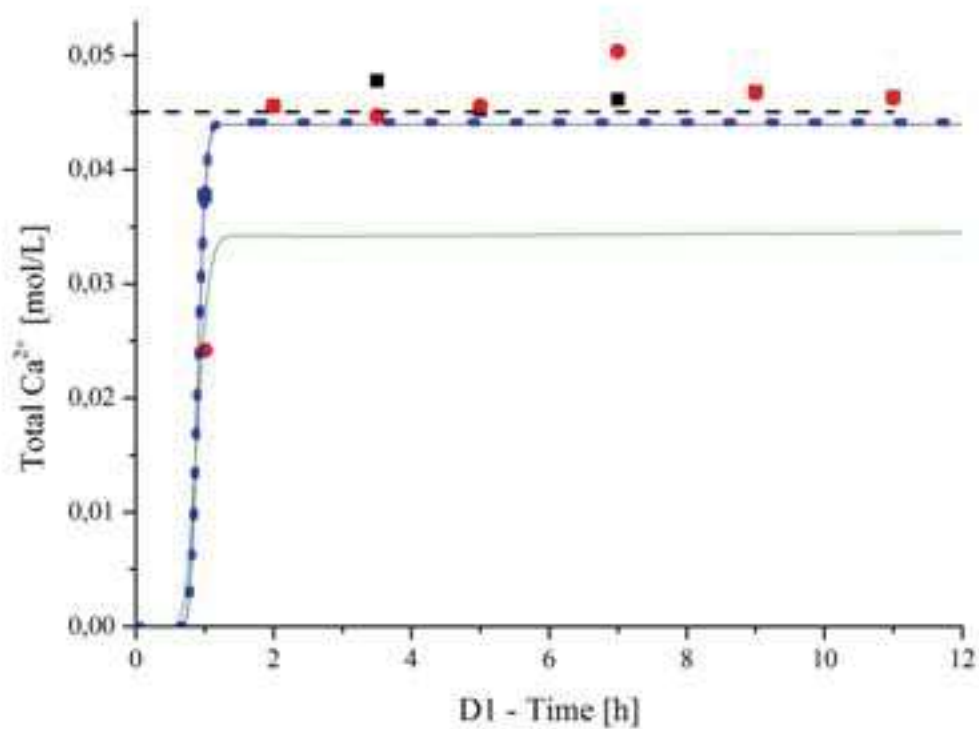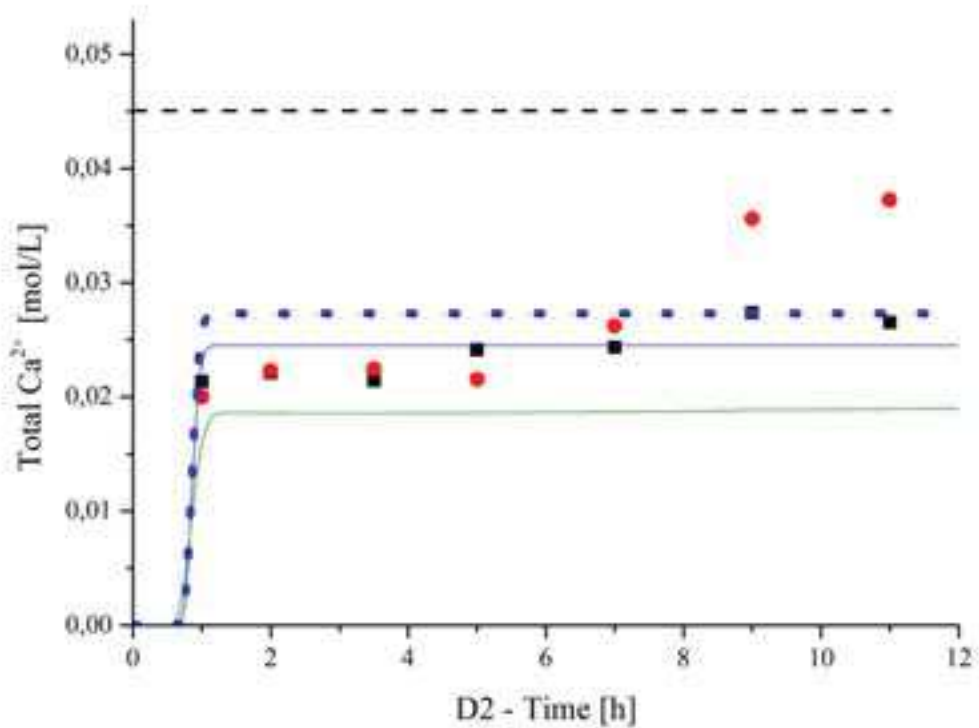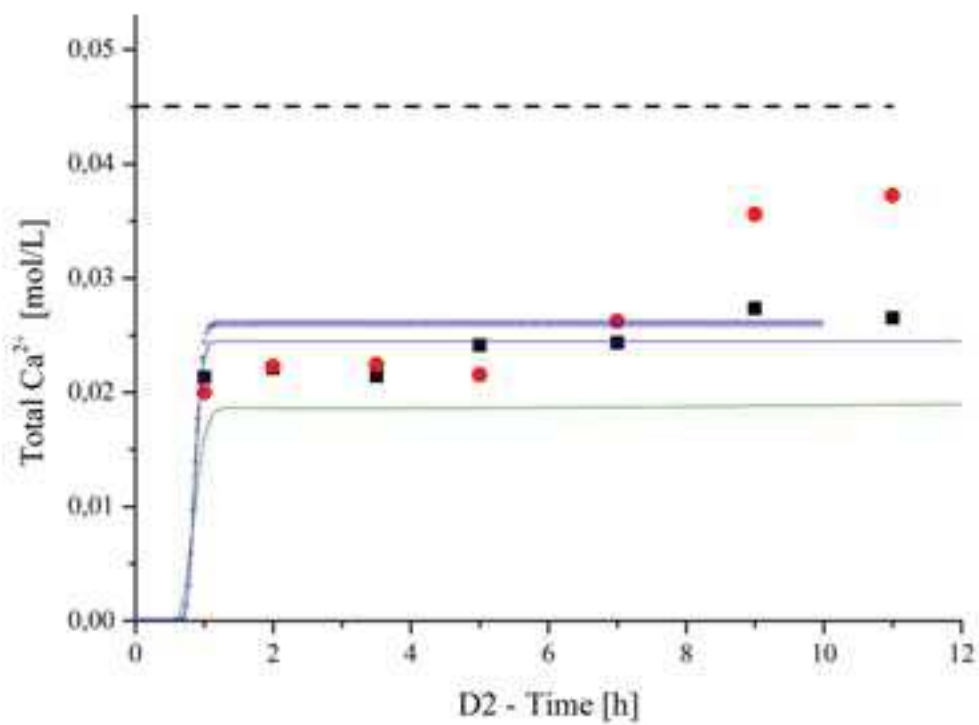
Figure 7.45 – Time evolution of Total Calcium concentration at sampling port D2 (legend in Figure 7.36).
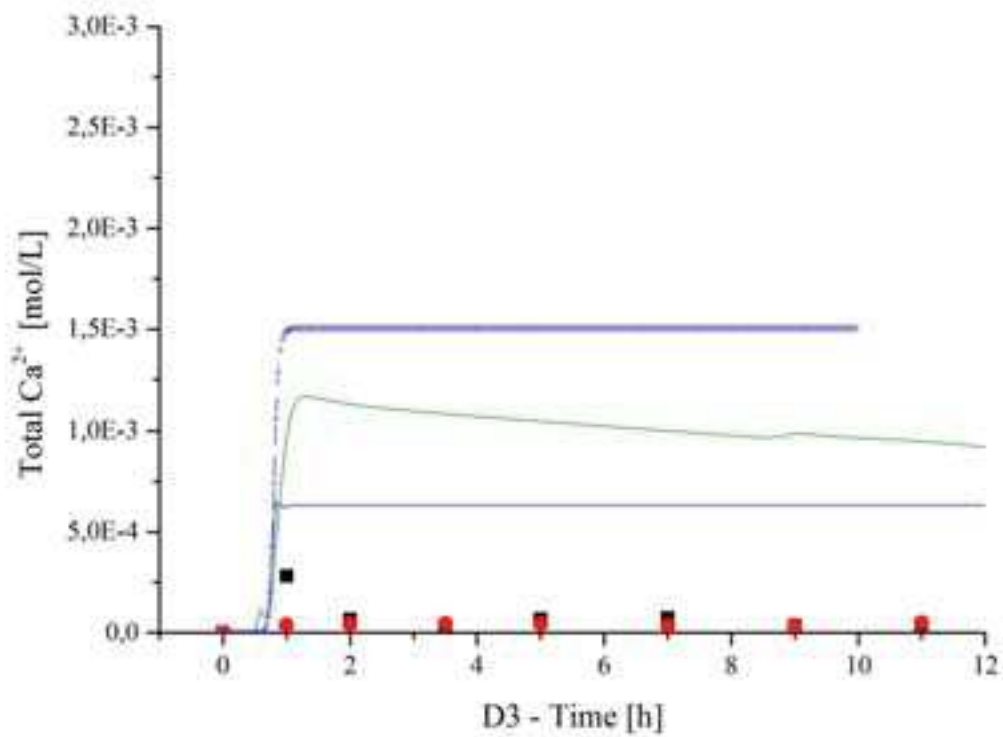
Figure 7.46 – Time evolution of Total Calcium concentration at sampling port D3 (legend in Figure 7.36).
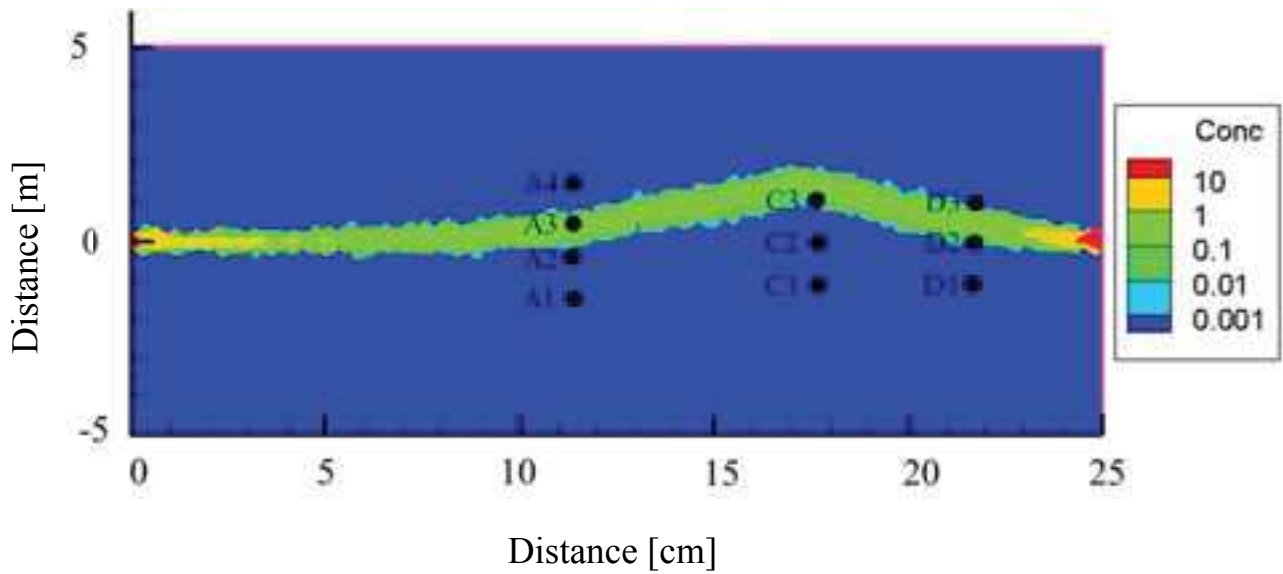
Figure 7.47 – Space distribution of Calcite after 10 h for CaCO$_3$ equilibrium precipitation [mol/L].

The introduction of variable porosity slightly modified the results of spatial distribution of precipitated CaCO$_3$. In fact, the zone near the inlet in Figure 7.47 shows greater concentrations of Calcite with respect to Figure 7.34, obtained with constant porosity, and therefore increasing the accord with Figure 7.35. Porosity changes simulated with RETRASO and SpeCTr are reported in Figures 7.49 and 7.48. While RETRASO predicts no porosity changes in the central zone of the domain and only slightly reduced values at the most of the interface zone, SpeCTr predict porosity changes all over the precipitation zone.
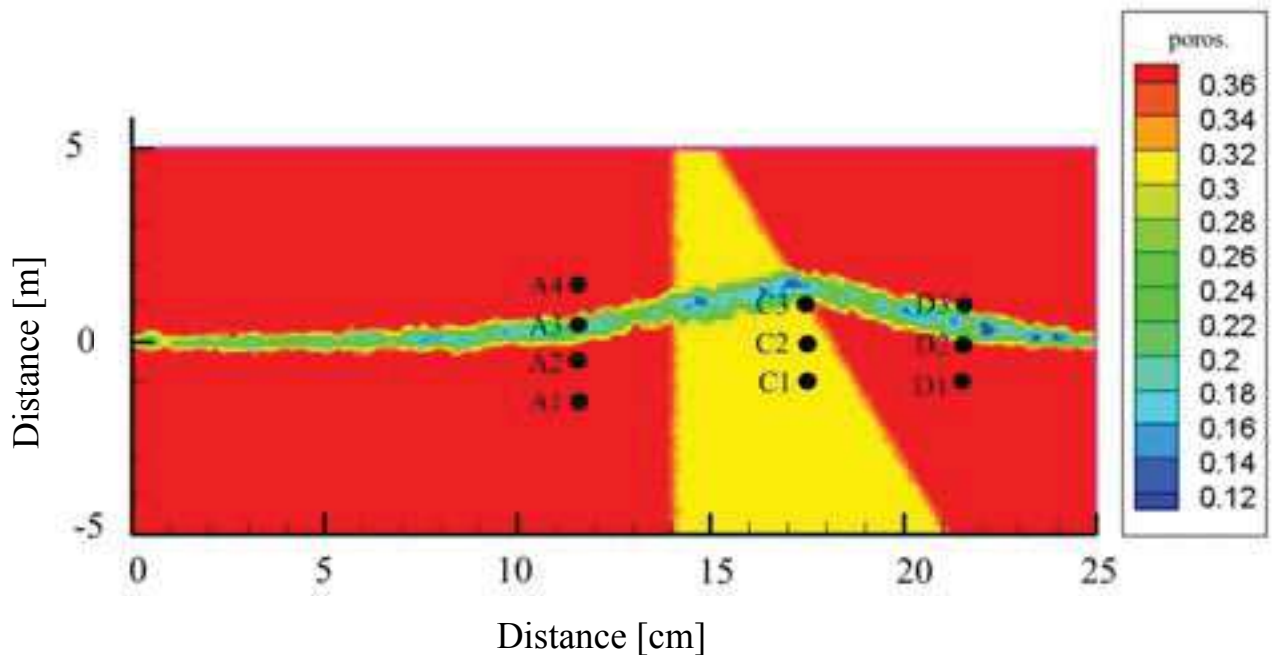
Figure 7.48 – Space distribution of porosity after 10 h, for CaCO$_3$ equilibrium precipitation.
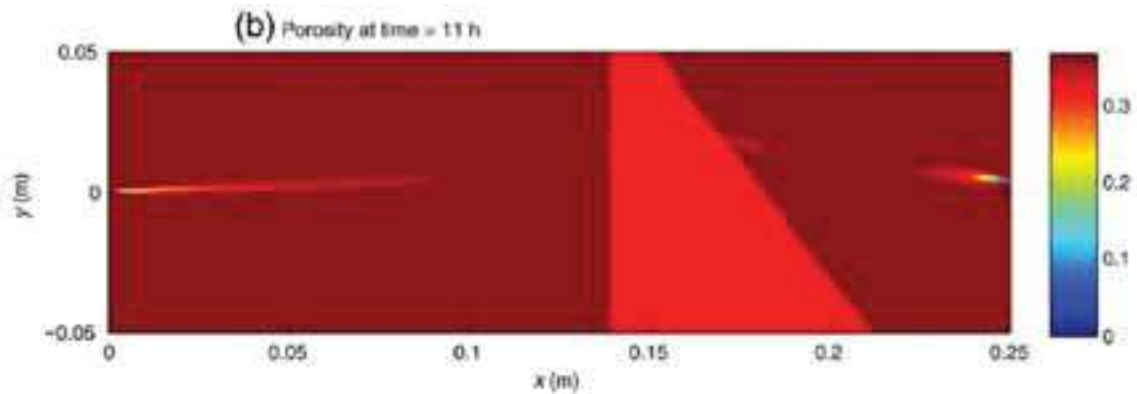
Figure 7.49 – Space distribution of porosity after 11 h, for CaCO$_3$ equilibrium precipitation with Retraso (Katz et al. 2009).

7.3.2.3 Results: variable porosity - kinetic CaCO$_3$ precipitation

In order to complete the set of simulations, kinetic precipitation of Calcite with varying porosity was performed too. In order to establish if the variations of concentrations subsequent to porosity changes were visible, simulations were run for 6 hours only. Results are shown in Figures 7.50 to 7.59. Although, as usual, sampling ports A1, C1 and D1 are immune to changes in the system (Figures 7.50, 7.54, 7.57), at sampling port A2 it is already possible to see that the model responds to porosity variation: concentration at sampling port A2 constantly increases with time. This behavior is more evident when concentrations are low, for example at sampling ports A4 and D3. It must be noted that the behavior is not coherent with the one simulated by RETRASO at these two locations. While concentrations computed with SpeCTr always increase with time, at sampling ports A4 and A3 they are supposed to decrease according to RETRASO.

Figures 7.60 and 7.61 show the spatial distribution of precipitated Calcite and porosity after 6 hours. It is clear that the precipitation zone is wider than in the equilibrium case and that quantity of precipitated Calcite are lower. This behavior is coherent with the kinetic precipitation. In fact, whereas at equilibrium, the supersaturated solution is instantaneously equilibrated, when precipitation is kinetically modeled, the solution remains slightly less supersaturated. Porosity changes are coherent with CaCO$_3$ precipitation and porosity is reduced also in the sand zone (note that in this zone porosity is lowered from a starting value of 0.32).
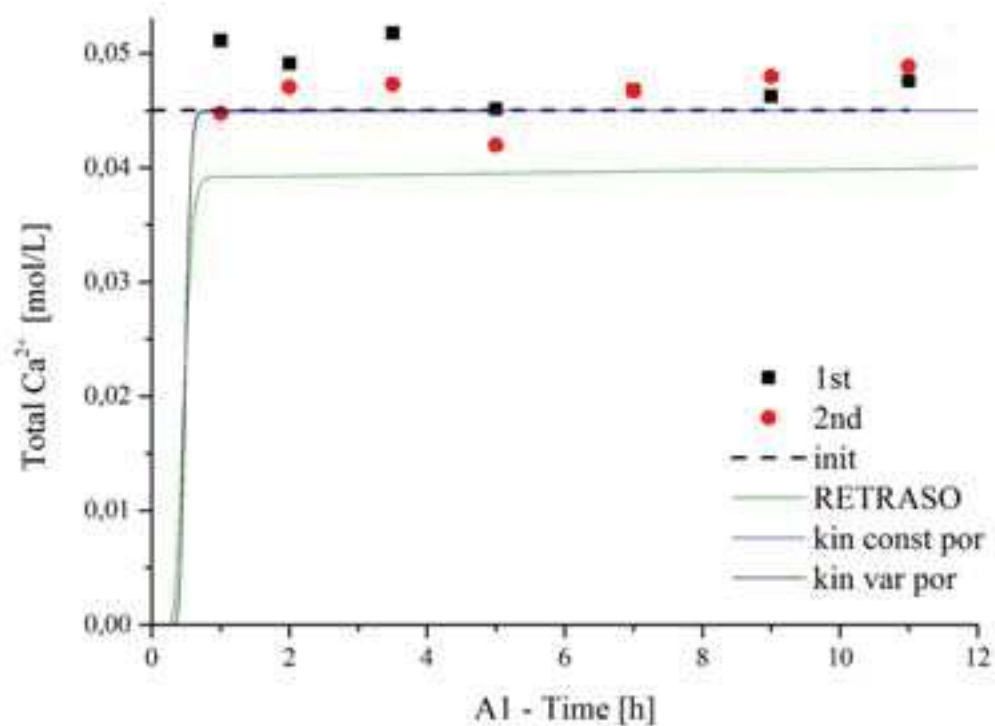
Figure 7.50 – Time evolution of Total Calcium concentration at sampling port A1.
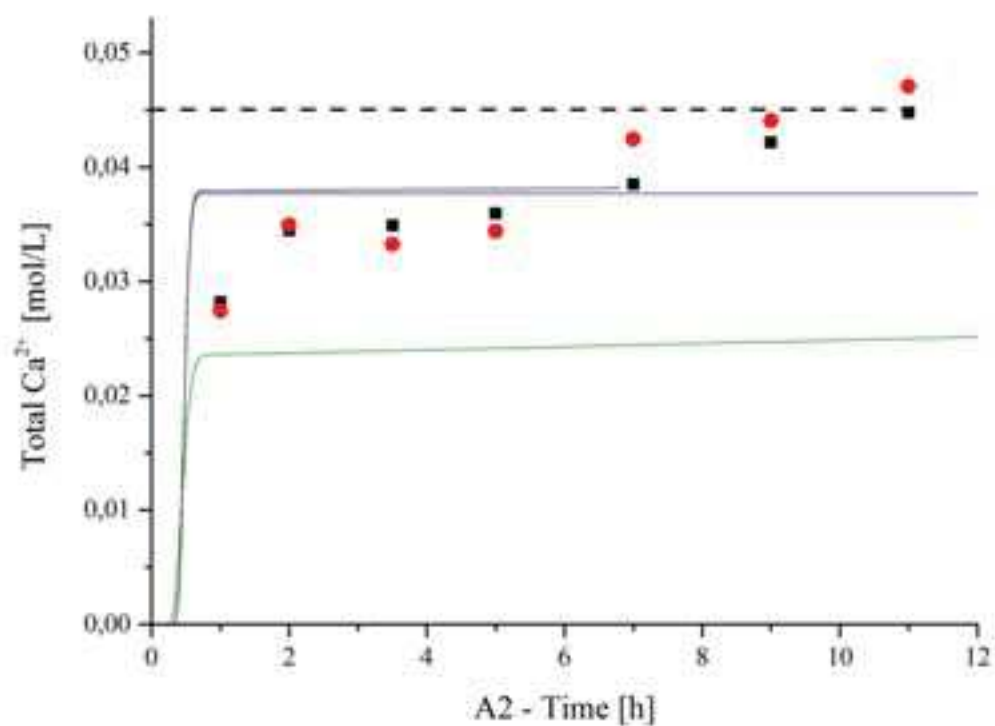
Figure 7.51 – Time evolution of Total Calcium concentration at sampling port A2 (legend in Figure 7.41).
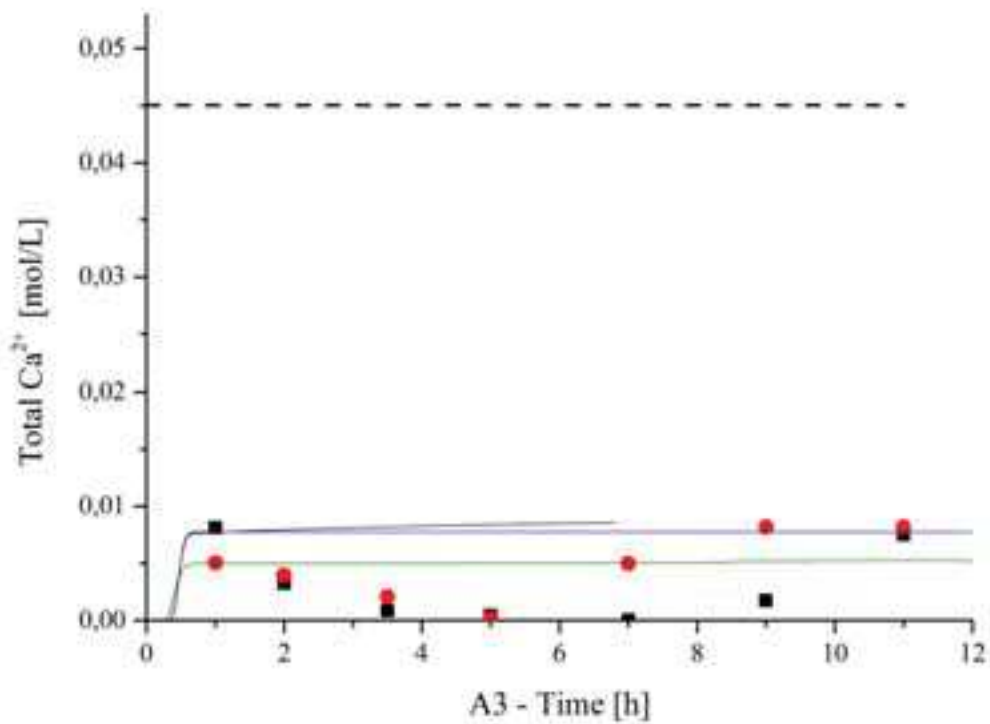
Figure 7.52 – Time evolution of Total Calcium concentration at sampling port A3 (legend in Figure 7.41).

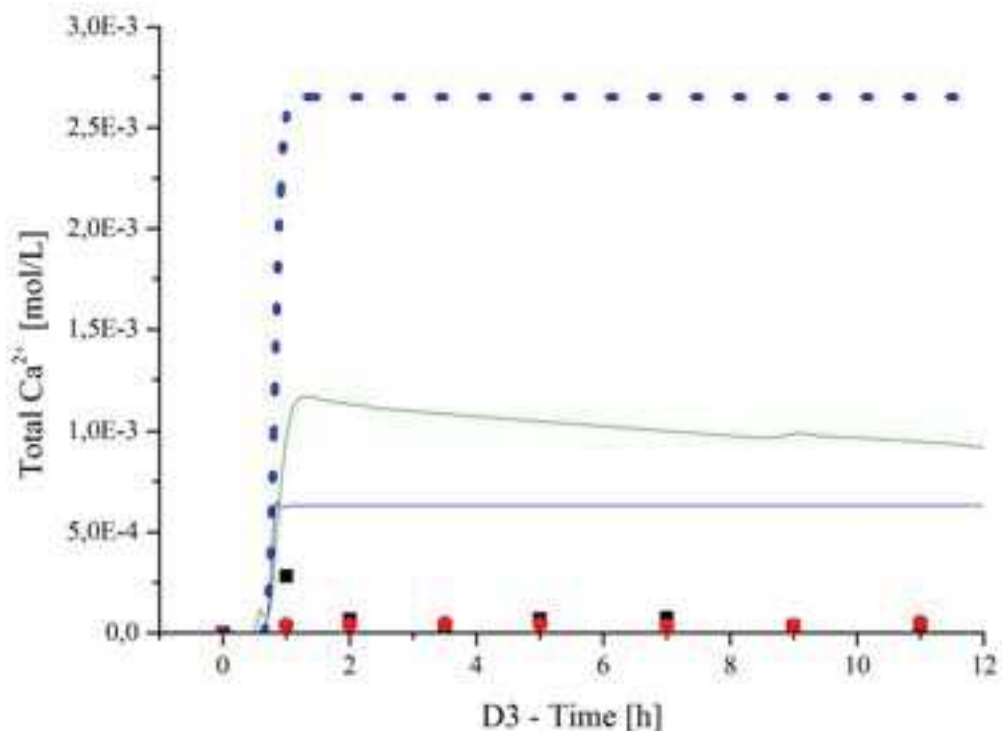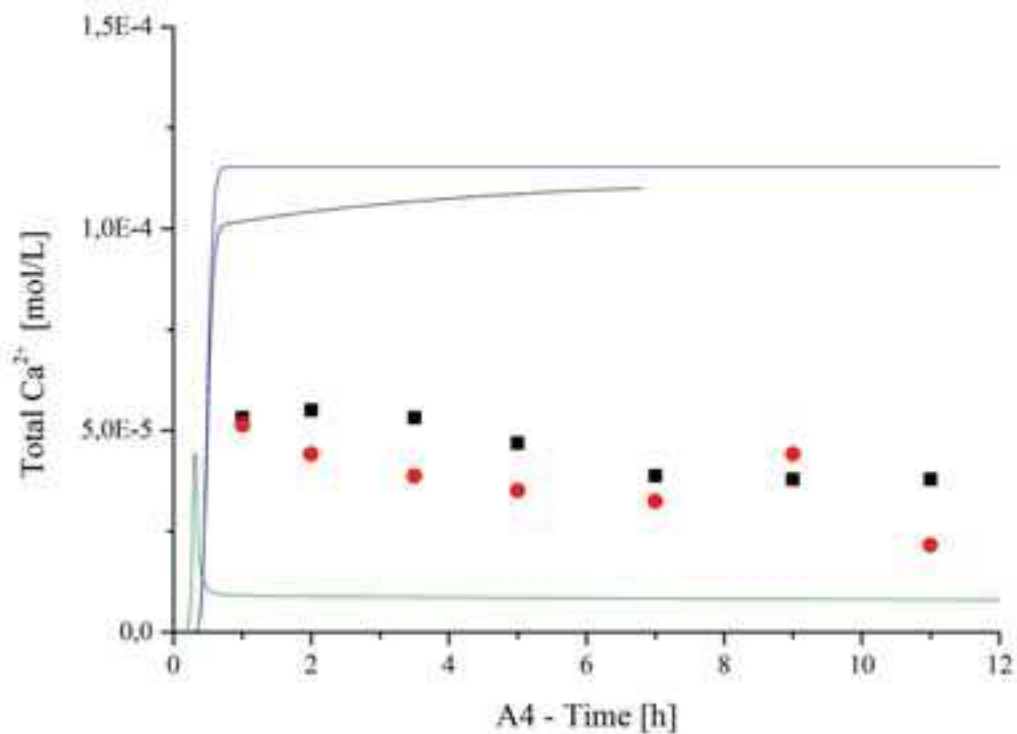Figure 7.53 – Time evolution of Total Calcium concentration at sampling port A4 (legend in Figure 7.41).
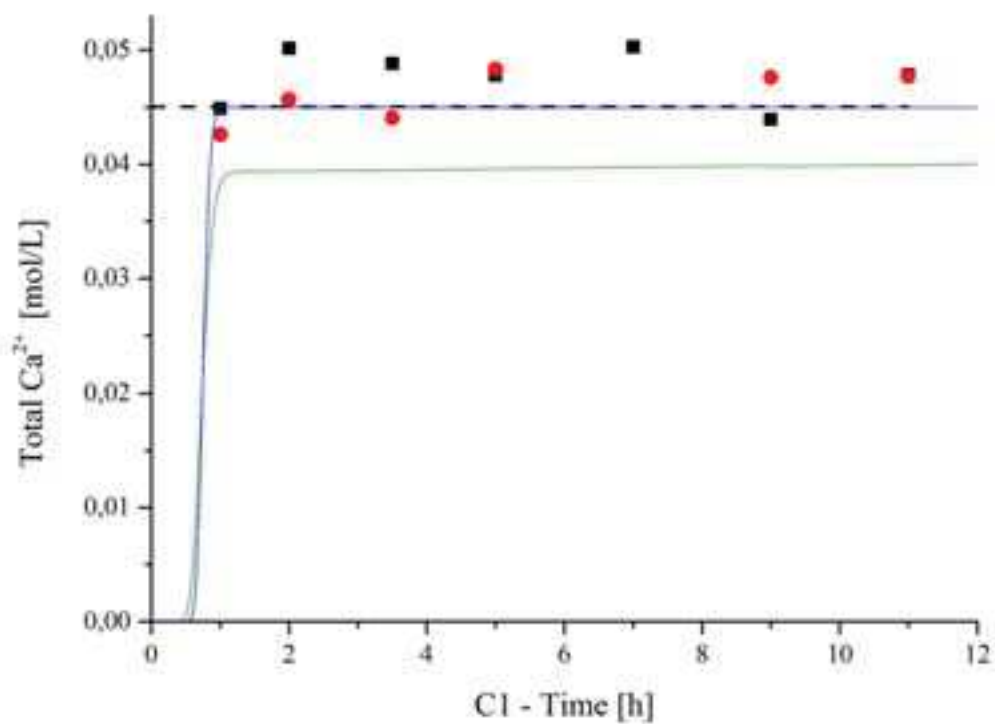
Figure 7.54 – Time evolution of Total Calcium concentration at sampling port C1 (legend in Figure 7.41).
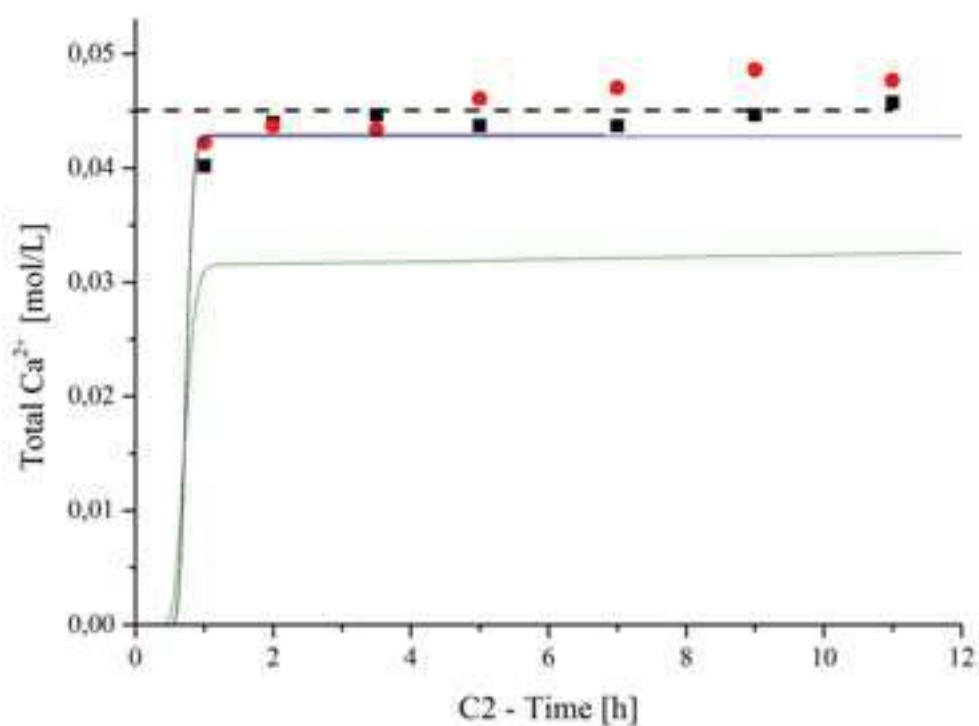
Figure 7.55 – Time evolution of Total Calcium concentration at sampling port C2 (legend in Figure 7.41).
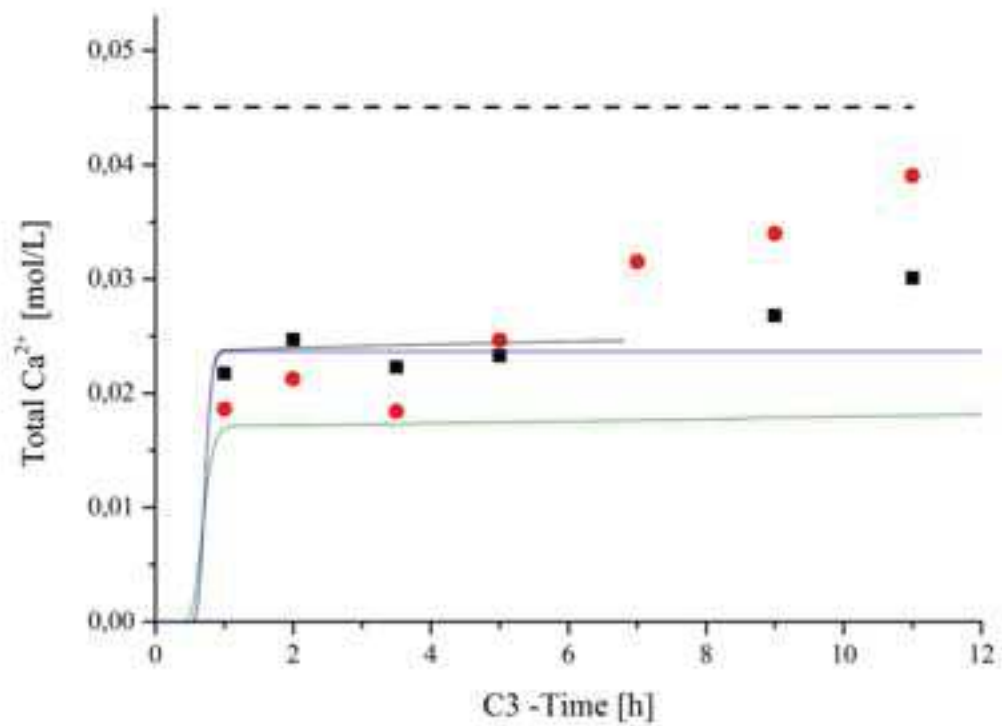
Figure 7.56 – Time evolution of Total Calcium concentration at sampling port C3 (legend in Figure 7.41).
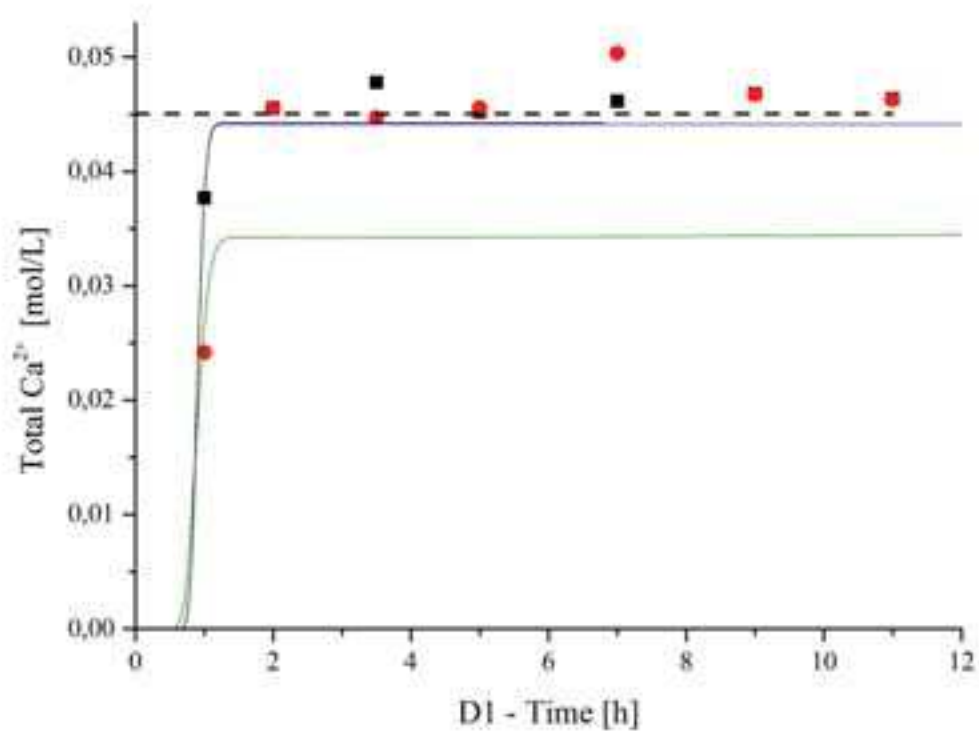
Figure 7.57 – Time evolution of Total Calcium concentration at sampling port D1 (legend in Figure 7.41).
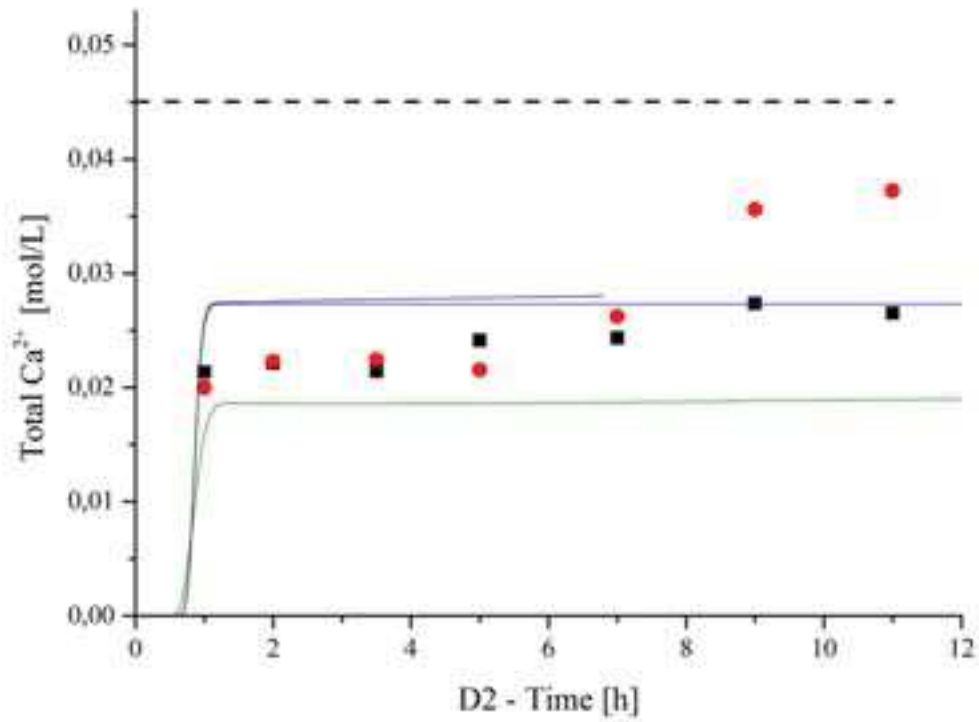
Figure 7.58 – Time evolution of Total Calcium concentration at sampling port D2 (legend in Figure 7.41).
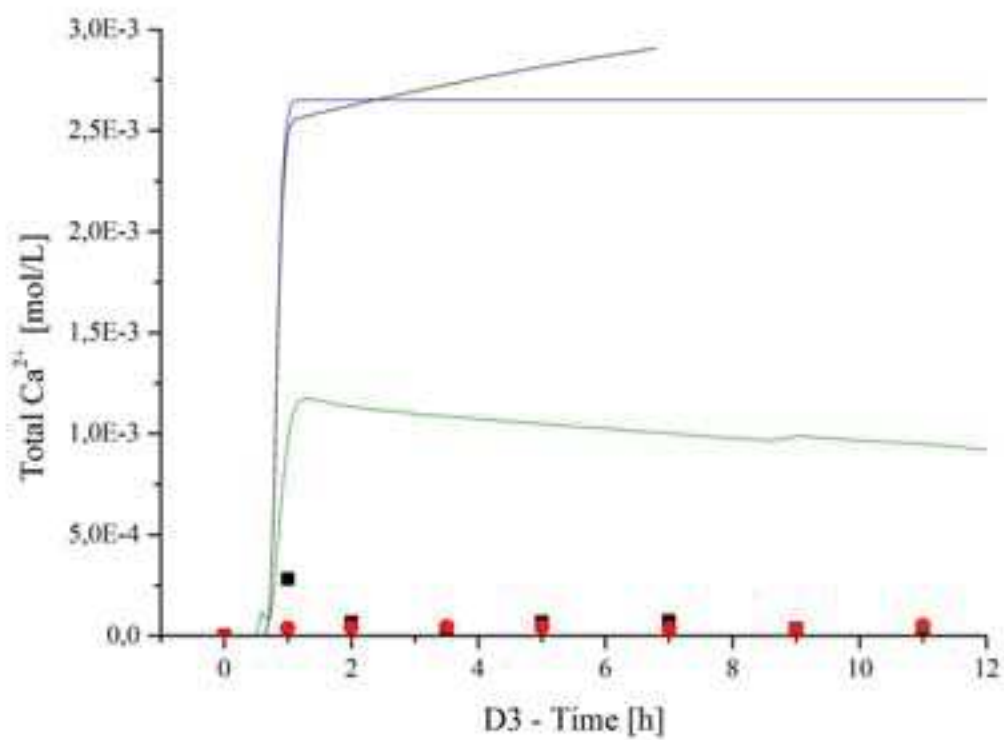
Figure 7.59 – Time evolution of Total Calcium concentration at sampling port D3 (legend in Figure 7.41).

227
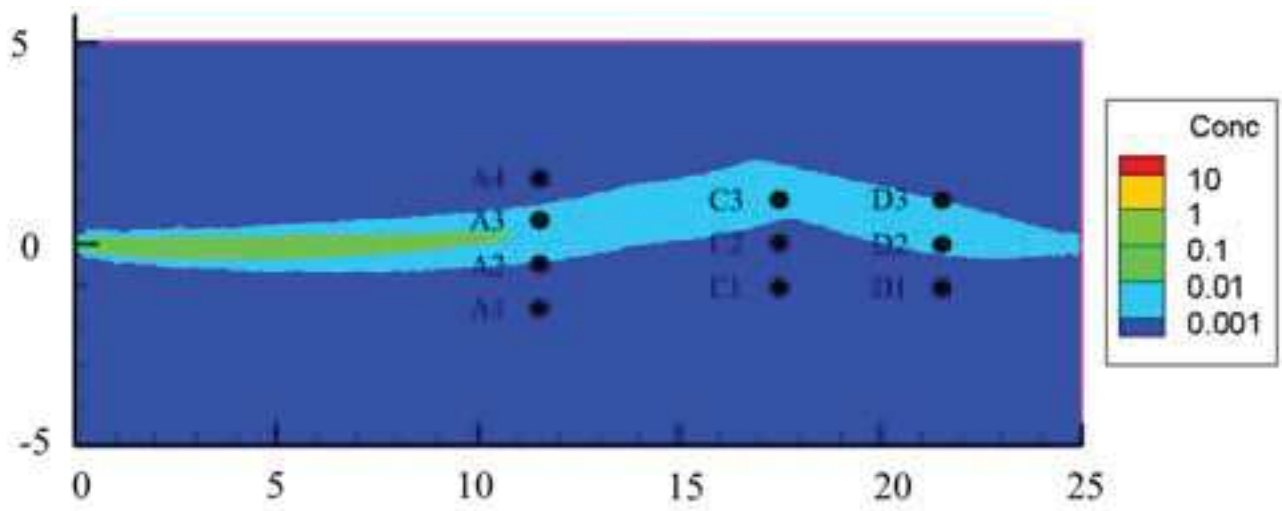
Figure 7.60 – Space distribution of Calcite after 6 h, for $CaCO_3$ kinetic precipitation.
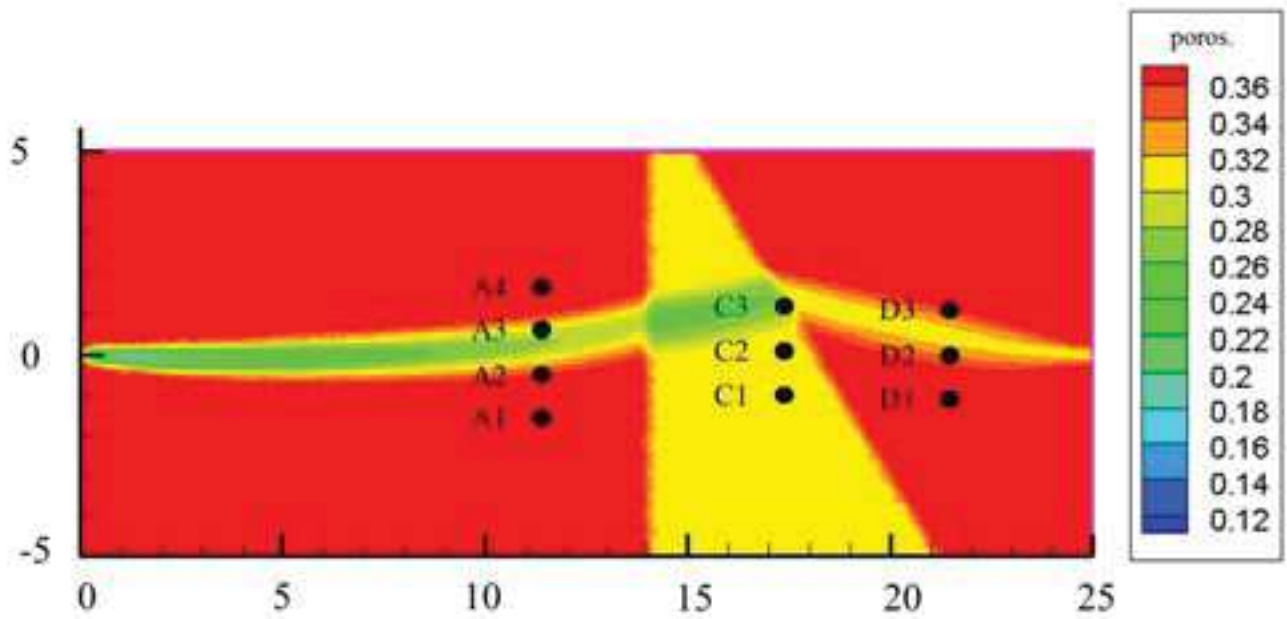
Figure 7.61 – Space distribution of porosity after 10 h, for $CaCO_3$ kinetic precipitation.

7.3.2.4 Conclusion about Calcite precipitation and porosity changes

Simulations were performed with both equilibrium and kinetic models for Calcite precipitation, at both constant and variable porosity. Results at constant porosity and equilibrium precipitation were in good agreement with experimental results, slightly overestimating concentration only at sampling port D3. Simulations with constant porosity and kinetic precipitation of Calcite lead to a systematic overestimation of concentrations (except at ports were injected concentrations were already reached) especially at sampling ports A4 and D3. This behavior is coherent with the assumptions of the two models (equilibrium brings the solution instantaneously to equilibrium leaving no extra concentration to precipitate farther.

The second series of simulations was performed taking into account porosity changes adopting a linear model for porosity update. The introduction of porosity changes improved the matching of numerical and experimental results at sampling ports A but caused an overestimation of concentration at sampling port D3. Moreover, changes in concentrations with time were visible only at sampling port A4 and zooming heavily on Figure 7.40.

The only way to see changes in concentrations dues to porosity changes is to adopt kinetic precipitation of Calcite. In this case, increasing in concentrations is systematic, making evident the response of the model to porosity changes. On the other hand, SpeCTr fails to predict concentration decreasing where RETRASO does. This might be due to the fact that kinetic precipitation doesn't clog completely pores where equilibrium precipitation does.

The choice of a linear model for porosity update makes easier working with concentrations but was not tested against other models or codes. For a further development of SpeCTr, benchmarks for models for porosity changes should be tested (i.e. Cochepin et al. 2008).

7.4 - 3D Calcite dissolution modeling

7.4.1 Presentation of the problem

As anticipated in Bouissonnié et al. (2018), 2D simulations could have led to an overestimation of concentrations at the outlet (see paragraph 7.1.5.2 and Figure 7.6). In this section a 3D simulation of the same problem is presented. Considering the symmetric configuration of the experiment, only a quarter of the column was modeled, with a 3D mesh of around 41000 tetrahedrons. Calcite crystals were modeled again as variations in the boundary conditions and $CaCO_3$ is available to dissolve in the adjacent elements (see Figure 7.6b2).

Average flow direction is now parallel to the z direction and has the prescribed value of 3.77 10^{-3} mm/s, flow and transport parameters are reported in table 7.10 and are the same than adopted in previous 1D and 2D simulations (see Table 7.4). The same is true for the reaction network, reported in Table 7.3, and the TST model was adopted for the reaction rate (see the now well-known equation 7.4).

Parameter	Value	Unit
Porosity ϕ	0.38	[-]
Conductivity	100	[mm/s]
V_y	3.77 10^{-3}	[mm/s])
α_L	1	[mm]
α_T	0.1	[mm]
D	10^{-4}	[mm^2/s]
K_S	1.8487	[-]
k	5.2 10^{-7}	[mol/m^2/s]

Table 7.10 – Summary of flow, transport and chemical parameters for 3D simulations

Reactive surface A_S in the TST model was computed as in equation 7.7 where the surface of the exposed Calcite is the area of the external face of the element and the volume is the volume of the element. Functions exist in SpeCTr (as they existed in TRACE) to compute volume of elements and surface of faces.
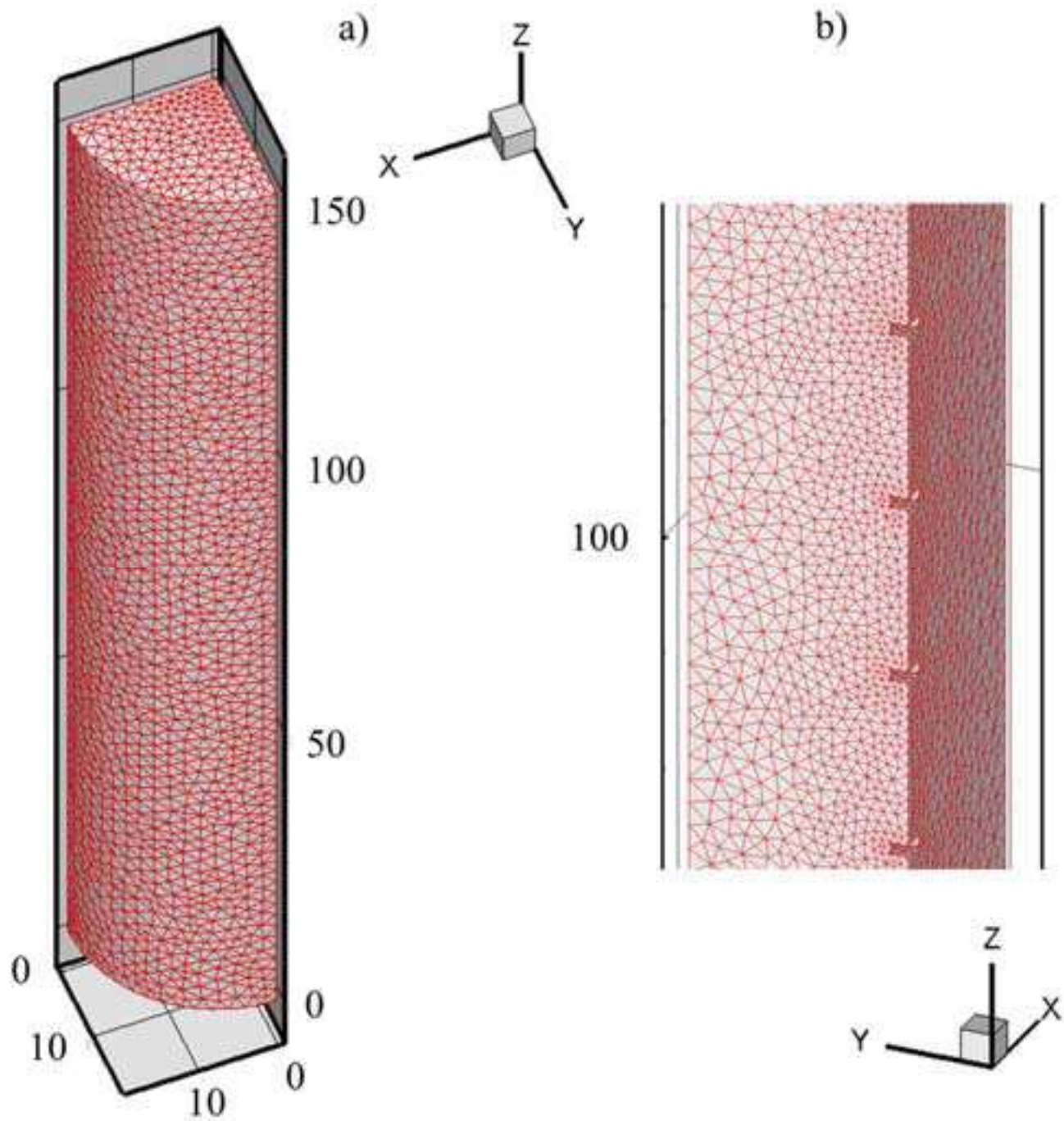
Figure 7.62 – The 3D mesh of around 41000 tetrahedrons reproduces one quarter of the column (a); presence of crystals is simulated by variations in the boundary conditions (b); z axis is parallel to the column axis.

7.4.2 Results of 3D simulation

The breakthrough curve of total Calcium concentration C^t at the outlet is reported in Figure 7.63. Values are flux weighted average of concentrations, meaning that at each element i the concentration is multiplied by the flux q_i leaving the column and the sum is divided by the global flux:

$$C^t = \frac{\sum_i C_i^t q_i^t}{\sum_i q_i^t}$$

Steps are clearly visible in Figure 7.63 until the final asymptote is reached. They are not a consequence of the weighted average, since the same behavior is present within single elements (see Figure 7.64). Steps are generally less sharp as concentrations grow (likely the closer to the axis of the column the higher the concentrations the more regular the shape of the column). This behavior is likely to be the result of successive contributions of different crystals.
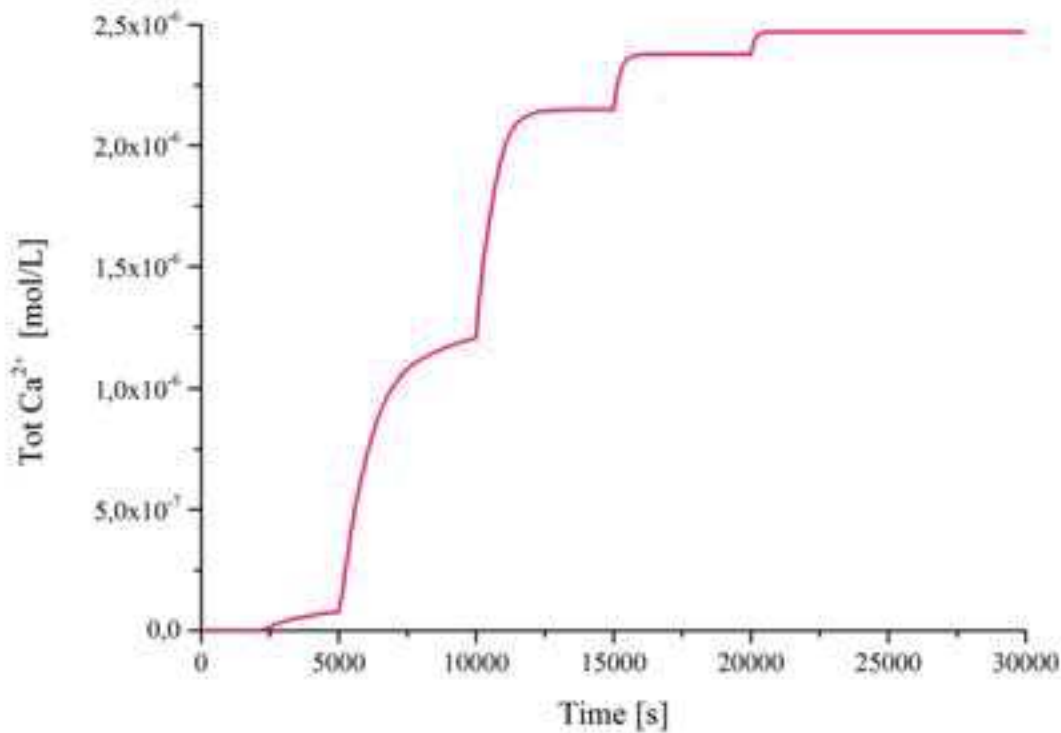
Figure 7.63 – Breakthrough curve for Ca^{2+} at the column outlet. Results are averaged over all the surface at z = 150 mm and weighted with respect to water fluxes.

While results of 2D simulations overestimated concentrations of Calcium at the outlet (see Figure 7.10), the final concentration of 2.5 10^{-6} mol/L obtained with the 3D underestimates experimental values. Nevertheless, values are comparable and somehow coherent with those coming from 2D simulations (concentrations around crystals are in the order of magnitude of 2.0 10^{-4} see Figure 7.65). A reduction of concentrations was expected (since another direction is available for dispersion and diffusion) but in the end it is too important with respect to experimental data (even for the TST model that is supposed to provide higher reaction rates and concentrations).

Reasons of this underestimation may reside in an underestimation of the dispersion (values adopted in the simulation are the lower boundary of the admissible values) or in an overestimation of porosity. In fact, lower values of dispersion may keep concentrations elevated in the proximity of the crystal, slowing down the dissolution rate. On the other hand, higher values of porosity may reduce the reactive surface in equation 7.7).
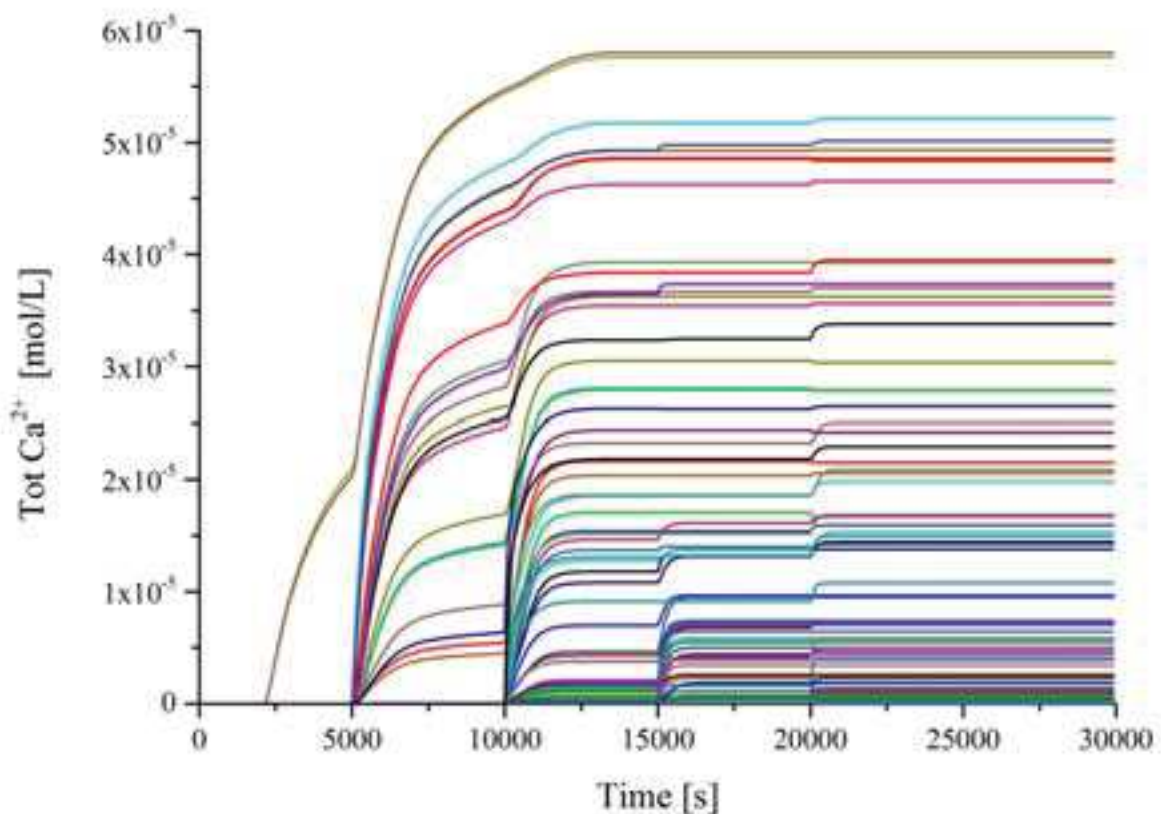
Figure 7.64 – Breakthrough curves for Ca^{2+} at the end of the column (at every element that registered a non-zero concentration). Contributions of crystals are distinguishable.
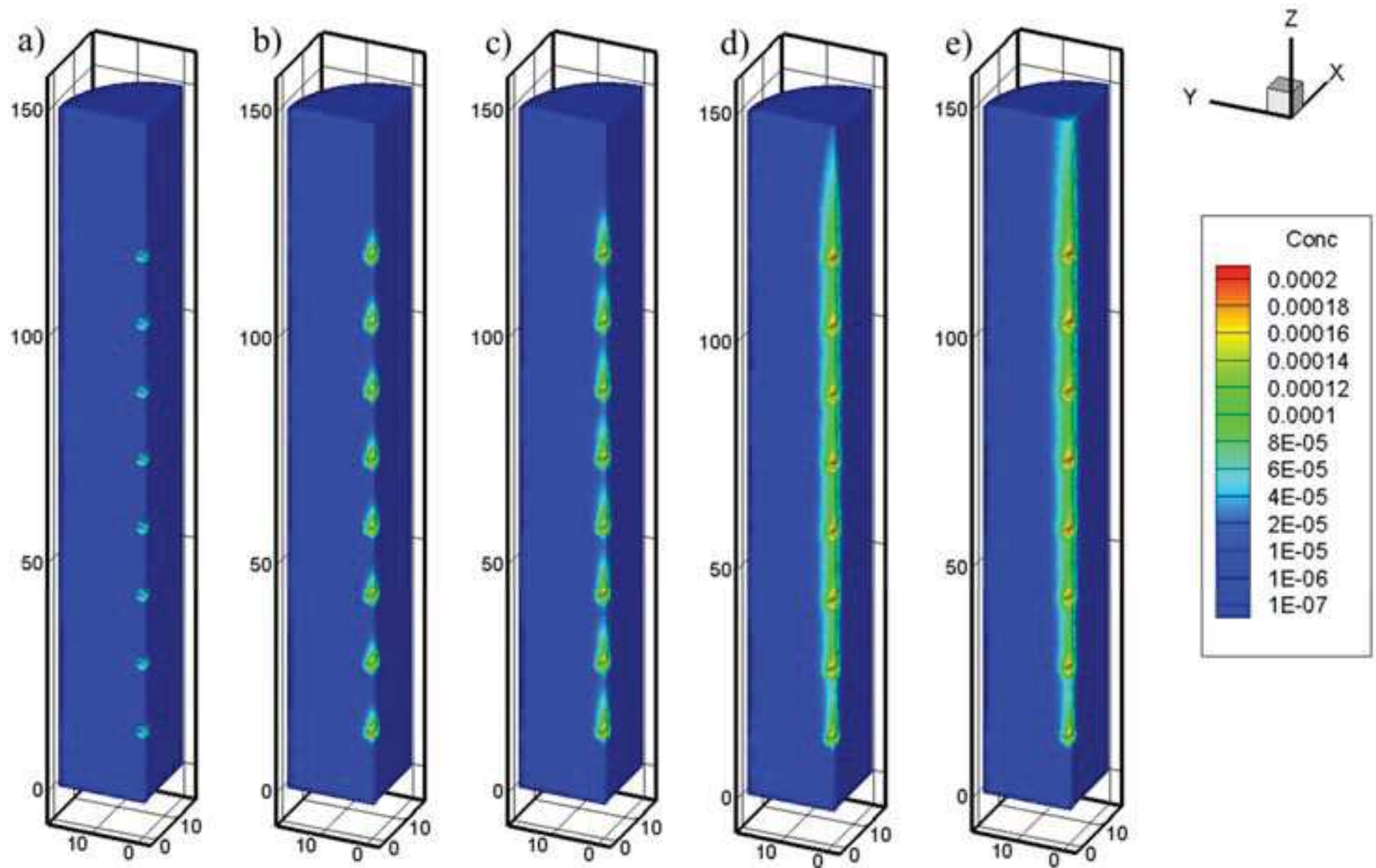
Figure 7.65 – Evolution is space of Ca^{2+} at different stages of the simulation at a) 30 s b) 500 s c) 1000 s d) 5000 s and e) 30000 s.

It also must be kept in mind that the actual experimental setup is slightly different from the simulated domain. In fact, while the inflow and the outflow of the real column were connected to tubes of a few millimeters, the boundary conditions describe a generalized outflow at z =150 mm (the simplification is licit in laminar flow).

Another aspect that was not widely explored in the 3D simulation is the effect of spatial discretization over results. While for the 2D simulation at least two different mesh sizes were tested (and results did not change or did but slightly), mesh convergence was not checked. Nevertheless, a (not entirely legitimate considering the configuration of the system) simulation test was performed on 1/8 of the column and provided coherent results.

In order to be more confident in the outlet concentrations, simulations with other meshes should be tested (considered the consistent computational effort, coarser meshes should be tested at first).

7.4.2 Conclusions about 3D simulation

The aim of this 3D simulation was mainly to show the potential of SpeCTr in simulating realistic laboratory experiments whose configuration may vary from the standard rectangular-like shapes. Results also show that 3D effects have an important impact on outcomes and that, if 1D simulations represent excessive simplification, 2D simulations may not be completely well-suited too.

Anyhow, one simulation is not enough to draw absolute conclusions. Further simulations should be conducted with different mesh sizes in order to gain confidence and assess the importance of spatial discretization over results.

Performing this kind of simulations, where the computational effort dedicated to chemistry is a fraction of the one dedicated to performing transport computations also put in evidence the need of implicit resolution schemes for transport equations to get rid of the CFL condition constraint.

General conclusion

The aim of this work was, as in its very title, the implementation of isotopes into coupled hydrogeochemical modeling. The idea was not to create another code from scratch but to integrate and enhance codes already existing at LHyGeS (KINDIS, KIRMAT, SPECY, TRACE...) to provide a reliable and flexible tool.

After accurate bibliographic studies, it was made clear that isotopes should be treated as independent species within the context of a reaction network. Too less is known about the various phenomena of fractionation to implement specific models. Classic formulas, such as Rayleigh fractionation, often fail to reproduce experimental data, which become every day more abundant.

Different isotopes of the same element are differentiated with slightly altered equilibrium or kinetic constants and they evolve according to reaction rates that are slight modifications of standard rates (such as first-order or Transition State Theory model). To model TST-like reaction rates, some authors exploited the concept of solid solutions since isotopic substitution is the closest approximation of ideal solid solutions. Nevertheless, reaction rates and solid solutions should be pulled together very carefully since almost no theoretical basis exists about the kinetics of solid solutions.

Including isotopes as independent species, therefore, means that i) no substantial modification of the original algorithms is required to obtain solutions and ii) classical issues of reaction (and reactive transport) modeling are exacerbated: the number of species to be included in the reaction network grows and greater degrees of accuracy are required. For these reasons, attention was dedicated to the efficiency of solvers for both algebraic non-linear systems that arise from equilibrium equations and systems of differential algebraic equations (DAEs) arising from combinations of equilibrium and kinetic reactions.

Thermodynamic equilibrium is an approximation to describe reaction networks that is viable whenever time is not a variable of interest. It considers reactions as instantaneous and generates systems of non-linear algebraic equations, which are generally solved through iterative methods (a first guess for the solution is picked and values are updated until a convergence criterion is satisfied). The most widely applied iterative method to solve this kind of systems is Newton Raphson method, which is known for its fast convergence (quadratic) but also for its fragility when inconvenient initial guesses are picked. Different strategies were put in place to limit the liabilities of the method: i) a zero order method (which do not require the computation of the Jacobian matrix), positive continuous fractions (PCF) method, was coupled with Newton Raphson and ii) Newton Raphson's algorithm was modified in order to reduce the condition number of the Jacobian matrix through different *scaling* techniques.

PCF proved extremely effective at reducing the number of failures and the number of iterations to convergence regardless of the type of problem faced. The effect of scaling was much more problem related and also varied according to the scaling strategy applied.

Whenever time is a variable of interest, equilibrium approximation is not sufficient and differential equations have to be included. The more realistic scenario is a mix of equilibrium and kinetic equations, which is also convenient from a computational point of view with respect to a fully kinetic approach. In this case, systems of differential algebraic equations arise. Although theoretical works have been proposed on this subject since the mid-nineties, while thermodynamic formulation is well documented and explicitly detailed in most codes technical notes, the strategy adopted to solve mixed kinetic equilibrium systems is often left aside. Three possible ways of writing the resulting system were tested: a system of DAEs where mass action laws are left explicit, a system of DAEs where mass action laws are lumped into mass conservation (written as a sum of concentrations) and a system of ODEs where mass action laws are lumped into mass conservation (written in its differential form). The first and third approaches proved systematically more efficient and easier to put in place than the second one. Literature suggests that the third approach should be preferred because of its reduced size, but in one of the two performed tests, the first DAEs approach converged faster. Additional tests should be performed, but suitable benchmarks are not so easy to find.

The implementation of solver DASPK resulted in a reduction of the CPU time required to compute mixed equilibrium kinetic systems with respect to the explicit QSSA method coded in SPECY, regardless of the strategy used to solve the system.

One of the peculiar capabilities of the solver KINDIS is the possibility of treating solid solutions (mixtures of minerals that are not merely mechanical) at thermodynamic equilibrium. This capability was implemented in SpeCTr on the basis of models included in KINDIS and PHREEQC. The algorithm was used to model precipitation of a Fe-Cr solid solution at the interface of two reactive solutions (the example constitutes an anticipation of the coupling between the reactive and transport modules). The agreement between numerical and experimental solutions was satisfying although some additional efforts should be dedicated to the choice of transport parameters (i.e. transversal dispersion).

The coupling between the reaction module (developed through Chapters 2 to 5) and the transport module (TRACES) resulted in a tool named SpeCTr (Speciation Cinétique Transport).

The coupling was tested jointly with the implementation of isotopes through a 1D reactive transport benchmark designed for testing Cr fractionation. The coupling proved successful and put in evidence the challenges related to isotope modeling through operator splitting. In fact, simulations that could have been considered acceptable if limited to the monitoring of concentrations were completely inadequate for the computation of isotopic delta (or ratio). The time step required by transport (whose formulation is explicit therefore demanding the respect of CFL condition) had to be further reduced to obtain acceptable isotopic deltas. Although there is no theoretical link between CFL number and

operator splitting errors, as pointed out by Steefel (2009) in CrunchFlow technical notes, a CFL number of 0.2 ensured acceptable coupling errors. The solution of the benchmark also drew the attention on the algorithm used to convert concentrations at nodes to the concentration at elements to make transport and reaction codes compatible. Easy algorithms should be preferred to more sophisticated ones in order to prevent uncontrollable effects of low concentrations.

The last Chapter is dedicated to the application of SpeCTr to various problems involving Calcite dissolution and precipitation. Calcite precipitation simulations (confronted to published results) drew the attention on issues such as the efficiency of models for porosity changes and their numerical implications. In fact, the reduction of porosity due to precipitation is one of the potential causes of time steps' reduction while respecting CFL condition.

Simulation of the dissolution of Calcite crystals showed the potential of the code and its adaptability (in terms of kinetic models and spatial discretization) to model laboratory experiments. The simulations also represent an example of collaboration between different Ph.D. works as one of the purposes of SpeCTr.

Perspectives

Although the test cases that were simulated throughout this work (both in batch and reactive transport configurations) were as numerous and different as possible (pure thermodynamic equilibrium, mixed equilibrium and kinetics, first order, Monod and TST reaction rates, precipitation of solid solutions within reactive transport, stable isotope fractionation etc.) it is advisable to continue solving as much problems and benchmarks as possible, since this is the only way to keep the code alive, individuate and fix potential weaknesses and enhance its capabilities. This is particularly true with respect to algorithms for the update of physical properties in consequence of chemical reactions (i.e. porosity changes).

Regarding isotopes, models that were implemented proved to be effective in a number of multiple scenarios, but it should be kept in mind that i) those models were developed starting from an exigency of reproducing experimental data and ii) in these models, isotopes were interesting as tracers of biogeochemical reactions, and the focus was not on the mechanism of fractionation itself. The code could evolve implementing ad-hoc models to reproduce particular experimental results or to treat *some* isotopes of *some* elements with peculiar behaviors. We hope that this work constitutes a good basis for further and more specific studies.

A graphic interface has been developed as well as a module for access to databases. This is crucial to reduce user errors and speed up tests preparations. Although this module already exists, it should be extensively tested.

Code performances were enhanced with respect to SPECY but there is indubitably still some work to do. Three are the main directions of possible improvement: i) other solvers than DASPK could be tested ii) parallelization should be taken into consideration and iii) an implicit formulation of transport equations should be considered. This last point emerged clearly while modeling variable porosity, who forced the model to adapt unsustainably small time-steps.

The implementation of alternative solvers should be easier than starting from scratch since vectors and matrices to be manipulated are already available and that test cases have already been selected. About parallelization, reactive transport Operator Splitting is well suited for this procedure (independent solutions are computed in every element of the mesh), that must be performed after that the code has proved to be reliable.

Despite further potential improvements, SpeCTr was tested with well-established codes (KINDIS, PHREEQC, CrunchFlow etc.) and its solutions should be considered reliable. SpeCTr is well suited to be coupled with other more specific models for flow computations, which can be more advanced or specific than those implemented in TRACES, the transport module.

Conclusions et Perspectives en Français

Le but de ce travail consistait en l'implémentation des isotopes dans la modélisation hydrogéochimique couplée, à travers l'intégration et l'extension de codes déjà existant au LHyGeS (KINDIS, KIRMAT, SPECY, TRACES...) afin d'obtenir un code fiable et adaptable.

A la suite d'une compilation bibliographique, aussi exhaustive que possible, il est apparu que les isotopes doivent être traités comme des espèces chimiques indépendantes. Très peu de données sont disponibles quant aux phénomènes de fractionnement isotopique. Ainsi, l'implémentation de modèles spécifiques et des formules classiques (par exemple les équations de distillation de Rayleigh) sont parfois inefficaces dans la représentation de données expérimentales, qui sont de plus en plus nombreuses.

Différents isotopes d'un même élément sont caractérisés par des différences dans leurs constantes d'équilibre thermodynamique et cinétiques. Ils évoluent selon des vitesses de réaction qui sont légèrement modifiées par rapport aux lois classiques (par exemple les vitesses du premier ordre ou de modèles de type TST, Transition State Theory). Afin de modéliser le fractionnement des isotopes stables, certains auteurs se sont inspirés du concept de solutions solides étant donné que la substitution isotopique est ce qui se rapproche le plus d'une solution solide idéale. Malgré certaines affinités conceptuelles, les vitesses de réaction et les solutions solides doivent être couplées avec précaution au vu du manque de base théorique sur la cinétique des solutions solides.

L'inclusion des isotopes dans le modèle, sous la forme d'espèces chimiques indépendantes, a deux implications : très peu de modifications des algorithmes originaux sont nécessaires, mais les problématiques classiques de la modélisation des réactions chimiques et du transport sont exacerbées. En effet, le nombre d'espèces chimiques devient plus important et les concentrations traitées peuvent être très faibles, nécessitant donc une précision très importante. Pour cette raison, l'efficacité des algorithmes pour la résolution i) des systèmes algébriques non-linéaires provenant de l'équilibre thermodynamique et ii) des systèmes d'équations différentielles et algébriques venant du mélange équilibre/cinétique ont fait l'objet d'une large partie de ce travail.

L'équilibre thermodynamique est une approximation utile pour décrire des réactions pour lesquelles la durée a très peu d'importance. Il considère les réactions comme instantanées et génère un système non-linéaire d'équations algébriques qui sont généralement résolues par voie itérative. La méthode la plus utilisée pour résoudre ce genre de problèmes est la méthode de Newton Raphson, qui est connue pour sa rapidité de convergence mais également pour les difficultés de convergence qu'elle peut générer quand les valeurs initiales sont trop lointaines de la solution. Dans ce travail, deux approches ont été testées afin de limiter les inconvénients de la méthode : i) une méthode d'ordre zéro (qui ne nécessite pas le calcul de la matrice Jacobienne), nommée fractions continues positives (PCF, *positive continuous fractions*), a été couplée à la méthode de Newton Raphson et ii) l'algorithme de Newton

Raphson a été modifié pour réduire le conditionnement de la matrice Jacobienne à travers des techniques de *scaling* (normalisation du système linéaire qui apparaisse dans l'algorithme).

Les résultats présentés dans le troisième chapitre ont montré que l'application des fractions continues produit une réduction dans le nombre d'échec de simulation et une réduction du nombre d'itération pour atteindre la convergence peu importe le problème considéré. Il est apparu que les effets du *scaling* sont fortement dépendants du problème étudié et de la technique de *scaling* appliquée.

Dès que le temps devient une variable d'intérêt, l'équilibre thermodynamique n'est plus suffisant et il apparait nécessaire d'inclure des équations différentielles. Le scénario le plus réel est représenté par un mélange de réactions cinétiques et à l'équilibre thermodynamique. Il s'agit également de la meilleure alternative d'un point de vue du numérique, par rapport à une approche purement cinétique. Un mélange entre équilibre thermodynamique et cinétique génère des systèmes d'équations différentielles et algébriques. Plusieurs travaux théoriques ont été proposés à ce sujet et mettent en évidence que même si la formulation thermodynamique est bien détaillée dans les manuels des codes, la stratégie de solution des mélanges d'équations cinétiques et à l'équilibre est très souvent laissée de côté. Trois façons d'écrire le système résultant ont été proposées et testées : i) un système de *DAEs* où les lois d'action de masse sont explicites, ii) un système de *DAEs* où les lois d'action de masse sont écrites dans les équations de conservation de la matière (écrites comme des sommes des concentrations) et iii) un système d'équations différentielles ordinaires (ODEs ou *ordinary differential equations* en anglais) où les lois d'action de masse sont écrites dans les équations de conservation de la matière (écrites dans leur forme différentielle). La première et la troisième approche se sont révélées les plus performantes et les plus simples à mettre en place par rapport à la deuxième. Malgré le fait que la littérature suggère que la troisième approche soit préférable car elle réduit la taille du système, dans un de deux cas test, utilisé au cours de ce travail, la première approche a convergé plus vite que la troisième. La résolution de cas test supplémentaires devrait être envisagée mais les benchmarks disponibles pour ce genre de comparaison restent rares.

L'implémentation du solver DASPK s'est traduite par une réduction des temps de calcul pour la solution des systèmes mélangeant équilibre thermodynamique et cinétique, par rapport à la méthode QSSA explicite qui était implémentée dans SPECY, et cela quelle que soit la stratégie des équations résultantes.

Une caractéristique très intéressante du modèle KINDIS est la possibilité de modéliser les solutions solides à l'équilibre thermodynamique. Cette capacité a été implémentée dans SpeCTr sur le modèle de KINDIS et PHREEQC. L'algorithme a été utilisé pour simuler la précipitation d'une solution solide contenant du fer et du chrome à l'interface entre deux solutions potentiellement réactives. Cet exemple constitue une anticipation du couplage du modèle de transport et de chimie mais s'avère très utile pour comprendre le potentiel des solutions solide. L'accord entre les résultats du modèle et les expériences en laboratoire s'est montré satisfaisant même si des études complémentaires apparaissent nécessaires et notamment sur la relation des résultats aux choix des paramètres de transport.

Le couplage du module de chimie (développé dans les chapitres 2, 3, 4 et 5) et du module de transport (TRACES) a produit un outil nommé SpeCTr (Spéciation Cinétique Transport). Le couplage et l'implémentation des isotopes ont été testés ensemble à travers la résolution d'un benchmark monodimensionnel mis au point pour tester le fractionnement du chrome. Les résultats ont validé le couplage mais ont aussi mis en avant des problématiques liées à la modélisation des isotopes à travers la séparation d'opérateur. Des simulations, pouvant être considérées satisfaisantes si limitées à l'évolution des concentrations, se sont révélées inutilisables pour le calcul des rapports isotopiques et des deltas (δ) en résultant. Le pas de temps nécessaire pour obtenir des résultats satisfaisants a dû être réduit par rapport à celui demandé par le transport (dont la formulation est explicite et doit donc respecter la condition de Courant). Même si aucunes bases théoriques ne lient la condition de Courant et les erreurs de séparation d'opérateur, il a été remarqué qu'un pas de temps correspondant à un numéro de Courant de 0.2 a produit des résultats satisfaisants. La même considération apparait dans le manuel de CrunchFlow (Steefel, 2009).

La résolution du benchmark a également permis de mettre en évidence l'importance de l'algorithme liant les outils chimiques et de transport, servant à convertir les concentrations aux noeuds en concentrations moyennes utilisées pour chaque élément. Il apparait donc que des algorithmes simples doivent être préférés à d'autres plus complexes afin de limiter les propagations d'erreurs quand les concentrations deviennent très faibles.

Le dernier chapitre a été consacré à l'application de SpeCTr dans un contexte de dissolution et de précipitation de calcite en laboratoire. Les résultats numériques obtenus pour les phénomènes de précipitation de la calcite ont soulignés le rôle des différents modèles de changement de porosité et mis en évidence les points faibles des méthodes explicites. En effet, la réduction de la porosité, liée à la précipitation de calcite, est une des raisons de la réduction du pas de temps afin de respecter la condition de Courant.

La simulation de la dissolution des cristaux de calcite a montré le potentiel du code et son adaptabilité (en ce qui concerne les modèles cinétiques et la discrétisation spatiale) dans la modélisation des expériences de laboratoire. Ces simulations représentent également un bon exemple de collaboration entre différentes travaux de thèse. Même si les cas test réalisés au cours de ce travail (en système de batch et dans un contexte de transport réactif) ont été aussi nombreux et variés que possible dans le temps imparti (équilibre thermodynamique, mélanges de réactions cinétiques et à l'équilibre, cinétiques du premier ordre, Monod et *Transition State Theory*, précipitation de solutions solides dans le transport réactif, fractionnement des isotopes stables, etc.), il est conseillé de continuer à résoudre des cas pratiques et des benchmarks afin de continuer à développer les capacités du code et d'en cerner les faiblesses. Une attention particulière doit être dédiée aux modifications des paramètres du sol résultant des réactions chimiques (par exemple les changements de porosité suite aux précipitations).

Concernant les isotopes, les modèles implémentés se sont montrés efficaces dans différents scénarios. Cependant, il est nécessaire de tenir compte du fait que : i) ces modèles ont été développés à partir de

la nécessité de reproduire des données expérimentales et ii) dans ces modèles le fractionnement isotopique est utilisé comme traceur d'autres phénomènes biogéochimiques sans que les mécanismes de fractionnement ne soient le centre d'intérêt. Le code pourrait pourtant évoluer avec l'implémentation de modèles ad-hoc afin de reproduire des résultats expérimentaux ou pour traiter certains isotopes présentant des comportements particuliers.

Une interface graphique et un module d'accès à des bases de données sont en cours de développement. Ces derniers sont cruciaux afin de minimiser les erreurs d'utilisation et faciliter la préparation de cas test. Même si ces modules existent déjà, ils doivent encore être méticuleusement testés.

SpeCTr a actuellement montré de meilleurs performances que SPECY et une marge d'amélioration reste encore envisageable. Pour cela, différentes options pourraient s'avérer positive: i) d'autres solvers que DASPK peuvent être testés ii) la parallélisation devrait être systématiquement appliquée et iii) une formulation implicite du transport devrait être prise en considération. Ce dernier point a montré toute son importance lors des simulations de variations de porosité, qui ont forcé le code à des pas de temps trop petits.

L'implémentation de nouveaux solvers devrait être plus simple qu'en partant de zéro étant donné que les matrices et les vecteurs à utiliser sont déjà à disposition. Concernant la parallélisation, la séparation d'opérateur s'adapte bien à cette procédure (des solutions indépendants sont calculées) et doit être mise en place une fois que le code est validé.

Malgré les possibles développements futurs, SpeCTr a été testé avec des codes reconnus (KINDIS, PHREEQC, CrunchFlow etc.) et ses solutions peuvent être considérées fiables. SpeCTr convient également au couplage avec d'autres modèles pour le calcul de l'écoulement qui peuvent être plus avancées ou plus spécifiques que ceux qui sont implémentés dans TRACES.

References

Allison, J. D., Brown, D. S., & Novo-Gradac, K. J. (1991). *MINTEQA2/PRODEFA2, A geochemical assessment model for environmental systems: Version 3.0 User's Manual*. Environmental Research Laboratory, Office of Research and Development, US Environmental Protection Agency.

Alvarez-Zaldívar, P., Centler, F., Maier, U., Thullner, M., & Imfeld, G. (2016). Biogeochemical modelling of in situ biodegradation and stable isotope fractionation of intermediate chloroethenes in a horizontal subsurface flow wetland. *Ecological Engineering*, *90*, 170-179.

Anderson, G. M., & Crerar, D. A. (1993). *Thermodynamics in geochemistry: The equilibrium model*. Oxford University Press on Demand.

Appelo, C. A. J., & Willemsen, A. (1987). Geochemical calculations and observations on salt water intrusions, I. A combined geochemical/minxing cell model. *Journal of Hydrology*, *94*(3-4), 313-330.

Bea, S. A., Carrera, J., Ayora, C., Batlle, F., & Saaltink, M. W. (2009). CHEPROO: A Fortran 90 object-oriented module to solve chemical processes in Earth Science models. *Computers & Geosciences*, *35*(6), 1098-1112.

Bethke, C. M. (2007). *Geochemical and biogeochemical reaction modeling*. Cambridge University Press.

Bradley, A. M. (2010). *Algorithms for the equilibration of matrices and their application to limited-memory Quasi-Newton methods*. STANFORD UNIV CA.

Brassard, P., & Bodurtha, P. (2000). A feasible set for chemical speciation problems. *Computers & Geosciences*, *26*(3), 277-291.

Brenan, K. E., Campbell, S. L., & Petzold, L. R. (1996). *Numerical solution of initial-value problems in differential-algebraic equations* (Vol. 14). Classics in Applied Mathematics 14. Philadelphia: Society for Industrial and Applied Mathematics.

Breukelen, B. M. V., & Prommer, H. (2008). Beyond the Rayleigh equation: reactive transport modeling of isotope fractionation effects to improve quantification of biodegradation. *Environmental science & technology*, *42*(7), 2457-2463.

Brown, P. N., Byrne, G. D., & Hindmarsh, A. C. (1989). VODE: A variable-coefficient ODE solver. *SIAM journal on scientific and statistical computing*, *10*(5), 1038-1051.

Bruno, J. (2007). *Chemical thermodynamics of solid solutions of interest in radioactive waste management: a state-of-the-art report*. OECD Publishing.

Buzzi-Ferraris, G., & Manenti, F. (2014). *Nonlinear systems and optimization for the chemical engineer: Solving numerical problems*. John Wiley & Sons.

Buzzi-Ferraris, G. (2011). New trends in building numerical programs. *Computers & Chemical Engineering*, *35*(7), 1215-1225.

Carrayrou, J., Hoffmann, J., Knabner, P., Kräutle, S., De Dieuleveult, C., Erhel, J., ... & Macquarrie, K. T. (2010). Comparison of numerical methods for simulating strongly nonlinear and heterogeneous reactive transport problems—the MoMaS benchmark case. *Computational Geosciences*, *14*(3), 483-502.

Carrayrou, J., Kern, M., & Knabner, P. (2010). Reactive transport benchmark of MoMaS. *Computational geosciences*, *14*(3), 385-392.

Carrayrou, J., Mosé, R., & Behra, P. (2002). New efficient algorithm for solving thermodynamic chemistry. *AIChE Journal*, *48*(4), 894-904.

Carrayrou, J., Mosé, R., & Behra, P. (2004). Operator-splitting procedures for reactive transport and comparison of mass balance errors. *Journal of Contaminant Hydrology*, *68*(3-4), 239-268.

Carrayrou, J. (2001). *Modélisation du transport de solutés réactifs en milieu poreux saturé* (Doctoral dissertation, Université Louis Pasteur (Strasbourg)).

Cederberg, G. A., Street, R. L., & Leckie, J. O. (1985). A groundwater mass transport and equilibrium chemistry model for multicomponent systems. *Water Resources Research*, *21*(8), 1095-1104.

Chabaux, F., Ma, L., Stille, P., Pelt, E., Granet, M., Lemarchand, D., ... & Brantley, S. L. (2011). Determination of chemical weathering rates from U series nuclides in soils and weathering profiles: Principles, applications and limitations. *Applied Geochemistry*, *26*, S20-S23.

Chapra, S. C., & Canale, R. P. (2015). *Numerical methods for engineers*. Seventh edition. New York: McGraw-Hill Education.

Chen, K. (2005). *Matrix preconditioning techniques and applications* (No. 19). Cambridge University Press.

Chilakapati, A., Ginn, T., & Szecsody, J. (1998). An analysis of complex reaction networks in groundwater modeling. *Water Resources Research*, *34*(7), 1767-1780.

Chilakapati, A. (1995). *RAFT: A simulator for reactive flow and transport of groundwater contaminants*. Pacific Northwest Lab., Richland, WA (United States).

Cochepin, B., Trotignon, L., Bildstein, O., Steefel, C. I., & Lagneau, V. (2008). Approaches to modelling coupled flow and reaction in a 2D cementation experiment. *Advances in Water Resources*, *31*(12), 1540-1551.

Craig, H. (1957). Isotopic standards for Carbon and Oxygen and correction factors for mass-spectrometric analysis of carbon dioxide. *Geochimica et Cosmochimica Acta*, *12*, 133-149.

Criss, R. E. (1999). *Principles of stable isotope distribution*. Oxford University Press on Demand.

Delay, F., Kaczmaryk, A., & Ackerer, P. (2007). Inversion of interference hydraulic pumping tests in both homogeneous and fractal dual media. *Advances in water resources*, *30*(3), 314-334.

DePaolo, D. J., & Getty, S. R. (1996). Models of isotopic exchange in reactive fluid-rock systems: Implications for geochronology in metamorphic rocks. *Geochimica et Cosmochimica Acta*, *60*(20), 3933-3947.

DePaolo, D. J. (2011). Surface kinetic model for isotopic and trace element fractionation during precipitation of calcite from aqueous solutions. *Geochimica et Cosmochimica Acta*, *75*(4), 1039-1056.

DePaolo, D. J., Maher, K., Christensen, J. N., & McManus, J. (2006). Sediment transport time measured with U-series isotopes: results from ODP North Atlantic drift site 984. *Earth and Planetary Science Letters*, *248*(1), 394-410.

DePaolo, D. J., Conrad, M. E., Maher, K., & Gee, G. W. (2004). Evaporation effects on oxygen and hydrogen isotopes in deep vadose zone pore fluids at Hanford, Washington. *Vadose Zone Journal*, *3*(1), 220-232.

Druhan, J. L., Steefel, C. I., Williams, K. H., & DePaolo, D. J. (2013). Calcium isotope fractionation in groundwater: Molecular scale processes influencing field scale behavior. *Geochimica et Cosmochimica Acta*, *119*, 93-116.

Druhan, J. L., Conrad, M. E., Williams, K. H., N'Guessan, L., Long, P. E., & Hubbard, S. S. (2008). Sulfur isotopes as indicators of amended bacterial sulfate reduction processes influencing field scale uranium bioremediation. *Environmental science & technology*, *42*(21), 7842-7849.

Druhan, J. L., Bill, M., Lim, H., Wu, C., Conrad, M. E., Williams, K. H., ... & Brodie, E. L. (2014). A large column analog experiment of stable isotope variations during reactive transport: II. Carbon mass balance, microbial community structure and predation. *Geochimica et Cosmochimica Acta*, *124*, 394-409.

Druhan, J. L. (2012). *Stable Isotope Fractionations in Biogeochemical Reactive Transport*. University of California, Berkeley.

Dzombak, D. A., Morel, F.M. (1990). *Surface complexation modeling: hydrous ferric oxide*. John Wiley & Sons.

Engesgaard, P., & Kipp, K. L. (1992). A geochemical transport model for redox‑controlled movement of mineral fronts in groundwater flow systems: A case of nitrate removal by oxidation of pyrite. *Water resources research*, *28*(10), 2829-2843.

Fahs, M., Carrayrou, J., Younes, A., & Ackerer, P. (2008). On the efficiency of the direct substitution approach for reactive transport problems in porous media. *Water, air, and soil pollution*, *193*(1-4), 299-308.

Fahs, M. (2007). *Modélisation du transport réactif multicomposants en milieu poreux saturé* (Doctoral dissertation, Université Louis Pasteur, Strasbourg).

Fang, Y., Yeh, G. T., & Burgos, W. D. (2003). A general paradigm to model reaction‑based biogeochemical processes in batch systems. *Water Resources Research*, *39*(4).

Ferry, J. M., RUMBLE III, D., Wing, B. A., & Penniston-Dorland, S. C. (2005). A new interpretation of centimetre-scale variations in the progress of infiltration-driven metamorphic reactions: case study of carbonated metaperidotite, Val d'Efra, Central Alps, Switzerland. *Journal of Petrology*, *46*(8), 1725-1746.

Gamsjäger, H., Königsberger, E., & Preis, W. (2000). Lippmann diagrams: theory and application to carbonate systems. *Aquatic Geochemistry*, *6*(2), 119-132.

Gear, C. (1971). Simultaneous numerical solution of differential-algebraic equations. *IEEE transactions on circuit theory*, *18*(1), 89-95.

Van Genuchten, M. T., & Wierenga, P. J. (1976). Mass transfer studies in sorbing porous media I. Analytical solutions 1. *Soil Science Society of America Journal*, *40*(4), 473-480.

Gérard, F., Clement, A., & Fritz, B. (1998). Numerical validation of a Eulerian hydrochemical code using a 1D multisolute mass transport system involving heterogeneous kinetically controlled reactions. *Journal of Contaminant Hydrology*, *30*(3-4), 201-216.

Glynn, P. (2000). Solid-solution solubilities and thermodynamics: sulfates, carbonates and halides. *Reviews in Mineralogy and Geochemistry*, *40*(1), 481-511.

Glynn, P. D. (1990). Modeling Solid—Solution Reactions in Low-Temperature Aqueous Systems. In Chemical modeling of aqueous systems II. Washington, DC: American Chemical Society.

Glynn, P. D. (1991). MBSSAS: A code for the computation of Margules parameters and equilibrium relations in binary solid-solution aqueous-solution systems. *Computers & Geosciences*, *17*(7), 907-966.

Glynn, P. D., & Reardon, E. J. (1990). Solid-solution aqueous-solution equilibria; thermodynamic theory and representation. *American Journal of Science*, *290*(2), 164-201.

Glynn, Pierre, Eric Reardon, L. Neil Plummer, and Eurybiades Busemberg. 1992. 'Reply to a comment by R.K. Stossell on "Reaction paths and equilibrium end-points in solid-solution aqueous solution systems"'. Geochimica et Cosmochimica Acta, no. 56:2559–72.

Goddéris, Y., François, L. M., Probst, A., Schott, J., Moncoulon, D., Labat, D., & Viville, D. (2006). Modelling weathering processes at the catchment scale: The WITCH numerical model. *Geochimica et Cosmochimica Acta*, *70*(5), 1128-1147.

Goldberg, S., Criscenti, L. J., Turner, D. R., Davis, J. A., & Cantrell, K. J. (2007). Adsorption–desorption processes in subsurface reactive transport modeling. *Vadose Zone Journal*, *6*(3), 407-435.

Golub, G. H., and Van Loan, C.F. 1996. Matrix Computations. Third Edition. Baltimore: John Hopkins University Press.

Golub, G. H., & Ortega, J. M. (2014). *Scientific computing: an introduction with parallel computing*. Boston: Academic Press.Elsevier.

Helgeson, H. C. (1968). Evaluation of irreversible reactions in geochemical processes involving minerals and aqueous solutions—I. Thermodynamic relations. *Geochimica et Cosmochimica Acta*, *32*(8), 853-877.

Helgeson, H. C., Garrels, R. M., & MacKenzie, F. T. (1969). Evaluation of irreversible reactions in geochemical processes involving minerals and aqueous solutions—II. Applications. *Geochimica et Cosmochimica Acta*, *33*(4), 455-481.

Helgeson, H. C., Brown, T. H., Nigrini, A., & Jones, T. A. (1970). Calculation of mass transfer in geochemical processes involving aqueous solutions. *Geochimica et Cosmochimica Acta*, *34*(5), 569-592.

Henderson, T. H., Mayer, K. U., Parker, B. L., & Al, T. A. (2009). Three-dimensional density-dependent flow and multicomponent reactive transport modeling of chlorinated solvent oxidation by potassium permanganate. *Journal of contaminant hydrology, 106*(3-4), 195-211.

Hindmarsh, A. C. (1983). ODEPACK, a systematized collection of ODE solvers. *Scientific computing*, 55-64.

Hoffmann, J. (2010). Reactive transport and mineral dissolution/precipitation in porous media: efficient solution algorithms, benchmark computations and existence of global solutions.

Horita, J., & Wesolowski, D. J. (1994). Liquid-vapor fractionation of oxygen and hydrogen isotopes of water from the freezing to the critical temperature. *Geochimica et Cosmochimica Acta*, *58*(16), 3425-3437.

Imfeld, G., Aragonés, C. E., Fetzer, I., Mészáros, É., Zeiger, S., Nijenhuis, I., ... & Richnow, H. H. (2010). Characterization of microbial communities in the aqueous phase of a constructed model wetland treating 1, 2-dichloroethene-contaminated groundwater. *FEMS microbiology ecology*, *72*(1), 74-88.

Imfeld, G., Estop Aragonés, C., Zeiger, S., Vitzthum von Eckstädt, C., Paschke, H., Trabitzsch, R., ... & Richnow, H. H. (2008). Tracking in situ biodegradation of 1, 2-dichloroethenes in a model wetland. *Environmental science & technology*, *42*(21), 7924-7930.

Imfeld, G., Braeckevelt, M., Kuschk, P., & Richnow, H. H. (2009). Monitoring and assessing processes of organic chemicals removal in constructed wetlands. *Chemosphere*, *74*(3), 349-362.

IMSL Fortran Library User's Guide MATH/LIBRARY Volume 1 of 2'.

Istok, J. (1989). Groundwater modeling by the finite element method, American geophysical union, 2000 Florida avenue, NW, Washington, DC 20009. *Water Resources Monograph Series*, *13*, 415.

Jackson, K. R., & Sacks-Davis, R. (1980). An alternative implementation of variable step-size multistep formulas for stiff ODEs. *ACM Transactions on Mathematical Software (TOMS)*, *6*(3), 295-318.

Jacques, D., & Šimůnek, J. (2005). User manual of the multicomponent variably-saturated flow and transport model HP1. *Description, Verification and Examples, Version*, *1*, 79.

Jamieson-Hanes, J. H., Amos, R. T., & Blowes, D. W. (2012). Reactive transport modeling of chromium isotope fractionation during Cr (VI) reduction. *Environmental science & technology*, *46*(24), 13311-13316.

Johnson, T. M., & DePaolo, D. J. (1994). Interpretation of isotopic data in groundwater-rock systems: Model development and application to Sr isotope data from Yucca Mountain. *Water Resources Research*, *30*(5), 1571-1587.

Johnson, T. M., & DePaolo, D. J. (1996). Reaction-Transport Models for Radiocarbon in Groundwater: The Effects of Longitudinal Dispersion and the use of Sr Isotope Ratios to Correct for Water-Rock Interaction. *Water resources research*, *32*(7), 2203-2212.

Johnson, T. M., & DePaolo, D. J. (1997). Rapid exchange effects on isotope ratios in groundwater systems: 1. Development of a transport-dissolution-exchange model. *Water Resources Research*, *33*(1), 187-195.

Katz, G. E., Berkowitz, B., Guadagnini, A., & Saaltink, M. W. (2011). Experimental and modeling investigation of multicomponent reactive transport in porous media. *Journal of contaminant hydrology*, *120*, 27-44.

Kee, R. J., Petzold, L. R., Smooke, M. D., & Grcar, J. F. (1985). Implicit methods in combustion and chemical kinetics modeling. In *Multiple Time Scales* (pp. 113-144).

Kern, M., & Amir, L. (2007). Newton-Krylov methods for coupling transport with chemistry in porous media. *CMWR XVI, Copenhagen*.

Kiusalaas, J. 2005. Numerical Methods in Engineering with MATLAB. New York: Cambridge University Press.

Knight, P. A., Ruiz, D., & Uçar, B. (2014). A symmetry preserving algorithm for matrix scaling. *SIAM journal on Matrix Analysis and Applications*, *35*(3), 931-955.

Kolditz, O., Bauer, S., Bilke, L., Böttcher, N., Delfs, J. O., Fischer, T., ... & Park, C. H. (2012). OpenGeoSys: an open-source initiative for numerical simulation of thermo-hydro-mechanical/chemical (THM/C) processes in porous media. *Environmental Earth Sciences*, *67*(2), 589-599.

Königsberger, E., & Gamsjäger, H. (1990). Solid-solute phase equilibria in aqueous solution. III. A new application of an old chemical potentiometer. *Marine chemistry*, *30*, 317-327.

Koenigsberger, E., Gamsjaeger, H., Glynn, P. D., & Reardon, E. J. (1992). Solid-solution aqueous-solution equilibria; thermodynamic theory and representation; discussion and reply. *American Journal of Science*, *292*(3), 199-225.

Kotaś, J., & Stasicka, Z. (2000). Chromium occurrence in the environment and methods of its speciation. *Environmental pollution*, *107*(3), 263-283.

Kräutle, S., & Knabner, P. (2005). A new numerical reduction scheme for fully coupled multicomponent transport-reaction problems in porous media. *Water resources research*, *41*(9).

Kulik, D. A., Wagner, T., Dmytrieva, S. V., Kosakowski, G., Hingerl, F. F., Chudnenko, K. V., & Berner, U. R. (2013). GEM-Selektor geochemical modeling package: revised algorithm and GEMS3K numerical kernel for coupled simulation codes. *Computational Geosciences*, *17*(1), 1-24.

Leal, A. M., Blunt, M. J., & LaForce, T. C. (2014). Efficient chemical equilibrium calculations for geochemical speciation and reactive transport modelling. *Geochimica et Cosmochimica Acta*, *131*, 301-322.

Leal, A. M., Blunt, M. J., & LaForce, T. C. (2015). A chemical kinetics algorithm for geochemical modelling. *Applied Geochemistry*, *55*, 46-61.

Van der Lee, J., & De Windt, L. (2002). *CHESS tutorial and cookbook. Updated for version 3.0., Manual Nr*. LHM/RD/02/13, Paris.

Van Der Lee, J., De Windt, L., Lagneau, V., & Goblet, P. (2003). Module-oriented modeling of reactive transport with HYTEC. *Computers & Geosciences*, *29*(3), 265-275.

Lichtner, P. C. (1985). Continuum model for simultaneous chemical reactions and mass transport in hydrothermal systems. *Geochimica et Cosmochimica Acta*, *49*(3), 779-800.

Lichtner, P. C., & Carey, J. W. (2006). Incorporating solid solutions in reactive transport equations using a kinetic discrete-composition approach. *Geochimica et Cosmochimica Acta*, *70*(6), 1356-1378.

Lichtner, P. C., Hammond, G. E., Lu, C., Karra, S., Bisht, G., Andre, B., ... & Kumar, J. (2015). *PFLOTRAN user manual: A massively parallel reactive flow and transport model for describing surface and subsurface processes* (No. LA-UR--15-20403). Los Alamos National Lab.(LANL), Los Alamos, NM (United States); Sandia National Lab.(SNL-NM), Albuquerque, NM (United States); Lawrence Berkeley National Lab.(LBNL), Berkeley, CA (United States); Oak Ridge National Lab.(ORNL), Oak Ridge, TN (United States); OFM Research, Redmond, WA (United States).

Lippmann, F. (1977). The solubility products of complex minerals, mixed crystals, and three-layer clay minerals. *N. Jb. Miner. Abh*, *130*(3), 243-263.

Lippmann, F. (1980). Phase diagrams depicting the aqueous solubility of mineral systems. *Neues Jahrbuch Mineralogische Abhandlungen*, *139*(1), 1-25.

Machat, H., & Carrayrou, J. (2017). Comparison of linear solvers for equilibrium geochemistry computations. *Computational Geosciences*, *21*(1), 131-150.

MacQuarrie, K. T., & Mayer, K. U. (2005). Reactive transport modeling in fractured rock: A state-of-the-science review. *Earth-Science Reviews*, *72*(3-4), 189-227.

Madé, B., Clément, A., & Fritz, B. (1994). Modeling mineral/solution interactions: the thermodynamic and kinetic code KINDISP. *Computers & Geosciences*, *20*(9), 1347-1363.

Maher, K., Steefel, C. I., DePaolo, D. J., & Viani, B. E. (2006). The mineral dissolution rate conundrum: Insights from reactive transport modeling of U isotopes and pore fluid chemistry in marine sediments. *Geochimica et Cosmochimica Acta, 70*(2), 337-363.

Maher, K., DePaolo, D. J., & Christensen, J. N. (2006). U–Sr isotopic speedometer: fluid flow and chemical weathering rates in aquifers. *Geochimica et Cosmochimica Acta, 70*(17), 4417-4435.

Maher, K., DePaolo, D. J., Conrad, M. E., & Serne, R. J. (2003). Vadose zone infiltration rate at Hanford, Washington, inferred from Sr isotope measurements. *Water Resources Research, 39*(8).

Marquardt, D. W. (1963). An algorithm for least-squares estimation of nonlinear parameters. *Journal of the society for Industrial and Applied Mathematics, 11*(2), 431-441.

Mayer, K. U., Frind, E. O., & Blowes, D. W. (2002). Multicomponent reactive transport modeling in variably saturated porous media using a generalized formulation for kinetically controlled reactions. *Water Resources Research, 38*(9).

Molins, S., Carrera, J., Ayora, C., & Saaltink, M. W. (2004). A formulation for decoupling components in reactive transport problems. *Water Resources Research, 40*(10).

Noguera, C., Fritz, B., Clément, A., & Amal, Y. (2010). Simulation of the nucleation and growth of binary solid solutions in aqueous solutions. *Chemical Geology, 269*(1-2), 89-99.

Noguera, C., Fritz, B., & Clement, A. (2016). Kinetics of precipitation of non-ideal solid-solutions in a liquid environment. *Chemical Geology, 431*, 20-35.

Nourtier-Mazauric, E., Guy, B., Fritz, B., Brosse, E., Garcia, D., & Clément, A. (2005). Modelling the dissolution/precipitation of ideal solid solutions. *Oil & gas science and technology, 60*(2), 401-415.

Öhman, L. O. (1983). *Equilibrium studies of ternary aluminium (III) hydroxo complexes with ligands related to conditions in natural waters* (Doctoral dissertation, Umeå University).

Pan, Y., Weill, S., Ackerer, P., & Delay, F. (2015). A coupled stream flow and depth-integrated subsurface flow model for catchment hydrology. *Journal of Hydrology, 530*, 66-78.

Parkhurst, D. L., & Appelo, C. A. J. (1999). User's guide to PHREEQC (Version 2): A computer program for speciation, batch-reaction, one-dimensional transport, and inverse geochemical calculations.

Plummer, L. N., & Busenberg, E. (1987). Thermodynamics of aragonite-strontianite solid solutions: Results from stoichiometric solubility at 25 and 76 C. *Geochimica et Cosmochimica Acta, 51*(6), 1393-1411.

Prieto, M., Fernández-González, A., Putnis, A., & Fernandez-Diaz, L. (1997). Nucleation, growth, and zoning phenomena in crystallizing (Ba, Sr) CO3, Ba (SO4, CrO4),(Ba, Sr) SO4, and (Cd, Ca) CO3 solid solutions from aqueous solutions. *Geochimica et Cosmochimica Acta*, *61*(16), 3383-3397.

Prommer, H., & Post, V. E. A. (2010). PHT3D, A Reactive Multicomponent Transport Model for Saturated Porous Media. User's Manual v2. 10.

Pruess, K., & Narasimhan, T. N. (1982). *Practical method for modeling fluid and heat flow in fractured porous media* (No. LBL-13487; CONF-820242-1). Lawrence Berkeley Lab., CA (USA).

Reed, M. H. (1982). Calculation of multicomponent chemical equilibria and reaction processes in systems involving minerals, gases and an aqueous phase. *Geochimica et Cosmochimica Acta*, *46*(4), 513-528.

Richter, F. M., & DePaolo, D. J. (1987). Numerical models for diagenesis and the Neogene Sr isotopic evolution of seawater from DSDP Site 590B. *Earth and Planetary Science Letters*, *83*(1-4), 27-38.

Rolle, M., Chiogna, G., Bauer, R., Griebler, C., & Grathwohl, P. (2010). Isotopic fractionation by transverse dispersion: Flow-through microcosms and reactive transport modeling study. *Environmental science & technology*, *44*(16), 6167-6173.

Uçar, D. R. B. (2011). A Symmetry Preserving Algorithm for Matrix Scaling.

Saaltink, M. W., Carrera, J., & Ayora, C. (2000). A comparison of two approaches for reactive transport modelling. *Journal of Geochemical Exploration*, *69*, 97-101.

Saaltink, M. W., Ayora, C., & Carrera, J. (1998). A mathematical formulation for reactive transport that eliminates mineral concentrations. *Water Resources Research*, *34*(7), 1649-1656.

Saaltink, M. W., Batlle, F., Ayora, C., Carrera, J., & Olivella, S. (2004). RETRASO, a code for modeling reactive transport in saturated and unsaturated porous media. *Geologica Acta: an international earth science journal*, *2*(3).

Saaltink, M. W., Carrera, J., & Ayora, C. (2001). On the behavior of approaches to simulate reactive transport. *Journal of Contaminant Hydrology*, *48*(3-4), 213-235.

Samper, J., Xu, T., & Yang, C. (2009). A sequential partly iterative approach for multicomponent reactive transport with CORE 2D. *Computational Geosciences*, *13*(3), 301.

Sánchez-Pastor, N., Pina, C. M., & Fernandez-Diaz, L. (2006). Relationships between crystal morphology and composition in the (Ba, Sr) SO4–H2O solid solution–aqueous solution system. *Chemical geology*, *225*(3-4), 266-277.

Sandu, A., Verwer, J. G., Blom, J. G., Spee, E. J., Carmichael, G. R., & Potra, F. A. (1997). Benchmarking stiff ODE solvers for atmospheric chemistry problems II: Rosenbrock solvers. *Atmospheric environment*, *31*(20), 3459-3472.

Schmitt, A. D., Vigier, N., Lemarchand, D., Millot, R., Stille, P., & Chabaux, F. (2012). Processes controlling the stable isotope compositions of Li, B, Mg and Ca in plants, soils and waters: A review. *Comptes Rendus Geoscience*, *344*(11-12), 704-722.

Shaff, J. E., Schultz, B. A., Craft, E. J., Clark, R. T., & Kochian, L. V. (2010). GEOCHEM-EZ: a chemical speciation program with greater power and flexibility. *Plant and soil*, *330*(1-2), 207-214.

Sigg, L., Behra, P., & Stumm, W. (2001). *Chimie des milieux aquatiques*. Paris. Dunod.

Šimůnek, J., & Suarez, D. L. (1994). Two-dimensional transport model for variably saturated porous media with major ion chemistry. *Water Resources Research*, *30*(4), 1115-1133.

Simunek, J., Jacques, D., Langergraber, G., Bradford, S. A., Šejna, M., & van Genuchten, M. T. (2013). Numerical modeling of contaminant transport using HYDRUS and its specialized modules. *Journal of the Indian institute of science*, *93*(2), 265-284.

Šimůnek, J., Jacques, D., Šejna, M., & van Genuchten, M. T. (2012). The HP2 program for HYDRUS (2D/3D): A coupled code for simulating two-dimensional variably-saturated water flow, heat transport, and biogeochemistry in porous media, version 1.0. *PC Progress, Prague, Czech Republic*.

Singleton, M. J., Sonnenthal, E. L., Conrad, M. E., DePaolo, D. J., & Gee, G. W. (2004). Multiphase reactive transport modeling of seasonal infiltration events and stable isotope fractionation in unsaturated zone pore water and vapor at the Hanford site. *Vadose Zone Journal*, *3*(3), 775-785.

Singleton, M. J., Maher, K., DePaolo, D. J., Conrad, M. E., & Dresel, P. E. (2006). Dissolution rates and vadose zone drainage from strontium isotope measurements of groundwater in the Pasco Basin, WA unconfined aquifer. *Journal of hydrology*, *321*(1-4), 39-58.

Steefel, C. I., DePaolo, D. J., & Lichtner, P. C. (2005). Reactive transport modeling: An essential tool and a new research approach for the Earth sciences. *Earth and Planetary Science Letters*, *240*(3-4), 539-558.

Steefel, C. I., Appelo, C. A. J., Arora, B., Jacques, D., Kalbacher, T., Kolditz, O., ... & Molins, S. (2015). Reactive transport codes for subsurface environmental simulation. *Computational Geosciences*, *19*(3), 445-478.

Steefel, C. I. (2009). CrunchFlow. Software for Modeling Multicomponent Reactive Flow and Transport. User's Manual. *Earth Sciences Division. Lawrence Berkeley, National Laboratory, Berkeley, CA. October*, 12-91.

Steefel, C. I., & Lasaga, A. C. (1994). A coupled model for transport of multiple chemical species and kinetic precipitation/dissolution reactions with application to reactive flow in single phase hydrothermal systems. *American Journal of science, 294*(5), 529-592.

Steefel, C. I., & MacQuarrie, K. T. (1996). Approaches to modeling of reactive transport in porous media. *Reviews in Mineralogy and Geochemistry, 34*(1), 85-129.

Steefel, C. I., & Yabusaki, S. B. (1995). *OS3D/GIMRT software for modeling multicomponent-multidimensional reactive transport*. Pacific Northwest National Lab., Richland, WA (US).

Stumm, W. (1980). A ligand exchange model for the adsorption of inorganic and organic ligands at hydrous oxide interfaces. *Croatica chemica acta, 53*, 291-312.

Tardy, Y., & Fritz, B. (1981). An ideal solid solution model for calculating solubility of clay minerals. *Clay minerals, 16*(3), 361-373.

Thorstenson, D. C., & Plummer, L. N. (1977). Equilibrium criteria for two-component solids reacting with fixed composition in an aqueous phase; example, the magnesian calcites. *American Journal of Science, 277*(9), 1203-1223.

Sonnenthal, E. L., Spycher, N., Xu, T., Zheng, L., Miller, N. L., & Pruess, K. (2014). TOUGHREACT V3. 0-OMP Reference Manual: a Parallel Simulation Program for Non-Isothermal Multiphase Geochemical Reactive Transport, LBNL, Report. *Lawrence Berkeley National Laboratory, Berkeley, CA*.

Tsai, C. H., Yeh, G. T., & Ni, C. F. (2013). HYDROGEOCHEM 6.0: a model to couple thermal-hydrology-mechanics-chemical (THMC) processes USER GUIDE. *Graduate Institute of Applied Geology, National Central University, Jhongli*.

Valocchi, A. J., & Malmstead, M. (1992). Accuracy of operator splitting for advection-dispersion-reaction problems. *Water Resources Research, 28*(5), 1471-1476.

Valocchi, A. J., Street, R. L., & Roberts, P. V. (1981). Transport of ion-exchanging solutes in groundwater: Chromatographic theory and field simulation. *Water Resources Research, 17*(5), 1517-1527.

Van Breukelen, B. M., Hunkeler, D., & Volkering, F. (2005). Quantification of sequential chlorinated ethene degradation by use of a reactive transport model incorporating isotope fractionation. *Environmental science & technology, 39*(11), 4189-4197.

Van Breukelen, B. M., Thouement, H. A., Stack, P. E., Vanderford, M., Philp, P., & Kuder, T. (2017). Modeling 3D-CSIA data: Carbon, chlorine, and hydrogen isotope fractionation during reductive dechlorination of TCE to ethene. *Journal of contaminant hydrology*, *204*, 79-89.

Van der Lee, J. (1998). Thermodynamic and mathematical concepts of CHESS.

Wanner, C., & Sonnenthal, E. L. (2013). Assessing the control on the effective kinetic Cr isotope fractionation factor: A reactive transport modeling approach. *Chemical geology*, *337*, 88-98.

Wanner, C., Druhan, J. L., Amos, R. T., Alt-Epping, P., & Steefel, C. I. (2015). Benchmarking the simulation of Cr isotope fractionation. *Computational geosciences*, *19*(3), 497-521.

Wanner, C., Eggenberger, U., Kurz, D., Zink, S., & Mäder, U. (2012). A chromate-contaminated site in southern Switzerland–Part 1: Site characterization and the use of Cr isotopes to delineate fate and transport. *Applied geochemistry*, *27*(3), 644-654.

Weill, S., Delay, F., Pan, Y., & Ackerer, P. (2017). A low-dimensional subsurface model for saturated and unsaturated flow processes: ability to address heterogeneity. *Computational Geosciences*, *21*(2), 301-314.

Westall, J. C. (1976). MINEQL: A computer program for the calculation of chemical equilibrium composition of aqueous systems. Department of Civil Engineering, Massachusetts Institute of Technology.

White, M. D., & McGrail, B. P. (2005). *STOMP subsurface transport over multiple phases version 1.0 addendum: ECKEChem equilibrium-conservation-kinetic equation chemistry and reactive transport* (No. PNNL-15482). Pacific Northwest National Laboratory (PNNL), Richland, WA (US), Environmental Molecular Sciences Laboratory (EMSL).

White, M. D., & Oostrom, M. (2006). *STOMP subsurface transport over multiple phases, version 4.0, user's guide* (No. PNNL-15782). Pacific Northwest National Laboratory (PNNL), Richland, WA (US), Environmental Molecular Sciences Laboratory (EMSL).

Press, W. H., Teukolsky, S. A., Vetterling, W. T., & Flannery, B. P. Numerical Recipes in Fortran 77, The Art of Scientific Computing, 1992.

Wolery, T. W., & Jarek, R. L. (2003). Software user's manual. *EQ3/6, version*, *8*, 376.

Wood, J. R. (1993). Calculation of fluid-mineral equilibria using the simplex algorithm. *Computers & Geosciences*, *19*(1), 23-39.

Xu, T., & Pruess, K. (2001). Modeling multiphase non-isothermal fluid flow and reactive geochemical transport in variably saturated fractured rocks: 1. Methodology. *American Journal of Science*, *301*(1), 16-33.

Xu, T., Sonnenthal, E., Spycher, N., & Pruess, K. (2006). TOUGHREACT—a simulation program for non-isothermal multiphase reactive geochemical transport in variably saturated geologic media: applications to geothermal injectivity and CO2 geological sequestration. *Computers & Geosciences*, *32*(2), 145-165.

Xu, T., Pruess, K., & Brimhall, G. (1999). An improved equilibrium-kinetics speciation algorithm for redox reactions in variably saturated subsurface flow systems. *Computers & Geosciences*, *25*(6), 655-666.

Xu, T., Spycher, N., Sonnenthal, E., Zhang, G., Zheng, L., & Pruess, K. (2011). TOUGHREACT Version 2.0: A simulator for subsurface reactive transport under non-isothermal multiphase flow conditions. *Computers & Geosciences*, *37*(6), 763-774.

Yabusaki, S. B., Steefel, C. I., & Wood, B. D. (1998). Multidimensional, multicomponent, subsurface reactive transport in nonuniform velocity fields: code verification using an advective reactive streamtube approach. *Journal of contaminant hydrology*, *30*(3-4), 299-331.

Yeh, G. T., & Tsai, C. H. (2013). HYDROGEOCHEM 6.0, a two-dimensional model of coupled fluid flow, thermal transport, HYDROGEOCHEMical transport, and geomechanics through multiple phase, systems version 6.0 (FACTM2D), theoretical basis and numerical approximation. *Graduate Institute of Applied Geology, National Central University, Jhongli*.

Yeh, G. T., & Tripathi, V. S. (1989). A critical evaluation of recent developments in hydrogeochemical transport models of reactive multichemical components. *Water resources research*, *25*(1), 93-108.

Yeh, G. T., & Tripathi, V. S. (1991). A model for simulating transport of reactive multispecies components: model development and demonstration. *Water Resources Research*, *27*(12), 3075-3094.

Yoon, H., Kang, Q., & Valocchi, A. J. (2015). Lattice Boltzmann-based approaches for pore-scale reactive transport. *Reviews in Mineralogy and Geochemistry*, *80*(1), 393-431.

Annexes

Annex I

The method to compute the Jacobian matrix is not affected by changing variables. We must compute the derivative of the system (3.9), which is written as a function of ξ with respect to ξ:

$$\frac{\partial Y_k}{\partial \xi_j} = \frac{\partial \left(\left[\tilde{T}_k \right] - \left[T_k \right] \right)}{\partial \xi_j} = -\frac{\partial T_k}{\partial \xi_j}. \tag{7.16}$$

The known total concentrations $\left[\tilde{T}_k \right]$ are constant values. The derivative takes the form:

$$\frac{\partial T_k}{\partial \xi_j} = \frac{\partial}{\partial \xi_j} \sum_{i=1}^{Nc} b_{i,k} \exp \left(\ln K_i + \sum_{j=1}^{Nx} b_{i,j} \xi_j \right). \tag{7.17}$$

The derivative of a sum is the sum of the derivatives:

$$\frac{\partial T_k}{\partial \xi_j} = \sum_{i=1}^{Nc} b_{i,k} \left(\frac{\partial}{\partial \xi_j} \exp \left(\ln K_i + \sum_{j=1}^{Nx} b_{i,j} \xi_j \right) \right). \tag{7.18}$$

The derivative of an exponential function is again an exponential function:

$$\frac{\partial T_k}{\partial \xi_j} = \sum_{i=1}^{Nc} b_{i,k} \exp \left(\ln K_i + \sum_{j=1}^{Nx} b_{i,j} \xi_j \right) \frac{\partial}{\partial \xi_j} \left(\ln K_i + \sum_{j=1}^{Nx} b_{i,j} \xi_j \right). \tag{7.19}$$

Then, K_i does not depend on ξ_j, and $\dfrac{\partial}{\partial \xi_{j*}} = \sum_{j=1}^{Nx} b_{i,j} \xi_j = b_{i,j*}$. Thus, we have:

$$\frac{\partial T_k}{\partial \xi_j} = \sum_{i=1}^{Nc} b_{i,k} b_{i,j} \exp \left(\ln K_i + \sum_{j=1}^{Nx} b_{i,j} \xi_j \right) = \sum_{i=1}^{Nc} b_{i,k} b_{i,j} \left[C_i \right]. \tag{7.20}$$

More equations are included in the optimization when precipitates are present. These equations are solubility products, but they are treated as totals because they are part of the minimization as well:

$$\ln K_{S_l} = \sum_{j}^{Nx} bp_{l,j} \xi_j \,, \tag{7.21}$$

where $l \in [1 + Nx, Nx + Ncp]$. In this case, the derivative takes the following form:

$$\frac{\partial}{\partial \xi_j} \sum_{j=1}^{Nx} bp_{l,j} \xi_j = bp_{l,j} \,. \tag{7.22}$$

In presence of precipitates we have additional unknowns $[Cp]$ that will be treated as regular concentrations $[C_i]$: the derivatives of equation (7.21) with respect to $[Cp]$ always equal zero because these equations only depend on ξ. On the other hand, the derivatives of equation (3.9) with respect to $[Cp]$ are nonzero and can be easily computed by looking at the equation itself:

$$\left[\tilde{T}_j\right] - \sum_{i=1}^{Nc} \frac{b_{i,j}}{\gamma_i} K_i \prod_{k=1}^{Nx} \left(\gamma_j \left[X_k\right]\right)^{b_{i,k}} + \sum_{l=1}^{Ncp} bp_{l,j} \left[Cp_l\right] \quad j = 1,\dots,N_x \,. \tag{7.23}$$

Notably, equation (7.16) contains a minus sign. If we consider the form of the linear system in the Newton Raphson algorithm, we can write the equation as follows:

$$-\mathbf{J}_n \Delta \mathbf{X}_n = \mathbf{Y}_n \,. \tag{7.24}$$

Thus, the Jacobian matrix is computed in the code as the sole derivative of the computed totals, avoiding the minus sign.

Annex II

The following tables provide stoichiometric coefficients, thermodynamic constants and total conserved concentrations for each test case presented in the work.

	H^+	Al^{3+}	H_3L	$\log_{10} K$
H^+	1	0	0	0
Al^{3+}	0	1	0	0
H_3L	0	0	1	0
OH^-	-1	0	0	-14
H_2L^-	-1	0	1	-4.15
HL^{2-}	-2	0	1	-12.59
L^{3-}	-3	0	1	-23.67
$AlHL^+$	-2	1	1	-4.93
AlL	-3	1	1	-9.43
AlL_2^{3-}	-6	1	2	-21.98
AlL_3^{6-}	-9	1	3	-37.69
$Al_2(OH)_2(HL)_3L^{2-}$	-8	2	3	-22.65
$Al_2(OH)_2(HL)_2L^{3-}$	-9	2	3	-27.81
$Al_2(OH)_2(HL)L^{4-}$	-10	2	3	-32.87
$Al_2(OH)_2L_3^{5-}$	-11	2	3	-39.56
$Al_4L_3^{3+}$	-9	4	3	-20.25
$Al_3(OH)_4(H_2L)L^{4+}$	-5	3	1	-12.52
$\left[T_j\right]$	$1.58\ 10^{-6}$	$1\ 10^{-3}$	$1\ 10^{-3}$	

Table II-I: Morel table for Gallic Acid test case. Gallic Acid is an organic aromatic compound that is also known as 3,4,5-trihydroxybenzoic. This acid can be easily found in plants and is largely used in the pharmaceutical industry. The system was originally studied in relation to Al(III) speciation in natural waters[50].

	H^+	O_2	Fe^{2+}	SO_4^{2-}	$Log_{10}K$
H^+	1	0	0	0	0
OH^-	-1	0	0	0	-14
O_2	0	1	0	0	0
Fe^{2+}	0	0	1	0	0
$Fe(OH)_2$	-2	0	1	0	-20.6
$Fe(OH)_3^-$	-3	0	1	0	-31
$Fe(OH)^+$	-1	0	1	0	-9.5
$FeSO_4$	0	0	1	1	2.2
Fe^{3+}	1	0.25	1	0	8.49
$Fe(OH)_2^+$	-1	0.25	1	0	2.82
$Fe(OH)_3$	-2	0.25	1	0	-3.51
$Fe(OH)_4^-$	-3	0.25	1	0	-13.11
$FeOH^{2+}$	0	0.25	1	0	6.3
$Fe_2(OH)_2^{4+}$	0	0.5	2	0	14.03
$Fe_3(OH)_4^{5+}$	-1	0.75	3	0	19.17
$Fe(SO)_2^-$	1	0.25	1	2	11.7
$FeSO_4^{4-}$	1	0.25	1	1	10.4
SO_4^{2-}	0	0	0	1	0
HSO_4^-	1	0	0	1	1.98
H_2SO_4	2	0	0	1	-1.02
SO_3^{2-}	0	-0.5	0	1	-46.62
HSO_3^-	1	-0.5	0	1	-39.42
H_2SO_3	2	-0.5	0	1	-37.41
SO_2	2	-0.5	0	1	-37.56
$HS_2O_3^-$	3	-2	0	2	-132.52
$S_2O_3^{2-}$	2	-2	0	2	-133.54
H_2S	2	-2	0	1	-131.33
HS^-	1	-2	0	1	-138.32
S^{2-}	0	-2	0	1	-151.25
S_2^{2-}	2	-3.5	0	2	-243.37
S_3^{2-}	4	-5	0	3	-335.56
S_4^{2-}	6	-6.5	0	4	-427.97
S_5^{2-}	8	-8	0	5	-520.6
$S_2O_4^{2-}$	2	-1.5	0	2	-118.46
$S_2O_5^{2-}$	2	1	0	2	-83.65
$S_2O_6^{2-}$	2	-0.5	0	2	-51.42
$S_2O_6^{2+}$	2	0.5	0	2	-22.5
$S_3O_6^{2-}$	4	-2	0	3	-146.1
$S_4O_6^{2-}$	6	-0.35	0	4	-22.88
$S_5O_6^{2-}$	8	-5	0	5	-332.54
Fe(s)	-2	-0.5	1	0	-59.03
FeS$_2$ (s)	2	-3.5	1	2	-217.40
FeSO$_4$(s)	0	0	1	1	-2.66
$\left[T_j \right]$	$2 \cdot 10^{-3}$	$-3.5 \cdot 10^{-3}$	$1 \cdot 10^{-3}$	$2 \cdot 10^{-3}$	

Table II-II: Morel table for Pyrite and Pyrite Mineral test cases.

	H^+	e^-	H_2CO_3	Fe^{2+}	CrO_4^{2-}	K^+	SO_4^{2-}	$Log_{10}K$
H^+	1	0	0	0	0	0	0	0
OH^-	-1	0	0	0	0	0	0	-14
O_2	-4	-4	0	0	0	0	0	-83.17
H_2	2	2	0	0	0	0	0	0
H_2O_2	-2	-2	0	0	0	0	0	-59
K^+	0	0	0	0	0	1	0	0
SO_4^{2-}	0	0	0	0	0	0	1	0
KSO_4^{2-}	0	0	0	0	0	1	1	0.5
$H_2CO_3^-$	0	0	1	0	0	0	0	0
HCO_3^-	-1	0	1	0	0	0	0	-6.3
CO_3^{2-}	-2	0	1	0	0	0	0	-16.6
Fe^{2+}	0	0	0	1	0	0	0	0
$FeOH^+$	-1	0	0	1	0	0	0	-8.98
$FeOOH^-$	-3	0	0	1	0	0	0	-33.21
$Fe(OH)_{2(aq)}$	-2	0	0	1	0	0	0	-20.6
$Fe(OH)_3^-$	-3	0	0	1	0	0	0	-31
$Fe(OH)_4^{2-}$	-4	0	0	1	0	0	0	-46
$FeHCO_3^+$	-1	0	1	1	0	0	0	-3.58
$FeSO_4$	0	0	0	1	0	0	1	1.2
Fe^{3+}	0	-1	0	1	0	0	0	-13.07
$FeOH^{2+}$	-1	-1	0	1	0	0	0	-15.2
$Fe(OH)_2^+$	-2	-1	0	1	0	0	0	-19.97
$Fe(OH)_4^-$	-4	-1	0	1	0	0	0	-34.62
$Fe_2(OH)_2^{4+}$	-2	-2	0	2	0	0	0	-29
$FeSO_4^+$	0	-1	0	1	0	0	1	-9.02
$Fe(SO_4)_2^-$	0	-1	0	1	0	0	2	-7.62
Cr^{2+}	8	4	0	0	1	0	0	68.09
$CrOH^+$	7	4	0	0	0	0	0	62.56
Cr^{3+}	8	3	0	0	1	0	0	74.98
$CrOH^{2+}$	7	3	0	0	1	0	0	71.17
$Cr(OH)_2^+$	6	3	0	0	1	0	0	64.95
$Cr(OH)_3$	5	3	0	0	1	0	0	80.9
$Cr(OH)_4^-$	4	3	0	0	1	0	0	47.5
CrO_4^{2-}	0	0	0	0	1	0	0	0
$HCrO_4^-$	1	0	0	0	1	0	0	6.45
H_2CrO_4	2	0	0	0	1	0	0	6.3
$FeCrO_4^+$	0	-1	0	1	1	0	0	-19.31
$CrSO_4^+$	8	3	0	0	1	0	1	76.3
$KCrO_4^-$	0	0	0	0	1	1	0	0.57
Fe(s)	0	2	0	1	0	0	0	13.12
Cr(OH)$_3$(s)	5	3	0	0	1	0	0	66.1
Cr$_{0.25}$Fe$_{0.75}$OOH(s)	-1	0	0	0.25	0.75	0	0	2.93
$[T_j]$	0	0	$1\ 10^{-6}$	$9\ 10^{-3}$	$3\ 10^{-3}$	$6\ 10^{-3}$	$9\ 10^{-3}$	

Table II-III: Morel table for Fe Cr and Fe Cr Min test cases.

	X_1	X_2	X_3	X_4	S	$Log_{10}K$
X_1	1	0	0	0	0	0
X_2	0	1	0	0	0	0
X_3	0	0	1	0	0	0
X_4	0	0	0	1	0	0
C_1	0	-1	0	0	0	-12
C_2	0	1	1	0	0	0
C_3	0	-1	0	1	0	0
C_4	0	-4	1	3	0	-1
C_5	0	4	3	1	0	35
S	0	0	0	0	1	0
CS_1	0	3	1	0	1	6
CS_2	0	-3	0	1	2	-1
$[T_j]$	0.3	0.3	0.3	2	10	

Table II-IV: Morel table for MoMaS Easy test case. MoMaS Easy and other synthetic benchmarks were designed specifically to evaluate the performances of computational codes.

	X_1	X_2	X_3	X_4	X_5	S	$Log_{10}K$
X_1	1	0	0	0	0	0	0
X_2	0	1	0	0	0	0	0
X_3	0	0	1	0	0	0	0
X_4	0	0	0	1	0	0	0
X_5	0	0	0	0	1	0	0
C_1	0	-1	0	0	0	0	-12
C_2	0	1	1	0	0	0	0
C_3	0	-1	0	1	0	0	0
C_4	0	-4	1	3	0	0	-1
C_5	0	4	3	1	0	0	35
C_6	0	10	3	0	0	0	32
C_7	0	-8	0	2	0	0	-4
S	0	0	0	0	0	1	0
CS_1	0	3	1	0	0	1	6
CS_2	0	-3	0	1	0	2	-1
Cp_1	0	3	1	0	0	0	10.9
Cp_2	0	1	0	0	1	0	1.3
$[T_j]$	0.3	0.3	0.3	2	0.3	10	

Table II-V: Morel table for MoMaS Hard test case. MoMaS Hard and other synthetic benchmarks were designed specifically to evaluate the performances of computational codes.

Annex III

In Table III- I are listed the $\log_{10}$ concentrations of the components that constitute the boundaries of the permitted intervals. When $X_1 = H^+$, the component concentration ranges between 0 and -14 coherently with the pH domain. Otherwise, the minimum value is linked to Avogadro's constant.

The values for the second component X_2 of the Fe Cr and Fe Cr Mineral test cases come from the following considerations regarding electric potential. H^+ is allowed to vary within the pH domain, i.e., from 0 to 14, while electrons e^- are allowed to generate a variation in electric potential from -1.2 V to +1.2 V. The electron activity and electric potential are linked through the following relationships at 25° C:

$$Eh = -\frac{RT}{F} \ln\{e^-\}$$

$$\{e^-\} = \exp\left(-\frac{F}{RT} Eh\right)$$

$$Eh = -\frac{8.314 \times (273.15 + 25)}{96\,485,3399} \ln\{e^-\} = -2.569 \times 10^{-2} \times \ln\{e^-\}$$

For an electric potential of Eh = -1.23 V, $\{e-\}$ = 1.6 10^{-21}. For Eh = 1.23 V, $\{e-\}$ = 6.2 10^{20}. On the other hand, the values for the second component of the Pyrite and Pyrite Mineral tests come from the following reaction:

$$O_2 + 4H^+ + 4e^- \rightleftharpoons 2H_2O .$$
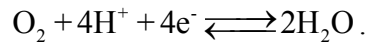
The concentrations of H^+ and activity of O_2 are linked through the following relationships:

$$Eh = E^0 + \frac{RT}{4F} \times \ln\left(\frac{\{O_2\}\left[H^+\right]^4}{\{H_2O\}}\right) = E^0 + \frac{RT}{4F} \times \ln\left(\{O_2\}\left[H^+\right]^4\right)$$

$$\left(Eh - E^0\right) \times \frac{4F}{RT} = \ln\left(\{O_2\}\left[H^+\right]^4\right)$$

$$\{O_2\} = \left[H^+\right]^{-4} \exp\left[\left(Eh - E^0\right) \times \frac{4F}{RT}\right]$$

For a pH of 14 and Eh = 1.23 V, $\{O2\}$ = 1. 10^{56}. For a pH = 1 and Eh = -1.23 V, $\{O2\}$ = 4.6 10^{-167}.

In table III-II are listed all the limitations that are imposed on the computation of the Newton Raphson increments and on the activity of components, where $\max H = \ln(1.0)$, $\min H^+ = \ln(10^{-14})$ and $\max X = 2$. No boundaries are imposed if the component is the activity of electrons. The only boundaries that are imposed on the concentrations of precipitates are the numbers that are allowed by the machine.

		X_1	X_2	X_3	X_4	X_5	X_6	X_7	Cp_1	Cp_2	Cp_3
Gallic	min	-14	-23	-23							
Acid	max	0	0	0							
Pyrite	min	-14	-164	-23	-23						
	max	0	54	0	0						
Pyrite M.	min	-14	-164	-23	-23				0	0	0
	max	0	54	0	0				0	0	0
MoMaS	min	-23	-23	-23	-23	-23					
E.	max	0	0	0	0	0					
MoMaS	min	-23	-23	-23	-23	-23	-23		0	0	
H.	max	0	0	0	0	0	0		0	0	
Fe Cr	min	-14	-21	-23	-23	-23	-23	-23			
	max	0	21	0	0	0	0	0			
Fe Cr	min	-14	-21	-23	-23	-23	-23	-23	0	0	0
Min.	max	0	21	0	0	0	0	0	0	0	0

Table III-I: Intervals for the initial guesses when searching for thermodynamic equilibrium. Activities expressed in $\log_{10}$ scale for components X_j and linear scale for concentration of precipitates Cp_l.

Maximum NR increment	$\max\left|\Delta X_j\right|$	5
Max concentration of $X_j = H^+$	$\max\left(X_j + \Delta X_j\right) =$	$9 + \max\left(H^+\right)$
Min concentration of $X_j = H^+$	$\min\left(X_j + \Delta X_j\right) =$	$-9 - \min\left(H^+\right)$
Max concentration of X_j	$\max\left(X_j + \Delta X_j\right) =$	$8\max\left(X\right)$

Table III-II: limitations that are imposed on the computation of the Newton Raphson increments and on the activities of the components.

Annex IV

The sequence of instructions below can be copied/pasted and run in PHREEQC Version 3.0.

```
TITLE test_validation -- Solid solution Modified Ex. 10
PHASES
        Strontianite
                SrCO3 = CO3-2 + Sr+2
                log_k           -9.271
        Aragonite
                CaCO3 = CO3-2 + Ca+2
                log_k          -8.336
SOLUTION 1
        -units mmol/kgw
        pH 7.0 charge
        Ca      3.932
        C       7.864
SAVE solution 1
END
USER_PRINT
-start
     10 sum = (S_S("Strontianite") + S_S("Aragonite"))
     20 if sum = 0 then goto 110
     30 xb = S_S("Strontianite")
     40 xc = S_S("Aragonite")
     50 PRINT "Log Sigma pi: ", LOG10 (ACT("CO3-2") * (ACT("Ca+2") + ACT("Sr+2")))
     60 PRINT "XAragonite   : ", xc
     70 PRINT "XStrontianite: ", xb
     80 PRINT "XCa          : ", TOT("Ca")/(TOT("Ca") + TOT("Sr"))
     90 PRINT "XSr          : ", TOT("Sr")/(tot("Ca") + TOT("Sr"))
-end
USER_PUNCH
-head   l_sigpi x_arag x_stront x_ca_aq x_sr_aq molmisc1 molmisc2 mol_arag
mol_stront
-start
     10 sum = (S_S("Strontianite") + S_S("Aragonite"))
     20 if sum = 0 then goto 60
     30 xb = S_S("Strontianite") #/(S_S("Strontianite") + S_S("Aragonite"))
     40 xc = S_S("Aragonite") #/(S_S("Strontianite") + S_S("Aragonite"))
     50 REM Sigma Pi
     60 PUNCH LOG10 (ACT("CO3-2") * (ACT("Ca+2") + ACT("Sr+2")))
     70 REM Mole Fraction Aragonite
     80 PUNCH xc
     90 REM Mole Fraction Strontianite
     100 PUNCH xb
     110 REM Mole Aqueous Calcium
     120 PUNCH TOT("Ca")/(TOT("Ca") + TOT("Sr"))
     130 REM Mole Aqueous Strontium
     140 PUNCH TOT("Sr")/(TOT("Ca") + TOT("Sr"))
     150 x1 = MISC1("Ca(x)Sr(1-x)CO3")
     160 x2 = MISC2("Ca(x)Sr(1-x)CO3")
     170 if (xb < x1 or xb > x2) then goto 270
     180    nc = S_S("Aragonite")
     190    nb = S_S("Strontianite")
     200    mol2 = ((x1 - 1)/x1)*nb + nc
     210    mol2 = mol2 / ( ((x1 -1)/x1)*x2 + (1 - x2))
     220    mol1 = (nb - mol2*x2)/x1
     230 REM Miscibility End Members If In Gap
     240    PUNCH mol1
     250    PUNCH mol2
     260    goto 300
```

```
      270 REM If Not In Miscibility Gap
      280 PUNCH 1e-10
      290 PUNCH 1e-10
      300 REM Moles Aragonite
      310 PUNCH S_S("Aragonite")
      320 REM Moles Strontianite
      330 PUNCH S_S("Strontianite")
-end
SELECTED_OUTPUT
        -file test_validation.sel
        -reset false
        -reaction true
USER_GRAPH
      -headings RXN Xss_CaCO3  Xss_SrCO3
      -chart_title "Validation Test"
      -axis_titles "LOG SrCO3 ADDED, in MOLES" "LOG Moles CaCO3, SrCO3"
      -axis_scale x_axis -5 1 1 1
      -axis_scale y_axis -5 1 1 1
      -connect_simulations true
      -start
      10 sum = (S_S("Strontianite") + S_S("Aragonite"))
      20 if sum = 0 then goto 70
      30 xb = S_S("Strontianite") #/ sum
      40 xc = S_S("Aragonite") #/ sum
       50 GRAPH_X LOG10(RXN)
       60 GRAPH_Y LOG10(xc), LOG10(xb)
       70 rem
       -end

USE solution 1
SOLID_SOLUTIONS 1
        Ca(x)Sr(1-x)CO3
                -comp    Aragonite       0
                -comp    Strontianite    0
REACTION 1
        SrCO3   1.0
        .005 in 500 steps
END
USE solution 1
USE solid_solutions 1
REACTION 1
        SrCO3   1.0
        .1 in 20 steps
END
USE solution 1
USE solid_solutions 1
REACTION 1
        SrCO3   1.0
        1.0 in 20 steps
END
```

271

Marianna MARINONI

Implémentation des isotopes dans un modèle hydrogéochimique couplé

Résumé

Ce travail décrit le développement d'un outil de simulation du transport réactif, nommé SpeCTr (Spéciation Cinétique Transport), intégrant le fractionnement isotopique. Ce modèle est obtenu à travers le couplage d'un module décrivant le transport et d'un module décrivant les principales réactions chimiques (approche de séparation d'opérateur).

Une grande partie du travail est dédiée à l'amélioration des algorithmes du module décrivant les réactions chimiques pour la résolution des équations de l'équilibre thermodynamique (méthode de Newton Raphson modifiée à travers les techniques du scaling et des Fractions Continues Positives) et du mélange de réactions cinétiques et à l'équilibre (étude sur la formulation et résolution des systèmes d'équations différentielles et différentielles-algébriques).

L'outil est validé à travers la résolution de plusieurs tests (batch et transport réactif) et appliqué pour la simulation d'expériences de laboratoire en 1D, 2D et 3D portant sur la dissolution des cristaux de calcite dans une colonne de milieu poreux.

MOTS CLES : Transport Réactif, séparation d'opérateur, isotopes, Newton Raphson, Equilibre thermodynamique, cinétique, 3D

Résumé en anglais

The work describes the development of a reactive transport code named SpeCTr (Spéciation Cinétique Transport in French). The code, able to describe isotopic fractionation, is obtained through the coupling of a transport module and a reaction module that describes the main chemical reactions (operator splitting approach).

A consistent portion of the work is dedicated to the improvement of the numerical methods employed in the reaction module for solving thermodynamic equilibrium (Newton Raphson method modified with scaling and Positive Continuous Fractions) and mixed equilibrium and kinetic reactions (formulation and solution of systems of differential and differential-algebraic equations).

The code was verified through the solution of different benchmarks (batch and reactive transport simulations) and applied to perform 1D, 2D and 3D simulations of laboratory experiments dedicated to calcite crystals dissolution in a column of porous medium.

KEYWORDS: Reactive Transport, operator splitting, isotopes, Newton Raphson, Thermodynamic Equilibrium, kinetics, 3D